

IN-SITU SPECTROSCOPIC STUDIES OF SINGLE-WALLED CARBON
NANOTUBES AND CONJUGATED POLYMERS IN ELECTROCHROMIC
DEVICES

By

MARIA NIKOLOU

A DISSERTATION PRESENTED TO THE GRADUATE SCHOOL
OF THE UNIVERSITY OF FLORIDA IN PARTIAL FULFILLMENT
OF THE REQUIREMENTS FOR THE DEGREE OF
DOCTOR OF PHILOSOPHY

UNIVERSITY OF FLORIDA

2005

ACKNOWLEDGMENTS

The past five years have been an intensely challenging, however enjoyable, life journey. During that time, I have been very fortunate to have been surrounded by exceptional people that greatly influenced my career and at the same time inspired me. The first person to whom I would like to express my sincere gratitude is my research advisor, Professor David B. Tanner, who welcomed me in his group, supported me and encouraged me from the very beginning. The time I have spent working under his supervision has proved to be an invaluable experience. Furthermore, I would like to thank him for his trust, and for allowing me to pursue a research path, which required close collaboration with the Chemistry Department.

In that different universe, a person that also had a major impact on my work, and to whom I would like to express my sincere gratitude, is Professor John R. Reynolds, who in reality has been a second advisor to me. For the last three years, he has welcomed me in his group, and he has tirelessly supported me, guided me, being always interested in and appreciative of my work. I have to admit that I feel extremely privileged having collaborated with these two excellent researchers and, above all, exceptional people.

I would also like to express my appreciation to many people: Professor Richard Woodard, for his help organizing my transition from Greece and with my initial adjustment to a new environment; Professor Katalin Kamaràs, for her help with the experiments, data analysis, guidance, input, and useful discussions involving the whole project described in Chapter 6; also, Professor Andrew G. Rinzler for providing high quality samples, and for always patiently answering all my questions concerning the subject of nanotubes which is covered in Chapters 6 and 7. I am also indebted to my supervisory committee, Professors Alan T. Dorsey, Arthur F. Hebard, and Pierre Sikivie, for their interest in serving on my committee.

Several coworkers have had an important role throughout the completion of the work presented in this dissertation. From the Chemistry Department I would like to thank my collaborators: Dr Irina Schwendeman, for her help when I was just starting my first project, and Dr Avni A. Argun for many useful and enjoyable discussions, as well as for his help in the chemistry laboratory. I am also very grateful to Aubrey L. Dyer for many useful and enjoyable discussions, her valuable help in the chemistry laboratory, and her friendship. I would also like to thank Timothy Steckler for providing me with the monomer for the work that is outlined in Chapter 7, and Nisha Ananthakrishnan for help with the AFM images. Finally, I would like to thank all remaining members of Prof. Reynolds' group; their group meeting presentations and useful discussions were an invaluable resource for me. I also wish to thank them for providing a pleasant, and productive environment to work.

From the Physics Department, I would like to thank my collaborators from Prof. Rinzler's group: Dr Zhihong Chen for providing the samples for the research outlined in Chapter 6 and for many useful discussions, Zhuangchun Wu for providing the samples for the research outlined in Chapter 7, and also Jennifer Sippel Oakley for help with the AFM images. From Prof. Kamaràs' group (Research Institute for Solid State Physics and Optics, Hungarian Academy of Sciences, in Budapest, Hungary), I thank Ferenc Borondics for collaboration on the research project outlined in Chapter 6. Last but not least, I would like to thank the people in Prof. Tanner's group, my past and present colleagues, the people I worked side by side with throughout my graduate years, for their cooperation, useful discussions, and their friendship. I would also like to thank Matt Cornick, an undergraduate student who joined our group through the REU program, for his help with the experiments outlined in Chapter 5, and Nathan Heston for his help with the last mid-infrared experiment outlined in Chapter 7.

I would also like to acknowledge the help of the members of the machine shop, especially Marc Link and John Van Leer, the people in the electronics shop, and the cryogenics team.

Furthermore, I wish to thank all my friends in Gainesville for the fun times we had together throughout these years. Finally, my deepest appreciation goes to my husband and my family for their constant support and love.

This work is dedicated to the memory of Maria B. Panousi.

TABLE OF CONTENTS

	<u>Page</u>
ACKNOWLEDGMENTS	ii
ABSTRACT	viii
CHAPTER	
1 INTRODUCTION	1
2 CONDUCTING, OR CONJUGATED, POLYMERS	5
2.1 Non-conjugated and Conjugated Polymers	5
2.2 Classification of Conjugated Polymers	9
2.2.1 Doping Mechanisms in DGSPs and NDGSPs	11
2.3 Theoretical Models	17
2.4 Conductivity in Conjugated Polymers (CPs)	19
2.5 Metal-Insulator (M-I) Transition	21
2.6 Doping Induced Properties in Conjugated Polymers	22
2.7 Doping Methods for Conjugated Polymers	24
2.8 Fundamentals of Electrochromism	28
2.9 Synthesis Methods of CPs	31
2.10 Characterization Methods of Electrochromic CPs	33
2.11 Electrochromic Devices (ECDs) Based on CPs	36
2.12 General Applications of CPs	38
3 THIN FILM OPTICS	40
3.1 Optical Processes and Optical Constants	40
3.2 Interaction of Electromagnetic Waves with Matter	42
3.3 Light Propagation Through a Planar Interface	49
3.4 Light Propagation Through a Single Layer Structure	53
3.5 Light Propagation Through a Multi-Layer Structure	58
3.5.1 Matrix Method	61
3.6 Kramers-Kronig, or Dispersion, Relations	62
3.7 Models for the Determination of Optical Constants	64
3.7.1 Lorentz Model	64
3.7.2 Drude Model	68
3.7.3 Drude-Lorentz Model	71
3.7.4 Sum Rules	72

4	INSTRUMENTATION AND EXPERIMENTAL TECHNIQUES	73
4.1	Dry Box	74
4.2	Electrochemical Methods	76
4.2.1	Electrochemical Polymerization	77
4.2.2	Cyclic Voltammetry (CV)	78
4.3	Optical Methods	79
4.3.1	Spectroelectrochemistry	79
4.3.2	Interferometric or FTIR Spectrometer	81
4.3.3	Monochromatic Spectrometer	93
5	REFLECTIVE ELECTROCHROMIC DEVICES (ECDS)	104
5.1	ECDs Fabrication	105
5.2	In-situ Reflectance Measurements and Analysis	109
5.3	Results and Discussion	110
5.4	Enhancing the Performance of ECDs	114
5.5	Conclusions	120
6	FREE-STANDING SINGLE WALLED CARBON NANOTUBE FILMS	122
6.1	Carbon Nanotubes	122
6.1.1	Electronic Structure of Carbon Nanotubes	125
6.1.2	Density of States (DOS) of SWNTs	127
6.1.3	Carbon Nanotube Synthesis and Purification	131
6.1.4	General Applications of CNs	132
6.2	Free-Standing SWNT Films: Transparency, and Optical Conductivity	133
6.2.1	Sample Preparation	133
6.2.2	In-situ Transmittance Measurements	136
6.2.3	Optical Constants, Data Analysis and Model Fit	146
6.2.4	Infrared Spectral Weights	152
6.2.5	Conclusions	152
7	TRANSMISSIVE/ABSORPTIVE EC DEVICES	155
7.1	Sample Preparation	155
7.1.1	Purification of Laboratory Chemicals and Materials	155
7.1.2	Electrode Preparation	157
7.1.3	Electrochemical Polymerization	157
7.1.4	Gel Electrolyte Preparation	159
7.2	PEDOT on SWNT Electrodes	160
7.2.1	Spectroelectrochemistry of PEDOT	160
7.2.2	Thickness Determination of PEDOT on SWNT Electrodes	164
7.2.3	Atomic Force Microscopy (AFM) Images	166
7.3	PBEDOT-Hx ₂ -Pyr-Pyr on SWNT Electrodes	168
7.3.1	Cyclic Voltammetry of PBEDOT-Hx ₂ -Pyr-Pyr	168
7.3.2	Spectroelectrochemistry of PBEDOT-Hx ₂ -Pyr-Pyr	169

7.4	Transmissive/Absorptive EC Device Construction	172
7.5	In-Situ Transmittance Measurements of EC Devices	174
7.5.1	Analysis of the Different Layers in the EC Device	175
7.5.2	Analysis of a PEDOT EC Device (with hole)	176
7.5.3	Results on PBEDOT-Hx ₂ -Pyr-Pyr EC Device (with hole)	183
7.6	Towards the construction of a Dual Device	189
7.6.1	Cyclic Voltammetry of PBEDOT-Hx ₂ -Pyr-Pyr dual device	189
7.6.2	In-Situ Absorbance Measurements	191
7.6.3	Switching Time	195
7.7	Conclusions	197

APPENDIX

A	NEXT GENERATION OF REFLECTIVE ECDS USING MICROPOROUS GOLD ELECTRODES	200
B	DRUDE-LORENTZ FITTING PARAMETERS	205
C	PBEDOT-HX ₂ -PYR-PYR	208
	REFERENCES	210
	BIOGRAPHICAL SKETCH	216

Abstract of Dissertation Presented to the Graduate School
of the University of Florida in Partial Fulfillment of the
Requirements for the Degree of Doctor of Philosophy

IN-SITU SPECTROSCOPIC STUDIES OF SINGLE-WALLED CARBON
NANOTUBES AND CONJUGATED POLYMERS IN ELECTROCHROMIC
DEVICES

By

Maria Nikolou

December 2005

Chairman: David B. Tanner
Major Department: Physics

Our initial focus has been the optimization of the performance of reflective electrochromic devices. In-situ reflectance measurements and extensive subsequent analysis enabled us to construct devices with significantly enhanced performance. Variable reflective electrochromic devices based on PProDOT-Me₂ and PBEDOT-NMeCz were optimized to exhibit contrast ratios of 60-70% in the mid-infrared region. In the latter region, two strong absorption peaks, O-H stretching mode and C-H stretching mode, were hindering the performance of the devices. A novel technique was developed in order to build water-free devices. In addition a new sample holder was designed that permits control of the electrolyte gel thickness, and reduces the C-H signature.

Building upon the aforementioned techniques, we designed an infrared transmissive/absorptive type of electrochromic cell. The construction of such a device had been previously impossible due to the absence of a suitable, infrared transparent, conducting material. An extensive study of single-walled carbon nanotubes as free-standing films showed that these films have the highest transmittance among transparent conductors in the 2-5 μm spectral range, at very low sheet resistance. Transmittance measurements on purified (p-doped) and vacuum annealed (de-doped) carbon nanotube films

were performed and analyzed from far infrared through ultraviolet, at temperatures between 50 K - 300 K. The result of this study led us to propose the construction of the very first transmissive/absorptive EC device in the infrared region using SWNTs as the conducting layer. The polymer that was used in the devices is PBEDOT-Pyr-Pyr which can be both p- and n- doped.

CHAPTER 1 INTRODUCTION

The main focus of this work is the optical characterization of conjugated polymers in different electrochromic device platforms, in an effort to optimize the performance of these devices. Furthermore, an attempt to develop the first infrared transmissive/absorptive electrochromic device, led to extensive studies on single-wall carbon nanotude (SWNT) films. This material proved to be the best candidate for the replacement of the conventional indium-doped tin oxide (ITO), which served as the conducting layer in electrochromic devices, for the infrared region. Preliminary results of the performance of this type of devices are also presented in this work.

More specifically, the second chapter offers an introduction to the theoretical background that is necessary for the understanding of conjugated polymer systems. This includes a presentation on the different types of conjugated polymers and their unique characteristics, such as the doping mechanisms, and the induced structural and optical property changes. A brief description in the charge transport mechanisms, and the metal-insulator transition occurring in conjugated polymers is also given in this chapter. Different polymerization, doping, and characterization methods, and several theoretical models that attempt to explain the behavior of these systems are introduced. Finally, the phenomenon of electrochromism is defined, and general applications based on conjugated polymers are presented.

The third chapter is a review of the basic laws that govern the interaction of electromagnetic waves with matter. Optical processes and common techniques for extracting the optical constants, which characterize each system, are introduced and explained. Light propagation through different structures is described, and the formulas for the calculation of the reflectance and transmittance through these structures, as well as the related optical parameters are derived. The chapter concludes with the presentation of

the dispersion, or Kramers-Kronig, relations and the models, Drude and Lorentz models, that are used for the determination of the optical properties of the media.

The fourth chapter introduces the instrumentation, and experimental techniques used throughout this work. A description of systems such as the dry box, or glove box, and the different types of spectrometers, interferometric and monochromatic, is provided. The concepts of Fourier spectroscopy are presented. Techniques for the production and/or characterization of samples, such as electrochemical polymerization and cyclic voltammetry are introduced.

In chapter five, the fabrication of reflective electrochromic devices is presented. Details on the design, the assembling, and the materials used are provided. In-situ reflectance measurements, and analysis of the experimental results are discussed. The problems that were encountered, and the ways to overcome them in an effort to enhance the performance of these devices are also presented. Finally, a design of a new type of sample holder, which is part of the problem solution is described here.

Chapter six includes an introduction on the theoretical background that is necessary for the understanding of carbon nanotube systems. This includes a presentation on the different types of nanotubes and their unique characteristics, such as the dependence of their electronic structure on the tube diameter and wrapping angle of a graphene sheet, with no doping impurities present. Furthermore, the electronic density of states (DOS) in carbon nanotubes is not continuous, as it is in graphite, but it divides into a series of spikes caused by the quantum confinement of electrons in the radial and circumferential directions. These spikes are known as van Hove singularities, and they comprise a typical signature of 1D systems. Typical synthesis, purification techniques and general applications of carbon nanotubes are mentioned, as well as a brief description of the sample preparation. Transmittance spectra of as-prepared (purified), p-doped, and vacuum annealed, de-doped, free-standing SWNT films of different thicknesses, are presented from the far infrared through the ultraviolet region, at different temperatures. The analysis of the data includes the use of Kramers-Kronig relations for

the determination of the optical properties of carbon nanotubes, optical conductivity and infrared spectral weights, and the Drude-Lorentz model for the fitting of the transmittance data and the optical conductivity. The conclusions that were drawn from this extensive study are presented at the end of the chapter.

In Chapter seven, transmissive/absorptive EC devices were built using two different electroactive polymers and, for the first time to the best of our knowledge, SWNT films were used as the conductive layers in EC devices. Initially, we conducted a comparison study between the performance of SWNT films, used as the conductive electrodes, and the well studied and extensively used ITO. Cyclic voltammograms and absorbance measurements in solution for both polymers used in the devices were performed, and conclusion were drawn. Furthermore, two different configuration were used, and transmittance or absorbance measurements, data analysis based on the Drude-Lorentz model, as well as stability studies were performed. The first configuration, is an EC device with hole on the counter electrode, employed PEDOT as the electroactive film which can be switched between a neutral and a p-doped state. The second configuration, is a dual EC device, employed PBEDOT-Hx₂-Pyr-Pyr as the electroactive film which is one of a few polymers that can be switched not only between neutral and p-doped states, but also between neutral and n-doped states. The constructed transmissive/absorptive dual EC device that exhibits electrochromic changes from the visible to the infrared region. This is the first transmissive/absorptive dual EC device exhibits electrochromism in the infrared spectral region. Further optimization studies are needed for both types of devices. The conclusions that were drawn from this extensive study are presented at the end of the chapter.

In spectroscopic studies, different energy units are often used for different techniques, different parts of the electromagnetic spectrum, and between different disciplines. In general, the most commonly used unit for the infrared region of the spectrum is the frequency or wavenumber, expressed in cm^{-1} , whereas for the visible region of the spectrum, is the wavelength expressed in nm. Throughout this work these units are used

interchangeably. Hopefully this fact does not cause any confusion to the reader, since these units are simply related to each other: $\bar{\nu}(\text{cm}^{-1}) = 10^4/\lambda(\mu\text{m}) = 10^7/\lambda(\text{nm})$. The relation between the frequency and energy units is provided in Table 1.1.

Table 1.1: Relation between energy units.

1 cm^{-1}	0.124 meV
1 meV	8.0658 cm^{-1}

CHAPTER 2 CONDUCTING, OR CONJUGATED, POLYMERS

The discovery of conducting polymers in 1977 by Alan J. Heeger, Alan G. MacDiarmid, and Hideki Shirakawa [1] created a new research field that has been studied intensively since. Although conducting polymers had been initially introduced in 1862 when poly(aniline), or PANI, was synthesized [2] it was the collaborating effort in 1977 of the 2000 Nobel laureates [3–7] which led to the discovery of poly(acetylene) (PAC), that invigorated the interest of the research community. This work showed that organic conjugated polymers have the ability to be doped over the full range from insulator to metal, and offered the promise of a new type of polymers: materials which exhibit the electrical and optical properties of metals, or semiconductors, while retaining the attractive mechanical properties and processing advantages of polymers. This new generation of polymers created a new field of interdisciplinary research, on the boundary between chemistry and physics, and new enormous potential applications.

2.1 Non-conjugated and Conjugated Polymers

Polymeric materials, such as plastics, date back to the 19th century. These materials, also called non-conjugated or saturated polymers, were basically known for their mechanical and chemical properties, and were considered to be electrically insulating materials. This is due to their electronic configuration which is $1s^2 2s^2 2p^2$, and thus, the carbon (C) atoms have their four valence electrons tied up in covalent bonds. These polymers have an sp^3 hybridization, which means that each carbon has four bonds with equivalent energy, four σ -bonds. The $\sigma - \sigma^*$ gap, or energy band gap, E_g , in condensed matter terminology, is large, i.e., 8-10 eV, and therefore non-conjugated polymers are electrically insulating and transparent in the visible region.

Conducting, or conjugated, polymers are the most recent generation of polymers, and their electronic configuration is fundamentally different. In conjugated polymers, carbon atoms have the following hybridization: sp^2p_z , which leads to three equivalent σ -bonds and one π -bond from the remaining p_z atomic orbital. The π -bonding, which occurs when two p_z orbitals of successive carbon atoms along the backbone overlap, results in electron delocalization, and hence in charge mobility along the polymer chain [8]. This delocalization is responsible for the unique properties of conjugated polymers. The π - π^* gap, or energy gap, E_g , is relatively small, i.e., 1-4 eV, and this is the reason for the semiconducting behavior of conjugating polymers. Therefore, the polymer chain symmetry plays an important role in determining the electronic structure, and consequently careful design of the monomer unit along with doping can result in systems with metallic properties. The bond formation of conjugated polymers is shown schematically in Figure 2.1.

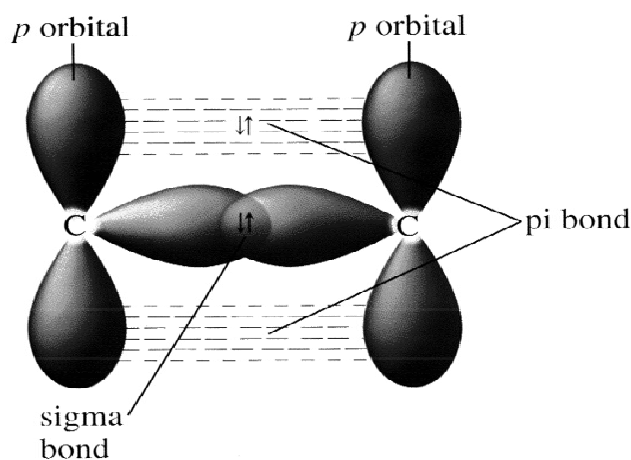


Figure 2.1: Formation of σ -bond by strong overlapping of two sp^2 - orbitals and formation of π -bonds by weak overlapping of the p_z -orbitals of two successive carbon atoms.

Each carbon atom along the backbone of conjugated polymers has one unpaired π -electron, the orbital of which overlaps strongly with the orbitals of the nearest unpaired π -electrons and weakly with orbitals of unpaired π -electrons in different polymer chains. The first one is known as intrachain interaction and the second as interchain interactions. These bonds, strong inside the polymer chain and weak, van der Waals type, between

different chains, make the system essentially quasi-one dimensional in the sense that the charge carriers move free only along the backbone of the polymer chain [9]. Based on this intrinsic low dimensional geometry of polymers, such as poly(acetylene), early theoretical studies treated them as one-dimensional metals, and expected them to have equal C-C bond lengths along the chain Figure 2.2.

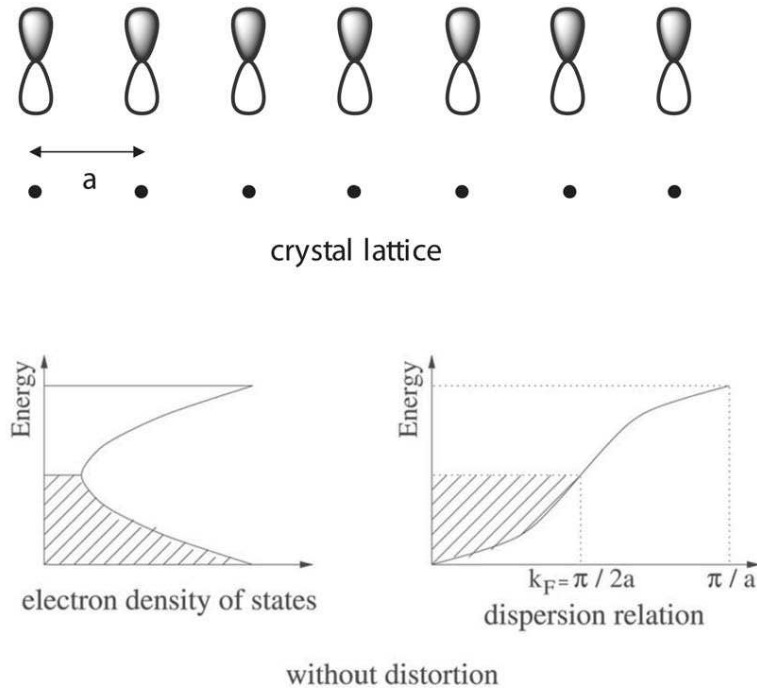


Figure 2.2: The polymer chain treated as one-dimensional metal, with equal C-C bond lengths along the polymer chain.

However, according to Peierl (1955) the ground state of such a one-dimensional metal is unstable with respect to a structural distortion, which results in the creation of alternating double and single bonds, as shown in Figure 2.3. As a result, a spontaneous symmetry breaking occurs, and an energy gap opens at the Fermi level rendering the material semiconductor [9]. This symmetry breaking, or Peierl's distortion, doubles the unit cell, as shown in Figure 2.4, and concentrates the π -electrons between alternating pairs of carbon atoms. This is consistent with conjugated polymers having alternating single and double bonds, or longer and shorter bonds (1.446 \AA and 1.346 \AA respectively

[10]) along their backbones. Figure 2.5 illustrates the bond alteration for a number of conjugated polymers.

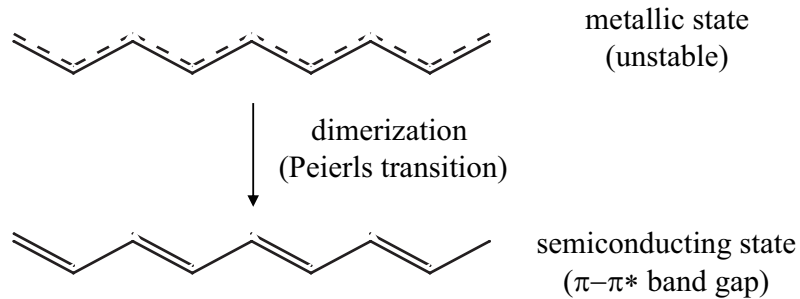


Figure 2.3: Peierls transition or dimerization, trans-poly(acetylene) is shown as an example.

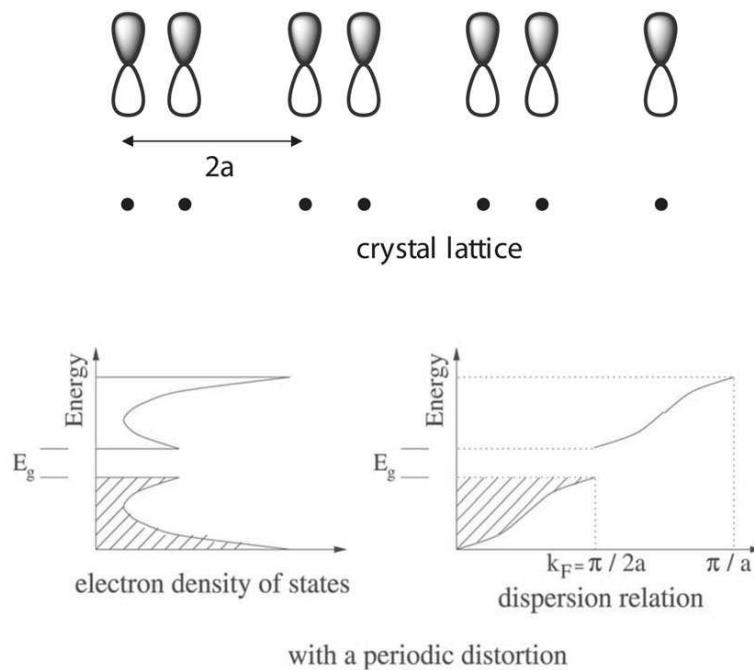


Figure 2.4: Periodic distortions or defects for systems with half filled band. E_g is the band gap cause by the distortion; k_F is the Fermi wavevector; a is the size of the unit cell before the distortion.

The lowering of the symmetry lowers the energy of the occupied states and stabilizes the distortion. Thus, the π band is split into two subbands, a fully occupied π band (also called the HOMO: Highest Occupied Molecular Orbital, valence band, or

bonding orbital), and an empty π^* band (also known as the LUMO: Lowest Unoccupied Molecular Orbital, conduction band, or anti-bonding band), with a certain energy band between, the so called $\pi - \pi^*$ energy band gap (Figure 2.4). The competition between the lowering of the electronic energy and the increase of the elastic energy of the polymer, caused by the distortion, leads to the equilibrium bond-length modulation. Therefore, Peierl's transition removes the states at the Fermi surface and renders the system a semiconductor [9].

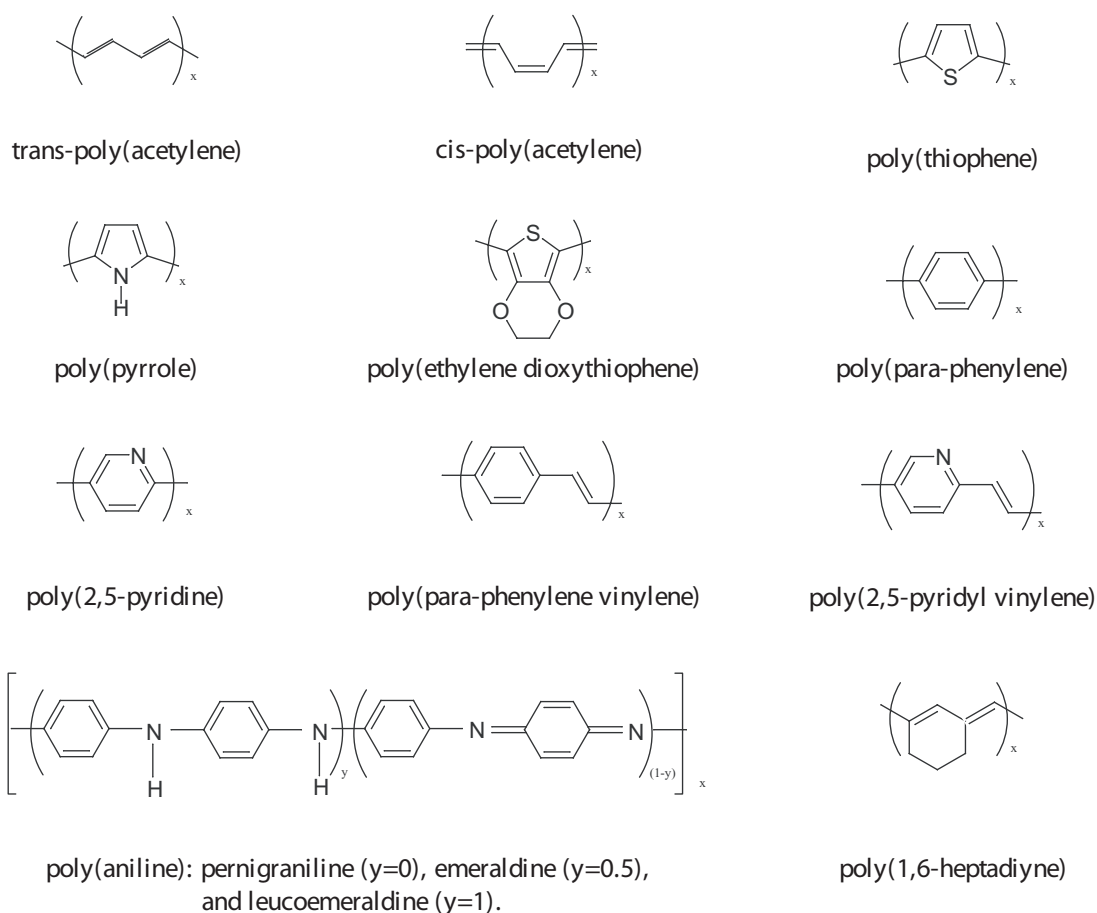


Figure 2.5: Typical conjugated polymers with alternating single and double bonds.

2.2 Classification of Conjugated Polymers

Conjugated polymers can be classified into two groups according to whether their ground state is degenerate or not. For degenerate ground state polymers (DGSPs) the double and single bonds can be interchanged without a change in the ground state

energy. Therefore, for this group of polymers the ground state has two configurations, A and B, with the same energy, as shown in Figure 2.6 for trans-polyacetylene, which is the simplest example of this category. Another example of degenerate ground state polymer, is poly(1,6-heptadiyne). The structure of these polymers is shown in Figure 2.5.

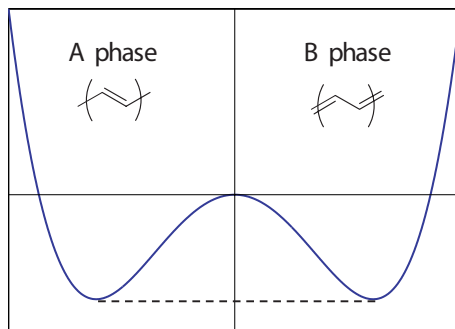


Figure 2.6: Potential energy curve for trans-PAc showing the two equivalent structures.

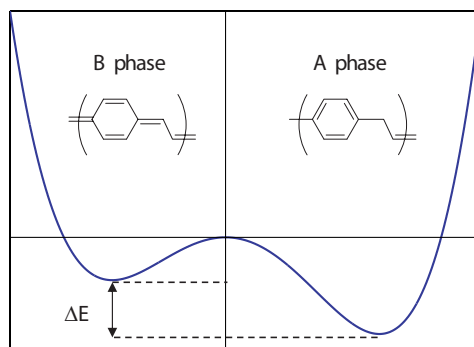


Figure 2.7: Potential energy curve for poly(para-phenylene vinylene) in its two energetically inequivalent structures, aromatic (A) and quinoid (B).

For the second group of conjugated polymers, the so called non-degenerate ground state polymers (NDGSPs), the interchange of the double and single bonds leads to two energetically inequivalent configurations. In Figure 2.7 poly(para-phenylene vinylene) is shown as an example in which the quinonoid (or quinoid) structure (B) is less stable

and therefore higher in energy than the aromatic phase or benzenoid (or benzoid) type of structure (A). Other polymers included in this category are cis-PAC, PTh, PPP, as shown in Figure 2.5.

2.2.1 Doping Mechanisms in DGSPs and NDGSPs

Initially, theoretical models from condensed matter physics that apply to conventional semiconductors were adopted by workers, in an effort to understand the doping mechanisms in conjugated polymers. However, it was soon realized through experimental results that the doping mechanisms in these organic materials is fundamentally different. Although conjugated polymers develop π and π^* orbital bands that can be thought of as the valence and conduction bands of a conventional semiconductor, the doping process is quite different. The introduction of charges in these polymer systems leads to a structural distortion of the lattice in the vicinity of the charge, which lowers the energy of the system and stabilizes the charge.

More specifically, upon doping of conjugated polymers, different types of excitations occur depending on which of the categories, DGSPs or NDGSPs, the polymer belongs. For degenerate ground state polymers, e.g., trans-polyacetylene, the introduction of electrons, and/or holes, to the polymer chain, creates a domain wall that separates regions of different bonding structure, i.e., phase A and B Figure 2.8. These excitations were initially called “misfits” but later, in view of the fact that the domain wall is a nonlinear shape preserving excitation which propagates freely along the polymer chain, they were called “solitons” [9]. Solitons are topological excitations, and since they convert phase A structure to phase B structure, and vice versa, in a perfect infinite chain they can only be created or destroyed in pairs.

While the soliton has an obvious effect on the lattice distortion pattern of the polymer chain, it also has a remarkable effect on the electronic structure. The localized distortion gives rise to a single localized electronic state in the middle of the energy band gap region. This mid-gap state is a solution to the Schrödinger equation in the presence of a structural distortion and therefore, can accommodate 0, 1, or 2 electrons.

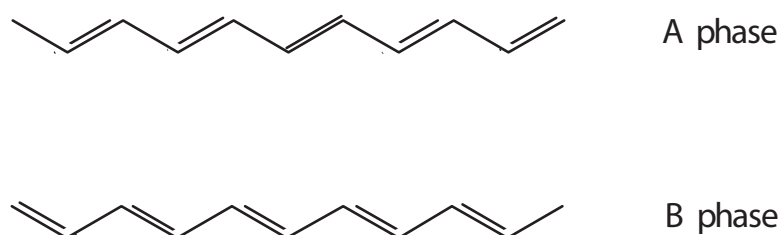


Figure 2.8: Different bonding structure of DGSPs, phase A and phase B.

When the state is singly occupied (i.e., occupied by one electron) the soliton possesses no charge, has spin $1/2$, and is said to be a neutral soliton or a neutral free radical. Upon doping, an electron can be introduced to, or removed from, this state leading to a charged soliton, negative or positive respectively, that carries no spin. A schematic diagram for these three types of solitons is shown in Figure 2.9, and a band diagram and the associated new optical transitions permitted by symmetry are shown in Figure 2.10.

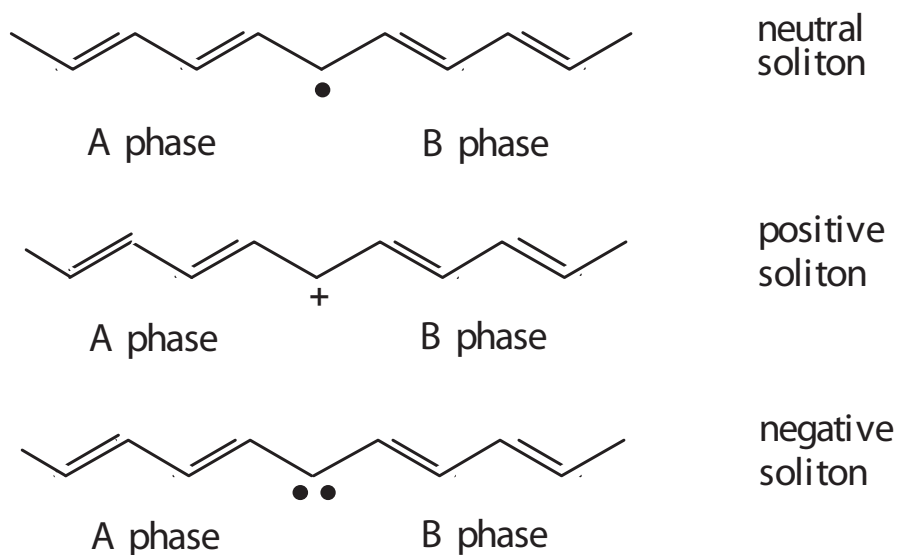


Figure 2.9: A schematic diagram of A and B phase, and of the neutral and charged solitons in trans-polyacetylene.

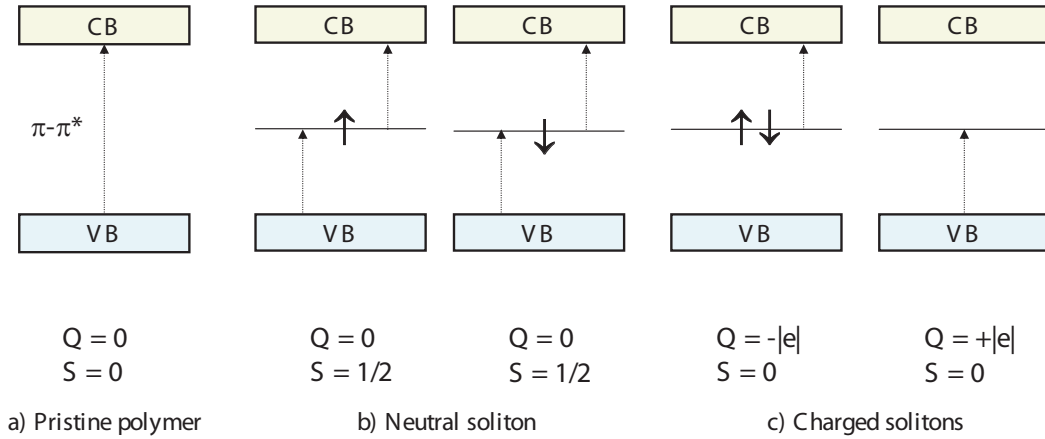
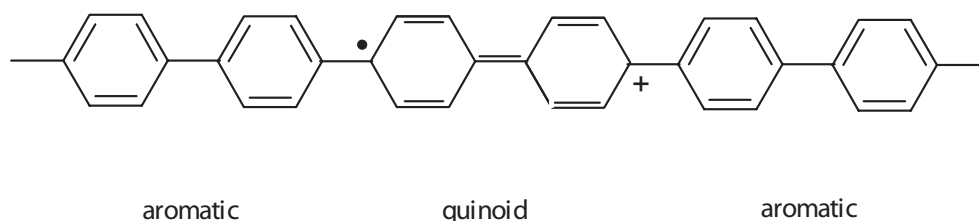


Figure 2.10: Electronic structure of solitons in trans-polyacetylene, DGSPs. The dashed lines show the symmetry allowed optical transitions.

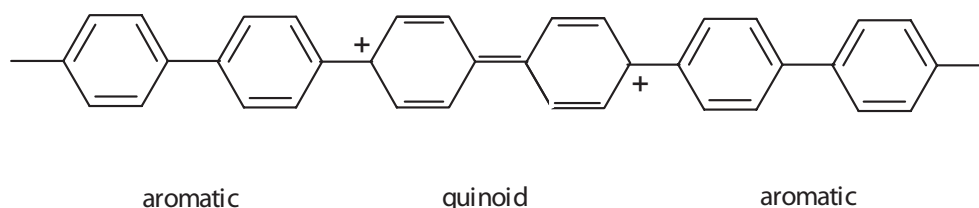
In degenerate ground state polymers, the soliton excitation is delocalized and free to extend over several monomer units. Therefore, the change from one structural phase to the other is not abrupt as shown in Figure 2.9, but rather gradual over the extended soliton where the lengths of the single and double bonds are changing slowly until they are reversed. It has been shown [11] that in trans-polyacetylene the soliton excitation extends approximately over fourteen monomer units.

Lifting the degeneracy of the ground state energy leads to significant changes not only for the ground state properties but also for the formation of the excitations. A consequence of the degeneracy lifting is that solitons are not the stable excitations anymore. Thus, upon doping the group of non-degenerate ground state polymers, e.g., poly(para-phenylene vinylene) or poly(thiophene), forms a different type of excitations, or charge storage species, called polarons and bipolarons. Polarons and bipolarons are non-topological because, in contrast with solitons, both sides of the chain are in the same bonding phase (A or B) when they are created Figure 2.11.

These excitations are simply charges in an extended lattice, which are stabilized by a local distortion. This localized distortion generates two symmetrically placed, with



a) Polaron excitation in PPP.



b) Bipolaron excitation in PPP.

Figure 2.11: Polaron (a), and bipolaron (b) excitations in NDGSPs, here shown in PPP.

respect to the center of the band gap, localized electronic states, or bonding and anti-bonding levels. The schematic band diagrams for these excitation types, and their associated new optical transitions permitted by symmetry, are shown in Figure 2.12 and Figure 2.13.

In more detail, the formation of a charged polaron, or radical cation or anion, is the stable excitation for NDGSPs when the system is slightly doped. A polaron can be thought of as a bound state of a charged soliton with a neutral soliton, and thus it possesses charge and has spin 1/2. It has been shown [9, 12] that by increasing the doping level of the conjugated polymer system, the formation of two polarons is energetically more favorable than the creation of a bipolaron. This is because the lattice distortion required for the creation of a bipolaron corresponds to greater shifts in the localized HOMO and LUMO (valence band and conduction band). Therefore, the system becomes saturated with polarons first, before the bipolarons begin to form. This is supported by Electron Spin Resonance (ESR) experiments [12], where at low doping

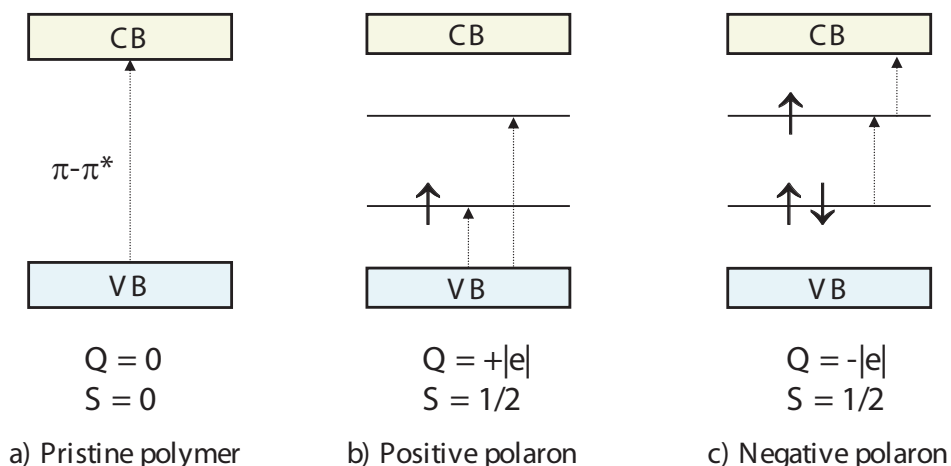


Figure 2.12: Electronic structure of polarons in NDGSPs. The dashed lines show the symmetry allowed optical transitions.

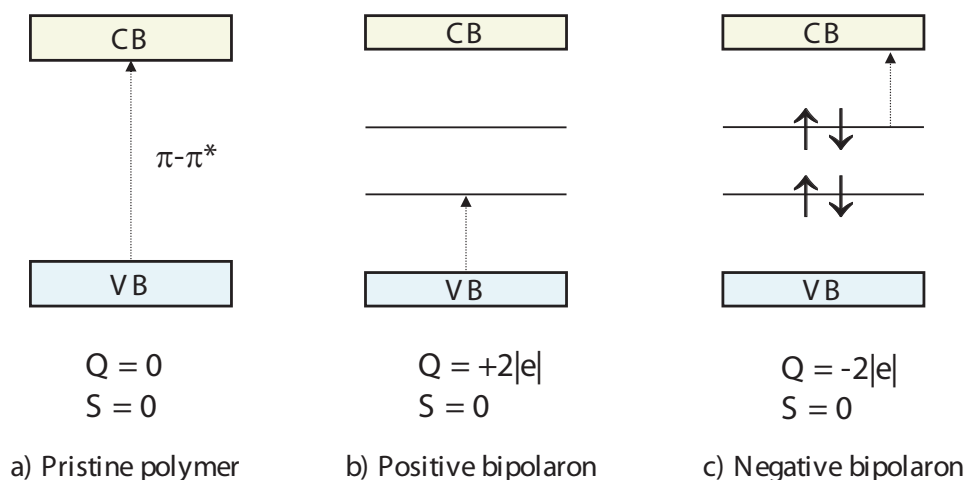


Figure 2.13: Electronic structure of bipolarons in NDGSPs. The dashed lines show the symmetry allowed optical transitions.

levels and as the doping increases, the ESR signal grows (formation of polarons with spin $1/2$) until at intermediate doping it saturates, and then decreases as the polarons combine to form bipolarons. The formation of two polarons instead of a bipolaron at low and intermediate doping levels has also been proven by spectroscopic studies. As it will be seen later in spectroscopic measurements, when the doping level is low, only absorptions due to polarons occur, whereas as the doping level increases absorptions due to bipolarons commence.

At higher doping levels, the formation of a charged bipolaron, or radical dication or dianion, is the stable excitation for NDGSPs. A bipolaron is a bound state of two charged solitons of the same charge, or two polarons of the same charge whose neutral solitons annihilate each other. Thus, bipolarons possess charge but carry no spin. The creation of a bipolaron generates two symmetrical mid-gap energy states, as in polarons but located closer to the center of the gap. When these mid-gap states are empty the bipolaron is positive (p-type doping), whereas when they are fully occupied the bipolaron is negatively charged (n-type doping). These excitations are delocalized over several monomer units, generally six to eight, and thus can propagate along the polymer chain.

As the doping level is further increasing, the individual bipolaron levels described above, shown in Figure 2.13, coalesce into bands. These bipolaron bands arise from the depletion of electronic states from the valence and conduction band edges, which results in a concomitant increase of the $\pi - \pi^*$ gap. At these high doping levels, bipolarons can give rise to high conductivity upon the application of an electric field. ESR experiments have proven that in highly conductive conjugated polymers (CPs) the charge carriers are spinless, and therefore bipolarons, since no signal can be detected [12].

Most cases considered in literature refer to positively charged polarons and bipolarons, i.e., p-type doping or oxidation of the conjugated polymers, because most CPs cannot form stable negatively polarons or bipolarons.

The concept of doping in CPs is unique for many reasons. First, the doping process is reversible, and the de-doping process produces the neutral polymer with little or no degradation. Second, it involves the formation of mobile excitations, such as solitons, polarons, and/or bipolarons, that couple to lattice vibrations. Third, unlike doping in conventional semiconductors, in CPs the dopant atoms do not substitute atoms within the lattice but are positioned between the polymer chains, and donate or accept electrons from the polymer backbone [13]. Finally, the doping level can be controllably adjusted, and thus the conductivity can be tuned over several orders of magnitude in the same

material. Conductivities varying from the insulating or semiconducting regime, when the CP is in the pristine form, to highly conducting regime, when the CP is fully doped, can be easily obtained.

2.3 Theoretical Models

Conjugated polymers are complicated systems, mainly due to the many degrees of freedom they possess, e.g., σ bands, π bands, lattice vibrations, intrachain and interchain interactions, and the nonlinear phenomena which are characteristic of one dimensional systems. Furthermore, real life makes the situation even more difficult, since the polymer chains have limited conjugation lengths, may contain defects or impurities, and cross-linking. Moreover, different synthetic methods can produce quite different morphologies, and hence different properties, for the same polymer. All these factors make a complete theoretical description a real challenge.

The highly anisotropic character shown by these one dimensional materials causes the electronic motion to be easy only along the backbone of the polymer chain. Therefore, the properties of these materials are mainly governed by the following types of interactions among the unpaired electrons that occupy the highest molecular orbitals in the solid: (1) the overlap of the wave functions of these electrons between adjacent sites in the polymeric chain; (2) the interactions of the electrons with their surroundings, in particularly with the lattice vibrations (electron-phonon coupling); and (3) the Coulomb interaction between the electrons (electron-electron coupling). Various theoretical models, based on the simple tight binding model, have been developed, taking into account some of the above interactions in an effort to provide a more realistic description of these system.

A very well known model, used for the theoretical treatment of conjugated polymer systems, is the Su-Schrieffer-Heeger (SSH) model. This method was initially applied to poly(acetylene), and yielded useful information for the interpretation of experimental data. This SSH treatment of polymeric systems includes the electron-lattice vibration interactions, omits the electron-electron interactions, and models the CP chain, or lat-

tice, potential in the form of classical springs between neighboring chain sites. Therefore, the SSH Hamiltonian is written as follows [9, 11, 14]:

$$H_{SSH} = - \sum_{n,s} t_{n+1,n} (c_{n+1,s}^\dagger c_{n,s} + c_{n,s}^\dagger c_{n+1}) + \frac{1}{2} \sum_n K (u_{n+1} - u_n)^2 + \frac{1}{2} \sum_n M \dot{u}_n^2 \quad (2.1)$$

where it has been assumed that the π electrons can be treated in the tight binding approximation with a hopping integral $t_{n+1,n}$, which can be expanded to first order around the undimerized state (before the Peierl's distortion, all bonds are of equal length):

$$t_{n+1,n} = t_0 + \alpha (u_{n+1} - u_n), \quad (2.2)$$

where t_0 is the hopping integral for the undimerized state, and α is the electron-lattice displacement (phonon) coupling constant. This linear approximation is valid, since the bond-length changes are small, of the order of 0.08 \AA . In equation (2.1), $c_{n,s}^\dagger$ and $c_{n,s}$ create and destroy π electrons of spin $\pm 1/2$ on the n^{th} repeated unit. These creation and annihilation operators satisfy the anticommutation relations of fermions. The second term in this equation corresponds to the σ bonding energy, which has been expanded to second order around the undimerized state. The first order term can be neglected due to symmetry. Finally, the third term in equation (2.1) is the kinetic energy of nuclear motion, where M is the total mass of the repeated unit. This term can also be written as $M \dot{u}_n = p_n$, where p_n and u_n satisfy canonical commutation relations:

$$[p_n, u_{n'}] = \frac{\hbar}{i} \delta_{nn'}. \quad (2.3)$$

Another model used for the theoretical treatment of conjugated polymer systems, is the Pariser-Parr-Pople (PPP) model. This model considers the electron-electron coupling, V , or Coulomb interaction, while neglecting the electron-phonon coupling. The PPP Hamiltonian is written as follows [15]:

$$H_{PPP} = - \sum_{i,s} t_{i+1,i} (c_{i+1,s}^\dagger c_{i,s} + c_{i,s}^\dagger c_{i+1,s}) + U \sum_i n_{i,\uparrow} n_{i,\downarrow} + \frac{1}{2} \sum_{i,i'} V_{i,i'} (n_i - 1)(n_{i'} - 1) \quad (2.4)$$

where

$$n_i = c_{i,\uparrow}^\dagger c_{i,\uparrow} + c_{i,\downarrow}^\dagger c_{i,\downarrow}, \quad (2.5)$$

is the number operator. U , $V_{i,i'}$ are a way to parameterize the electron-electron interaction. The potential U is effective only when two electrons occupy the same site, whereas $V_{i,i'}$ is effective for electrons that occupy different sites.

In addition to the ones generally described above, there are other well known models used for the theoretical treatment of conjugated polymer systems. These include the Hubbard model, the extended Hückel model, the Valence Effective Hamiltonian (VEH) method, the Peierl-Fröhlich method, and more.

2.4 Conductivity in Conjugated Polymers (CPs)

Since the discovery of conjugated polymers [1] the main goal has been the replacement of conventional metals and inorganic semiconductors with these low cost and light weight materials. The un-doped, or pristine, materials are generally semiconductors with conductivities typically in the range 10^{-10} - 10^{-5} S/cm, but upon doping their conductivity can increase by several orders of magnitude and render them metallic. Poly(acetylene), which initially was the most studied CP, upon heavy doping with iodine can achieve very high electrical conductivity, close to the electrical conductivity of copper ($\sim 10^6$ S/cm). However, its high chemical instability under ambient conditions has precluded the use of P(Ac) from commercial applications, and has confined it to its scientific aspects. Figure 2.14 shows the range of electrical conductivities of the most common conjugated polymers as the doping level is varied.

Experimental studies have shown [5] that the electrical conductivity of CPs improves as the degree of chain extension and chain alignment is increased. The studies

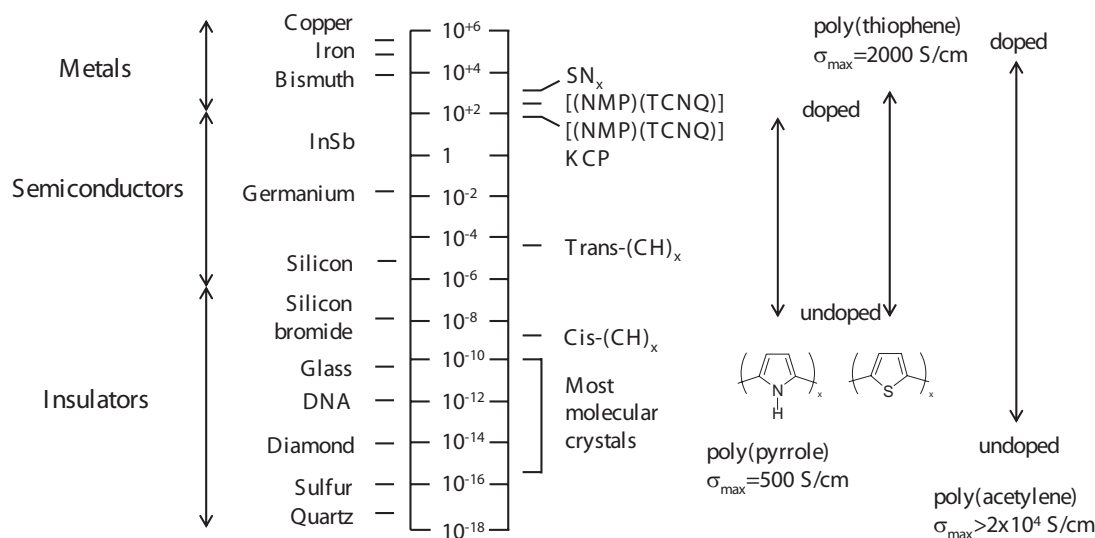


Figure 2.14: The conductivity of conjugated polymers ranges from values close to those of metals to value for insulators depending on the level of doping.

were performed in thin CP films, which can be made of high quality and in which homogeneous doping can be achieved.

The mechanism of charge transport in CPs has been the subject of research over a long period of time. An important feature of these systems in their doped state is that the variation of conductivity with temperature is different compared to conventional metals. In general, as the temperature lowers the conductivity decreases, although for some of the most highly conducting polymers the conductivity remains high even at low temperatures [13, 16]. This difference in behavior between CPs and metals seems to be the result of disorder effects [13, 17]. When the doping of CPs does not occur in a homogeneous way, the films consist of highly conductive islands, or ordered domains, surrounded by less conductive, or even insulating, material. These latter, less ordered or amorphous regions, serve as potential barriers for the charge transport.

A variety of different transport processes contribute to the conduction mechanism. These include intrachain and interchain transport within the ordered domains, as well as hopping or tunneling across disordered regions. Hence, several conduction models have been developed over the years in an effort to understand, and account for the different

conduction mechanisms. Some of the most well known models are the Mott Variable Range Hopping (VRH) model, Sheng model, and the Kivelson model [17]. Each of these models is valid under different conditions, such as different doping levels, temperature ranges, etc.

Finally, given that conjugated polymers show tunable conductivities in their doped states with values, in some cases, that can reach those of conventional metals, one cannot help but wonder if there is a possibility that these systems will exhibit superconductivity. Although conjugated polymers share many features with organic materials, such as the tetramethyltetraselenafulvalence family, $(\text{TMTSF})_2\text{X}$ [18], and methylenedithio-tetraselenafulvalene family $(\text{MDT-TSF})\text{X}_{1.27-1.29}$ [19] where X is usually a halogen, which exhibit superconductivity, this phenomenon has not been observed yet for doped conjugated polymeric systems. Workers in the field appear to be optimistic towards this idea but there is still a lot of progress that needs to be done. Currently available materials are barely metallic with electronic properties which are dominated by disorder, rendering the characteristic mean free paths in the region for disorder-induced localization. Therefore, the first step in the direction of truly metallic conjugated polymers is the improvement of the materials quality, which will eventually result in longer mean free paths, ideally of the order of the monomeric unit.

2.5 Metal-Insulator (M-I) Transition

X-ray studies have shown that CP systems generally consist of ordered, highly conductive, regions, surrounded by less ordered or amorphous material [13]. As the degree of disorder increases in a metallic system, there is a point at which the mean free path becomes equal to the interatomic spacing, and that results in the localization of the charge carriers which renders the material in a non-conducting state. The criterion for this metal-insulator transition, proposed by Ioffe and Regel in 1960, is defined as:

$$k_F l \approx 1 \tag{2.6}$$

where k_F is the Fermi wavenumber, and l is the mean free path. The metallic regime exists for $k_F l \gg 1$.

Based on the above criterion, Mott stated that for a metal-insulator transition to occur, the disorder should be sufficiently large that $k_F l > 1$ [20–22]. In the limit where $k_F l \ll 1$, the average disorder potential becomes large compared to the bandwidth and thus, all states become localized. In this case, the system becomes an insulator and is called a Fermi glass. Even though Fermi glasses have a continuous density of states and no energy gap, they behave as insulators as a result of the spatially localized states at the Fermi level.

In conjugated polymeric systems, this metal-insulator transition is very interesting. This, is due to the ability to control the critical regime by varying the degree of disorder of the system, or by applying external pressure and/or magnetic fields. The critical behavior, close to the phase transition, has been observed by several workers in a number of conjugated polymers, such as poly(acetylene), poly(pyrrole), poly(paraphenylenevinylene), poly(aniline) [23], as well as in poly(3,4-ethylene dioxythiophene) [16], in a relatively wide range of temperatures. Although metallic behavior has been demonstrated for conjugated polymers, the truly metallic regime for which $k_F l \gg 1$ has not been achieved yet.

2.6 Doping Induced Properties in Conjugated Polymers

In a preceding section, it was described how the band structure of DGSPs and NDGSPs is modified upon doping. These structural changes can be observed through experimental measurements, i.e., spectroscopic measurements or ESR experiments, performed on conjugated polymers in different doping levels. For the case of DGSPs, there are three important signatures of charged soliton formation. First, the generation of localized structural distortions is associated with localized vibration modes (lattice vibrations or phonons). These characteristic vibration modes are known as infrared active vibration, or IRAV, modes because they are active in the infrared region. These soliton induced modes, which can be observed by spectroscopic measurements in the mid-

infrared frequency range, show intensities proportional to the doping level [24]. Second, the electronic transitions associated with the generation of the localized mid-gap energy state can also be observed by spectroscopic measurements, in the near infrared frequency range. Finally, the charge storage in spinless solitons can be verified by electron-spin resonance experiments.

For the case of NDGSPs, there are also significant signatures of charged polaron and bipolaron formation. First, the generation of localized structural distortions which is associated with phonon modes. These polaron and bipolaron induced IRAV modes are active in the mid-infrared region, and can be observed by spectroscopic measurements, as it will be seen later in this section. Second, the electronic transitions associated with the generation of the two, symmetrically placed, mid-gap energy states can also be observed by spectroscopic measurements in the near infrared frequency range. Finally, the charge storage initially in charged polarons with spin $1/2$ and, as the doping level increases, in charged, but spinless, bipolarons can be verified through electron-spin resonance experiments. These experiments show a small signal at low doping levels that grows as the doping increases and saturates at intermediate doping levels, consistent with the formation of charged polarons with spin $1/2$. At higher doping levels the formation of bipolarons commence, and therefore the signal is gradually lost [12].

Figure 2.15 shows a schematic band diagram, and the absorption spectra of poly (3,4-ethylene dioxythiophene), a NDGSP, in the neutral, slightly p-doped, and heavily p-doped states. In the neutral state, only the $\pi-\pi^*$, or E_g , transition is possible and therefore, only one absorption band appears in the spectrum. When the polymer is in its slightly p-doped state, the $\pi-\pi^*$ transition diminishes and, due to the formation of positively charged polarons, two symmetric mid-gap states are generated. This results in two additional absorption bands in the spectrum. Finally, upon heavy p-doping, the created positively charged bipolarons, move the two symmetric mid-gap states closer to the center of the band gap and the HOMO and LUMO (the valence and conduction bands) further apart. Therefore, the $\pi-\pi^*$ transition is totally bleached and, based on the

symmetry allowed transitions, a single broad bipolaron absorption band appears in the spectrum. These doping-induced properties have been observed through spectroscopic measurements for poly(3,4-ethylenedioxythiophene), and the results can be found in reference [25]. A very important note that needs to be made here is the fact that these structural and optical changes are reversible.

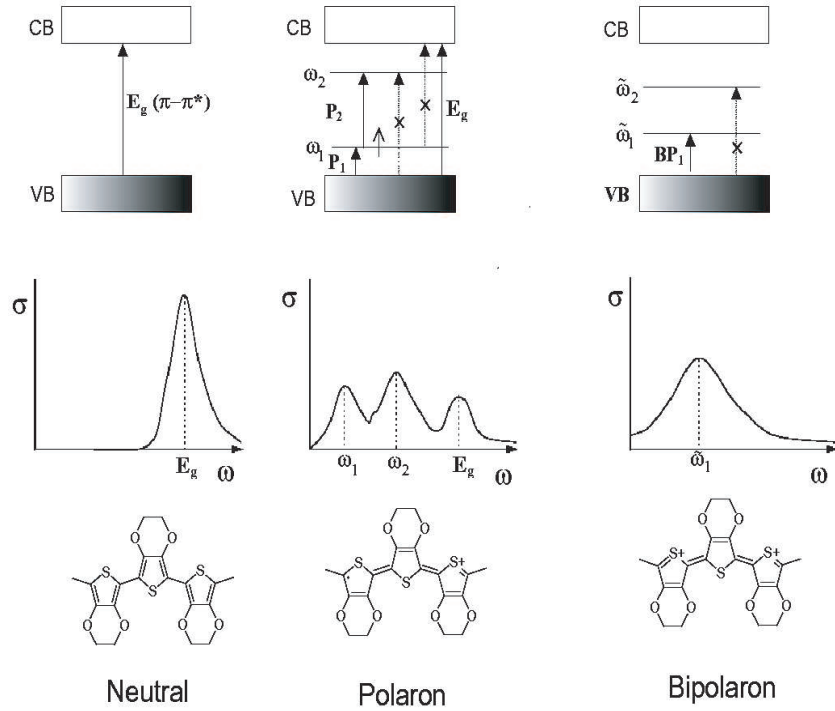


Figure 2.15: Electronic structure, and absorption spectra of positively charged polarons and bipolarons in poly(3,4-ethylene dioxythiophene), a NDGSP. The solid lines show the symmetry allowed transitions or dipole selection rules: $P_1=\omega_1$, $P_2=\omega_2 - \omega_1$, and $BP_1=\tilde{\omega}_1$, and the dashed lines show the forbidden transitions.

2.7 Doping Methods for Conjugated Polymers

The injection of charges into conjugated polymers leads to fascinating, and important phenomena. The ion insertion in the polymeric chains induces major changes in the optical, electrical, and morphological properties of these materials. Therefore, these properties can be tuned by judicious use of different dopants. This reversible charge injection, doping and de-doping, is of great interest due to the many applications. The doping of conjugated polymers can be accomplished in several different ways. The choice

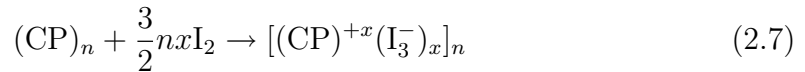
of the doping method depends on the nature of the polymer, and the application is intended for.

- Chemical doping by charge transfer.

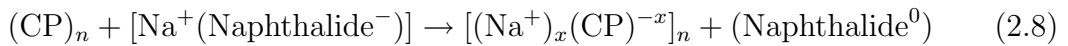
This method involves charge transfer redox chemistry, oxidation (p-type doping, the system loses electrons) and reduction (n-type doping, the system receives electrons), and produces conjugated polymers with high electrical conductivities. As the chemical doping level increases, the electronic structure evolves to that of a metal [6].

This method was the one used in the initial discovery of the ability to dope conjugated polymers by charge-transfer redox chemistry [1]. The oxidation, or p-doping, of poly(aniline), PANI, was achieved by exposing the polymer to iodine vapors, and the reduction, or n-doping, involved treatment with sodium naphthalenide. Chemical doping can also be achieved with protonation by acid-base chemistry. This type of doping leads to an internal redox reaction, and for the case of PANI to the conversion of emeraldine base, a semiconductor, to emeraldine salt, a metal [5].

The charge transfer redox chemistry, oxidation and reduction, is illustrated in the following examples:



for oxidation, or p-type doping, and



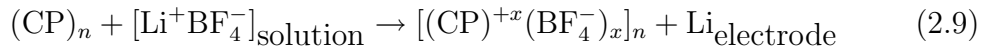
for reduction, or n-type doping.

Materials produced by chemical doping have very high electrical conductivities, and can be used in applications as transparent electrodes, antistatics, electromagnetic interference (EMI) shielding, and intrinsic conducting fibers.

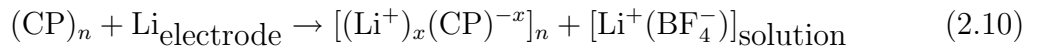
- Electrochemical doping.

This method of doping is the one used throughout this work. Although chemical doping is an efficient process that can yield fully doped and high quality materials, it has a major disadvantage: there is no way to control the doping, and obtain intermediate doping levels. Attempts to reach such levels resulted in inhomogeneous doped films. Electrochemical doping came as a solution to this problem [26]. In this case, an electrode supplies charge to the conjugated polymer in the redox process, while ions from a supported electrolyte diffuse into (or out of) the polymer chain for electronic charge compensation. The doping level is determined by the “cell voltage”, which is the potential difference between the conducting polymer on the working electrode (WE) and the counter electrode (CE). Homogeneous doping can be achieved at any intermediate level by simply adjusting the “cell voltage”, and wait for the system to reach equilibrium, indicated by the current through the cell approaching zero. In our experiments, we required that the current had dropped to about 1% of its peak value to consider that the doping level had stabilized.

Electrochemical doping is illustrated in the following examples:



for oxidation, or p-type doping, and



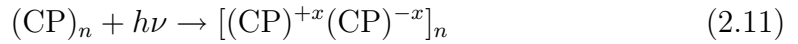
for reduction, or n-type doping.

Materials produced by electrochemical doping can be used in electrochemical batteries for charge storage, light emitting electrochemical cells, and electrochromic applications, e.g., “smart windows”, optical switches, and low energy displays.

In both methods described above, chemical and electrochemical doping, the induced electrical structure is permanent until the system is purposely “un-doped”, i.e., the charge is removed or chemically compensated.

- Photodoping.

Using this method, the semiconducting polymer is locally oxidized (hole creation) and reduced (electron creation) by photoabsorption, which leads to charge carrier separation. The created electron-hole pairs are separated into “free” carriers:

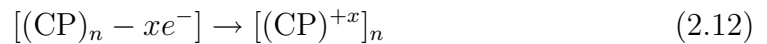


where x is the number of electron-hole pairs. This number depends upon the competition of the pump rate with the recombination rate. The “photoconductivity” lasts only until the excitations are either trapped, or have decayed back to the ground state. Following the photoexcitation from the ground state to the lowest excited state with the proper symmetry, the recombination or decay of an electron-hole pair to the ground state can be either radiative (luminescence) or non-radiative. Some conjugated polymers, e.g., PPV, and PPP, show luminescence with high quantum efficiencies while others, e.g., PAc and Pth, do not [9].

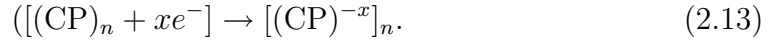
Photodoping by photoexcitation produces high-performance optical materials, which are suitable for photovoltaic devices, and also provides a route for materials with tunable nonlinear optical (NLO) response for electro-optic and optical devices, e.g., waveguides.

- Charge injection at a metal-semiconducting (MS) polymer interface without counter ions.

Electrons and holes can be injected into an empty π^* (HOMO or conduction band), and a filled π (LUMO or valence band) bands respectively from metallic contacts:



and



This method is fundamentally different from chemical and electrochemical doping, because there are no counterions introduced in the system, although the polymer becomes oxidized or reduced. In the case of charge injection at a metal-semiconductor interface, electrons reside in the π^* band, and/or holes at the π band only as long as biasing voltage is applied. Then the injected electrons and holes recombine with the emission of radiation (electroluminescence).

This electron or hole injection at a metal-semiconducting polymer interface is particular useful for applications such as organic field effect transistors (FET's), and light emitting diodes (LED's) [27, 28].

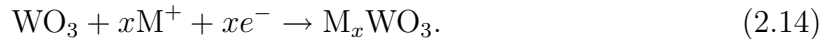
2.8 Fundamentals of Electrochromism

The electrochromic effect is defined as the ability of some materials to reversibly modify their electronic structure upon doping induced by the application of an external voltage. This leads to a change in the optical absorption spectra, and therefore a change in the color of the material. The term “electrochromism” was suggested by J. R. Platt in 1960 [29] in analogy to the effects of “thermochromism” which describes the change in color upon the application of different temperatures, and “photochromism”, which describes the change in color produced by light.

Electrochromic materials change color in a reversible way by an electrochemical reaction, and they can be classified into three categories based on their electronically accessible optical states, or simply stated, based on their capability to access different colors. The first category includes materials that have one colored state, i.e., in this state the material absorbs within the visible region, and one transparent or bleached state, i.e., in this state the absorption is outside the visible region. This class of materials is mostly used in transmissive/absorptive type of devices. The second category includes materials that have two distinctive colored states, i.e., both states absorb within the

visible region, and the last category includes materials that are able to access multiple states, or multiple colors. These latter materials are often called poly-electrochromic, or it is said that they exhibit multi-color electrochromism. The last two classes of materials are used in reflective type of devices.

Many different materials, inorganic and organic, exhibit electrochromism. Among them are the inorganic transition metal oxide systems, and especially the high band gap semiconductor tungsten oxide, WO_3 , which, has been the main focus of research for the last three decades, [30–34]. Tungsten oxide, upon reduction, changes from being transparent in the visible region to having a blue color:



The fabrication of thin films of, amorphous or polycrystalline, WO_3 requires sputtering under high vacuum, which is a complicated and expensive process. This high manufacturing cost, in addition to other reasons such as the very long lifetime requirements, as well as the insufficiently fast response times, proclaims that there is still work that needs to be done.

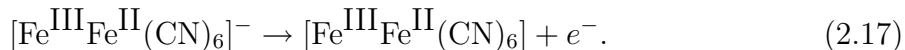
Other inorganic materials that exhibit electrochromism are mixed oxides of vanadium (V), molybdenum (Mo), niobium (Nb), titanium (Ti), nickel (Ni), cobalt (Co), and iridium (Ir), phthalocyanine metal complexes, and also transition metal hexacyanometallates, such as Prussian Blue (PB). Prussian Blue, an example of poly-electrochromic material, has a blue color in its “natural” form, and upon reduction it becomes transparent, the so-called Prussian White (PW) but also known as Everitt’s salt:



while partial oxidation of Prussian Blue results in Prussian Green (PG), which, as indicated by the name, has a green color:



and further oxidation yields Prussian Brown, which has a yellow-golden color:



Another family of materials that exhibits the electrochromic effect includes small organic molecules, such as bipyridilium salts, otherwise known as viologens. The most well known viologens are the 1,1'-dimethyl-4,4'-bipyridilium or otherwise called methyl viologen (MV) [32], and the 1,1'-di-n-heptyl-4,4'-bipyridilium, also known as heptyl viologen [35,36]. This type of materials upon reduction undergoes a change from a transparent to a colored state, with the colored state depending on suitable choices of nitrogen, or alkyl, or other group substitutions. Until recently, the only widespread electrochromic commercial application is the automatic rear-view dimming mirror system by Gentex, called Night Vision Safety (NVS), which utilizes solution-phase electrochromic viologens. Despite the success of this reflective device, the development of other electrochromic systems, e.g., “smart windows” for buildings, have not shown the expected breakthrough in the market yet.

Conjugated polymers are the third family of electrochromic materials, and the one that has gained a lot of attention in the recent years. Although not as developed as the materials discussed earlier in this section, their popularity is basically due to the fact that conjugated polymers are easier to process than inorganic electrochromic materials, and they offer the major advantage of color tunability. More specifically, their color can be tailored through structural modification of the repeat unit, i.e., monomer functionalization and copolymerization, or through the use of blends, laminates, and composites. Hence, one can find conjugated polymers in any of the three categories mentioned above for the use in transmissive/absorptive or reflective type of devices, and in a wide selection of colors. Conjugated polymers also promise rapid response times,

high contrast ratios, and long lifetimes, which are very important characteristics for the development of commercial electrochromic devices. Of all conjugated polymers the derivatives of poly(pyrrole) (PPy), poly(aniline) (PANI), and poly(thiophene) (PTh) are the most widely studied [32, 33, 36–38].

The fact that electrochromic materials have been intensively studied the last decades, and lately have been employed in numerous applications, forced the definition of electrochromism to be modified in order to fit within the demands of the modern world. Therefore, although previously electrochromism was the reversible and visible change of the color associated with the reduction-oxidation, or doping/de-doping, process of an electrochromic material, this definition has been extended to include a wider spectral range modulation. This spectral range now covers ultraviolet (UV), visible (Vis), near infrared (NIR), mid infrared (MIR), far infrared (FIR), and microwave (MW) regions. In the case of these regions, “color” corresponds to the response of the detectors at the different wavelengths, and can be studied as the change in the transmittance, and/or reflectance, induced by doping or de-doping of the electrochromic material.

2.9 Synthesis Methods of CPs

The synthesis of conjugated polymers by oxidation methods can be generally divided into two main classes, chemical and electrochemical polymerization. In the chemical case, the basic mechanism can be simply described as follows. A radical ion is generated from a monomer molecule with the use of a chemical oxidant, and then couples to another monomer molecule, which results on the generation of a dimer radical ion. This coupling between the radical ion and the monomer molecule occurs due to the abundance of monomer molecules in the bulk of the reaction environment. These reactions propagate until the completion of the polymer chain.

In the electrochemical case, the polymerization is also initiated by the generation of a radical ion, which occurs at an electrode surface by oxidation via an applied electric potential. Due to the fact that in the electrode vicinity, where the reactions take place, the concentration of radical ions is large, radical-radical coupling occurs and this, leads to

the formation of a dication. The dication upon proton elimination generates a neutral dimer, which oxidizes to a radical cation dimer. These reactions progress until the completion of the polymer chain.

Electrochemical polymerization is the method that has been used throughout this work because it provides a quick and easy way for the deposition of CP films on various substrates. This process employs a three-electrode configuration that consists of a working electrode (WE), an auxiliary (counter) electrode (CE), and a reference electrode (RE). The working electrode is the electrode where the polymerization of interest takes place, and there is a number of different materials, solid or flexible substrates, that can be used. The choices include indium-doped tin oxide (ITO) on glass or PET, PEDOT-PSS on PET, and thin metal films on grids, when transmittance measurements need to be performed, whereas, solid platinum (Pt) or gold (Au), and gold on Mylar, are used when reflectance measurements need to be performed. The counter electrode provides the required current to sustain the developing processes at the working electrode. In order to ensure that the electrochemical reactions taking place on its surface are not limiting, the area of the counter electrode needs to be larger, or at least similar, to the area of the working electrode. A Pt flag, which is a piece of Pt foil and Pt wire welded together, is usually employed as a counter electrode. Finally, the reference electrode provides control of the applied electrical potential. There are several different types of reference electrodes that are commercially available, such as saturated calomel, Hg_2Cl_2 (SCE), Ag/AgCl saturated in KCl, and Ag/Ag⁺ electrodes. In addition to these standard references, quasi- or pseudo-references can be used, e.g., silver wire. The latter ones need to be calibrated every time before their use. For the polymerization, the WE, CE, and RE electrodes are placed in a monomer solution, and they are connected to a potentiostat/galvanostat. This three-electrode arrangement prevents large currents from passing through the reference electrode, and change its potential.

The electrochemical deposition of the CP on a conductive surface of choice can be achieved in several different ways. In the case where the applied electric potential

is held constant during the deposition, the method is called potentiostatic deposition and it generally yields polymers with consistent morphology. If the current that passes through the electrodes is constant, the method is called galvanostatic, which generally yields polymers of poorer morphology when compared to the films produced by the previous method. Both methods can use either the time or the charge as a parameter for the termination of the deposition process. Control of charge is desirable when a film of specific thickness is needed.

Cyclic voltammetry (CV) is another method that can be used for CP deposition. In this method, the potential is repeatedly cycled over a specified voltage range, while the resulting current is measured. The obtained voltammogram is a display of current density as a function of the applied voltage. The scan rate, expressed in mV/s, is a dynamic parameter and can be changed in order for different types of reactions, fast or slow, to be followed effectively. This method results in films of comparable quality to the potentiostatic method.

2.10 Characterization Methods of Electrochromic CPs

Many characterization methods have been developed in an effort to gain a deeper understanding of the electrochromic processes in CPs. A very important, and widely used, characterization method is spectroelectrochemistry. This method provides a way to probe the electronic structure of CPs through the optical changes occurring upon doping. Hence, information about the energy band gap, and the mid-gap states created upon oxidation or reduction, can be deduced by carefully studying the resulting spectra.

Spectroelectrochemistry can be performed using the three electrode configuration, described in the previous section, to initially characterize the conjugated polymer film in monomer-free solution. In this method, different potential values are applied, and after the system reaches an equilibrium, the absorption spectrum is measured. Figure 2.16 shows the spectra of a PEDOT film deposited on ITO/Glass substrate, at different doping levels, from which the absorption of the monomer-free solution, and of the ITO/Glass substrate have been subtracted.

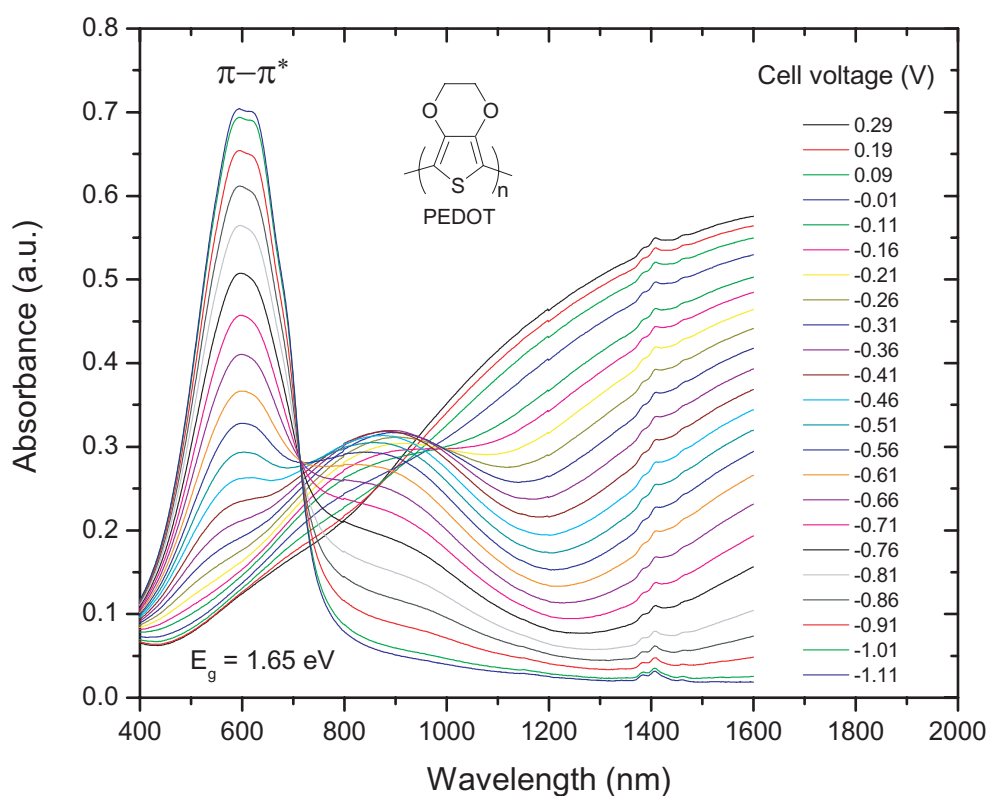


Figure 2.16: Absorbance spectra of poly(3,4-ethylene dioxythiophene), PEDOT, in different doping levels. The potential voltages are versus Fc/Fc^+ . These measurements have been performed by A. Dyer.

As can be clearly seen from the spectrum, when the polymer is in its neutral (undoped) state it behaves as a semiconductor with an energy band gap of 1.65 eV. The band gap is determined by extrapolating the onset of the strong $\pi-\pi^*$ absorption band in the visible region. Upon electrochemical doping (oxidation or p-type doping), the band structure of the polymer is modified; lower energy mid-gap states are generated and charge carriers, polarons and bipolarons are created. Therefore, the absorption spectra evolves accordingly. Upon low doping, the strength of the $\pi-\pi^*$ absorption band is reduced, while absorption bands due to polarons emerge. As the doping level continue to increase, the $\pi-\pi^*$ and polaron bands are slowly depleted, and a broad bipolaron absorption band at lower energies forms. At the highest level of doping, only

the bipolaron absorption is observed. These structural and optical changes are reversible through de-doping (reduction) of the polymer system.

Spectroelectrochemistry measurements can also be performed in reflective or transmissive, electrochromic devices. For devices, the three electrode configuration is replaced by a suitable holder. In order to apply a voltage across the devices, the counter and the reference leads have to be connected to one another. Different potential values are applied and, after the system reaches equilibrium, the absorption spectrum is measured. From the resulting spectra, useful information can be deduced concerning the electrochromic mechanisms within the device.

Another important characterization method consists of a kinetics experiment, which allows for measuring of the switching times between two extreme electrochromic states, neutral and doped for the polymer films in solution or in devices. In this experiment, a square-wave potential is applied at specified time intervals, while concurrently the absorbance at λ_{max} is monitored, where λ_{max} is the wavelength of maximum electrochromic contrast, and can be determined from the spectroelectrochemistry measurements described above. Furthermore, the same experimental setup can be used to perform a long-time redox switching stability, or lifetime, test. By applying the square-wave potential over a long period of time, hundreds or even thousands of cycles, one can study the degradation of the performance of the polymer film itself, or in the device under investigation. The switching times and the lifetimes can vary significantly not only between different polymers, but also for the same polymer, e.g., when different dopants are used.

Other characterization methods include cyclic voltammetry; a technique that provides information about the potential values at which oxidation and reduction occur for each polymer, in-situ conductivity measurements, and in-situ colorimetric analysis. This latter method accurately defines the color, taken into account the sensitivity of the human eye, and the electrochromic contrast ratios in conjugated polymers. Although

these techniques provide useful information, they have not been used in the course of this work.

2.11 Electrochromic Devices (ECDs) Based on CPs

Electrochromism is the ability of electrochromic materials to reversibly change their transmittance, or reflectance, upon the application of an electric field. Therefore, electrochromic devices which employ these type of materials, are used for the modulation of light. An electrochromic device can be envisioned as an electrochemical cell, which consists of two or more redox active materials separated by an electrolyte layer. Upon the application of a small voltage, usually no more than a few volts, optical changes occur due to electrochemical reactions that take place within the cell. The electrochromic switching time of the device between two extrema states, e.g., colored and bleached, is limited by the ion diffusion from one layer to another. Liquid electrolytes provide rapid switching times due to high ion mobility, but cause faster degradation of the device due to the risk of solvent evaporation or leakage. Gel and solid, electrolytes provide slower switching times but they do not share the degradation problems with their liquid counterparts, and therefore are the most commonly used in device applications.

There are two basic categories of ECDs based on their function mode or, in other words, the type of light modulation they perform. The first of these categories, is the reflective ECDs in which the light incident to the device is controllably reflected. The typical design of an ECD that operates in reflectance mode is an outward-facing platform, and was originally developed by Bennett [39] and Chandrasekhar [40]. More specifically, the device consists of an outward-facing working electrode, usually gold coated on a slitted Mylar or on a porous membrane, onto which an active electrochromic CP is deposited. The porous membrane can be polycarbonate, polysulfone, polyester, or nylon, and compared to the slitted Mylar it allows for faster and more uniform ion diffusion [41, 42]. The counter electrode, usually gold on Mylar, does not contribute directly to the modulation of light but the counter electrode EC polymer serves to balance the charge. To assemble the device, the counter electrode is placed facing the

back side of the working electrode, with a porous separator (polypropylene) soaked in electrolyte in between them. A transparent window, placed on top of this configuration, seals the device. This window should allow the probing of the optical properties of the reflective ECD, and thus the choice of the material depends on which region of the electromagnetic spectrum the device is needed to operate. Typical windows that are used are polyethylene (for almost over the entire spectrum from far infrared to visible), zinc selenide (for the mid- and near infrared region), and glass (for the near infrared and the visible regions).

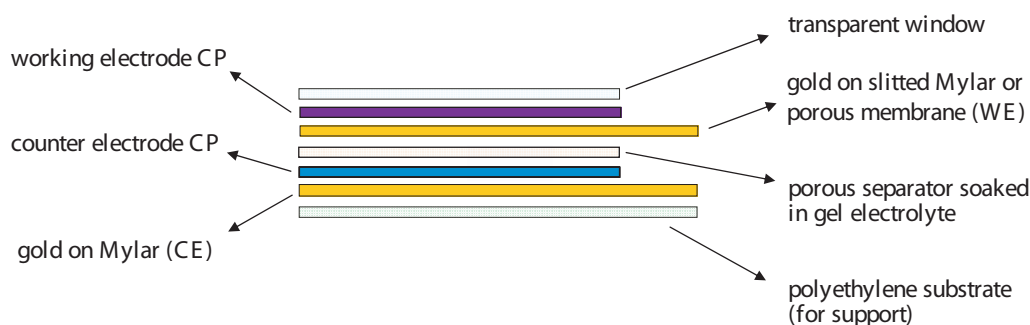


Figure 2.17: Schematic diagram of a reflective electrochromic device.

More details about the design of this type of devices are given in Chapter 5. Another type of fabrication of reflective ECDs includes patterning of the working electrode, and use of more than one electrochromic CPs in the same device. This design provides high resolution pixel devices in which each pixel can be addressed individually [38, 43].

The most common applications of reflective ECDs are displays although, there is still a lot of work to be done for these devices to be widely commercial available. Many workers are putting a serious effort into making devices with faster switching times, longer stability, and higher electrochromic contrast. Reflective ECDs based on CPs offer many advantages compared to LCDs (Liquid Crystal Devices). They are easy to process, have low production cost, low voltage requirements, offer a wide selection of colors, and the quality of the image does not depend on the viewing angle. Furthermore, reflective ECDs can be made flexible and, in any size and shape. Other applications

include mirror devices, optical shutters for thermal control in spacecraft, and battlefield camouflage countermeasures against night vision sensors.

The second category of ECDs is the transmissive/absorptive device, in which the incident light controllably passes through the device. The design of this type of ECDs consists of two electrochromic CPs deposited on transparent electrodes which are facing each other and are separated by an electrolyte layer, as shown in Figure 2.18. The electrochromic CPs employed in transmissive/absorptive ECDs, must be complimentary to each other, a cathodically coloring polymer and an anodically coloring polymer, in order for high contrast values to be achieved. A cathodically coloring polymer has a low band gap, ideally around 1.8-2.2 eV, is colored in its neutral (undoped) state, and upon oxidation it becomes transparent in the visible region. Whereas, an anodically coloring polymer has a high band gap, ideally higher than 3.0 eV, is transmissive in the visible region when it is in its neutral state, and upon oxidation it absorbs the visible light. Therefore, the ECD can be reversibly switched between a colored, absorptive, and a transmissive, bleached, state. The conducting electrodes employed in these devices, depend on the region of the electromagnetic spectrum the device is needed to operate. Typical transparent electrodes for the visible region, consist of indium-doped tin oxide (ITO) films deposited on glass, and ITO or poly(3,4-ethylene dioxythiophene)-poly(styrene sulfonate) (PEDOT-PSS), deposited on poly(ethylene terephthalate) (PET) for flexible ECDs. This type of devices can be used as “smart windows” for cars, e.g., rear-view mirrors, sunroofs, and for buildings, providing huge energy saving cost.

2.12 General Applications of CPs

Initially, this new class of polymers held the hope that will serve as replacements of the existing heavy metals in weight sensitive applications, such as air and space applications. However, due to instabilities of these systems under ambient conditions alternative practical uses were exploited. The promise of of the so-called “plastic” electronic devices attracted a lot of attention not only as basic research in academia but also

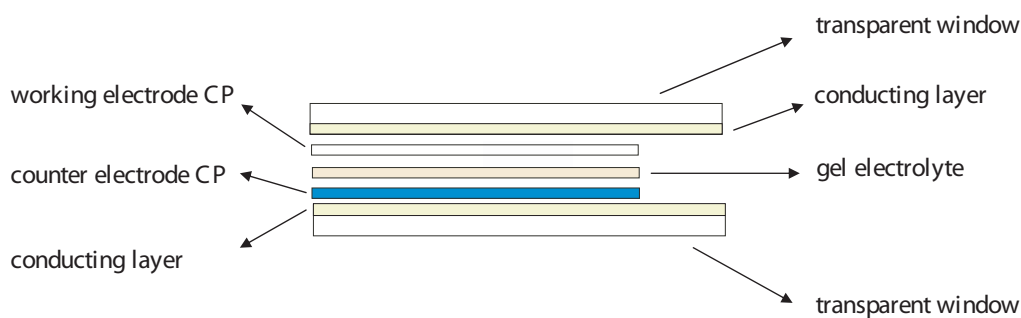


Figure 2.18: Schematic diagram of a transmissive/absorptive electrochromic device.

from a commercial point of view. Although there are not many commercial applications available yet, the future of “plastic” electronics seems very promising.

In particular, conducting polymers exhibit interesting and important properties not typically available in other materials. Their advantages over other materials, organic and inorganic, lay on their light weight, relatively inexpensive fabrication, easy processibility and ability to be formed into odd shapes and sizes, low voltage requirements, compatibility with many organic liquid and solid electrolytes, and fast switching color changes. In addition, a wide variety of colors is available with conjugated polymers, as well as the ability of color tunability based for example on the doping level, or the choice of dopant. These unique properties make possible a number of applications such as transparent electrodes, antistatics, electromagnetic interference (EMI) shielding, conducting fibers, electrochemical batteries, anti-corrosion coatings, sensors, “smart windows”, optical switches, thermal control devices, low energy displays, light emitting electrochemical cells, photovoltaic devices, organic field emission transistors, and more [5, 17, 26, 27, 32, 33, 36, 38, 44].

CHAPTER 3 THIN FILM OPTICS

Optical experiments on thin films provide a valuable method of understanding the properties of materials that are in a solid state form. The materials specific parameters, directly available through these experiments are the frequency-dependent reflectance \mathcal{R} , or transmittance \mathcal{T} , spectrum over a region of interest. This region does not refer only to the relatively narrow visible region but extends and covers the whole range of the electromagnetic spectrum from far infrared to ultra-violet. From the experimental measurements, \mathcal{R} and/or \mathcal{T} , and calculations based on theoretical models, the dielectric function can be deduced which is the property most directly related to the electronic structure of the material under consideration. This way, the optical phenomena can be quantified, and a number of optical constants can be derived describing the response of the medium to light.

3.1 Optical Processes and Optical Constants

The basic optical phenomena that can be observed as light travels through matter are reflection from a surface between two different media, and propagation within a medium in the solid state form. The amount of light transmitted through a film relatively to the amount of incident light depends on the way light propagates within each medium. For example, if the frequency of the light wave is resonant with any of the transition frequencies of the atoms in the medium, part of the light will be absorbed and thus, as the light travels through the medium its intensity will be decreased. The intensity of the transmitted light within the medium, is described by Beer's law:

$$I(z) = I(z_0)e^{-\alpha z}, \quad (3.1)$$

where α is called the absorption coefficient and is a strong function of frequency, and z_0 is the interface plane.

Another phenomenon that causes attenuation of the light intensity within a medium is scattering. Scattering is responsible for re-directing the light to all possible directions. Consequently, it diminishes the amount of light that proceeds in the forward direction and therefore, the amount of light which transmits through the material. Thus, scattering has an effect similar to absorption, and the resulted attenuation of light can be expressed in an analogous form as the equation above:

$$I(z) = I(z_0)e^{-N\sigma z}, \quad (3.2)$$

where N is the number of scattering centers per unit volume, and σ is the scattering cross-section of the scattering center. A number of different factors can be responsible for the scattering process, such as inhomogeneities, impurities, defects, etc.

Furthermore, the light waves travel within a medium with a smaller velocity compared to the velocity of light in free space, and with a velocity that differs for different materials. This phenomenon, called refraction, is described by the refractive index n . The refractive index is, in general, a function of frequency and this effect is known as dispersion. The refractive index n is defined as the ratio of the velocity of light in free space c (where $c=2.998 \times 10^8 \text{m s}^{-1}$), to the velocity of light in a medium v :

$$n = \frac{c}{v}. \quad (3.3)$$

The velocity change causes the light rays to bent with respect to the normal on the interface as the light goes through two different materials, and it is described by Snell's law [45].

The two quantities that describe the propagation of the light wave within a medium, the absorption coefficient α and the refraction index n , can be combined into a single parameter called the complex refractive index:

$$\tilde{n} = n + i\kappa, \quad (3.4)$$

where the real part of the complex refractive index is the refractive index n , as defined in equation (3.3), and the imaginary part κ , is related to the absorption coefficient, as it will be shown later. The imaginary part κ is called the extinction coefficient.

In the above description of the phenomena that occur when light travels through a medium, it has been assumed that the result of this interaction is independent of the intensity of the light beam. Therefore the analysis is based on linear optics where properties such as the refractive index n and the absorption coefficient α are taken to be independent of the optical power of the source. This is indeed the case when conventional light sources are used, and our research throughout this dissertation falls into this domain. However, now that high power lasers are available, there are a number of other phenomena that can occur as a light beam of high intensity propagates through a medium. These are described by nonlinear optics. Nonlinear effects cause the properties of the material under investigation to depend on the intensity of the light source. An example of a nonlinear effect is the doubling of the frequency, where the frequency of part of the beam doubles as it interacts with a medium.

3.2 Interaction of Electromagnetic Waves with Matter

The response of a material to an incident light beam can be described by the following macroscopic vectors: the electric field \mathbf{E} , the polarization \mathbf{P} , the electric displacement \mathbf{D} , the magnetic field \mathbf{H} , the magnetic flux density \mathbf{B} , and the magnetization \mathbf{M} .

The application of an external electric field to an isotropic and homogeneous medium tends to align the microscopic dipole moments within the atoms along the external field direction. This produces a net dipole moment within the medium, and therefore a polarization. More specifically, the polarization \mathbf{P} is defined as the net di-

pole moment per unit volume, it is parallel to the applied electric field, and it can be expressed as follows¹

$$\mathbf{P} = \tilde{\chi}_e \mathbf{E} \quad (3.5)$$

where $\tilde{\chi}_e$ is the electric susceptibility of the medium.

The electric displacement \mathbf{D} of the medium is defined as

$$\mathbf{D} = \mathbf{E} + 4\pi\mathbf{P}, \quad (3.6)$$

and by combining the last two equations we can write

$$\mathbf{D} = \tilde{\epsilon}\mathbf{E} \quad (3.7)$$

where

$$\tilde{\epsilon} \equiv \epsilon_1 + i\epsilon_2 = 1 + 4\pi\tilde{\chi}_e \quad (3.8)$$

is the complex dielectric function, which is a very important parameter for the understanding of the interaction of light with matter.

The current density \mathbf{J} , which comes as a response of the medium to the application of \mathbf{E} , is related to the electric field as follows

$$\mathbf{J} = \tilde{\sigma}\mathbf{E} \quad (3.9)$$

where

$$\tilde{\sigma} \equiv \sigma_1 + i\sigma_2. \quad (3.10)$$

is the complex conductivity of the medium. In general, the current density is the result of the contributions arising from the bound and free charges: $\mathbf{J} = \mathbf{J}_{bound} + \mathbf{J}_{free}$, where

¹ CGS units are used throughout unless otherwise specified.

\mathbf{J}_{bound} represents the localized motion of the restricted charges, and \mathbf{J}_{free} represents the charge carriers that are free to move within the medium. Combining the equations above, we find a useful relationship between the dielectric constant and the conductivity:

$$\tilde{\epsilon} = 1 + i \frac{4\pi\tilde{\sigma}}{\omega}. \quad (3.11)$$

The last equation can also be expressed as follows

$$\sigma_1 = \frac{\omega\epsilon_2}{4\pi} \quad (3.12)$$

and

$$\sigma_2 = \frac{\omega(1 - \epsilon_1)}{4\pi}. \quad (3.13)$$

Another useful expression that relates the complex dielectric function and the real part of the conductivity is the following:

$$\tilde{\epsilon} = \epsilon_1(\omega) + \frac{4\pi i}{\omega} \sigma_1(\omega) \quad (3.14)$$

where $\epsilon_1(\omega)$ is the real dielectric function, while $\sigma_1(\omega)$ is the real part of the complex conductivity, also called optical conductivity. An interesting case is the zero frequency limit of the above equation, which specifies the response of the medium to static fields. In this limit, $\epsilon_1(\omega = 0)$ becomes the static dielectric constant, while $\sigma_1(\omega = 0)$ becomes the dc electrical conductivity.

In an analogous way, as the application of an external electric field, the application of an external magnetic field to an isotropic and homogeneous medium produces a magnetization \mathbf{M} to the medium, which is proportional to applied magnetic field \mathbf{H} :

$$\mathbf{M} = \tilde{\chi}_m \mathbf{H} \quad (3.15)$$

where $\tilde{\chi}_m$ is the magnetic susceptibility of the medium.

The magnetic flux density \mathbf{B} of the medium is defined as:

$$\mathbf{B} = \mathbf{H} + 4\pi\mathbf{M}, \quad (3.16)$$

and by combining the last two equations we can write

$$\mathbf{B} = \tilde{\mu}\mathbf{H}, \quad (3.17)$$

where

$$\tilde{\mu} = 1 + 4\pi\tilde{\chi}_m \quad (3.18)$$

is the complex magnetic permeability.

The interaction of a medium with an applied electromagnetic field, is described by Maxwell's equation's:

$$\nabla \cdot \mathbf{D} = 4\pi\rho_f \quad (3.19)$$

$$\nabla \cdot \mathbf{B} = 0 \quad (3.20)$$

$$\nabla \times \mathbf{E} = -\frac{1}{c} \frac{\partial \mathbf{B}}{\partial t} \quad (3.21)$$

$$\nabla \times \mathbf{H} = \frac{4\pi}{c} \mathbf{J}_f + \frac{1}{c} \frac{\partial \mathbf{D}}{\partial t}, \quad (3.22)$$

where ρ_f is the free charge density, and \mathbf{J}_f is the free current density.

In the absence of external charges, $\rho_f = 0$, and currents, $\mathbf{J}_f = \mathbf{0}$, Maxwell's equations can be written as follows:

$$\nabla \cdot \mathbf{D} = 0 \quad (3.23)$$

$$\nabla \cdot \mathbf{B} = 0 \quad (3.24)$$

$$\nabla \times \mathbf{E} = -\frac{1}{c} \frac{\partial \mathbf{B}}{\partial t} \quad (3.25)$$

$$\nabla \times \mathbf{H} = \frac{1}{c} \frac{\partial \mathbf{D}}{\partial t}. \quad (3.26)$$

Eliminating \mathbf{D} , and \mathbf{H} from the above equations results in:

$$\nabla \cdot \mathbf{E} = 0 \quad (3.27)$$

$$\nabla \cdot \mathbf{B} = 0 \quad (3.28)$$

$$\nabla \times \mathbf{E} = -\frac{1}{c} \frac{\partial \mathbf{B}}{\partial t} \quad (3.29)$$

$$\nabla \times \mathbf{B} = \frac{\mu\epsilon}{c} \frac{\partial \mathbf{E}}{\partial t}. \quad (3.30)$$

Using the following vector identity:

$$\nabla \times (\nabla \times \mathbf{A}) = \nabla \cdot (\nabla \cdot \mathbf{A}) - \nabla^2 \mathbf{A} \quad (3.31)$$

we obtain the final result:

$$\nabla^2 \mathbf{E} = \frac{\mu\epsilon}{c^2} \frac{\partial^2 \mathbf{E}}{\partial t^2} \quad (3.32)$$

which has the form of a wave equation with velocity:

$$\frac{1}{v^2} = \frac{\mu\epsilon}{c^2} \implies v = \frac{c}{\sqrt{\mu\epsilon}}. \quad (3.33)$$

Comparing the last equation with equation (3.3), and taking into account the fact that for optical frequencies the magnetic permeability can be set equal to one, $\mu = 1$, the refractive index can be expressed as follows

$$n = \sqrt{\epsilon}. \quad (3.34)$$

This equation allows us to relate the refractive index, a parameter associated with the way an electromagnetic wave propagates within a medium, to the dielectric function, which is a constant directly related to the electronic structure of the medium.

Based on the above analysis, the solutions to Maxwell's equations will have the form of a plane wave of angular frequency ω :²

$$\mathbf{E}(\mathbf{r}, t) = \mathbf{E}_0 e^{i(\mathbf{k}\cdot\mathbf{r} - \omega t)} \quad (3.37)$$

$$\mathbf{H}(\mathbf{r}, t) = \mathbf{H}_0 e^{i(\mathbf{k}\cdot\mathbf{r} - \omega t)}, \quad (3.38)$$

where \mathbf{E}_0 , \mathbf{H}_0 are constant amplitudes, in general complex numbers, and \mathbf{k} is the wave vector, which in a non-absorbing medium is given by:

$$k = \frac{2\pi}{\lambda/n} = \frac{\omega}{v} n, \quad (3.39)$$

where λ is the free space wavelength $\lambda = 2\pi c/\omega$.

In the most general case of an absorbing medium, k is a complex number and it represents the energy dissipation as the wave propagates through the medium:

$$\tilde{k} = \frac{\omega}{c} \tilde{n} = \frac{\omega}{c} (n + i\kappa). \quad (3.40)$$

Substituting equation (3.40) to equation (3.37), and taking \mathbf{E} along the z direction, we obtain

$$\mathbf{E}(z, t) = \mathbf{E}_0 e^{i(\omega \tilde{n} z/c - \omega t)} = \mathbf{E}_0 e^{-\kappa \omega z/c} e^{i(\omega n z/c - \omega t)} \quad (3.41)$$

²It must be noted that the signs in the phase argument are chosen arbitrary, and do not change the physics of the problem. Therefore, a solution of the form:

$$\mathbf{E}(\mathbf{r}, t) = \mathbf{E}_0 e^{i(\omega t - \mathbf{k}\cdot\mathbf{r})} \quad (3.35)$$

and

$$\mathbf{H}(\mathbf{r}, t) = \mathbf{H}_0 e^{i(\omega t - \mathbf{k}\cdot\mathbf{r})}, \quad (3.36)$$

could equally be used.

Thus, in the case of an absorbing medium, there is an extra term in the wave equation which represents the exponential decay of the wave within the medium. If we take into account the fact that the intensity of a light beam is proportional to the square of the electric field $I \propto \mathbf{E}\mathbf{E}^*$ [45–47], and we compare this with equation (3.1), it can be shown that the extinction coefficient κ is proportional to the absorption coefficient α :

$$\alpha = \frac{2\omega\kappa}{c} = \frac{4\pi\kappa}{\lambda}, \quad (3.42)$$

where λ is the free space wavelength. Combining equations (3.8), (3.34), and (3.42), we can relate $\tilde{\epsilon}$, \tilde{n} , α , and κ to each other:

$$\epsilon_1 = n^2 - \kappa^2 \quad (3.43)$$

$$\epsilon_2 = 2n\kappa \quad (3.44)$$

$$n = \frac{1}{\sqrt{2}} \sqrt{\epsilon_1 + (\epsilon_1^2 + \epsilon_2^2)^{\frac{1}{2}}} \quad (3.45)$$

$$\kappa = \frac{1}{\sqrt{2}} \sqrt{\epsilon_1 + (-\epsilon_1^2 + \epsilon_2^2)^{\frac{1}{2}}} \quad (3.46)$$

This analysis proves that the refractive index and dielectric constant are not independent parameters, and thus, if we know one of them we can calculate the other.

In the analysis above, only isotropic and homogeneous media were considered. In the case of highly anisotropic media, the polarization and induced currents lie in a different direction from that of the electric field of the electromagnetic wave. In this situation, the dielectric function becomes a tensor quantity. The response of the media is well characterized by this tensor, however if the direction of the electric field is not along one of the principal directions of the dielectric tensor, the analysis can be rather complicated.

3.3 Light Propagation Through a Planar Interface

In order to determine the reflected and transmitted light at a plane surface between two semi-infinite media of different dielectric properties, we need to apply boundary conditions to the solutions of Maxwell's equations. These boundary conditions require the tangential components of both the electric and magnetic field to be continuous at the interface that separates the different materials.

We consider a plane wave, incident on a surface at $z = 0$, as shown in Figure 3.1. The amplitudes of the incident, reflected, and transmitted waves of the electric vectors are the following³

$$\mathbf{E}_{0p}^+ = [E_{0p}^+ \cos \varphi_0 \hat{x} - E_{0p}^+ \sin \varphi_0 \hat{z}] e^{i(\omega t - [\frac{2\pi n_0 x \sin \varphi_0}{\lambda} + \frac{2\pi n_0 z \cos \varphi_0}{\lambda}])} \quad (3.49)$$

$$\mathbf{E}_{0s}^+ = E_{0s}^+ \hat{y} e^{i(\omega t - [\frac{2\pi n_0 x \sin \varphi_0}{\lambda} + \frac{2\pi n_0 z \cos \varphi_0}{\lambda}])} \quad (3.50)$$

$$\mathbf{E}_{0p}^- = [E_{0p}^- \cos \varphi_0 \hat{x} + E_{0p}^- \sin \varphi_0 \hat{z}] e^{i(\omega t - [\frac{2\pi n_0 x \sin \varphi_0}{\lambda} - \frac{2\pi n_0 z \cos \varphi_0}{\lambda}])} \quad (3.51)$$

$$\mathbf{E}_{0s}^- = E_{0s}^- \hat{y} e^{i(\omega t - [\frac{2\pi n_0 x \sin \varphi_0}{\lambda} - \frac{2\pi n_0 z \cos \varphi_0}{\lambda}])} \quad (3.52)$$

$$\mathbf{E}_{1p}^+ = [E_{1p}^+ \cos \varphi_1 \hat{x} - E_{1p}^+ \sin \varphi_1 \hat{z}] e^{i(\omega t - [\frac{2\pi n_1 x \sin \varphi_1}{\lambda} + \frac{2\pi n_1 z \cos \varphi_1}{\lambda}])} \quad (3.53)$$

$$\mathbf{E}_{1s}^+ = E_{1s}^+ \hat{y} e^{i(\omega t - [\frac{2\pi n_1 x \sin \varphi_1}{\lambda} - \frac{2\pi n_1 z \cos \varphi_1}{\lambda}])} \quad (3.54)$$

where $k = 2\pi n/\lambda$, and the subscripts p , s denote the transverse magnetic polarization, also known as TM, and the transverse electric polarization, also known as TE, respectively. The incident, reflected, and transmitted waves of the magnetic field vectors can be calculated from:

$$\left(\frac{\mu\omega}{c}\right)\mathbf{H} = -(\mathbf{k} \times \mathbf{E}) \quad (3.55)$$

³ The sign convention for Maxwell's solutions used in this section is of the following form:

$$\mathbf{E}(\mathbf{r}, t) = \mathbf{E}_0 e^{i(\omega t - \mathbf{k} \cdot \mathbf{r})} \quad (3.47)$$

$$\mathbf{H}(\mathbf{r}, t) = \mathbf{H}_0 e^{i(\omega t - \mathbf{k} \cdot \mathbf{r})}. \quad (3.48)$$

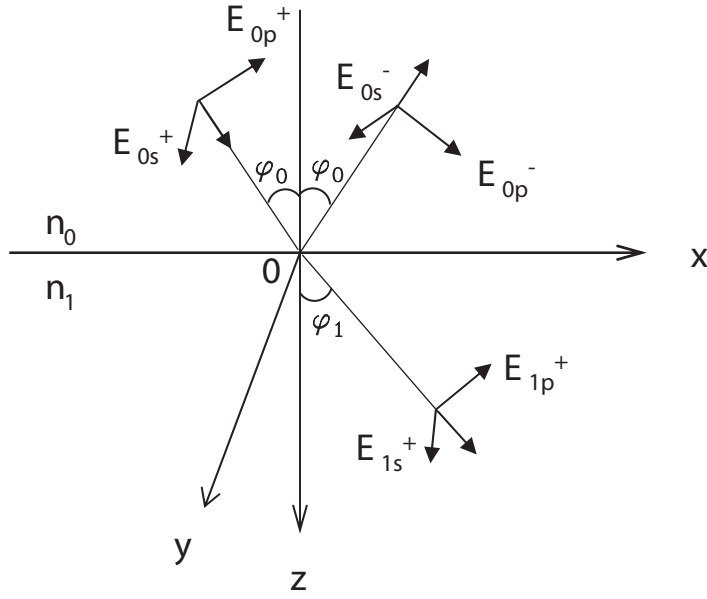


Figure 3.1: Light beam propagates through an interface between two media with different optical properties.

The total components of the electric and magnetic vectors at the surface, at $z = 0$, for the incident, reflected, and transmitted waves are

$$\mathbf{E}_{0x} = (E_{0p}^+ + E_{0p}^-) \cos \varphi_0 \quad (3.56)$$

$$\mathbf{E}_{0y} = E_{0s}^+ + E_{0s}^- \quad (3.57)$$

$$\mathbf{H}_{0x} = n_0(-E_{0s}^+ + E_{0s}^-) \cos \varphi_0 \quad (3.58)$$

$$\mathbf{H}_{0y} = n_0(E_{0p}^+ - E_{0p}^-) \quad (3.59)$$

$$\mathbf{E}_{1x} = E_{1p}^+ \cos \varphi_1 \quad (3.60)$$

$$\mathbf{E}_{1y} = E_{1s}^+ \quad (3.61)$$

$$\mathbf{H}_{1x} = -n_1 E_{1s}^+ \cos \varphi_1 \quad (3.62)$$

$$\mathbf{H}_{1y} = n_1 E_{1p}^+ \quad (3.63)$$

The boundary conditions require the tangential components of both the electric and magnetic field to be continuous at the interface, at $z = 0$, thus:

$$\mathbf{E}_{0x} = \mathbf{E}_{1x} \quad (3.64)$$

$$\mathbf{E}_{0y} = \mathbf{E}_{1y} \quad (3.65)$$

$$\mathbf{H}_{0x} = \mathbf{H}_{1x} \quad (3.66)$$

$$\mathbf{H}_{0y} = \mathbf{H}_{1y} \quad (3.67)$$

Substituting the total components of the electric and magnetic vectors at the surface, $z = 0$, for the incident, reflected, and transmitted waves into the latter equations, we obtain the well known Fresnel coefficients for reflection and transmission:

$$r_p = \frac{\mathbf{E}_{0p}^-}{\mathbf{E}_{0p}^+} = \frac{n_0 \cos \varphi_1 - n_1 \cos \varphi_0}{n_0 \cos \varphi_1 + n_1 \cos \varphi_0} \quad (3.68)$$

$$t_p = \frac{\mathbf{E}_{1p}^+}{\mathbf{E}_{0p}^+} = \frac{2n_0 \cos \varphi_0}{n_0 \cos \varphi_1 + n_1 \cos \varphi_0} \quad (3.69)$$

$$r_s = \frac{\mathbf{E}_{0s}^-}{\mathbf{E}_{0s}^+} = \frac{n_0 \cos \varphi_0 - n_1 \cos \varphi_1}{n_0 \cos \varphi_0 + n_1 \cos \varphi_1} \quad (3.70)$$

$$t_s = \frac{\mathbf{E}_{1s}^+}{\mathbf{E}_{0s}^+} = \frac{2n_0 \cos \varphi_0}{n_0 \cos \varphi_0 + n_1 \cos \varphi_1} \quad (3.71)$$

The reflectance \mathcal{R} , defined as the ratio of the intensity of the reflected light to the intensity of the incident light on the surface, and the transmittance \mathcal{T} , defined as the ratio of the intensity of the transmitted light to the intensity of the incident light on the surface are given by:

$$\mathcal{R}_p = r_p^2 \implies \mathcal{R}_p = \left(\frac{\mathbf{E}_{0p}^-}{\mathbf{E}_{0p}^+} \right)^2 \quad (3.72)$$

$$\mathcal{R}_s = r_s^2 \implies \mathcal{R}_s = \left(\frac{\mathbf{E}_{0s}^-}{\mathbf{E}_{0s}^+} \right)^2 \quad (3.73)$$

$$\mathcal{T}_p = \frac{n_1}{n_0} t_p^2 \implies \mathcal{T}_p = \frac{n_1}{n_0} \left(\frac{\mathbf{E}_{1p}^+}{\mathbf{E}_{0p}^+} \right)^2 \quad (3.74)$$

$$\mathcal{T}_s = \frac{n_1}{n_0} t_s^2 \implies \mathcal{T}_s = \frac{n_1}{n_0} \left(\frac{\mathbf{E}_{1s}^+}{\mathbf{E}_{0s}^+} \right)^2 \quad (3.75)$$

or, in terms of the refractive indices, and the reflected and transmitted angles, the reflectance and transmittance are given by:

$$\mathcal{R}_p = \left(\frac{n_0 \cos \varphi_1 - n_1 \cos \varphi_0}{n_0 \cos \varphi_1 + n_1 \cos \varphi_0} \right)^2 \quad (3.76)$$

$$\mathcal{R}_s = \left(\frac{n_0 \cos \varphi_0 - n_1 \cos \varphi_1}{n_0 \cos \varphi_0 + n_1 \cos \varphi_1} \right)^2 \quad (3.77)$$

$$\mathcal{T}_p = \frac{n_1}{n_0} \left(\frac{2n_0 \cos \varphi_0}{n_0 \cos \varphi_1 + n_1 \cos \varphi_0} \right)^2 \quad (3.78)$$

$$\mathcal{T}_s = \frac{n_1}{n_0} \left(\frac{2n_0 \cos \varphi_0}{n_0 \cos \varphi_0 + n_1 \cos \varphi_1} \right)^2. \quad (3.79)$$

Furthermore, in case of normal incidence, on an isotropic non-absorbing medium, the above equations become

$$\mathcal{R}_p = \mathcal{R}_s = \left(\frac{n_0 - n_1}{n_0 + n_1} \right)^2 \quad (3.80)$$

$$\mathcal{T}_p = \mathcal{T}_s = \frac{4n_0 n_1}{(n_0 + n_1)^2}. \quad (3.81)$$

The above equations can be used even when the angle of the incident light does not meet the medium surface at exactly right angle. For example, comparing the above equations for reflectance for normal incident and an arbitrary angle, we can calculate,⁴ the magnitude of the error approximation. Using $n_0 = 1$ and $n_1 = 2$ we find that for

⁴ Using Snell's law to calculate φ_1 : $n_1 \sin \varphi_1 = n_0 \sin \varphi_0$.

an angle φ_0 up to 5.5° the difference between the obtained reflectance values lies within 1%. Therefore, the choice of the right equation can be made depending on the accuracy that is needed to be used in a particular experiment.

In case of normal incidence, on an isotropic but absorbing medium, the refractive index n_1 , in the above equations should be replaced by the complex refractive index $\tilde{n}_1 = n_1 + i\kappa_1$, in order for the absorption to be taken into account. Therefore, reflectance and transmittance are given by:

$$\mathcal{R}_p = \mathcal{R}_s = \frac{(n_0 - n_1)^2 + \kappa_1^2}{(n_0 + n_1)^2 + \kappa_1^2} \quad (3.82)$$

$$\mathcal{T}_p = \mathcal{T}_s = \frac{4n_0(n_1^2 + \kappa_1^2)}{(n_0 + n_1)^2 + \kappa_1^2}. \quad (3.83)$$

For other than normal incidence in an absorbing medium the calculations for the reflectance and transmittance become tedious, and approximations need to be used for each case. More details on this subject can be found in the references [48–52].

Although in our experimental part we are considering the case of normal incidence, we are not dealing with single surfaces but with multi-layered structures; this fact makes the problem a lot more complicated.

3.4 Light Propagation Through a Single Layer Structure

We consider a single homogeneous, isotropic, non-absorbing, layer of thickness d intercalated within two semi-infinite, non-absorbing, layers of different refractive indices. As the incident light beam meets the interface, part of the beam is reflected off, and the rest of the beam is transmitted through the interface. These phenomena occur every time the light beam encounters an interface between two media of different optical properties. Therefore, the reflectance of, and the transmittance through a single layer of thickness d are obtained by summing the multiple reflected and transmitted parts of the beam from the two parallel interfaces that define the single layer structure. There are different methods that can be used for the determination of the Fresnel coefficients

of reflection and transmission for a single layer. One way to deal with this problem is to sum the amplitudes of the successively reflected and transmitted beams in terms of the Fresnel coefficients as were determined in the previous section. Although this method works well for the case of a single layer, it becomes very complicated for the case of multiple layers, and thus another approach is going to be used for this problem, which is to work with the vector sums of the waves.

We consider an incident light beam on a layer of refractive index n_1 between two semi-infinite media of refractive indices n_0 , and n_2 , as shown in Figure 3.2.

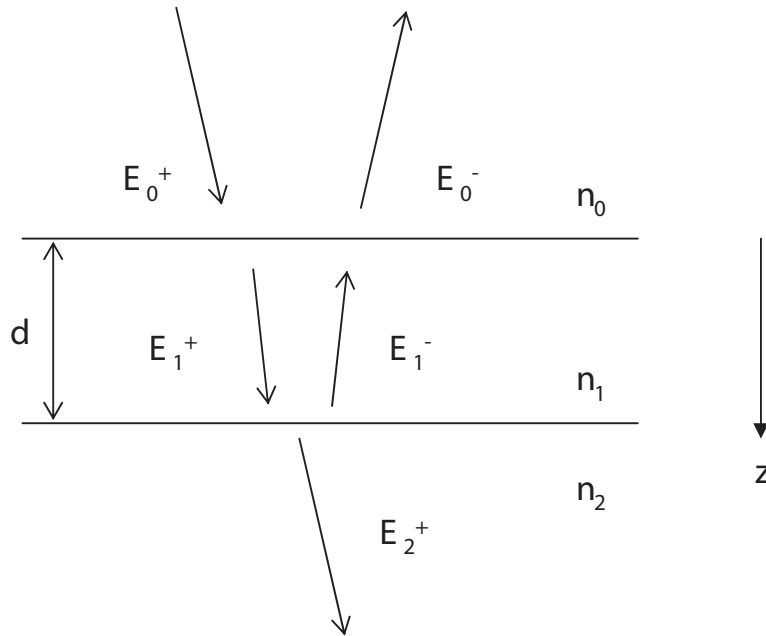


Figure 3.2: Reflection and transmission through a single-layer structure of refractive index n_1 , where the incident beam meets the surface at almost right angle.

The electric and magnetic vectors of the incident, reflected, and transmitted waves at the first interface, at $z = 0$, are the following:

$$E_{0x} = (E_{0p}^+ e^{-ik_0z} + E_{0p}^- e^{+ik_0z}) \cos \varphi_0 \quad (3.84)$$

$$E_{0y} = E_{0s}^+ e^{-ik_0z} + E_{0s}^- e^{+ik_0z} \quad (3.85)$$

$$H_{0x} = n_0(-E_{0s}^+ e^{-ik_0z} + E_{0s}^- e^{+ik_0z}) n_0 \cos \varphi_0 \quad (3.86)$$

$$H_{0y} = n_0(E_{0p}^+ e^{-ik_0z} - E_{0p}^- e^{+ik_0z}) \quad (3.87)$$

$$H_{0y} = n_0(E_{0p}^+ e^{-ik_0z} - E_{0p}^- e^{+ik_0z}) \quad (3.88)$$

$$E_{1x} = (E_{1p}^+ e^{-ik_1z} + E_{1p}^- e^{+ik_1z}) \cos \varphi_1 \quad (3.89)$$

$$E_{1y} = E_{1s}^+ e^{-ik_1z} + E_{1s}^- e^{+ik_1z} \quad (3.90)$$

$$H_{1x} = n_1(-E_{1s}^+ e^{-ik_1z} + E_{1s}^- e^{+ik_1z}) \cos \varphi_1 \quad (3.91)$$

$$H_{1y} = n_1(E_{1p}^+ e^{-ik_1z} - E_{1p}^- e^{+ik_1z}) \quad (3.92)$$

and the electric and magnetic vectors of the incident, reflected, and transmitted waves at the second interface, at $z = d$, are the following:

$$E_{2x} = E_{2p}^+ e^{-ik_2z} \cos \varphi_2 \quad (3.93)$$

$$E_{2y} = E_{2s}^+ e^{-ik_2z} \quad (3.94)$$

$$H_{2x} = n_2(-E_{2s}^+ e^{-ik_2z}) \cos \varphi_2 \quad (3.95)$$

$$H_{2y} = n_2 E_{2p}^+ e^{-ik_2z}. \quad (3.96)$$

The boundary conditions require the tangential components of both the electric and magnetic field to be continuous at the interfaces, at $z = 0$ and $z = d$, thus we obtain

$$(E_{0p}^+ + E_{0p}^-) \cos \varphi_0 = (E_{1p}^+ + E_{1p}^-) \cos \varphi_1 \quad (3.97)$$

$$(E_{0p}^+ - E_{0p}^-) n_0 = (E_{1p}^+ - E_{1p}^-) n_1 \quad (3.98)$$

$$E_{0s}^+ + E_{0s}^- = E_{1s}^+ + E_{1s}^- \quad (3.99)$$

$$(-E_{0s}^+ + E_{0s}^-) n_0 \cos \varphi_0 = (-E_{1s}^+ + E_{1s}^-) n_1 \cos \varphi_1 \quad (3.100)$$

$$(E_{1p}^+ e^{-ik_1 d_1} + E_{1p}^- e^{+ik_1 d_1}) \cos \varphi_1 = E_{2p}^+ e^{-ik_2 d_1} \cos \varphi_2 \quad (3.101)$$

$$(E_{1p}^+ e^{-ik_1 d_1} - E_{1p}^- e^{+ik_1 d_1}) n_1 = E_{2p}^+ e^{-ik_2 d_1} n_2 \quad (3.102)$$

$$E_{1s}^+ e^{-ik_1 d_1} + E_{1s}^- e^{+ik_1 d_1} = E_{2s}^+ e^{-ik_2 d_1} \quad (3.103)$$

$$(-E_{1s}^+ e^{-ik_1 d_1} + E_{1s}^- e^{+ik_1 d_1}) n_1 \cos \varphi_1 = E_{2s}^+ e^{-ik_2 d_1} n_2 \cos \varphi_2. \quad (3.104)$$

Using the Fresnel coefficients, as were defined in the previous section, the latter equations can be written as follows

$$E_0^+ = \frac{1}{t_1} E_1^+ + \frac{r_1}{t_1} E_1^- \quad (3.105)$$

$$E_0^- = \frac{r_1}{t_1} E_1^+ + \frac{1}{t_1} E_1^- \quad (3.106)$$

$$E_1^+ e^{-ik_1 d_1} = \frac{1}{t_2} E_2^+ e^{-ik_2 d_1} \quad (3.107)$$

$$E_1^- e^{-ik_1 d_1} = \frac{r_2}{t_2} E_2^- e^{-ik_2 d_1}. \quad (3.108)$$

The suffixes p and s have been omitted in the above equations because it has been shown that, the relations between the vectors polarized in the plane of incidence and those polarized in the perpendicular plane are the same [49]. One thing that should be kept in mind while using these equations is that the Fresnel coefficients themselves depend on the type of polarization. Based on these relations, the amplitudes of the light beam in each medium can be expressed in terms of the amplitude of the incident beam, and hence the reflected and transmitted amplitudes can be determined by:

$$R = \frac{E_0^-}{E_0^+} = \frac{r_1 + r_2 e^{-i2\delta_1}}{1 + r_1 r_2 e^{-i2\delta_1}} \quad (3.109)$$

$$T = \frac{E_2^+}{E_0^+} = \frac{t_1 t_2 e^{-i\delta_1}}{1 + r_1 r_2 e^{-i2\delta_1}}, \quad (3.110)$$

where

$$\delta_1 = \frac{2\pi}{\lambda} = n_1 d_1 \cos \varphi_1 \quad (3.111)$$

is the phase change upon the light beam traversing the film once.

Thus, the reflectance and transmittance are given by:

$$\mathcal{R} = RR^* = \frac{r_1^2 + 2r_1 r_2 \cos 2\delta_1 + r_2^2}{1 + 2r_1 r_2 \cos 2\delta_1 + r_1^2 r_2^2} \quad (3.112)$$

$$\mathcal{T} = \frac{n_2}{n_0} TT^* = \frac{n_2}{n_0} \frac{t_1^2 t_2^2}{1 + 2r_1 r_2 \cos 2\delta_1 + r_1^2 r_2^2}. \quad (3.113)$$

For the simple case of normal incidence, the Fresnel coefficients expressed in terms of the refractive indices have the following compact form:

$$r_1 = \frac{n_0 - n_1}{n_0 + n_1}, \quad (3.114)$$

$$r_2 = \frac{n_1 - n_2}{n_1 + n_2}, \quad (3.115)$$

$$t_1 = \frac{2n_0}{n_0 + n_1}, \quad (3.116)$$

$$t_2 = \frac{2n_1}{n_1 + n_2}. \quad (3.117)$$

Substituting the above Fresnel coefficients in the expression for reflectance and transmittance, we obtain the expressions for reflectance and transmittance at normal incidence in terms of the refractive indices of the media. In case of absorbing media, the real

refractive indices should be replaced by the complex refractive indices in order for the absorption to be taken into account.

3.5 Light Propagation Through a Multi-Layer Structure

Applying the method that was described for the single layer structure to a double layer structure, as the one shown in Figure 3.3 we obtain for the reflected and transmitted amplitudes the following:

$$R = \frac{E_0^-}{E_0^+} = \frac{r_1 + r_2 e^{-i2\delta_1} + r_3 e^{-i2(\delta_1+\delta_2)} + r_1 r_2 r_3 e^{-i2\delta_2}}{1 + r_1 r_2 e^{-i2\delta_1} + r_1 r_3 e^{-i2(\delta_1+\delta_2)} + r_2 r_3 e^{-i2\delta_2}} \quad (3.118)$$

$$T = \frac{E_3^+}{E_0^+} e^{-ik_3 d_2} = \frac{t_1 t_2 t_3 e^{-i(\delta_1+\delta_2)}}{1 + r_1 r_2 e^{-i2\delta_1} + r_1 r_3 e^{-i2(\delta_1+\delta_2)} + r_2 r_3 e^{-i2\delta_2}}, \quad (3.119)$$

where

$$\delta_m = \frac{2\pi}{\lambda} = n_m d_m \cos \varphi_m \quad (3.120)$$

is the phase change upon the light beam traversing the layer $m = 1, 2$, or 3 .

Thus, the reflectance and transmittance will be given by:

$$\mathcal{R} = RR^* \quad (3.121)$$

and

$$\mathcal{T} = \frac{n_3}{n_0} TT^*. \quad (3.122)$$

Another way to express the Fresnel coefficients r_1 , r_2 , and r_3 is by using the amplitude and the phase change of the light reflected at an interface. For example, the Fresnel coefficient, known also as effective Fresnel coefficient, corresponding to the light reflected at the back surface of the second film Figure 3.3 can be written in the form:

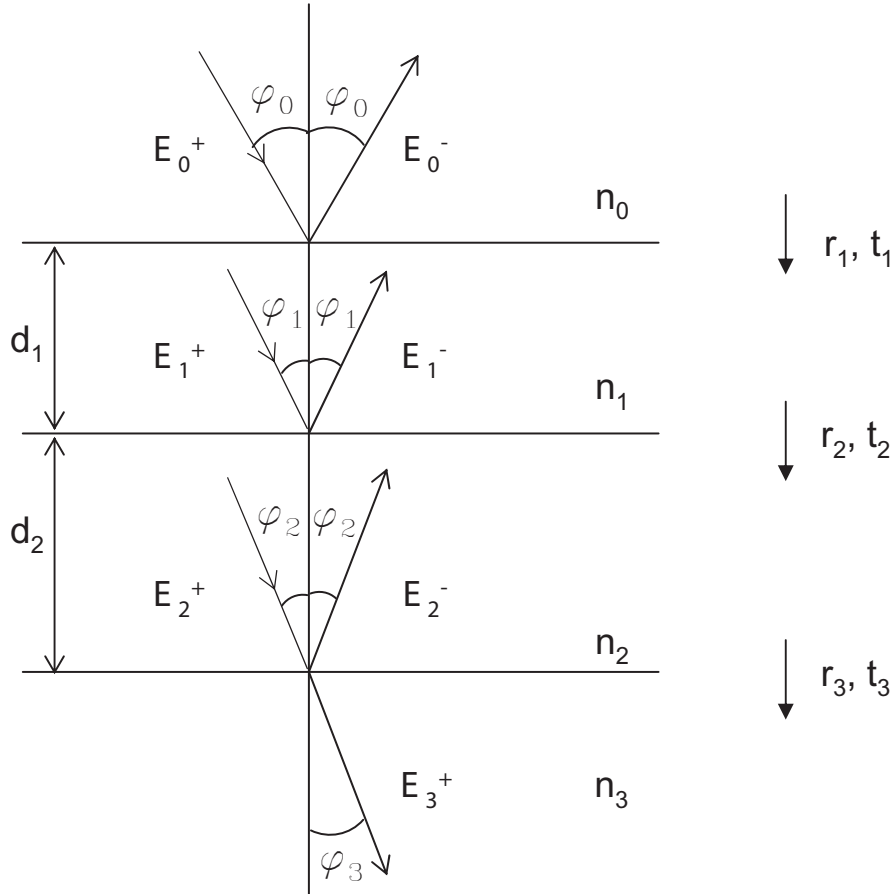


Figure 3.3: Reflection and transmission through a double-layer structure of refractive indices n_1 , and n_2 .

$$\varrho_2 e^{i\theta_2} = \frac{r_2 + r_3 e^{-i2\delta_2}}{1 + r_2 r_3 e^{-i2\delta_2}} \quad (3.123)$$

The first film, with refractive index of n_1 and thickness d_1 , can then be regarded as lying on top of the surface of a medium whose Fresnel coefficient is $\varrho_2 e^{i\theta_2}$, and therefore we can write

$$\varrho_1 e^{i\theta_1} = \frac{r_1 + \varrho_2 e^{i\theta_2} e^{-i2\delta_1}}{1 + r_1 \varrho_2 e^{i\theta_2} e^{-i2\delta_1}} \quad (3.124)$$

If we now consider a system of m layers, the effective Fresnel coefficient of the last one can be expressed as:

$$\varrho_m e^{i\theta_m} = \frac{r_m + r_{m+1} e^{-i2\delta_m}}{1 + r_m r_{m+1} e^{-i2\delta_m}} \quad (3.125)$$

where ϱ_m and θ_m are given by:

$$\varrho_m^2 = \frac{r_m^2 + r_{m+1}^2 + 2r_m r_{m+1} \cos 2\delta_m}{1 + r_m^2 r_{m+1}^2 + 2r_m r_{m+1} \cos 2\delta_m}, \quad (3.126)$$

and

$$\theta_m = \eta_m - \xi_m \quad (3.127)$$

where

$$\tan \eta_m = \frac{r_{m+1} \sin 2\delta_m}{r_m + r_{m+1} \cos 2\delta_m} \quad (3.128)$$

$$\tan \xi_m = \frac{r_m r_{m+1} \sin 2\delta_m}{1 + r_m r_{m+1} \cos 2\delta_m}. \quad (3.129)$$

For the $(m - 1)^{th}$ layer the effective Fresnel coefficient can now be calculated from:

$$\varrho_{m-1} e^{i\theta_{m-1}} = \frac{r_{m-1} + \varrho_m e^{i\theta_m} e^{-i2\delta_{m-1}}}{1 + r_{m-1} \varrho_m e^{i\theta_m} e^{-i2\delta_{m-1}}}. \quad (3.130)$$

Thus, the amplitude and the phase of the reflected light by a multi-layer structure can be calculated from the Fresnel coefficients at each interface and the thicknesses of the films, by simply repeating this process until all layers have been taken into account.

In the case of a multi-layer structure of absorbing media, the real refractive indices, introduced through the Fresnel coefficients must be replaced by complex quantities in order to take into account absorption. In this case, the problem becomes very complicated. Several methods of approaching this problem have been developed, and there are a few approximations that can be applied based on specific cases. For the analysis of our experimental data, the matrix method has been used.

3.5.1 Matrix Method

For a multi-layer structure, the matrix method can be demonstrated as follows. Starting with the boundary conditions, we can write

$$E_{m-1}^+ = (e^{i\delta_{m-1}} E_m^+ + r_m e^{i\delta_{m-1}} E_m^-) / t_m \quad (3.131)$$

$$E_{m-1}^- = (r_m e^{-i\delta_{m-1}} E_m^+ + e^{-i\delta_{m-1}} E_m^-) / t_m, \quad (3.132)$$

where $\delta_m = k_m d_m$, and r_m , t_m can be derive the same way as equations (3.114), and (3.116). The above recurrence relations can be written in a matrix form:

$$\begin{pmatrix} E_{m-1}^+ \\ E_{m-1}^- \end{pmatrix} = \frac{1}{t_m} \begin{pmatrix} e^{i\delta_{m-1}} & r_1 e^{i\delta_{m-1}} \\ r_m e^{-i\delta_{m-1}} & e^{-i\delta_{m-1}} \end{pmatrix} \begin{pmatrix} E_m^+ \\ E_m^- \end{pmatrix}. \quad (3.133)$$

For a system with n layers we require to know the relations between E_{n+1}^+ and E_0^+ , which will allow us to obtain the transmission coefficient, and between the E_0^- and E_0^+ , for the reflection coefficient. Based on equation (3.133), we can write

$$\begin{pmatrix} E_0^+ \\ E_0^- \end{pmatrix} = \frac{C_1 C_2 \dots C_{n+1}}{t_1 t_2 \dots t_{n+1}} \begin{pmatrix} E_{n+1}^+ \\ E_{n+1}^- \end{pmatrix} \quad (3.134)$$

where $E_{n+1}^- = 0$ since there is no negative-going wave in the $(n+1)^{th}$ layer, and

$$C_m = \begin{pmatrix} e^{i\delta_{m-1}} & r_1 e^{i\delta_{m-1}} \\ r_m e^{-i\delta_{m-1}} & e^{-i\delta_{m-1}} \end{pmatrix}. \quad (3.135)$$

Therefore, E_{n+1}^+ , and E_0^- can be expressed in terms of E_0^+ , and this is the way we calculate the transmission and reflection coefficients. This method is described in more detail in Chapter 4 of reference [49].

3.6 Kramers-Kronig, or Dispersion, Relations

The Kramers-Kronig technique is based on the law of causality, which states that the response of the medium can not precede the external cause, in this case the applied electromagnetic field, and it is also based in the application of complex analysis. General relations, known as Kramers-Kronig relations can be derived between the real and imaginary parts of a quantity. Thus, for the real and imaginary parts of the complex refractive index, and the dielectric function it can be written

$$n(\omega) - 1 = \frac{2}{\pi} \mathcal{P} \int_0^{\infty} \frac{\omega' \kappa(\omega')}{\omega'^2 - \omega^2} d\omega' \quad (3.136)$$

$$\kappa(\omega) = -\frac{2\omega}{\pi} \mathcal{P} \int_0^{\infty} \frac{n(\omega') - 1}{\omega'^2 - \omega^2} d\omega', \quad (3.137)$$

and

$$\epsilon_1(\omega) - 1 = \frac{2}{\pi} \mathcal{P} \int_0^{\infty} \frac{\omega' \epsilon_2(\omega')}{\omega'^2 - \omega^2} d\omega' \quad (3.138)$$

$$\epsilon_2(\omega) = -\frac{2\omega}{\pi} \mathcal{P} \int_0^{\infty} \frac{\epsilon_1(\omega') - 1}{\omega'^2 - \omega^2} d\omega', \quad (3.139)$$

where \mathcal{P} denotes the principal part of the integration. As can be seen from the latter equations, the real and imaginary parts of a linear response function are not independent with each other. Therefore, the Kramers-Kronig relations allows us, for example, to calculate the refractive index from the absorption coefficient and vice versa. This method provides us with a very important tool because we can perform one measurement which will provide us, i.e., the frequency dependence of the optical absorption, and then calculate the dispersion, without the need to perform a separate measurement.

It should be noted that, for a physical system the response function taken as an example the dielectric function, should satisfy the following relation:

$$\tilde{\epsilon}(\omega) = \tilde{\epsilon}^*(-\omega) \quad (3.140)$$

which for a dielectric system can be expressed as:

$$\epsilon_1(\omega) = \epsilon_1(-\omega) \quad (3.141)$$

$$\epsilon_2(\omega) = -\epsilon_2(-\omega) \quad (3.142)$$

and it requires the real part of the dielectric function ϵ_1 , to be an even function of the frequency ω , and the imaginary part of the dielectric function ϵ_2 , to be an odd function of the frequency ω .

The most common route to determine the optical parameters of a system is to perform reflectance measurements and make use of the Kramers-Kronig relations. It was shown in the previous section that the Fresnel reflective coefficient can be expressed in terms of the amplitude and phase change as follows

$$R = \rho(\omega)e^{i\theta(\omega)}, \quad (3.143)$$

where

$$\rho(\omega) = \sqrt{\mathcal{R}(\omega)}, \quad (3.144)$$

and

$$\tan \theta = \frac{Im[R]}{Re[R]} \quad (3.145)$$

which for the simple case where the incident light travels in vacuum $\tilde{n}_0 = 1$ before it meets an absorbing medium $\tilde{n}_1 = n + i\kappa$, the phase change is related to n and κ of the medium as follows

$$\tan \theta = \frac{-2\kappa}{1 - n^2 - \kappa^2}. \quad (3.146)$$

Equation (3.143) can be written as:

$$\ln R = \ln \rho(\omega) + i\theta(\omega) \quad (3.147)$$

and since the reflectance should also obey the law of causality, we can use the Kramers-Kronig relations to calculate the phase change dispersion:

$$\theta(\omega) = -\frac{\omega}{\pi} \int_0^{\infty} \frac{\ln \mathcal{R}(\omega') - \ln \mathcal{R}(\omega)}{\omega'^2 - \omega^2} d\omega' \implies \theta(\omega) = -\frac{1}{2\pi} \int_0^{\infty} \ln \left| \frac{\omega' + \omega}{\omega' - \omega} \right| \frac{d\mathcal{R}(\omega')}{d\omega'} d\omega'. \quad (3.148)$$

The determination of the phase change $\theta(\omega)$, enables us to obtain the refractive index n and extinction coefficient κ through equation (3.146).

A few drawbacks of the Kramers-Kronig technique are the facts that only a single bounce is taken into account, and the requirement that the measurements should be performed over the complete frequency spectral range $0 < \omega < \infty$, which is not practically possible. In a real experiment, the measurements are performed over a wide spectral range and then, extrapolations techniques are used for the frequencies beyond the measured frequency interval. These extrapolation procedures should be performed cautiously because they can result to false calculations of optical quantities, and therefore to false conclusions.

3.7 Models for the Determination of Optical Constants

3.7.1 Lorentz Model

The Lorentz model is employed for insulating solids, and it describes the motion mechanism of the bound electrons upon the application of an external field, and other excitations, such as lattice vibrations, also known as phonons. The bound electrons are

treated as if they were attached to the nucleus by springs and, upon the application of an electric field, they are subject to harmonic motion:

$$m \frac{d^2 \mathbf{r}}{dt^2} + m\gamma \frac{d\mathbf{r}}{dt} + m\omega_0^2 \mathbf{r} = -e\mathbf{E}_{loc} \quad (3.149)$$

where m , e are the mass and the charge of the electron respectively, and \mathbf{r} is the electron displacement from the equilibrium position. The second term on the left hand side of the above equation represents the damping term and provides for energy loss mechanisms, which in the case of solids are various scattering processes. The third term on the left hand side represents the harmonic restoring force (Hooke's law) with which the electron is bound to the core. The term on the right hand side represents the driving force, where \mathbf{E}_{loc} is the local electric field acting on the electron. We assume the local electric field varies in time as $\mathbf{E}_{loc}(\mathbf{t}) \propto \mathbf{e}^{-i\omega\mathbf{t}}$, and that the displacement \mathbf{r} has the same time dependence. Therefore the solution to the equation of motion is

$$\tilde{\mathbf{r}}(t) = -\frac{e}{m} \frac{1}{(\omega_0^2 - \omega^2) - i\gamma\omega} \mathbf{E}_{loc}(t). \quad (3.150)$$

The induced dipole moment is given by:

$$\tilde{\mathbf{p}} = e\mathbf{r} = \frac{e^2}{m} \frac{1}{(\omega_0^2 - \omega^2) - i\gamma\omega} \mathbf{E}_{loc}. \quad (3.151)$$

Assuming that the displacement \mathbf{r} is sufficiently small, the dipole moment can be written

$$\tilde{\mathbf{p}} = e\mathbf{r} = \tilde{\alpha}(\omega) \mathbf{E}_{loc} \quad (3.152)$$

where the frequency dependent quantity $\tilde{\alpha}$ is the atomic polarizability. Combining the last two equations, we can write for the polarizability of one electron atom:

$$\tilde{\alpha}(\omega) = \frac{e^2}{m} \frac{1}{(\omega_0^2 - \omega^2) - i\gamma\omega}. \quad (3.153)$$

It is obvious from the above expression that, the polarizability is a complex quantity due to the inclusion of the damping term, and thus it has a phase difference compared to the local electric field at all frequencies.

In case there are N atoms per unit volume, the macroscopic polarization is

$$\mathbf{P} = N \langle \mathbf{p} \rangle = N\tilde{\alpha} \langle \mathbf{E}_{loc} \rangle = \tilde{\chi}_e \mathbf{E}. \quad (3.154)$$

In order to relate the microscopic atomic polarizability to the macroscopic electric susceptibility, we should determine the relationship between the microscopic electric field \mathbf{E}_{loc} , and the macroscopic electric field \mathbf{E} . In general, $\langle \mathbf{E}_{loc} \rangle \neq \mathbf{E}$ because the local electric field is the average over atomic sites and not over regions between sites. For simplicity, in the case of bound electrons can be assumed that the two fields are equal since the inclusion of the restoring force contains all the necessary features for the description of the optical properties of the system. Therefore, it can be written

$$\mathbf{P} = N\tilde{\alpha}\mathbf{E} = \tilde{\chi}_e \mathbf{E} \quad (3.155)$$

from which $\tilde{\chi}_e$ can be deduced

$$\tilde{\chi}_e = \frac{Ne^2}{m} \frac{1}{(\omega_0^2 - \omega^2) - i\gamma\omega}. \quad (3.156)$$

Since the dielectric function is related to the macroscopic electric susceptibility as $\tilde{\epsilon} = 1 + 4\pi\tilde{\chi}_e$, it can be expressed in terms of the damped harmonic oscillators as:

$$\tilde{\epsilon} = 1 + \frac{4\pi Ne^2}{m} \frac{1}{(\omega_0^2 - \omega^2) - i\gamma\omega}, \quad (3.157)$$

or

$$\tilde{\epsilon} = 1 + \frac{\omega_p^2}{(\omega_0^2 - \omega^2) - i\gamma\omega} \quad (3.158)$$

where ω_p is the plasma frequency in Lorentz model, defined as:

$$\omega_p^2 = \frac{4\pi N e^2}{m}. \quad (3.159)$$

The real and imaginary parts of the dielectric function can also be written as:

$$\epsilon_1 = n^2 - \kappa^2 = 1 + \frac{4\pi N e^2}{m} \frac{\omega_0^2 - \omega^2}{(\omega_0^2 - \omega^2)^2 + \gamma^2 \omega^2} \quad (3.160)$$

and

$$\epsilon_2 = 2n\kappa = \frac{4\pi N e^2}{m} \frac{\gamma^2 \omega}{(\omega_0^2 - \omega^2)^2 + \gamma^2 \omega^2} \quad (3.161)$$

In case there are more than one characteristic resonant frequencies due to the oscillation of the bound electron within the atom and to the lattice vibrations, or there are more than one electrons per atom, the dielectric function is classically expressed as:

$$\tilde{\epsilon} = 1 + \frac{4\pi e^2}{m} \sum_j \frac{N_j}{(\omega_j^2 - \omega^2) - i\gamma_j \omega}, \quad (3.162)$$

where

$$\sum_j N_j = N. \quad (3.163)$$

N_j and ω_j are the density of bound electrons and their resonance frequency respectively.

Quantum mechanically, the dielectric function is expressed as:

$$\tilde{\epsilon} = 1 + \frac{4\pi e^2}{m} \sum_j \frac{N f_j}{(\omega_j^2 - \omega^2) - i\gamma_j \omega} \quad (3.164)$$

The ω_j represents the transition frequency of an electron between two atomic states of energy difference $\Delta E = \hbar\omega_j$, and the parameter f_j is called oscillator strength and is a measure of the relative probability of a quantum mechanical transition. In case of free

atoms with Z number of electrons, f_j should obey the following oscillator strength sum rule:

$$\sum_j f_j = Z. \quad (3.165)$$

In this analysis, it was assumed that the electrons are in vacuum, where $\epsilon_\infty = 1$. ϵ_∞ is the contribution from the high frequency absorption, beyond the measured range. However, in solid state $\epsilon_\infty \neq 1$ and thus in this case, the first term in equation (3.162), or (3.164), should be replaced by ϵ_∞ .

3.7.2 Drude Model

The Drude model is applicable to free charge carriers, free electrons in metals, and it is obtained from the same equation of motion used in Lorentz model by simply setting the restoring force term equal to zero:

$$\mathbf{F} = k\mathbf{r} = \mathbf{0} \quad (3.166)$$

where $k = m\omega_0^2$ is the spring constant which is chosen so that ω_0 coincides with the natural frequency of an atom. Therefore, the equation of motion for the Drude model is

$$m^* \frac{d^2 \mathbf{r}}{dt^2} + m^* \gamma \frac{d\mathbf{r}}{dt} = -e\mathbf{E} \implies m^* \frac{d\mathbf{v}}{dt} + \frac{m^*}{\tau} \mathbf{v} = -e\mathbf{E}, \quad (3.167)$$

where m^* is the effective electron mass, and the damping constant γ has been replaced by $1/\tau$. The relaxation time, τ , characterizes the energy loss due to scattering in a way similar to γ . More specifically, τ is associated with collisions between the free charge carriers and impurities, lattice vibrational phonons, or other scattering centers in metals. Assuming that the velocity varies in time as $\mathbf{v}_{loc} \propto e^{-i\omega t}$, the solution to the equation of motion has the form:

$$\tilde{\mathbf{v}} = \frac{e\tau}{m^*} \frac{1}{1 - i\omega\tau} \mathbf{E}. \quad (3.168)$$

In case of N free electrons per unit volume, the current density can be expressed as follows

$$\mathbf{J} = Ne\tilde{\mathbf{v}} = \frac{Ne^2\tau}{m^*} \frac{1}{1 - i\omega\tau} \mathbf{E}. \quad (3.169)$$

From this last equation and equation (3.9), we obtain the AC conductivity:

$$\tilde{\sigma}_D(\omega) = \frac{Ne^2\tau}{m^*} \frac{1}{1 - i\omega\tau} = \frac{\sigma_0}{1 - i\omega\tau}, \quad (3.170)$$

where

$$\sigma_0 = \frac{Ne^2\tau}{m^*} \quad (3.171)$$

is called the DC conductivity, and it is the zero frequency limit of the Drude conductivity. The real and imaginary parts of the conductivity in the Drude model are

$$\sigma_{D1} = \frac{\sigma_0}{1 + \omega^2\tau^2} \quad (3.172)$$

$$\sigma_{D2} = \frac{\sigma_0\omega\tau}{1 + \omega^2\tau^2}. \quad (3.173)$$

The dielectric function in Drude model is given by:

$$\tilde{\epsilon}_D(\omega) = 1 - \frac{\omega_{Dp}^2}{\omega^2 + i\omega/\tau} \quad (3.174)$$

where ω_{Dp} is the plasma frequency in Drude model, defined as:

$$\omega_{Dp}^2 = \frac{4\pi Ne^2}{m^*} \quad (3.175)$$

and typically lies in the visible or ultraviolet spectral region. The real and imaginary parts of the dielectric function can be obtained either from equations (3.12) and (3.13) and equations (3.172) and (3.173), or from equations (3.160) and (3.161) by simply setting $\omega_0 = 0$, $\gamma = 1/\tau$, and $m = m^*$:

$$\epsilon_{D1} = 1 - \frac{\omega_{Dp}^2 \tau^2}{1 + \omega^2 \tau^2} \quad (3.176)$$

$$\epsilon_{D2} = \frac{\omega_{Dp}^2 \tau}{\omega(1 + \omega^2 \tau^2)}. \quad (3.177)$$

In the limit of low frequency, where

$$\omega \ll \tau^{-1} \quad (3.178)$$

the dielectric function from equation (3.174), can be written as

$$\tilde{\epsilon}_D(\omega) = 1 - \frac{4\pi\sigma_0}{\omega\tau} \frac{1}{\omega + i/\tau} \approx 1 - \frac{4\pi\sigma_0\tau}{\omega} \left(\omega - \frac{i}{\tau} \right) \quad (3.179)$$

thus, the real and imaginary parts of the dielectric function, are

$$\epsilon_{D1} = 1 - 4\pi\sigma_0\tau \quad (3.180)$$

$$\epsilon_{D2} = \frac{4\pi\sigma_0}{\omega}. \quad (3.181)$$

For sufficiently low frequencies $\omega \ll \tau^{-1}$, we have $|\epsilon_1| \ll |\epsilon_2|$, and therefore, equations (3.45) and (3.46) will give

$$n = \kappa. \quad (3.182)$$

Using equations (3.41), (3.42), (3.180), (3.181), and (3.182) an expression for the skin, or penetration, depth can be written as follows

$$\delta = \frac{2}{\alpha} \approx \frac{c}{\sqrt{2\pi\sigma_0\omega}}. \quad (3.183)$$

The penetration depth provides a measure of the decay of the electric field within the medium, and as can be deduce from the above equation, the higher the dc conductivity of the medium the shorter the penetration depth of the AC field at a frequency ω .

3.7.3 Drude-Lorentz Model

The Drude-Lorentz model is used to describe the optical properties of materials under investigation. The Lorentz model is employed for the bound carrier interband transitions or the lattice vibrations, whereas the Drude model is used for the free carrier intraband transitions. Thus, the total dielectric function can be expressed as follows

$$\tilde{\epsilon} = \epsilon_\infty + \tilde{\epsilon}_D + \tilde{\epsilon}_L \quad (3.184)$$

where ϵ_∞ is the contribution from the high frequency absorption, beyond the measured range; in vacuum $\epsilon_\infty = 1$, $\tilde{\epsilon}_D$ is the Drude dielectric function given by equation (3.174), and $\tilde{\epsilon}_L$ is the Lorentz dielectric function given by equation (3.162). Therefore, the dielectric function can be expressed as:

$$\tilde{\epsilon}(\omega) = \epsilon_\infty + \sum_j \frac{\omega_{pj}^2}{\omega_j^2 - \omega^2 - i\gamma_j\omega} - \frac{\omega_{Dp}^2}{\omega^2 + i\omega/\tau} \quad (3.185)$$

This expression, obtained by combining the Drude and Lorentz models is used to fit the experimental reflectance data and provides an alternative to the Kramers-Kronig method for extracting the optical properties. The advantage of the Drude-Lorentz technique over the Kramers-Kronig technique is the fact that it does not require the data to be obtained over a wide spectral range. The fitting procedure can be performed over a finite spectral range, and no extrapolation processes are needed.

Another major advantage of the Drude-Lorentz technique over the Kramers-Kronig is the fact that, this technique can be employed for the analysis of thin films and multi-

layered structures. A separate parameter file is used for each layer, and $\tilde{\epsilon}(\omega)$ is obtained in terms of ϵ_∞ , and a set of three parameters, ω_j , ω_{pj} , and γ_j for every absorption band. Then, from the dielectric function, the refractive index can be calculated through equation 3.34, and finally, from the refractive index and the thickness of each layer, the reflectance and transmittance of the multilayered structure can be determined.

More detailed information about the Drude and Lorentz models can be found in the references [48, 53].

3.7.4 Sum Rules

Sum rules provide mainly a useful guide for the interpretation of the experimental results, as well as a way of checking the validity of the experimental data. A sum rule has already been introduced in a previous section, equation (3.165), but when we deal with solids there are a few sum rules that are more important. The following sum rule, expressed by the real part of the conductivity, states that the absorption energy at all frequencies is constant. For the quantum mechanic Lorentz model, the oscillator strength sum rule, or f-sum rule can be expressed

$$\int_0^\infty \sigma_1(\omega) d\omega = \frac{\omega_p^2}{8} \sum_j f_j \quad (3.186)$$

with ω_p given by equation (3.159), while for the Drude model the f-sum rule can be expressed

$$\int_0^\infty \sigma_1(\omega) d\omega = \frac{\omega_{Dp}^2}{8}. \quad (3.187)$$

Sum rules can frequently be found to be expressed in terms of an effective number of electrons per atom N_{eff} , contributing to the optical properties over a finite spectral range, as shown for example in reference [48].

CHAPTER 4 INSTRUMENTATION AND EXPERIMENTAL TECHNIQUES

This chapter describes the experimental equipment and the techniques used to handle the materials, to grow the films, to monitor their stability, and to perform measurements of absorbance, reflectance, and/or transmittance at near normal incidence over a wide frequency range, from 20 cm^{-1} to $40,000\text{ cm}^{-1}$, or equivalently 2.5 meV to 5 eV . In order to cover this entire region, various types of light sources, detectors, gratings, beam-splitters, filters, and different types of spectrometers must be used. Narrow regions of the electromagnetic spectrum are measured separately, using the appropriate optical components, and then merged together to form the spectrum of the entire frequency range of interest.

The following different spectrometers are used to measure the optical properties of our samples:

- StellarNet Photo Diode Array spectrometer (6250 cm^{-1} to $52,600\text{ cm}^{-1}$, or equivalently 0.77 eV to 6.5 eV),
- Varian Cary 500 spectrometer (3030 cm^{-1} to $57,100\text{ cm}^{-1}$, or equivalently 0.37 eV to 7.0 eV),
- Zeiss 800 MPM microscope photometer (4000 cm^{-1} to $40,000\text{ cm}^{-1}$, or equivalently 0.52 eV to 5.0 eV),
- Modified Perkin-Elmer 16U monochromator (1000 cm^{-1} to $40,000\text{ cm}^{-1}$, or equivalently 0.12 meV to 5.0 eV), and
- Bruker 113v fast scan Fourier Transform Interferometer, or FT-IR (20 cm^{-1} to 5500 cm^{-1} , or equivalently 2.5 meV to 0.68 eV).

A more detailed description of these spectrometers will follow later in this chapter.

4.1 Dry Box

Initially, all the samples were handled in ambient conditions. However, in-situ reflectance and transmittance measurements showed two strong absorption bands; one was coming from water (O-H stretching mode at 3570 cm^{-1} , or equivalently $2.8\ \mu\text{m}$) and the other one was coming from C-H stretching (at around 3000 cm^{-1} , or equivalently $3.3\ \mu\text{m}$), that hindered the performance of the samples in the mid-infrared region. In order to overcome this problem, all the materials were handled, and the samples were prepared in dry conditions. For this reason a dry box (VAC HE-series Dri Lab) was used, shown in Figure 4.1. This system provides a working area, hermetically sealed from the ambient environment, consisting of an inert atmosphere nearly free of moisture, oxygen, and sometimes nitrogen if desired. The principal gas, which is the one used in our labs too, is argon (Ar). Hence, helium (He), nitrogen (N_2), or any combination of the above gases can also be used. An antechamber mounted on the side of the dry box is used for passing materials in and out without disturbing the inert atmosphere of the box. Any time the antechamber is exposed to ambient atmosphere for the insertion of articles in the dry box there is a specific procedure that should be followed. This procedure includes three cycles of evacuation and filling of the antechamber with inert gas before any of the articles can be safely brought inside the dry box, without contaminating the inert atmosphere. Finally, two butyl rubber gloves, mounted in the full view window, provide easy access to the working area.

A very important part of this system is the chemical purifier mounted on the back side of the dry box, shown in Figure 4.2. The gas within the box circulates continuously through the purifier. The purifier canister contains a moisture absorbent (molecular sieves) and an oxygen reducing agent Q1, which is a material consisting of finely divided copper on an Alumina Matrix (made by Dow Chemical Company) [54]. As the gas from the glove box passes through the purifier, the absorbent removes the water vapor, and the oxygen reducing agent removes the oxygen before the gas enters the controlled atmosphere of the dry box again. The oxygen reducing agent, copper, combines che-

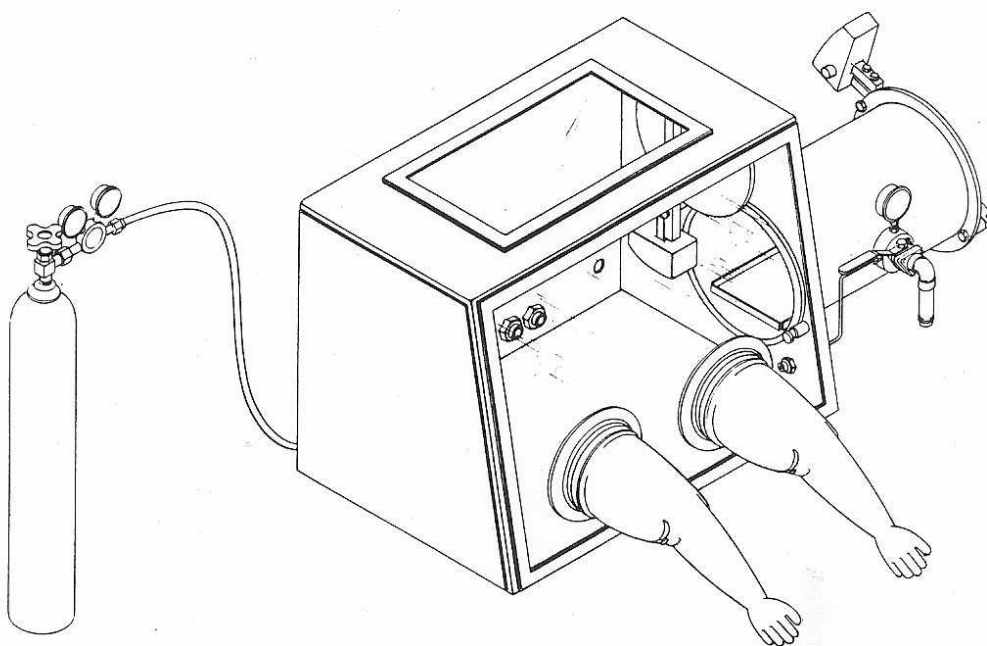


Figure 4.1: Schematic diagram of Dry or Glove Box.

mically with the oxygen forming cuprous or cupric oxide. When the agent is saturated with oxygen, the purifier is regenerated with the use of a special regeneration/forming gas that contains 3 to 10 per cent hydrogen. However, it should be noted that there are certain chemicals, like sulfur and sulfur compounds, such as H_2S , SO_2 , SO_3 , etc., that will poison the reactant material and they should not be used in the dry box. If their use is necessary, a suitable trap should be installed in advance in the circulating path to prevent these chemicals from getting into the purifier.

Other parts that can be mounted on the dry box are an oxygen analyzer (model AO-316-C, VAC, mounted on the dry box in our laboratory in the Physics department) to monitor the trace oxygen in the controlled atmosphere, and a pedatrol (model HE-63-P, VAC, mounted on the dry box in our laboratory in the Chemistry department) to provide both automatic and manual pressure control of the atmosphere inside the dry box. Due to the absence of an oxygen analyzer mounted on the dry box in the Chemistry laboratory, other methods had to be employed for oxygen and moisture testing of the inert atmosphere. Since it is recommended that the atmosphere inside the dry box

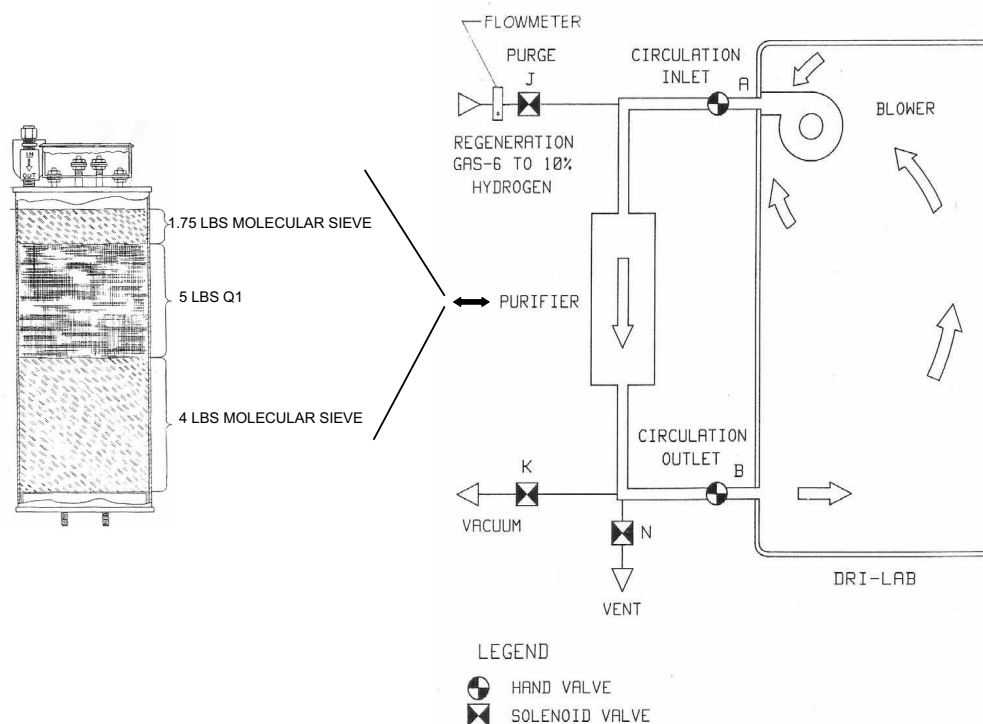


Figure 4.2: Schematic diagram of the chemical purifier and the gas flow through the chemical circulation.

be continuously monitored, a bottle of diethylzinc and a bottle of boron trifluoride diethyletherate are kept inside at all times. Diethylzinc is used for oxygen detection and boron trifluoride diethyletherate is used for water detection. To perform the test, the bottles should be uncovered and in case smoke is observed, then the atmosphere is contaminated and a regeneration of the purifier is needed; in case smoke is not observed, then the levels of oxygen and/or water are within the acceptable limits. However, it should be noted that this test only provides an indication of the condition of the dry box atmosphere.

4.2 Electrochemical Methods

For the study and characterization of chemical systems, electrochemical methods have been used throughout this work. Their application requires an understanding of the

fundamental principles of electrode reactions, and the electrical properties of electrode-solution interfaces. The electrochemical measurements provide information about the chemical changes caused by the passage of an electric current, and the production of electrical energy by chemical reactions [55]. In the electrochemical systems studied in this work, the processes that affect the transport of charge across the interface between chemical phases, for example, between an electrode (electronic conductor), and an electrolyte (ionic conductor), are of main concern. The charge transport through the electrode occurs by the movement of electrons or holes, whereas in the electrolyte phase it occurs by the movement of ions. There are several different types of materials that can be used as electrodes including solid metals (e.g., Pt, Au), liquid metals (e.g., Hg), and semiconductors (e.g., ITO, Si). For the electrolytes, the most frequently used are liquid solutions containing ionic species, such as H^+ , Na^+ , Cl^- , Li^+ , ClO_4^- in either aqueous or non-aqueous solvent. In order for the electrochemical experiment to take place, the solvent/electrolyte system must have sufficiently low resistance.

An important parameter in the electrochemical experiments is the measurement and control of the cell potential, which is the difference in electric potential between the electrodes in an electrochemical cell.¹ The magnitude of the potential difference at an interface determines the direction and the rate of charge transfer [55].

4.2.1 Electrochemical Polymerization

All the electrochemical experiments have been performed inside the dry box using an EG&PAR model 273A potentiostat/galvanostat. For the film deposition, a three electrode configuration has been used, shown in Figure (4.3), that consisted of a glass container, a working electrode (WE), an auxiliary (counter) electrode (CE), and a reference electrode (RE). The working electrode is the electrode where the polymerization of interest takes place. For this work, a number of different working electrodes have been used, such as Gold/Mylar, Gold/KaptonTM, ITO/Glass, and SWNTs/PET. A Pt flag,²

¹ Electrochemical cell: two or more electrodes separated by an electrolyte phase.

² Pt flag: a piece of Pt foil, with a relatively large area compared to the WE, and a Pt wire welded together.

used as the counter electrode, provides the required current to sustain the developing processes at the working electrode. This arrangement prevents large currents from passing through the reference electrode and change its potential. There are several different types of reference electrodes [56] that are commercially available, such as saturated calomel (Hg_2Cl_2) electrode (SCE), Ag/AgCl saturated in KCl electrode, and Ag/Ag⁺ electrode. However, for use in the dry box the choices are limited. In our experiments, a silver wire (Ag) has been used as a pseudo-reference electrode. Frequent calibrations have been performed versus Fc/Fc⁺ because the potential of the pseudo-reference electrode changes with time, and sample solution deposition. The electrochemical polymerization of the films has been carried out in 0.2 M electrolyte solution containing 10 mM monomer, that is added in the glass container until a big portion of all the electrodes is bathed in the solution, as shown in Figure 4.3. Finally, the electrodes are connected to the potentiostat by either alligator clips, or micro clips since the passing currents are small.

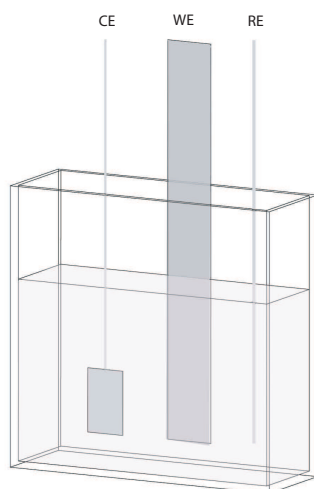


Figure 4.3: Schematic diagram of three-electrode configuration cell.

4.2.2 Cyclic Voltammetry (CV)

Cyclic voltammetry (CV) is one of several methods [57] used to characterize conducting polymers. It is a simple and valuable technique that provides both quantitative and qualitative information about the system under study. In this method, the current

density at the working electrode is measured as a function of the applied potential. More specifically, the potential is repeatedly cycled over a specified voltage range while the resulting current is measured. The obtained voltammogram is a display of current density as a function of the applied potential. The scan rate expressed in mV/s is a dynamic parameter and can be changed accordingly in order for different types of reactions, fast or slow, to be followed effectively. This cyclic voltammogram reveals information regarding the electrochemical potential at which the oxidation and reduction processes occur for each polymer, the degree of reversibility of the electrode reaction, and the electrochemical stability of electroactive species through repeated cycles. Important parameters of a polymer cyclic voltammogram are the scan rate dependence of the anodic and cathodic peak currents, I_{pa} and I_{pc} , the anodic and cathodic peak potentials, E_{pa} and E_{pc} , and the reversibility of the potential wave.

4.3 Optical Methods

For the experiments that are going to be presented in this work, reflectance and/or transmittance (in or out of solution) measurements had to be taken over a wide frequency range, from 20 cm^{-1} to $45,000\text{ cm}^{-1}$. To perform these experiments, various types of light sources, detectors, gratings, beam-splitters, filters, and even different types of spectrometers had to be used. Several regions of the electromagnetic spectrum have been measured separately, using the appropriate optical components, and then merged together to form the spectrum of the entire frequency range of interest.

4.3.1 Spectroelectrochemistry

Spectroelectrochemistry plays a key role in probing the optical changes that occur upon doping and de-doping of a conducting polymer. It is an important method that can also provide information about the electronic structure of the material, such as the band gap and the intraband states created upon doping.

Spectroelectrochemical experiments were performed using a StellarNet Photo Diode Array (PDA) UV-Vis-NIR spectrophotometer (made by StellarNet, Inc.) located inside

the dry box, and/or a UV/Vis-NIR Varian Cary 500 spectrophotometer (Varian Optical Spectroscopy Instruments) located on the bench top.

The StellarNet spectrophotometer (EPP2000C UV-Vis and EPP2000 NIR In-GaAs) is a portable fiber optic instrument used for absorbance/transmittance measurements in the UV-Vis-NIR range. This spectrophotometer utilizes a special concave holographic grating for aberration correction in order to provide better imaging. Without mirrors, the grating maintains low stray light, and the instrument losses are minimized. In addition, the absence of moving parts makes the instrument more stable and very reliable. This system is equipped with a linear Photo Diode Array detector and a tungsten halogen (tungsten krypton bulb) source. The spectrometer covers 190 - 890 nm for the UV-Vis region, and 900 - 1600 nm for the NIR region.

The UV/Vis - NIR Varian Cary 500 spectrophotometer is a double beam monochromator that covers the wavelength range from 175 - 3300 nm. The instrument is equipped with a high performance R928 photomultiplier detector for the UV-Vis region and an electrothermally controlled lead sulfide (PbS) photocell for the NIR region. The available light sources for this system are a tungsten halogen source with quartz window for NIR and visible regions, and a deuterium arc UV source.

For typical thin film polymer samples deposited potentiostatically on a number of different substrates, a three-electrode cell configuration has been used, as the one described above, to allow potential application while monitoring the absorption/transmission spectra. The samples are placed in monomer free solution, and the electrodes are connected to an EG&PAR model 273A potentiostat/galvanostat. For EC devices, only the UV - Vis - NIR Varian Cary 500 spectrophotometer is used, in which the three-electrode cell is replaced by a suitable holder available in the Cary 5 kit. In order to apply a voltage across the EC devices, the counter and the reference leads have to be connected to one another. Finally, for both cases, EC polymer films on electrodes and in devices, the experiment is performed by sequentially stepping the applied potential in either 0.1 V or 0.2 V increments, starting from a potential at which the polymer is in its neutral

form and ending at a potential value for which the polymer is fully doped, while the absorption/transmission spectra is monitored.

The UV/Vis - NIR Varian Cary 500 spectrophotometer provides one more method of EC polymer on electrode or in device characterization in addition to the one outlined above. Using the same experimental set up we can perform a kinetics experiment and measure the speed with which the material is able to switch between two extrema states. In this case, a single wavelength is used, the wavelength of maximum contrast which can be determined from the experiment described above, and a square potential waveform is applied at desired time intervals. The percentage transmittance ($\mathcal{T}\%$) is monitored at the wavelength of maximum contrast λ_{max} as a function of time, while the EC polymer on electrode (in solution), or in device, is repeatedly switched between the two extrema states.

4.3.2 Interferometric or FTIR Spectrometer

An interferometer or Fourier Transform Spectrometer is a type of spectrometer mostly used in the infrared region. The spectrometer relies on two major advantages compared to the monochromatic spectrometer:

- Jacquinot (or throughput, or étendue) advantage, which is the ability of interferometers to collect large amounts of energy at high resolution due to the use of circular apertures, which have high throughput, and
- Fellgett (or multiplex) advantage, which is the ability of interferometers to receive information about an entire spectral range during one scan. In other words, all frequencies in the region of interest are sampled simultaneously.

As a result of these advantages an interferometer has large resolving power, fast sampling times, reduced stray light, and high signal-to-noise ratio (S/N) [58–60]. However, even though the Jacquinot (or throughput or étendue) advantage holds for low and high frequencies, the Fellgett (or multiplex) advantage is lost for higher frequencies. This is due to the fact that although for the infrared region the noise is usually detector

noise which is independent of the signal, for higher frequency regions the noise depends on the source intensity (photon noise) [59].

More specifically, in the infrared region the signal-to-noise ratio for an interferometer is proportional to the square root of the total time T , required for a scan of a broad band $\Delta\bar{\nu}$:

$$(S/N)_I \propto T^{1/2}, \quad (4.1)$$

but in the visible region, the signal-to-noise ratio is also proportional to the square root of the source intensity I :

$$(S/N)_I \propto [(T/M)I(\Delta\bar{\nu})]^{1/2}, \quad (4.2)$$

where M is the number of spectral elements of width $\delta\bar{\nu}$ in a broad band $\Delta\bar{\nu} = \bar{\nu}_2 - \bar{\nu}_1$. Comparing the above results with the signal-to-noise ratio for a monochromator, which in the infrared region is

$$(S/N)_M \propto (T/M)^{1/2}, \quad (4.3)$$

and in the visible region is

$$(S/N)_M \propto [(T/M)I(\Delta\bar{\nu})]^{1/2}, \quad (4.4)$$

we conclude that although the interferometer has an advantage over the monochromator at low frequency regions due to the Fellgett advantage, equations (4.1) and (4.3), at higher frequencies this advantage is lost and the two spectrometers provide the same signal-to-noise ratio, equations (4.2) and (4.4) [58, 59].

There are several advantages and limitations for both types of spectrometers. The Fellgett (or multiplex) advantage makes the interferometer an excellent choice for the low frequency regions but the loss of it at higher frequencies in combination with the

availability of stronger sources and more sensitive detectors in that region, make the monochromator a more suitable choice for high frequency regions.

Fourier Transform Infrared (FTIR) Spectroscopy

The principle of interferometry is based on the idea of the Michelson interferometer which is depicted in Figure 4.4. There exist several variations of the interferometer: Prism, Grating, Fabry-Perot, Lamellar and others, but here only the simplest version is going to be described. As shown in Figure 4.4 the Michelson interferometer consists of two plane mirrors, one stationary ($\mathcal{M}1$) and one movable ($\mathcal{M}2$), and a beam splitter. The light beam coming from the source is divided by the beam splitter into two ideally equal parts. One part is reflected by the beam splitter to the stationary mirror and has a fixed path length, and the other part is transmitted through the beam splitter to the movable mirror and has a path length that can be varied by translating the movable mirror. The two beam parts are reflected from the mirrors and they are recombined again at the beam splitter. Due to the path length difference or optical retardation of the two beams, which is twice the displacement of the movable mirror from its balanced position (ZPD) a phase difference equal to $2\pi\bar{\nu}\delta$ is introduced, where $\bar{\nu}$ is the wave number and it is defined as $\bar{\nu} = 1/\lambda$. The partial beams are spatially coherent and will interfere when they recombine.

In more detail, assume that the source is emitting monochromatic plane waves of the form:

$$\mathcal{E}_S(z) = \mathcal{E}_0(z)e^{i(\omega t - 2\pi\bar{\nu}z)}. \quad (4.5)$$

In a Michelson interferometer, after the amplitude splitting takes place, there are two beams that have traveled different distances z_1 and z_2 , before they recombined at the beam splitter. As was mentioned above, each beam has undergone one reflection and one transmission at the beam splitter.

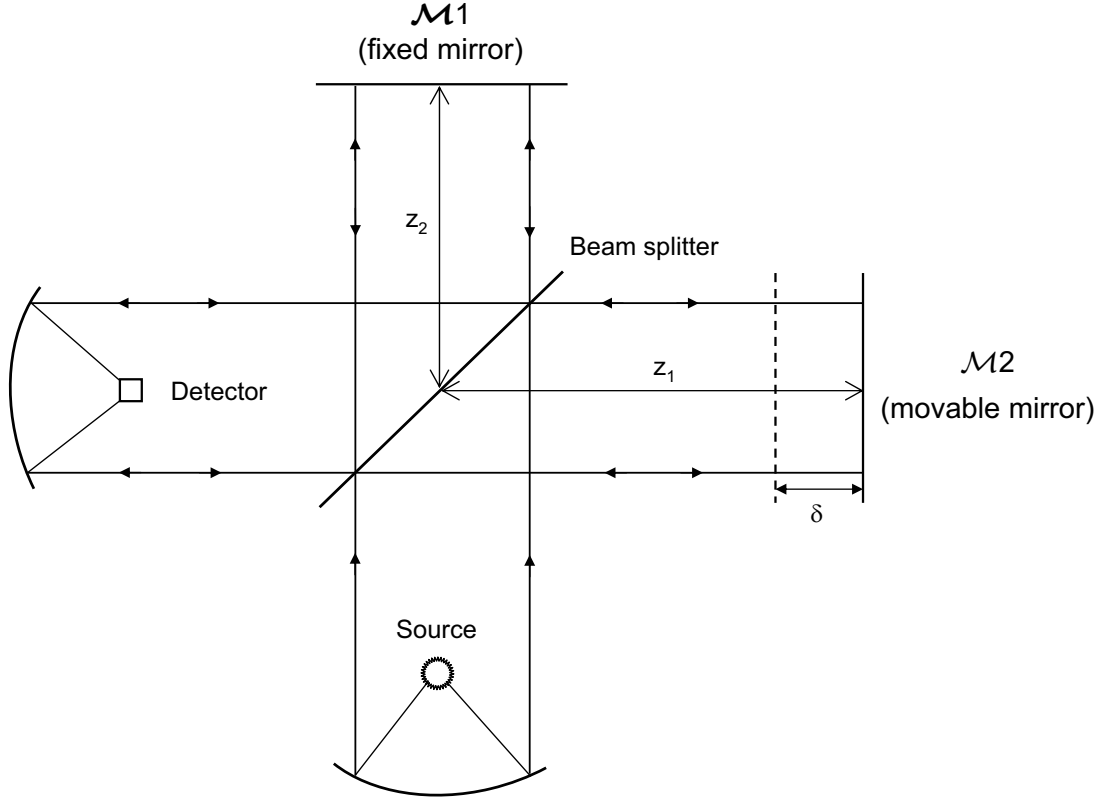


Figure 4.4: Schematic diagram of the Michelson Interferometer.

If r_{bs} is the reflection coefficient and t_{bs} the transmission coefficient of the beam splitter, then the resultant field of the recombined beams, using the superposition law, will be

$$\mathcal{E}_R(z_1, z_2, \bar{\nu}) = r_{bs}t_{bs}\mathcal{E}_0[e^{i(\omega t - 2\pi\bar{\nu}z_1)} + e^{i(\omega t - 2\pi\bar{\nu}z_2)}]d\bar{\nu} \quad (4.6)$$

and the intensity (irradiance or flux density) $I_R(z_1, z_2, \bar{\nu})$ at the detector will be

$$I_R(z_1, z_2, \bar{\nu}) = \mathcal{E}_R(z_1, z_2, \bar{\nu})\mathcal{E}_R^*(z_1, z_2, \bar{\nu}) = 2\mathcal{E}_0|r_{bs}t_{bs}|^2[1 + \cos(2\pi\bar{\nu}(z_1 - z_2))], \quad (4.7)$$

where $z_1 - z_2 = \delta$ is the optical path difference between the two beams. Hence, equation (4.7) can be written

$$I_R(\delta, \bar{\nu}) = 2\mathcal{E}_0|r_{bs}t_{bs}|^2[1 + \cos(2\pi\bar{\nu}\delta)]. \quad (4.8)$$

In the case of a polychromatic source emitting a continuous spectrum from $\bar{\nu} = 0$ to $\bar{\nu} = \infty$, the total intensity at the detector will be

$$I_R(\delta) = \int_0^{\infty} I_R(\delta, \bar{\nu})d\bar{\nu} = 2|r_{bs}t_{bs}|^2 \left(\int_0^{\infty} \mathcal{E}_0^2(\bar{\nu})d\bar{\nu} + \int_0^{\infty} \mathcal{E}_0^2(\bar{\nu}) \cos(2\pi\bar{\nu}\delta)d\bar{\nu} \right), \quad (4.9)$$

where the first term on the right side of the above equation is constant and it represents the total intensity emitted by the source. At zero path difference $\delta = 0$ the intensity at the detector is

$$I_R(0) = 4|r_{bs}t_{bs}|^2 \int_0^{\infty} \mathcal{E}_0^2(\bar{\nu})d\bar{\nu}. \quad (4.10)$$

Thus, equation (4.9) can be written

$$[I_R(\delta) - \frac{1}{2}I_R(0)] = 2|r_{bs}t_{bs}|^2 \int_0^{\infty} \mathcal{E}_0^2(\bar{\nu}) \cos(2\pi\bar{\nu}\delta)d\bar{\nu}, \quad (4.11)$$

in which the quantity $[I_R(\delta) - \frac{1}{2}I_R(0)]$ is known as interferogram. The Fourier cosine transform of the interferogram provides the actual spectrum:

$$B_R(\delta, \bar{\nu}) \propto \mathcal{E}_0^2(\bar{\nu}) = \frac{1}{\pi|r_{bs}t_{bs}|^2} \int_0^{\infty} [I_R(\delta) - \frac{1}{2}I_R(0)] \cos(2\pi\bar{\nu}\delta)d\delta. \quad (4.12)$$

However, in practice it is not possible to measure an interferogram over an infinite path difference. The finite optical path displacement results in the introduction of numerous peaks into the transformed spectra, in addition to the main, which is one centered approximately at $\bar{\nu} = 0$. These peaks need to be corrected because they cause a “leakage” of spectral intensity; the intensity is not localized to the main peak at $\bar{\nu} = 0$ anymore but it is distributed to all peaks. These peaks are called side lobes, or “feet”,

and the corrective procedure used for modifying the basic Fourier transform integral is called apodization. For the correction of this error, the interferogram is multiplied by a function, the apodization function, which vanishes outside the range of the acquisition data. Their product is then Fourier transformed, in order to give the actual spectrum. There are several apodization functions that can be used, the simpler ones are the rectangular, or “boxcar”, shown in Figure 4.5:

$$G_1(z) = \begin{cases} 1, & \text{if } |z| \leq L \\ 0, & \text{if } |z| > L \end{cases} \quad (4.13)$$

and the triangular, also shown in Figure 4.5:

$$G_2(z) = \begin{cases} 1 - \frac{|z|}{L}, & \text{if } |z| \leq L \\ 0, & \text{if } |z| > L \end{cases} \quad (4.14)$$

where L is the maximum path difference. Other apodization functions that can be used are the trapezoidal which is shown in Figure 4.5, the Happ-Genzel, the Blackman-Harris, and the Norton-Beer (week, medium, or strong). Further details on the effects and the choices of other apodization functions used, can be found in the literature [58, 59, 61]. It must be noted though, that the convolution of the apodization function with the interferogram will result in reduction of the resolution \mathfrak{R} , where $\mathfrak{R} \sim 1/L$.

Another assumption that was made in this section, which is not always true in a real experiment is that the interferogram is symmetric with respect to the zero path difference (ZPD) $\delta = z_1 - z_2 = 0$. Usually, the sampling of the interferogram starts at $\delta = 0$, and the interferogram function has a maximum value at this point; but if this is not the case, then all sampling points are displaced by the same small amount. This results in an asymmetric interferogram with respect to the $\delta = 0$ point, and it introduces a phase error.

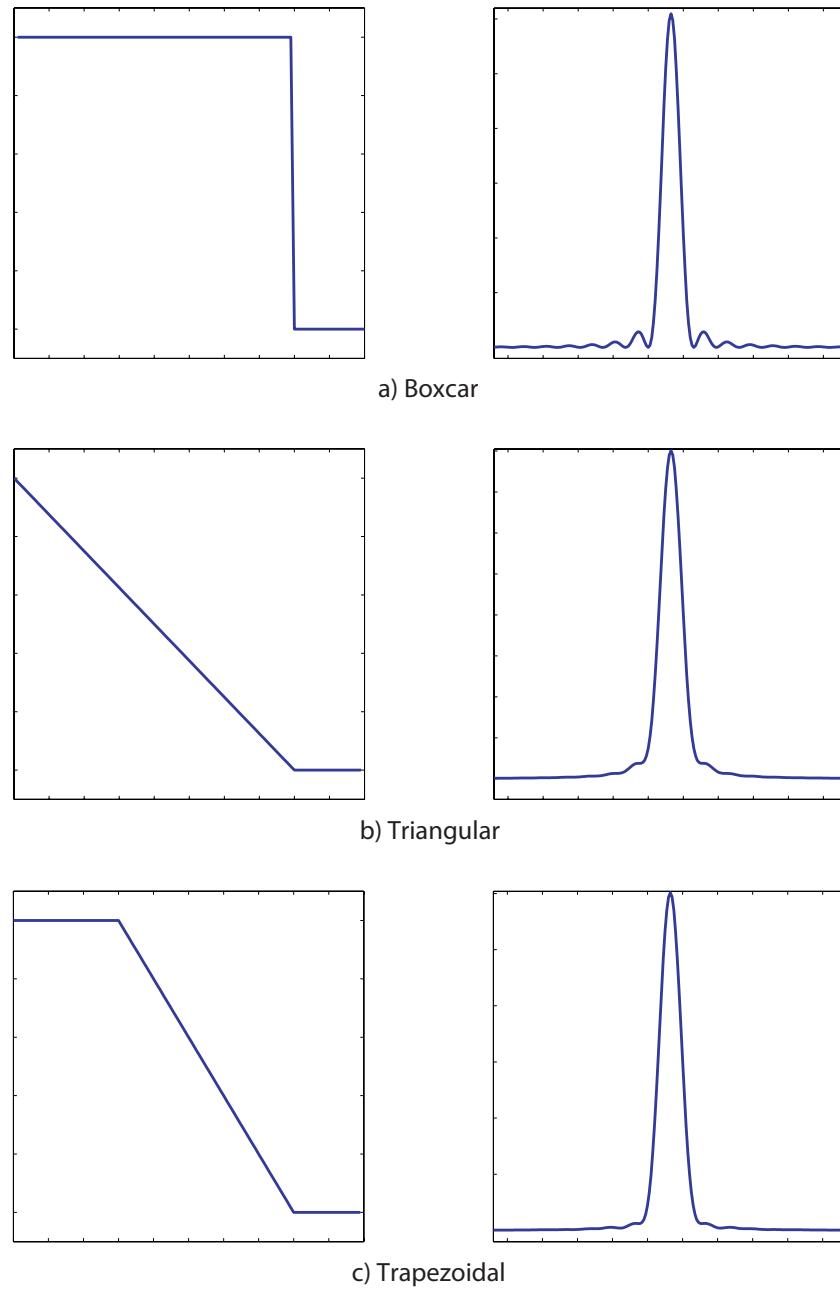


Figure 4.5: Several apodization functions (right), and their Fourier transforms (left) plotted together.

Furthermore, in the calculation of the spectrum, equation (4.12), a symmetrical interferogram was assumed. However, in the case of an asymmetrical interferogram, a complete cosine and sine Fourier transformation is needed for the calculation of the spectrum. The application of the cosine Fourier transformation alone will result in a distorted spectrum, and the creation of spurious lines. Unfortunately using the complete Fourier transformation, twice as many points need to be collected in order to achieve the same spectral resolution which translates into longer times for data acquisition. Furthermore, the use of a phase correction mode is necessary in order for the phase error to be corrected, and for the scanning time to be kept short.

Finally, the data acquisition requires the use of a digital computer for the calculation of the spectrum from the interferogram function. In order for this calculation to take place, the recorded data have to be digitized into a number of discrete values. For this reason, the interferogram is sampled at steps of path difference $\Delta\bar{\nu}$. The discrete nature of the real experiment can be handled mathematically by using Dirac delta functions. The interested reader can find more details about this process in the literature, references [59, 62]. The spectrum that is obtained from the sampled interferogram is periodic, it repeats itself at multiples of $\Delta\bar{\nu}$. If the repeated spectra overlap then an error effect, called aliasing or “folding”, is introduced. For this error to be avoided, the maximum frequency of the true spectrum must obey the following condition:

$$\bar{\nu}_{max} = \frac{\Delta\bar{\nu}}{2}. \quad (4.15)$$

Other errors can occur from electronic filtering, misalignment, optical effects caused by various parts of the instrument optics, such as the use of non-ideal mirrors (ideal: 100% reflective), and non-ideal beam splitters (ideal: non-absorbing, 50% transmissive and 50% reflective), and not accurate adjustment of the movable mirror. These errors introduce a phase factor that usually can be taken care of by the use of a phase correction mode. The most commonly used correction mode, which is also the one used in our equipment, is the Mertz but there are several more that can be used.

Brucker 113v Interferometer

The reflectance, and transmittance measurements in the far infrared (FIR), and mid-infrared (MIR) regions were obtained with a Brucker 113v fast-scan Fourier transform, or FT-IR, interferometer. The covered frequency range is from 20 cm^{-1} to 5500 cm^{-1} . The spectrometer, a schematic diagram of which is shown in Figure 4.6, consists of four main chambers: source, interferometer, sample, and detector chambers. During the measurements the system is evacuated to avoid the appearance of absorption bands from water (H_2O), and carbon dioxide (CO_2) in the spectra. The sample region is divided into two identical chambers, one for reflectance and the other for transmittance measurements with the use of special designed optical stages. The reflectance stage is shown in Figure 4.7. For far infrared measurements (20 cm^{-1} - 700 cm^{-1}), a mercury (Hg) arc lamp is used as a source, and a liquid helium (He) cooled 4.2 K silicon (Si) bolometer as a detector, shown in Figure 4.8. In the mid-infrared region (400 cm^{-1} - 5500 cm^{-1}), a globar (Silicon Carbide SiC) lamp is used as a source, and a room temperature pyroelectric deuterated triglycerine sulfate (DTGS) as a detector.

The principle of the FT-IR Brucker interferometer is based on the Michelson interferometer described above. The light beam generated by the source, as shown in Figure 4.6 (a), goes through an automated circular aperture³ to the beam splitter, mounted on an automatic changer 4.6 (d), where is divided into two parts. Each part of the beam is reflected by fixed mirrors, and after imaged onto the faces of the movable double-sided mirror 4.6 (e), the two beams recombine at the beam splitter. Part of the recombined beam is reflected by a series of mirrors, focused in the sample chamber 4.6 (i) or 4.6 (j), and sent to the detector through another set of mirrors. The rest of the recombined beam is reflected back to the light source. The recorded interferogram has a maximum amplitude when the two arms of the interferometer have a zero path difference (ZPD). When the double-sided mirror moves due to a scanning mechanism at a constant speed v , a path difference of $\delta = 4vt$, where the time t is measured from the ZPD, is introduced.

³ The aperture diameter can vary from 1.25 mm to 10 mm.

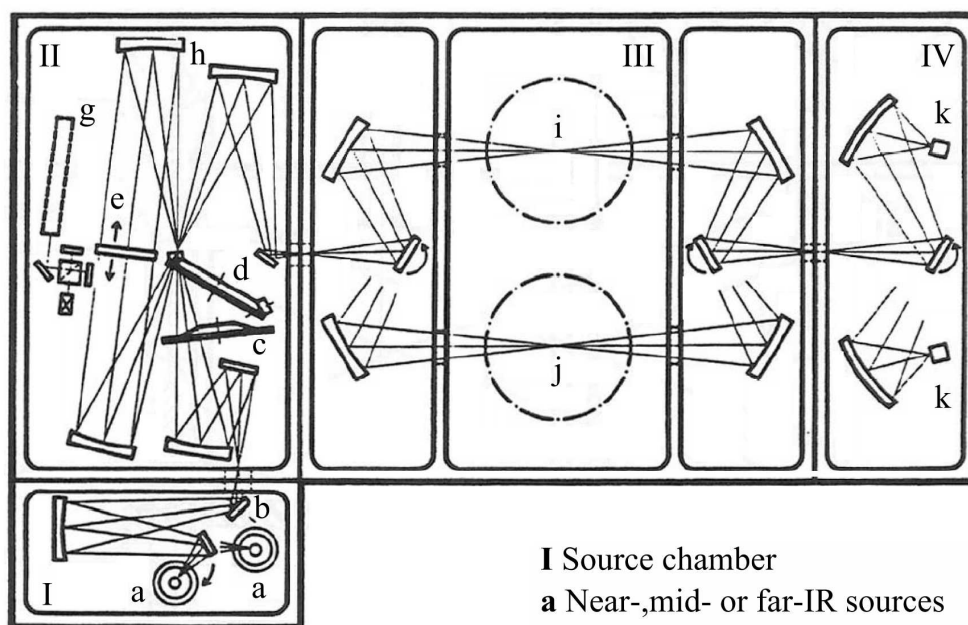


Figure 4.6: Schematic diagram of Brucker (IBM) 113v FT-IR spectrometer.

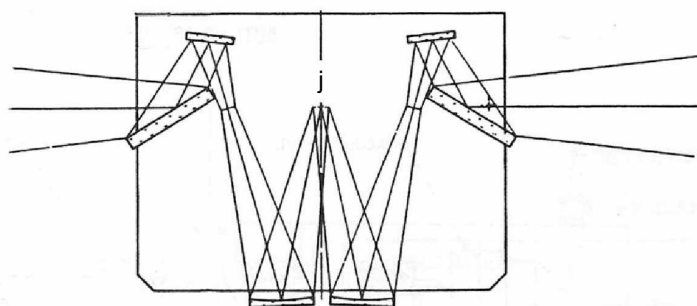


Figure 4.7: Schematic diagram of the reflectance stage.

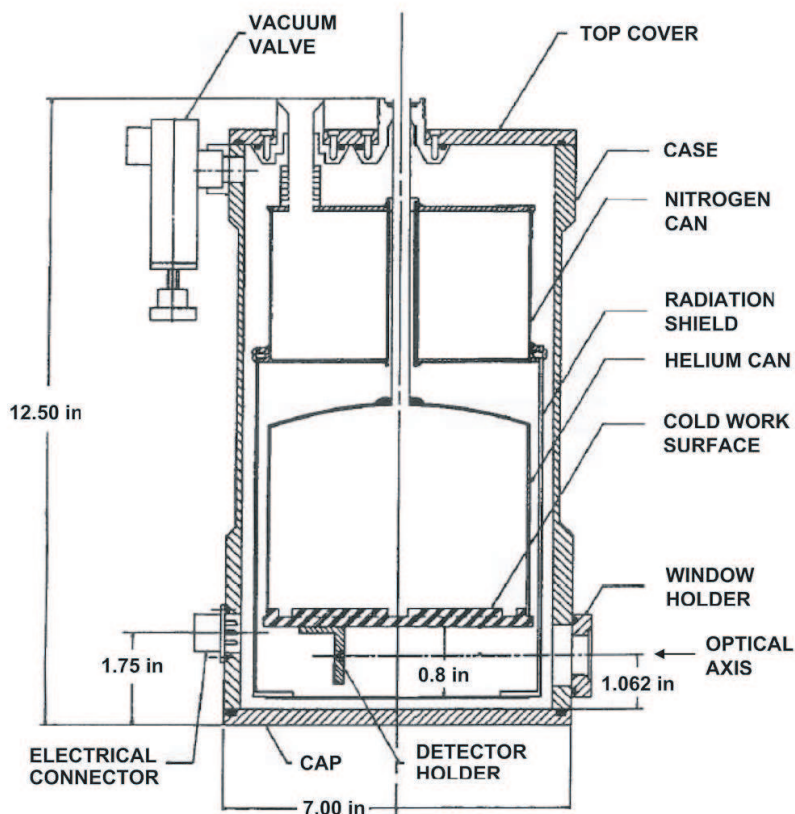


Figure 4.8: Schematic diagram of the liquid helium cooled detector.

In this system the mirror is air-bearing and is moving continuously. The calibration of the position of the double-sided mirror is monitored by a He-Ne laser Figure 4.6 (g) and a white-light reference interferometer.

The detected signal is amplified by a preamplifier, and sent to a 16-bit analog-to-digital converter. The data are collected by a computer system, where the interferogram is Fourier transformed to produce the single beam spectrum. The reflectance spectrum is then calculated by taking the ratio of the single beam spectrum of the sample to the single beam spectrum of the background reference, usually an aluminum (Al) mirror. Additional calculations need to be done in this case, in order for the Al mirror/reference reflectance to be taken into account.⁴ For case of transmittance measurements, the

⁴ The aluminum (Al) mirror is used as a reference for reflectance measurements but since it does not reflect 100% throughout the whole spectral range that is being used for, the spectrum needs to be corrected. This is called "Al mirror correction".

spectrum is calculated by taking the ratio of the single beam spectrum of the sample to the single beam spectrum of an empty hole of the same size. Finally, the software that is being used to control the experimental set up, and for data manipulation is the commercial OPUS spectroscopic software.

Table 4.1⁵ provides the experimental parameters for the spectral regions, and the various types of beam-splitters, optical filters, etc, for each one of the regions.

Table 4.1: Bruker 113v FT-IR interferometer parameters.

Spectral Range (cm ⁻¹)	Source	Detector	Beam Splitter (μm)	Scanner Velocity (kHz)	Phase Correct. Mode	Optical filter	Apod. function
20 - 100	Hg arc	Bolo-meter	Mylar 23	12; 29.73	Mertz	Black	Norton Beer (med)
35 - 200			Mylar 12	7; 12.5		Poly-	
150 - 650			Mylar 3.5	7; 12.5		ethylene	
400 - 5500	Globar	DTGS	Ge/KBr	7; 12.5		Open	

As shown in Table 4.1, the FT-IR spectrometer employs two thermal detectors, a bolometer and a deuterated triglycine sulfate or DTGS. During an experiment, the part of the recombined beam that reaches one of these detectors, gets absorbed from a sensor, and causes heating effects. This change of the temperature induces some measurable parameter change. More specifically, the bolometer signal-detection-operation is based on the change of the electrical resistance of a semiconductor material, whereas the DTGS detector relies on the change of the spontaneous polarization of a dielectric material as a function of the temperature [63].

The bolometer, shown in Figure 4.8, is used for signal detection in the far infrared region. It is a He-cooled 4.2 K Si bolometer and consists of three main parts: liquid

⁵ The scanner velocity can be converted from KHz to cm/s using the following equation:

$$v(\text{cm/s}) = \frac{v(\text{Hz})}{\bar{\nu}_{laser}(\text{cm}^{-1})}, \quad (4.16)$$

where the He-Ne wavenumber is $\bar{\nu}_{laser} = 15,798 \text{ cm}^{-1}$.

helium (LHe) can, detector, and the preamplifier. The detector is mounted on the cold surface under the helium can. The dewar is initially diffusion pumped, and pre-cooled with liquid nitrogen (LN_2); after about an hour the pre-coolant is removed, and the liquid helium is transferred into the helium can to maintain the detector at 4.2 K. The room temperature pyroelectric deuterated triglycerine sulfate (DTGS) is used as a detector for the mid-infrared region.

4.3.3 Monochromatic Spectrometer

A monochromatic spectrometer, or monochromator, is a type of spectrometer mostly used in the range from near infrared to ultraviolet. Monochromators select a narrow spectral range of radiation by spatially separating light of different wavelengths. In the early days, the primary dispersive element was the prism. In modern spectrometers, the prism is replaced by plane ruled diffraction gratings or holographic gratings, plane or concave. A typical diffraction grating consists of a substrate, such as glass, with a large number of grooves, ruled or holographically produced, coated with a reflecting material, usually aluminum. The quality and the spacing of the grooves are crucial for the performance of the grating, and the accuracy of the spectroscopic results. The development of the grating manufacturing process has made possible several kinds of different groove shapes; some examples are shown in Figure 4.9.

In a monochromator, the light from the source forms a narrow image through an entry slit and the beam is collimated towards a grating which spatially separates the individual frequency components. An exit slit selects an individual frequency which is either transmitted through, or reflected by the sample, depending on the type of measurement in progress, and finally, is focussed on the detector. A spectrum is produced after scanning the entire region of interest by rotating the dispersive element stepwise, by changing the rotation angle θ . Therefore, the wavelength is related to the element orientation.

The grating diffraction equation for normal incidence is

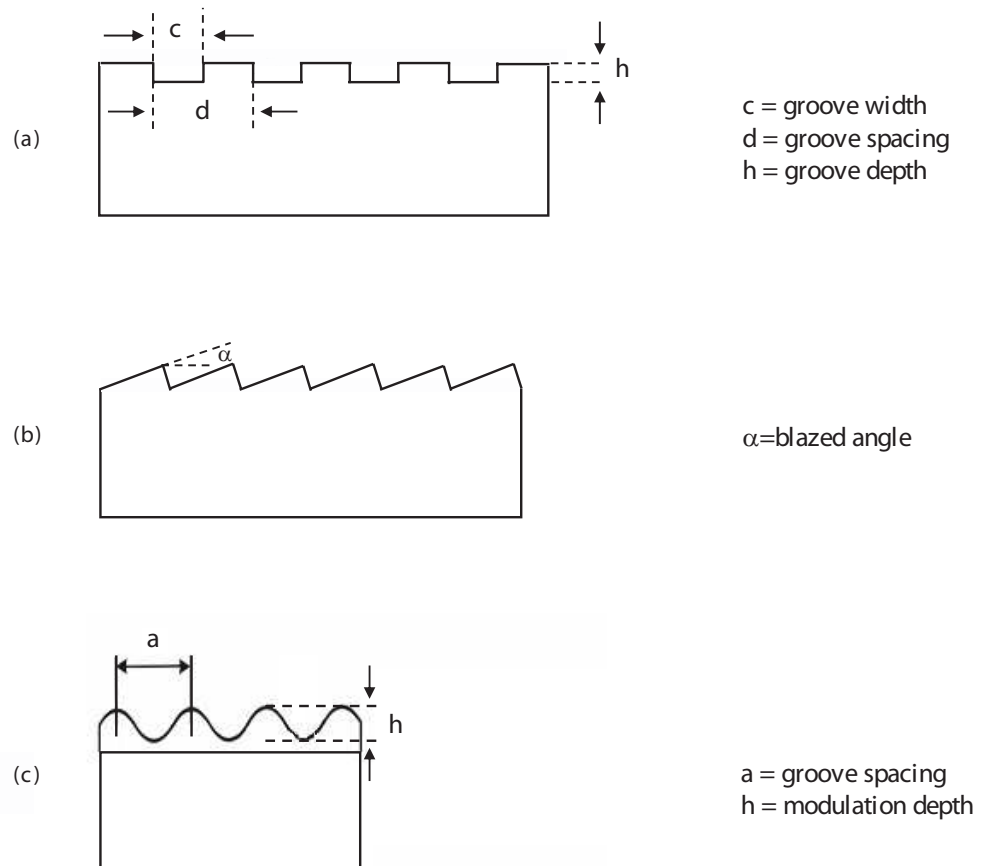


Figure 4.9: Schematic diagram of three types of grating: (a) Laminar groove, (b) Triangular groove, and (c) Sinusoidal groove.

$$m\lambda = d(\sin I + \sin D) \quad (4.17)$$

where $m = 0, \pm 1, \pm 2, \pm 3, \dots$ is the order of diffraction, I is the incident angle, D is the diffracted angle, and d is the grating constant (in number of lines per mm). As the grating rotates, the incident and diffracted angles change but the angle 2δ between them remains constant, because it depends on the geometry of the monochromator and hence is fixed, see Figure 4.10.

An important parameter of this system is the angular dispersion $\delta D / \delta \lambda$, which gives the change of diffraction angle that corresponds to a small change in wavelength.

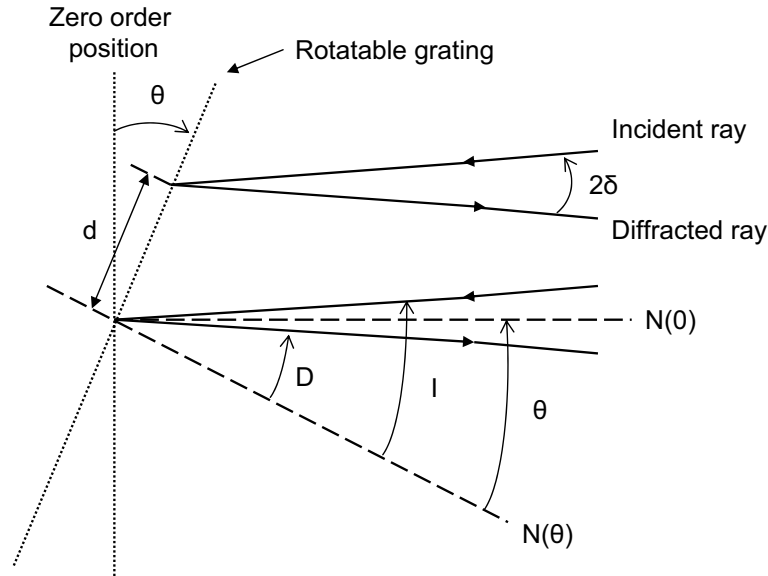


Figure 4.10: Schematic diagram of the diffraction grating, where d is the grating constant.

The angular dispersion is obtained by differentiating the grating equation with respect to the wavelength, while keeping the incident angle I fixed:

$$\frac{\delta D}{\delta \lambda} = \frac{m}{d \cos D}. \quad (4.18)$$

This quantity is greater for smaller groove spacings d , larger orders m , and larger diffraction angles D [64].

Furthermore, one can calculate the linear dispersion $\delta L/\delta \lambda$ at the exit slit of the monochromator, which will vary with the output focal length f , and the diffracted angle D . More specifically, the linear dispersion is the product of the focal length and the angular dispersion

$$\frac{\delta L}{\delta \lambda} = f \frac{\delta D}{\delta \lambda} = f \frac{m}{d \cos D}. \quad (4.19)$$

Another parameter that should be mentioned is the resolution of the instrument, which is defined as the ability of the monochromator to separate two spectral lines that

are very close together. The resolution is used to obtain the chromatic resolving power \mathfrak{R} of the spectrometer, which is defined as:

$$\mathfrak{R} = \frac{\lambda}{\delta\lambda_{min}} = \frac{Nd(\sin I + \sin D)}{\lambda} \quad (4.20)$$

where $\delta\lambda_{min}$ is the smallest wavelength difference that can be resolved, λ is the mean wavelength, and Nd is the grating width.

The main disadvantage of this type of spectrometer is the slow scanning process. The completion of a single scan is time consuming due to the fact that information from each frequency is collected individually.

Microscope Photometer

Reflectance and transmittance measurements from near infrared (NIR) through visible and ultraviolet (Vis/UV) regions were obtained with a Zeiss MPM 800 microscope photometer. The covered frequency range is from 4200 cm^{-1} to $45,000 \text{ cm}^{-1}$. The microscope, a schematic diagram of which is shown in Figure 4.11, is a system capable for micrometer size spot measurements. The main parts of this system are

- the sources, a tungsten (W) lamp for NIR (4200 cm^{-1} to $12,000 \text{ cm}^{-1}$) and a xenon (Xe) lamp for Vis/UV ($11,800 \text{ cm}^{-1}$ to $45,000 \text{ cm}^{-1}$),
- the detectors, a lead sulfide (PbS) cell for NIR, and a Photo Multiplier Tube (PMT) for Vis/UV, and
- the gratings, two holographically ruled concave gratings with blaze effect, one for NIR/Vis II⁶ and another one for Vis/UV.

However, there are a few other important optical components and features of this system that should be mentioned. The first one is the objective, item (10) in Figure 4.11, the basic function of which is to gather the light that is reflected from, or transmitted through the specimen, and produce an accurate image of the specimen into the body of

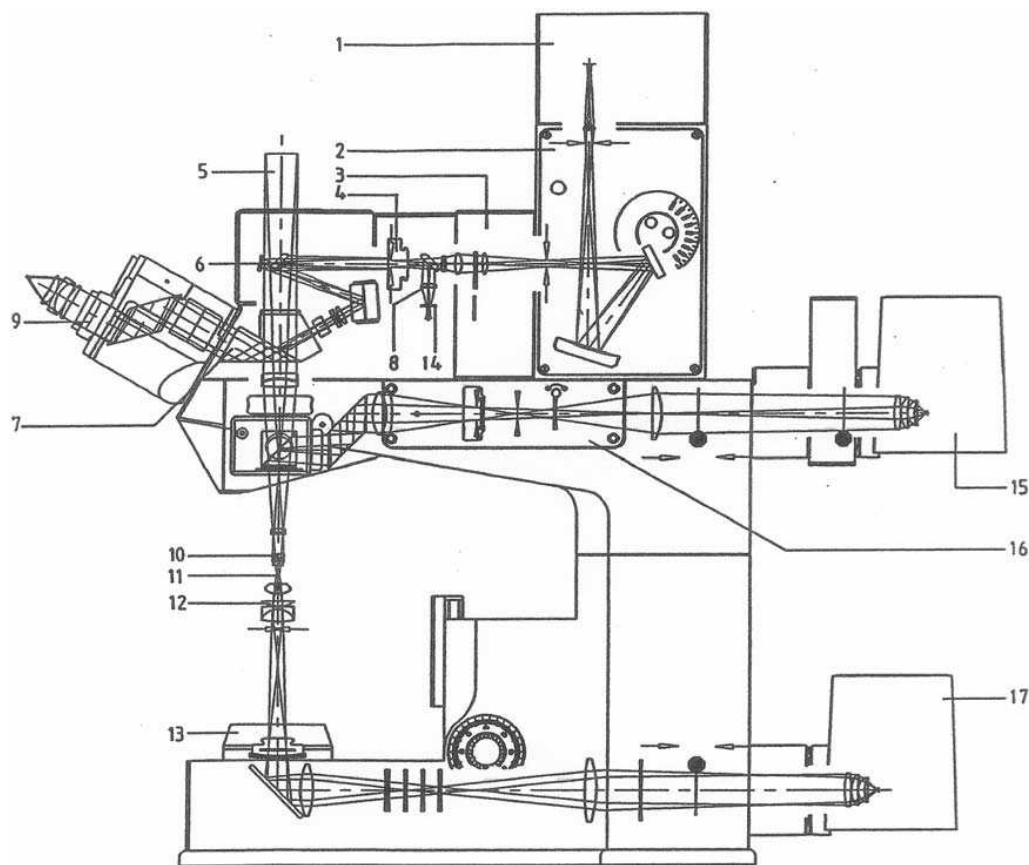
⁶ Vis II is the second order of diffraction for visible light.

the microscope. The MPM 800 microscope is equipped with a nosepiece that holds up to six objectives for a variety of magnifications. Objectives are inscribed with a color ring to allow the user to easily identify the magnification.⁷ Rotation of the nosepiece can bring the chosen objective into the light path. Another important optical component is the substage condenser (Achromatic-aplanatic condenser) item (12) in Figure 4.11. Its basic function is to concentrate the light that comes from the source in parallel beams onto the specimen, and correct for chromatic aberration and spherical aberration. The condenser holder has two small knobs for centering the condenser to the optical axis of the microscope for Koehler illumination [65, 66], and another two concentric coarse and fine focusing knobs for raising or lowering the condenser.

Other optical components of the microscope include collector lenses, tube lenses, mirrors, variable iris and field diaphragms, light shutters, light modulator, prism, and observation tubes. Moreover, a motorized 8x filter turret with eight apertures, item (3) in Figure 4.11, is placed closed to the detector item (1). A filter, selected with the software, can be accommodated through an opening in each aperture. Finally, a scanning stage (4" x 4") is built into a stand between the objective, item (10), and the condenser, item (12). The mounting frame has plates with or without an opening for reflectance or transmittance measurements respectively. The stage can be translated in the X and Y directions, and can be precisely moved in the Z direction with a coarse and fine focusing mechanism.

For measurements, the light beam spot size on the specimen is selected with the variable iris diaphragm and has a minimum spot size of $1\ \mu m$. Independent of the spot size, the entrance and exit slits may be set to the following fixed bandwidths: 4 nm, 10 nm, 20 nm, 40 nm, and 80 nm for the NIR grating, and 1 nm, 2.5 nm, 5 nm, 10 nm, and 20 nm for the Vis/UV grating [67]. Polarizers and analyzers are also available in this system for polarized measurements.

⁷ Color code: red for 4X, yellow for 10X, green for 20X, blue for 40X or 60X, and white for 100X [65].



- | | |
|---|---|
| 1 Detector unit PMT with/without PbS cell | 11 Specimen |
| 2 Grating monochromator | 12 Condenser |
| 3 Motorized 8x filter changer | 13 Luminous field diaphragm for transmitted light |
| 4 Intermediate image plane with measuring diaphragm | 14 Pilot lamp |
| 5 TV/photo port | 15 HBO illuminator with fast shutter |
| 6 Switching mirror TV/measurement | 16 Aperture and luminous field diaphragms for reflected light |
| 7 Beam splitter in photometer tube | 17 Halogen illuminator with light shutter |
| 8 Image-forming beam path of measuring diaphragms | |
| 9 Intermediate image plane | |
| 10 Objective | |

Figure 4.11: Schematic diagram of the reflected and transmitted light beam path at Zeiss MPM 800 Microscope Photometer.

For reflectance measurements the light beam generated by one of the sources, housed on the upper back side of the microscope item (15) in Figure 4.11, passes through the collector lens, aperture, and field diaphragm to the beam splitter item (7). The part of the light beam that is being reflected goes through the objective item (10), to illuminate the specimen item (11), which is placed on the stage. Light from the surface

of the specimen re-enters the objective and is directed either to the eyepieces through the photometer tube for observation, or to the camera port for photomicrography item (5), or through an aperture diaphragm, filters and a grating, to the detector in order for the signal to be recorded. The basic formula for calculating the corrected reflectance at wavelength λ is

$$Q(\lambda) = \frac{O(\lambda) - P(\lambda)}{S(\lambda) - P(\lambda)} R(\lambda) \quad (4.21)$$

where Q (Quotient) is the reflectance spectrum after spectral correction, O (Object) is the single beam spectra of the sample, S (Standard) is the single beam spectra of the source lamp,⁸ P (Parasitic) is the measured spectrum of the stray light, and R (Reference) is the reflectance of the standard. The default from the software is set $R(\lambda) = 100\%$, so the quotient needs an additional correction for the reference, which for this work is the aluminum reflectance.

For transmittance measurements, the light beam generated by one of the sources, which are housed on the lower back side of the microscope item (17) in Figure 4.11, passes through a series of filters, the field diaphragm item (13), through the condenser item (12), and through the specimen item (11), which is placed over an opening on the stage. Light is then gathered by the objective item (10), and is directed either to the eyepieces through the photometer tube for observation, or to the camera port for photomicrography item (5), or through an aperture diaphragm, filters and a grating, to the detector item (1) in order for the signal to be recorded. It should be noticed that the arm, which houses the two sources, needs to be placed according to the type of measurements required, upper position for reflectance measurements and lower position for transmittance measurements. The basic formula for calculating the transmittance at wavelength λ is

$$Q(\lambda) = \frac{O(\lambda)}{S(\lambda)} \quad (4.22)$$

⁸ The measurement is done using an Aluminum (Al) mirror as a reference.

where Q (Quotient) is the transmittance spectrum, O (Object) is the single beam spectra of the sample, and S (Standard) is the single beam spectra of the source lamp.

The system also offers the option for photoluminescence measurements but there was no use for this option throughout this work. More information about it can be found in the literature [67, 68].

Perkin-Elmer Monochromator

Reflectance and transmittance measurements from mid-infrared (MIR) through visible (Vis), and ultraviolet (UV) regions were obtained with a modified Perkin-Elmer (PE) 16U monochromator. The covered frequency range is from 800 cm^{-1} to $45,000\text{ cm}^{-1}$. The monochromator, a schematic diagram of which is shown in Figure 4.12, consists of three main chambers: source, monochromator, and sample/detector chambers. During the measurements the system can be evacuated to avoid the appearance of absorption bands from water (H_2O), and carbon dioxide (CO_2) in the mid- and near infrared spectra. There are three available sources in this system that cover the above frequency range; for mid-infrared measurements, a globar (Silicon Carbide SiC) lamp is used as a source, for the visible region a quartz-envelope tungsten lamp (W), and for the ultraviolet region a deuterium lamp (D_2). Table 4.2 provides the experimental parameters and optical components used to cover each spectral region.

During the experimental measurements the light beam generated by one of the above sources passes through a chopper, a set of low or high frequency band-pass filters, and a narrow rectangular entrance slit, and enters the grating monochromator. The chopper generates a square wave signal for lock-in detection and the filters reject the unwanted higher order diffraction from the grating, which occurs at the same angle as the desired first-order component. This can easily be seen by the diffraction equation: $d\sin\theta = n\lambda$, where d is the grating constant, as shown in Figure 4.10. At an angle θ , the first-order component of wavelength λ , for $n = 1$, that satisfies the diffraction equation is selected, while all the higher order components, that pass through the slit are absorbed by the filters. The angle θ is changed at predetermined intervals by rotating

Table 4.2: Perkin-Elmer grating monochromator parameters.

Frequency (cm^{-1})	Grating (lines/mm)	Slit Width (μm)	Source	Detector
801 - 965	101	2000	Globar (SiC)	Thermocouple (TC)
905 - 1458	101	1200		
1403 - 1752	101	1200		
1644 - 2613	240	1200		
2467 - 4191	240	1200		
4015 - 5105	590	1200		
4793 - 7977	590	1200	Quartz Tungsten (W)	Lead Sulfide (PbS)
3893 - 5105	590	225		
4793 - 7822	590	75		
7511 - 10,234	590	75		
9191 - 13,545	1200	225		
12,904 - 20,144	1200	225		
17,033 - 24924	2400	225	Deuterium (D_2)	Si Photo Conductance (576)
22,066 - 28,059	2400	700		
25,706 - 37,964	2400	700		
36,386 - 45,333	2400	700		

the grating. The rotation of the diffraction grating is achieved by the use of a step motor which provides scanning of a frequency range sequentially. The diffracted beam leaves the monochromator through a narrow rectangular exit slit. The exit slits width determines the resolution of the monochromator. An increase in the slits width will result in an increase of intensity of the light beam, resulting in higher signal-to-noise ratio (S/N) at the cost of lower resolution. Mirror $\mathcal{M}1$, shown in Figure 4.12, is a reference mirror which for reflectance measurements is replaced by the sample. For transmittance measurements, the sample is mounted at a different place as shown in Figure 4.12. In this position, the transmittance sample and the Si detector are the two focal points of the ellipsoidal mirror in between them.

Furthermore, in this system there are three detectors available to cover the frequency range from 800 cm^{-1} to $45,000\text{ cm}^{-1}$, a thermocouple (TC), a room temperature lead sulfide (PbS) photoconductor, and a silicon (Si) photodiode detector. The thermocouple is a thermal detector that consists of a series connection of two dissimilar materials. When the light beam reaches this detector, it is producing an electrical voltage as a function of the temperature difference between the two junctions. The thermocouple was not installed in the monochromator during this work, so this detector has not been used. The lead sulfide (PbS) detector's operation is based on the mechanism of photoconductivity. The incident photons are absorbed in a PbS layer, and create an electron-hole pair by exciting an electron from the valence to the conduction band. The electron and hole move freely and thus, the conductivity increases temporarily until they recombine. The third detector of this system is a Si photodiode or photovoltaic detector. This detector is made by building a p-n junction in a semiconductor. The incident light beam is absorbed at the junction of the two materials, and produces an external current to flow or develops a voltage [63].

Finally, the recorded signal from the detectors is amplified by a SR510 lock-in amplifier (Stanford Research Systems), averaged over time, and convert into a digital signal. The collected data are then transferred to a PC computer and stored for analysis. It must be noted that in case of reflectance measurements, the data acquisition program in this system corrects automatically for the reference mirror. More information about this system can be found in the literature [69].

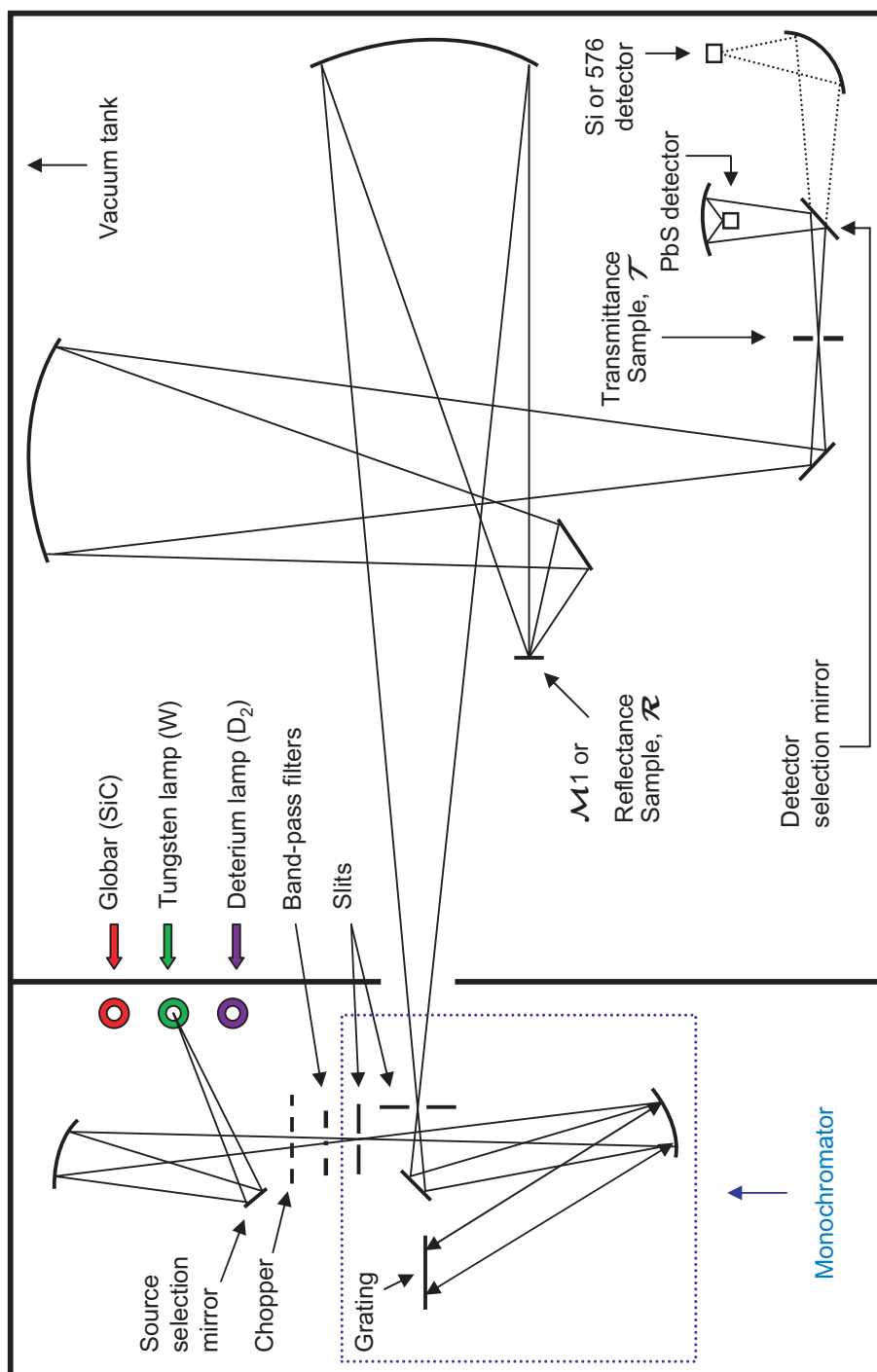


Figure 4.12: Schematic diagram of the Perkin Elmer 16U spectrometer.

CHAPTER 5 REFLECTIVE ELECTROCHROMIC DEVICES (ECDS)

Electrochromic (EC) materials exhibit reversible changes in their electronic structure and therefore, in their optical properties driven by a change in the electrochemical potential. Among all the groups of EC materials, mentioned in Chapter 2, conjugated polymers have been singled out over the past decade as promising EC materials due to their easy processability, low cost, rapid switching times, and high optical contrast ratios. Another important aspect of this type of materials is the ability of fine tuning of the energy band gap over the whole visible spectrum through the derivatization of the monomer structure, which provides access to different color states.

Previously materials were considered “electrochromic” when they could undergo a visible color change upon application of an external field. Lately the definition of electrochromism has been extended to include a multi-spectral energy modulation by reflectance or transmittance that might cover ultraviolet (UV), near infrared (NIR), mid-infrared (MIR), and microwave region (MW), with “color” corresponding to the response of the detectors at these wavelengths [70–74].

Reflective electrochromic devices (ECDs) are designed to modulate the reflectance of incident electromagnetic radiation upon application of voltage. The most common applications of these type of devices include mirrors, optical displays, spacecraft thermal control, and camouflage [33, 75]. In order for conjugated polymers to be useful as electrochromic (EC) materials for commercial applications, they should exhibit large changes in reflectance or transmittance between neutral and doped states (large optical contrast $\% \Delta \mathcal{R}$), rapid redox switching times, and long term stability [76].

Our group and collaborators, in Prof. Reynolds’ group, have studied extensively [25, 41, 77, 78] the optical properties of dioxythiophene-based conjugated polymers (PXDOT), and have incorporated them in electrochromic devices. In this chapter we

provide a brief summary on the design, fabrication, and characterization of these ECDs that operate in the reflective mode, and are able to modulate the reflectivity in a wide range of the electromagnetic spectrum; from the visible (VIS), to near infrared (NIR), and mid-infrared (MIR) regions.

Furthermore, we address the optimization of this type of devices through the development of a fabrication method for the removal of unwanted absorption bands in the mid-infrared region. These bands hinder the performance of the EC devices by drastically reducing the lifetime (long term switching stability), and the electrochromic contrast $\% \Delta \mathcal{R}$. Further improvements that need to be addressed, or have already been considered, are also being discussed.

5.1 ECDs Fabrication

A device platform which allows the characterization of electrochromic properties of conjugated polymers in a reflective mode is depicted schematically in Figure 5.1. The structure of the above electrochromic cell is an outward facing active electrode device sandwich, that has been previously described in the patent literature [39, 40]. This type of electrochromic device structure allows the probing of the optical properties of the EC material through a highly transmissive window. The optical window used in the device construction is chosen depending on the part of the electromagnetic spectrum that needs to be probed. Three candidates were employed in these studies, which are covering the range from far infrared to the visible region:

- Polyethylene. This optical window can be used almost over the entire spectrum from far infrared to visible (20 cm^{-1} - $25,000 \text{ cm}^{-1}$) because it is 90% transmissive, with the exclusion of four strong absorption bands in the mid-infrared region and of frequencies higher than $25,000 \text{ cm}^{-1}$ [77]. In our measurements it has been used in the far infrared region.

- Zinc Selenide (ZnSe). This optical window is 70% transmissive for the spectral range from mid- to near infrared (500 cm^{-1} - $20,000\text{ cm}^{-1}$) [77], and it is being used for the mid-infrared region.
- Glass. This optical window is 90% transmissive from 3800 cm^{-1} to $30,000\text{ cm}^{-1}$, and 76% transmissive for the spectral range from 2200 cm^{-1} to 3800 cm^{-1} [77]. In our measurements this window is being used for the near infrared and the visible regions.

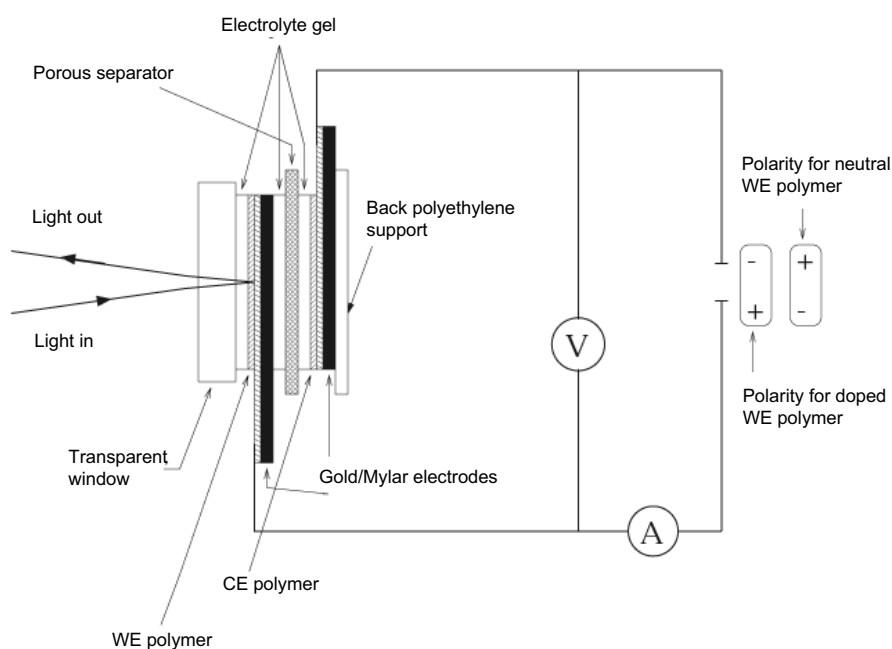


Figure 5.1: Side-view schematic diagram of a dual polymer reflective electrochromic device in a circuit [77].

In detail, the electrochemical cell depicted in Figure 5.1 consists of twelve layers. The device is flexible if the polyethylene window is used. The layers are, from left to right: optical window, gel electrolyte layer, an upper, initially p-doped, polymer film (WE polymer) on gold-coated Mylar reflective conducting substrate (polymer/gold/Mylar), a polypropylene porous separator soaked in electrolyte gel (electrolyte gel/separator/electrolyte gel), a lower, initially neutral, polymer film (CE polymer) on gold-coated Mylar reflective conducting substrate (polymer/gold/Mylar), and a polyethylene sheet for back support. An important issue that should be noted is that the

working electrode is facing the transmissive window, and the counter electrode is facing the back of the working electrode. Therefore, in order for the ion diffusion between the working electrode polymer film, the electrolyte gel, and the counter electrode to be possible, and moreover to provide a closed circuit, the top electrode has a series of parallel slits (slit separation 1 - 2 mm) across the active surface. The high-viscosity electrolyte gel used in these devices, consists of four different chemical components; Acetonitrile (ACN): Propylene Carbonate (PC): Poly (methyl methacrylate) (PMMA): Lithium Perchlorate (LiClO_4), with weigh ratio of 70:20:7:3.

For the encapsulation of the cell, two methods can be employed depending on the optical window that is being used. In the case of polyethylene, two big pieces of polyethylene are used as the back support and the front window, and the three sides around the electrodes are heat-sealed, whereas the fourth side is used to evacuate the cell, and then is heat-sealed too. Copper wires that have been attached to the gold electrodes with conductive silver paste, come out of the “polyethylene bag” through punched holes that have been sealed using an epoxy-based glue. The advantage of this method is that it permits the use of liquid electrolytes. In the case where the optical window used is either ZnSe or glass, the encapsulation is provided by the electrolyte gel. The electrochromic cell is self-sealed along the edges as the ACN in the electrolyte evaporates, and the PMMA becomes insoluble. Thus, further evaporation is minimized and leaks are prevented.

Finally, the cell is connected to an electrical supply, as shown in Figure 5.1. As different voltages are applied, the potential difference between the two electrodes changes, and causes the doping levels of the conjugated polymer films to change reversibly. Figure 5.2 shows a photograph of the top view of a real electrochromic device in its two extrema states. On the left side, the active polymer is in the neutral, colored, state and on the right side is switched to its oxidized, transparent (bleached), state. This color change is attributed to the creation of new mid-gap states, upon doping. The doping modifies the electronic structure of the polymers causing the depletion of the $\pi - \pi^*$ transition while

creating polaron, for light doping, or bipolaron, for heavy doping, absorption bands in lower energies.

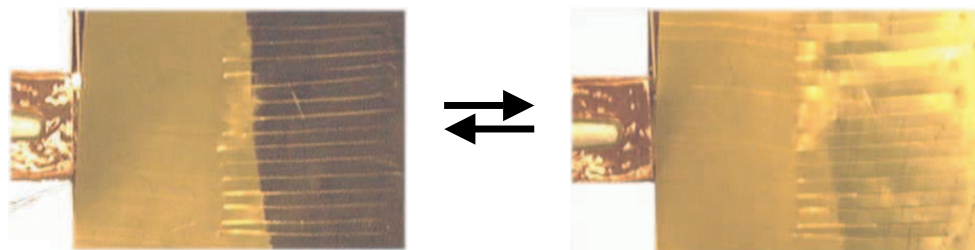


Figure 5.2: Top-view photograph of an EC device, using PProDOT-Me₂ polymer as the working electrode polymer, in its two extrema states. Left side: PProDOT-Me₂ in neutral state, colored state ($V_{cell} = -1.1$ V). Right side: PProDOT-Me₂ in p-doped, oxidized, state ($V_{cell} = +1.1$ V) [41, 78].

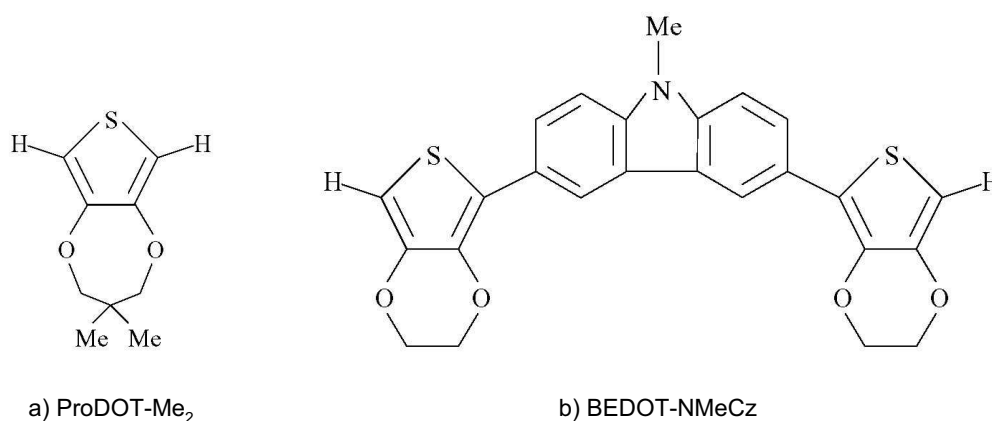


Figure 5.3: Monomer structures: a) 3,4-(2,2-dimethylpropylenedioxy)-thiophene, ProDOT-Me₂, and b) 3,6-bis(2-(3,4-ethylenedioxy)thienyl)-N-methylcarbazole, BEDOT-NMeCz.

The working electrode polymer used in the device shown above, is poly[3,4-(2,2-dimethyl-propylenedioxy)-thiophene] or PProDOT-Me₂, and the counter electrode polymer, used for charge and coloration balance, is poly[3,6-bis(2-(3,4-ethylenedioxy)thienyl)-N-methylcarbazole] or PBEDOT-NMeCz. Both polymers have been electrochemically deposited from solution (10 mM monomer, ProDOT-Me₂ or BEDOT-NMeCz, in 0.1 M

LiClO₄ in ACN) in a three electrode configuration using an EG&G Model 273A potentiostat/galvanostat. The monomer structures are shown in Figure 5.3.

5.2 In-situ Reflectance Measurements and Analysis

The reflective electrochromic cell introduced in the previous section allows us to probe the optical properties of the working electrode polymer. All layers described above, except for the polyethylene support, play an important role towards the device function because all components form a closed circuit during the in-situ measurements. However, only the upper four layers contribute directly to the reflectance measurements. More specifically, during the reflectance measurements most of the light coming from the source passes through the optical window, which is chosen to be transmissive in the particular region of interest, and through a layer of electrolyte gel.

In spectral regions where the polymer has low absorption (infrared region when the polymer is in its neutral state and either far infrared, or visible region when the polymer is in its p-doped state), the light passes through the polymer, reflects from the gold surface and passes again through the polymer film, the electrolyte gel layer, and the optical window and travels towards the detector where it will be collected. Thus, the light passes twice through the upper active polymer layer. For this case, if there were no absorptions from the upper three layers, optical window, electrolyte gel, and polymer film, we would have had the same reflectivity as gold ($\sim 99\%$ from far infrared to mid-visible, and after the plasma absorption edge, at $\sim 18,500\text{ cm}^{-1}$ or $\sim 540\text{ nm}$, the reflectivity would have dropped at $\sim 40\%$ [41]). However, there is always some absorption and hence, the reflectance spectra are similar to the transmittance spectra, of a transmissive device with a polymer film twice as thick as the one used in the reflective device.

In spectral regions where the absorption is large (visible when the polymer is in the neutral state and mid-infrared when the polymer is in the p-doped state) most of the light enters the polymer layer, where it is absorbed either on the way towards the gold surface (WE), or on the way out, after it has been reflected from the gold. Although

some of the light is still reflected by the polymer surface, the percentage of this reflected light is very small, especially since the polymer film is covered by electrolyte gel which acts as an index-matching region.

As one should have already noticed, the optics of the electrochromic cell is quite complicated. Even though we probe the optical properties of the EC material in reflectance mode, we do not measure the real reflectance of the polymer. The measured reflectance contains contributions from all four upper layers of the cell. In order for the optical properties of the polymer film to be extracted, the Drude-Lorentz model for multi-layered systems needs to be used to fit the reflectance data. Each of the four layers is fitted separately, using a parameter file that contains information about the center frequency, plasma frequency, and oscillator strength of each oscillator, as well as the dielectric function at infinity, and thickness of the fitted film. From the parameters obtained, we compute optical constants which yield information about the electronic structure of the neutral and doped states of the polymer film. For the interested reader, this part of the analysis and the relevant parameter files can be found in reference [25].

5.3 Results and Discussion

The structure of the electrochromic cell described above, allows us to probe the electronic properties of polymers through in-situ reflectance measurements in a wide range of the electromagnetic spectrum. After studying the optical properties of several different polymers, our group and collaborators in Prof. Reynolds' group, built an optimized electrochromic cell that exhibits high reflectance contrast between the polymer extrema states, $\% \Delta \mathcal{R} = |\% \mathcal{R}_{neutral} - \% \mathcal{R}_{doped}|$, and in addition, shows rapid switching times [25, 41, 77, 78]. The reflectance spectra of an optimized EC device is shown in Figure 5.4.

In order to study the electrochromic effect over a large spectral range, two different windows had to be used. For the reflectance measurements shown in Figure 5.4, two electrochromic cells were constructed, one with a zinc selenide (ZnSe) window 2 mm thick for measurements in the mid-infrared (MIR) region and one with a glass window

around 1 mm thick for the near infrared (NIR), and visible (VIS) ranges. The same polymers were used in both cells; poly[3,4-(2,2-dimethylpropylenedioxy)-thiophene], or PProDOT-Me₂, as the upper, working electrode polymer (200 nm film thickness under the ZnSe window, and 150 nm under the glass window) and poly[3,6-bis(2-(3,4-ethylenedioxy)thienyl)-N-methylcarbazole] or PBEDOT-NMeCz, as the lower, counter electrode polymer. As shown in Figure 5.2, PProDOT-Me₂ switches from a dark opaque violet color when in its neutral or un-doped state, to a highly transparent polymer in its p-doped or bleached state, which subsequently allows the gold surface underneath it to be visible. This color change is attributed to the generation of new electronic states within the energy gap of the polymer, and the creation of polarons and bipolarons. These symmetric mid-gap states are due to the modification of the electronic structure of the polymer upon doping. Consequently, the $\pi - \pi^*$ transition diminishes and the electronic absorptions are shifted towards lower energies.

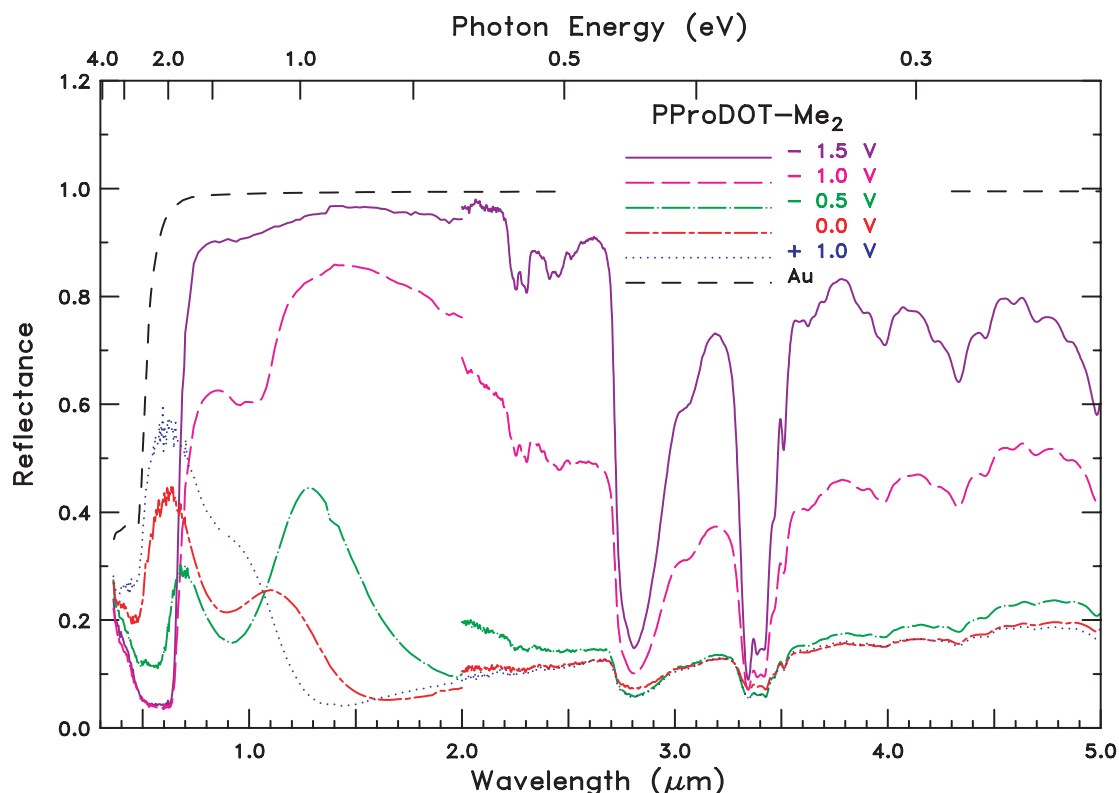


Figure 5.4: Reflectance measurements of PProDOT-Me₂/PBEDOT-NMeCz dual polymer electrochromic device from visible to mid-IR regions at various potentials.

For these wide range measurements, two different instruments had to be employed; a Bruker 113v was used for mid-infrared (MIR) region measurements, and a Zeiss MPM 800 microscope photometer for near infrared (NIR) and visible (VIS) region measurements. In Figure 5.4 there is a difference between the data taken for the mid-infrared region and the data taken for the near infrared region. This mismatch is due to the different thicknesses of the upper active polymers, as well as the different thicknesses of the optical windows between the two cells, that were used for these particular measurements. However, the above differences can be taken into account and the data can be corrected accordingly. In the data presented here, the parasitic reflectivity of the windows has been subtracted. For commercial applications in order for the parasitic reflectivity to be minimized, the windows can be coated with an anti-reflective material, this was not done for the optical windows used in these measurements.

In Figure 5.4 the electronic transitions characteristic of the neutral, intermediate doped, and heavily doped states can be clearly observed. For these measurements, positive voltage represents the neutral polymer, and negative voltage represents the p-doped polymer. The reflectance shows large electrochromic contrast, $\% \Delta \mathcal{R}$, between the neutral ($V_{cell} = -1.5 \text{ V}$, purple line), and the fully doped ($V_{cell} = +1.0 \text{ V}$, blue line) states up to $5 \mu\text{m}$. At longer wavelengths, above $5 \mu\text{m}$, there are strong absorptions due to the electrolyte gel [77]. The highest reflectance contrast, $\% \Delta \mathcal{R}$, is detected at $1.8 \mu\text{m}$, where $\% \Delta \mathcal{R}$ is greater than 90%. At longer wavelengths, between $3.5 - 5.0 \mu\text{m}$, the contrast is reduced to a value of around 60%, and at shorter wavelengths, around $0.6 \mu\text{m}$, $\% \Delta \mathcal{R}$ is $\sim 55\%$. At the range $3.5 - 5.0 \mu\text{m}$, the reflectance of the neutral polymer decreases and that of the fully p-doped polymer increases, thus resulting in lower contrast value, compared to $\% \Delta \mathcal{R}$ at $1.8 \mu\text{m}$. At the visible range, the situation is reversed; the polymer in its p-doped state exhibits high reflectance, and in its neutral state exhibits low reflectance, but the contrast is still less than the maximum value reached within the near infrared region.

In more detail, the polymer in its neutral, insulating, state ($V_{cell} = -1.5\text{ V}$) is strongly absorbing in the visible region, where the $\pi - \pi^*$ transition is ($0.4 - 0.65\ \mu\text{m}$). Therefore, the reflectance of the device in this region is very low. At wavelengths longer than $0.9\ \mu\text{m}$, the polymer film becomes quite transparent and thus, the gold layer underneath dominates the reflectance and hence, the device reflectivity is very high. At even longer wavelengths, longer than $5.5\ \mu\text{m}$, the reflectance of the device is diminished due to strong vibrations [77]. When the upper polymer is at its fully p-doped state, ($V_{cell} = +1.0\text{ V}$), the visible absorption is absent, while a strong infrared absorption band due to bipolarons, that hides the underlying gold electrode, appears. At the intermediate doped states ($V_{cell} = 0.0\text{ V}$, -0.5 V , and -1.0 V), the visible absorption decreases as the doping level increases, while at the same time strong absorption bands appear at longer wavelengths due to polaronic states. In general, at these intermediate doped states, the reflectance of the EC cell lies between the reflectance of the two extrema states; fully oxidized (p-doped) and fully reduced (neutral) states. This is true for the whole spectrum range that was measured except from the region between $0.4\ \mu\text{m}$ and $1.1\ \mu\text{m}$, where two of the intermediate states have lower reflectance, stronger absorption bands, than any of the extrema states shown in Figure 5.4.

In conclusion, the neutral (insulating) polymer has its $\pi - \pi^*$ transition in the visible region, and it is transparent in the infrared region, except from vibrational absorptions. At the lightly doped states, two symmetric sub-gap states are introduced upon doping and thus, absorption bands appear in the spectrum at lower energies due to the presence of polaron states; the $\pi - \pi^*$ transition is still present but diminished. At the fully doped state, a single broad bipolaron absorption band is produced, whereas the polaron and $\pi - \pi^*$ transitions are absent.

Other characteristics than the electrochromic contrast of these type of electrochromic cells that are important for applications, such as displays and thermal control, are the switching time, and the lifetime, or long term stability, of the cell. The switching time is the time that is needed for the active polymer to switch between the two extrema

states. In order for the switching time to be determined, the cell is connected to a power supply that allows a square-wave potential to be applied, with controllable period and amplitude, while the reflectance is being monitored. The response time of these devices is three seconds for the active polymer to switch from the fully reduced (neutral) state to the fully oxidized (p-doped) state, and six seconds for the reverse switching, from the p-doped to the neutral state. The time difference between doping and de-doping of the upper active polymer is attributed to the difference in the time required for the exchange ions to enter and the time required them to leave the polymer film. Another factor that affects the switching time in a negative way in this type of device structure, is the fact that the change between the two extrema states begins at the slits and then spreads over the whole active polymer surface. Therefore, the switching time depends directly on the distance between the slits.

The second characteristic, the lifetime, or long term stability, of these devices is the number of switching cycles a cell can undergo before degradation results in significant loss of the electrochromic contrast $\% \Delta \mathcal{R}$. In order for the lifetime time of the cell to be determined, the same setup as for the switching time is being used; double potential steps are applied, and the reflectance is monitored at a fixed wavelength λ_{max} where the contrast $\% \Delta \mathcal{R}$ has a high value. For these PProDOT-Me₂ based devices with LiClO₄ based electrolyte gel, the degradation sets in after about 1500 cycles. The reflectivity of the polymer in its p-doped state is relatively constant but the reflectivity of the neutral form of the polymer gradually decreases. PProDOT-Me₂ based devices that used a lithium bis(trifluoromethyl-sulfonyl)imide, or Li[N(CF₃SO₂)₂], based electrolyte gel survived 10,000 cycles with reflectance contrast $\% \Delta \mathcal{R} \sim 80\%$ measured at 1.3 μm (or equivalently 7692 cm^{-1}) [77].

5.4 Enhancing the Performance of ECDs

In the reflectance spectra of Figure 5.4 there are two strong absorptions in the mid-infrared region that were not mentioned in the analysis above. The strength of these mid-infrared absorption bands is relatively independent from the polymer state, neutral

or doped, and hinder the performance of the electrochromic cell. These absorptions, one at $2.8\ \mu\text{m}$ and the other one at $3.3\text{-}3.4\ \mu\text{m}$, are due to water absorption (O-H stretching mode) [79], and C-H stretching [80] respectively, and are responsible for the drastic reduction of the reflectance contrast, $\% \Delta \mathcal{R}$, in the mid-infrared region.

In addition, the presence of water in the electrochromic cell can cause over-oxidation of the oxygen-sensitive polymer film, which is an irreversible process and thus, reduce significantly the lifetime, or long term stability, of the device. These absorption bands, dips in the reflectance spectra in Figure 5.4 are attributed mainly to the electrolyte gel, since the thickness of the upper active polymer is only 150-200 nm and thus, the contribution of the polymer film to the intensity of the C-H mode is very small. Our work focuses on the reduction, or removal, of the absorptions due to the above vibrational stretches and therefore, the enhancing of the performance of the electrochromic cell. The first step towards this direction was to carry out the preparation of the electrodes, the electrolyte gel, and the assembly of the device in a dry environment. The purpose of this precaution is to avoid any exposure of the materials to the ambient humidity and therefore to exclude the water from the cell.

The four chemical components used for the electrolyte are brought in the dry box, and the electrolyte gel (ACN:PC:PMMA:Li[N(CF₃SO₂)₂]) with weight ratio of 70:20:7:3) is prepared in an inert (Ar) environment. In detail, Li[N(CF₃SO₂)₂] purchased from 3M was dried in a vacuum oven for 24 h at 60 °C, while the PC purchased from Aldrich in Sure Seal[®] was percolated through type 3A molecular sieves followed by vacuum distillation (10 mm). Moreover, the ACN purchased from Aldrich in Sure Seal[®] is distilled at atmospheric pressure under Ar over calcium hydride (CaH₂). Finally, activated molecular sieves were added to the solvents PC and ACN to remove any residual water, and then they were stored in argon atmosphere.

The mixing procedure of the above chemical components is the following: the acetonitrile (ACN) is put in a glass container on a heated plate and stirred vigorously. After about ten minutes, the salt Li[N(CF₃SO₂)₂] is added. Upon dissolution of the salt,

the addition of poly(methyl methacrylate) (PMMA) follows. The latter component is not easily dissolved, hence it is stirred and heated, at 60 °C, on the plate for about two hours. During that time the ACN solvent evaporates. Then, as soon as the PMMA is dissolved, propylene carbonate (PC) is introduced to the medium and when the mixture has a viscous consistency, after about two more hours of stirring and heating, it is either stored under argon environment, or used in a device. The polymer films used in the reflective devices in this chapter, PProDOT-Me₂, and PBEDOT-NMeCz, were prepared on the electrodes electrochemically at constant potential in a three-electrode configuration, which is placed inside the dry box. The electrochromic cell was also assembled in the inert atmosphere.

In order to test if the precautions that were taken for the assembling of the electrochromic cell were sufficient to eliminate the water signature (O-H stretching mode) from the reflectance spectra of the EC device, the transmittance of the anhydrous electrolyte gel is measured. The configuration that was used is the following: two ZnSe windows for transmittance measurements in the mid-infrared region, where the water absorption lies, sandwiched together, and in between, a layer of electrolyte gel the thickness of which is controlled by a 25 μm spacer. The components were put together inside the dry box, and the transmittance of the configuration was measured. Then, the ZnSe windows were taken apart, the electrolyte gel was exposed in the ambient environment for one minute, and then the transmittance of the above configuration was measured again. The transmittance data of the anhydrous electrolyte gel, and the electrolyte gel after one minute exposure to ambient environment are shown in Figure 5.5.

As can be clearly seen in Figure 5.5, the absorbing O-H mode in the “water protected” electrolyte gel (solid line) is almost non-existing, while the same absorption mode becomes very prominent even after only a very short time, one minute, of exposure in the ambient environment (dotted line). These results demonstrate that our process successfully prevents moisture from entering the electrolyte gel and therefore, eliminates the water signature from the reflectance spectra of the cell.

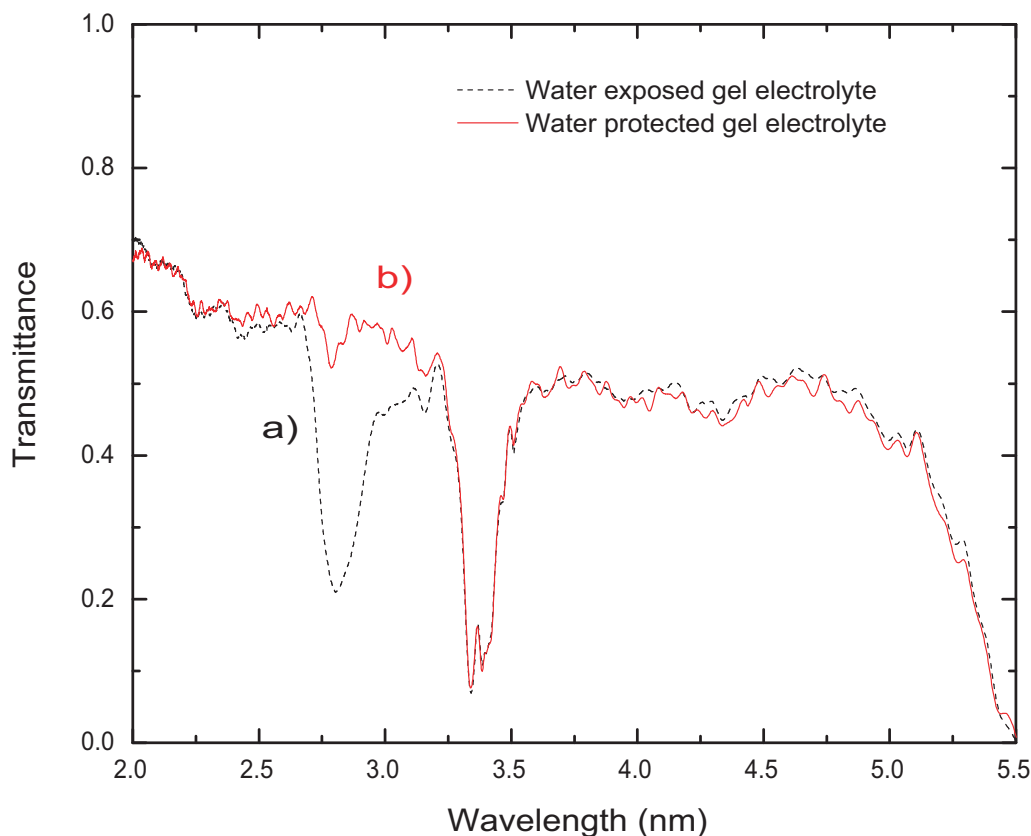


Figure 5.5: Transmittance data of ZnSe/Gel Electrolyte/ZnSe configuration; a) gel electrolyte exposed in air for a period of 1 minute, and b) gel electrolyte prepared in argon, (Ar), environment.

However, the removal of the second absorption band, the C-H stretching mode, was not quite as successful. Although it could be achieved through the substitution of some of the components the electrolyte was made of, with components that have, for example, C-F bonds the absorption band of which is $\sim 8-9 \mu\text{m}$, instead of C-H bonds. However, we used the electrolyte described above and worked towards the reduction of the intensity of the unwanted band through careful control of the thickness of the electrolyte gel layer between the transparent window and the upper active polymer film. For the purpose of controlling the thickness of the electrolyte gel layer, a new sample holder was designed. This sample holder, which is shown in Figure 5.6, fits perfectly inside the shroud of our reflectance stage, and meets all the requirements for reflectance measurements by having five degrees of freedom; two rotational and three translational, in order to achieve a good alignment for maximum detector signal. The new sample

holder offers additional sealing from the ambient environment, while at the same time allows us to control the electrolyte gel thickness through the application of pressure with two pairs of adjustable screws. More specifically, the device is assembled by adding an extra component, a thin spacer, on top of the upper active polymer film. Then, without applying an electrolyte gel layer, the optical window is set. The tuning of the electrolyte gel thickness is achieved by placing the electrochromic cell inside the pocket-like sample holder, and subsequently screwing the top plate so that the optical window is pressed against the top (WE) electrode. This process ensures that the amount of electrolyte gel that passes through the electrode slits depends on the thickness of the spacer used and the applied pressure. More details on the design of the sample holder can be found in [81].

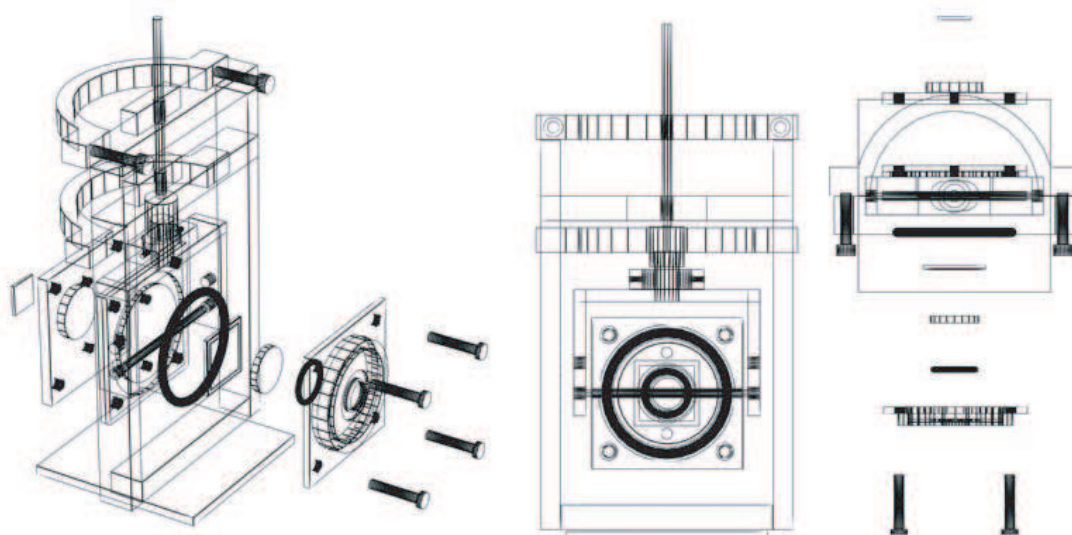


Figure 5.6: Reflectance sample holder for measurements of the electrochromic cell, shown in the side, front, and top views. This design provides control of the thickness of the upper electrolyte gel layer [81].)

Using the above technique, an electrochromic device had been assembled that consisted of a 2 mm ZnSe window, a 125 μm Mylar spacer, a 200 nm PProDOT-Me₂ film on slitted gold/Mylar, as the working electrode, a porous separator soaked in electrolyte gel, and a PBEDOT-NMeCz film on gold/Mylar as the counter electrode. The device was mounted on the new sample holder, in which the thickness of the electrolyte gel

coming through the slits is controlled, and the reflectance for the mid-infrared region was measured at different voltages, V_{cell} from +1.0 V to -1.0 V. Higher potential values did not give different results. The reflectance data are shown in Figure 5.7, where it can be clearly seen that the water signature is absent, and the intensity of the C-H signature is significantly reduced compared to the reflectance data in Figure 5.4. The removal of the former, and the reduction of the intensity of the latter, result in an improvement of the electrochromic contrast: $\% \Delta \mathcal{R} > 65\%$ in the mid-infrared region, 2.0-5.5 μm . The reflectance data of this type of measurements have been repeated with several different devices to ensure reproducibility of the technique.

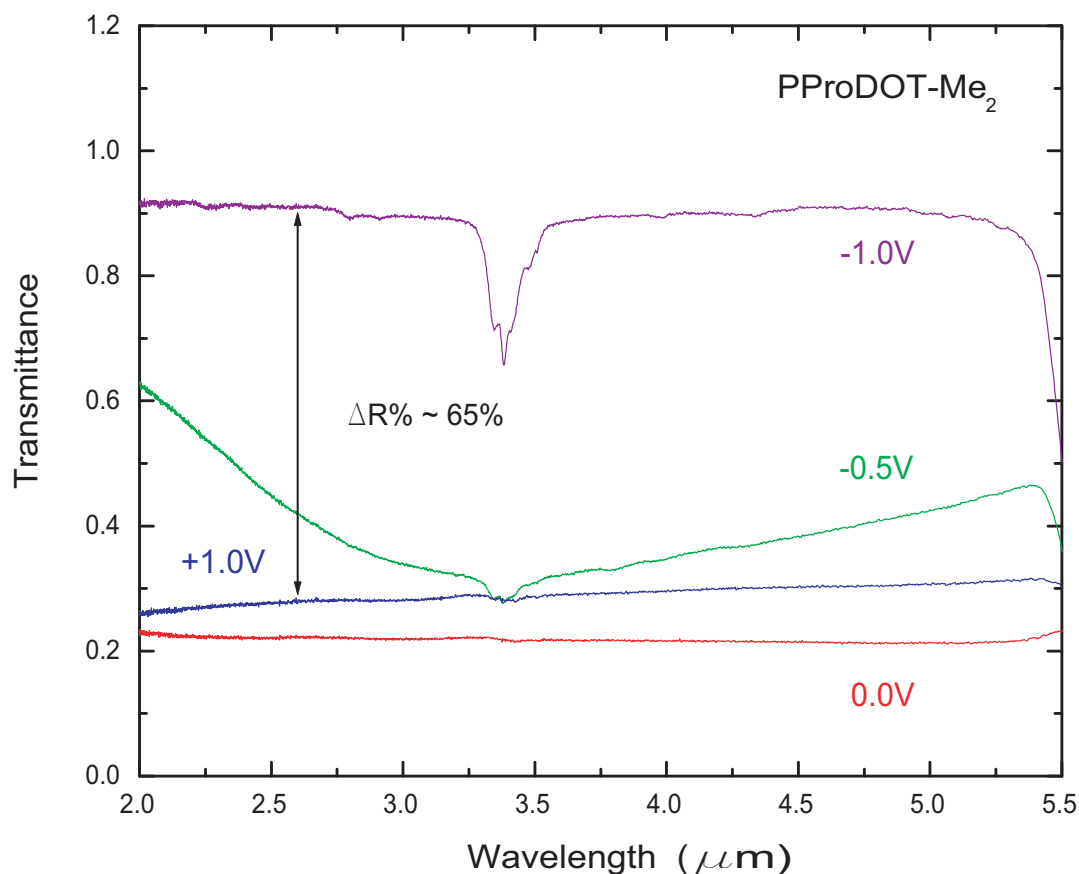


Figure 5.7: Reflectance measurements of PProDOT-Me₂/PBEDOT-NMeCz electrochromic device from visible to mid-IR regions of the electromagnetic spectrum, at various potentials.

One thing that should be mentioned at this point is that although theoretically the fully p-doped state ($V_{cell} = +1.0$ V) is expected to be less reflective than the intermediate

p-doped state ($V_{cell} = 0.0\text{ V}$) this is not observed in the above data. In Figure 5.7 the reflectance of the electrochromic cell is higher for applied voltage of $+1.0\text{ V}$, compared to the reflectance for applied voltage of 0.0 V . One possible explanation is that the broad bipolaron band is less absorbing in this spectral range than the corresponding polaron band. Thus, some light could have gone through the polymer in the heavily p-doped state, and could have been reflected from the gold electrode underneath it. Had the polymer been thicker, this result might not have occurred. Further study is needed in order for source of this to be determined.

The use of the new sample holder enables us to control the thickness of the electrolyte gel, which results to the reduction of the C-H absorption band in the reflectance spectra, but it has a major disadvantage: due to the applied pressure the slits on the working electrode are squeezed together and thus, the diffusion of the electrolyte gel through the slits is difficult. As a consequence the ion transport is very slow. The switching time for an EC device, mounted in the new sample holder increased by a factor of 10^3 , compared to the switching time of the same device under no pressure. Hence, further study is required to modify the existing sample holder in order to avoid this problem, or to find a different way to control the thickness of the electrolyte gel. Moreover, the option of using different chemical components for the creation of an electrolyte gel, which will lack C-H bonds should also be explored.

5.5 Conclusions

Further measurements of the old type of devices, using the slitted gold/Mylar sheet, need to be performed in order for the source of the infrared anomaly to be determined, (see Figure 5.7), where $\%R(V_{cell} = +1.0\text{ V})$ is higher than $\%R(V_{cell} = 0.0\text{ V})$). A first step would be to measure the reflectance of devices with different polymer thicknesses and examine whether this phenomenon is consistent, or whether it disappears at some polymer thickness. If the latter happens, it should be investigated further, in order for an explanation to be found.

Additional work needs to be done towards the elimination of the C-H stretching mode that appears in the mid-infrared region. Using the current chemical components for the electrolyte gel, we need to either modify the new sample holder in order to avoid the long switching times caused by the large applied pressure, or to find different ways to control the upper gel layer thickness. Another possibility that could lead to a resolution of this problem, is the use of different chemical components for the electrolyte gel that lack C-H bonds but have instead, for example, C-F bonds the absorption band of which is far from the region of interest.

In conclusion, based on reflectance measurements and extensive study that lead to deep understanding of the optical and electrochemical properties of conjugated polymers, we were able to construct electrochromic devices with enhanced performance. Variable reflective electrochromic devices based on PProDOT-Me₂ and PBEDOT-NMeCz, were initially optimized to exhibit contrast ratios of 60-70% in the mid-infrared region where two strong absorption peaks, water absorption (O-H stretching mode), and C-H stretching mode were hindering the performance of the devices. A novel technique was developed in order to build water-free devices, and a new sample holder was designed, that allows for control of the electrolyte gel thickness and thus, significantly reduces the C-H signature.

An effort to further optimize this type of devices led to the replacement of the slitted gold-coated Mylar by a metallized porous membrane (polycarbonate, 10 μm pore size). This replacement provided more homogeneous ion diffusion, faster switching times (of the order of sub-seconds) between the extrema states of the polymer film, and longer lifetime stability. This new generation of reflective electrochromic devices proved to be better light modulators than the previous one using the slitted gold-coated Mylar. However, several difficulties were encountered with this type of devices too. More details can be found in Appendix A.

CHAPTER 6

FREE-STANDING SINGLE WALLED CARBON NANOTUBE FILMS

During the past two decades, various conjugated polymers have been synthesized with unique optical, electrical, and magnetic properties due to their extended π -electron delocalization along their backbone. Carbon nanotubes are conjugated, one dimensional, all-carbon systems that also possess remarkable electronic and mechanical properties. They consist of one, or more, graphene sheets rolled-up to form a seamless nanometer-diameter cylinder, or concentric cylinders if more than one, capped at the ends with half-fullerene molecules. An important characteristic of this system is the fact that carbon nanotubes can be either metallic or semiconducting depending, solely for the case of isolated tubes, on their geometry, i.e., diameter and chirality. Their discovery by S. Iijima in 1991 [82] stimulated the interest of many researchers who envisioned numerous possible applications for these exotic materials. Carbon nanotubes have been studied intensively ever since, and they are constantly attracting more attention.

6.1 Carbon Nanotubes

Carbon nanotubes can be thought of as graphene sheets that have been wrapped up to form a seamless cylinder. They provide a remarkable model for one dimensional (1D) systems, one atom in thickness, a few tens of carbon atoms in circumference (20 to 40), and many microns in length. There exist two main types of nanotubes namely the single-walled carbon nanotubes (SWNTs), which consist of a single graphene sheet, and the multi-walled carbon nanotubes (MWNTs), which comprise of two or more concentric tubes with different diameters. The electronic properties of perfect MWNTs are very similar to those of SWNTs due to the fact that the coupling between concentric cylinders is weak [83]. In the theoretical literature, the focus is on SWNTs since they provide a simpler system to model. Our focus in this work has also been on SWNTs.

Although carbon nanotubes share many structural characteristics with the single graphene sheet, which is a semiconductor with a zero energy band gap, carbon nanotubes with no doping impurities present can be either metallic or semiconducting depending sensitively on the tube diameter and wrapping angle. Therefore, small differences in parameters can provide similarly shaped tubes consisting of only one element, carbon, with very different electronic properties.

The carbon nanotube structure is defined in terms of the tube diameter d_t , and the wrapping, or chiral, angle ϕ as shown in Figure 6.1. The chiral vector \mathbf{C}_h determines the rolling direction of the graphene sheet by connecting two crystallographically equivalent sites O and A on a two-dimensional (2D) graphene sheet, where a carbon atom is located at each vertex of the hexagonal structure. This vector is expressed as follows

$$\mathbf{C}_h = n\boldsymbol{\alpha}_1 + m\boldsymbol{\alpha}_2 \equiv (n, m) \quad (6.1)$$

in terms of the basis, or unit, vectors of the honeycomb lattice $\boldsymbol{\alpha}_1$, $\boldsymbol{\alpha}_2$, and in terms of a pair of integers (n, m) , which represents \mathbf{C}_h coordinates in the lattice.

In the graphene sheet shown in Figure 6.1, OBB'A defines the unit cell of a 1D nanotube. \overrightarrow{OB} is the shortest repeat distance along the carbon nanotube axis, and therefore defines the translation vector \mathbf{T} , which can also be expressed in terms of the unit vectors $\boldsymbol{\alpha}_1$, $\boldsymbol{\alpha}_2$, and a new pair of integers (t_1, t_2) as follows

$$\mathbf{T} = t_1\boldsymbol{\alpha}_1 + t_2\boldsymbol{\alpha}_2 \equiv (t_1, t_2). \quad (6.2)$$

The translation vector \mathbf{T} is perpendicular to the chiral vector \mathbf{C}_h . Therefore, using the condition for orthogonality, $\mathbf{C}_h \cdot \mathbf{T} = \mathbf{0}$, a relationship between the coefficients (t_1, t_2) and (n, m) can be derived, and the result is the following

$$t_1 = \frac{2m + n}{d_R} \quad (6.3)$$

$$t_2 = -\frac{m+2n}{d_R}, \quad (6.4)$$

where d_R is the greatest common divisor of $(2m+n)$ and $(m+2n)$.

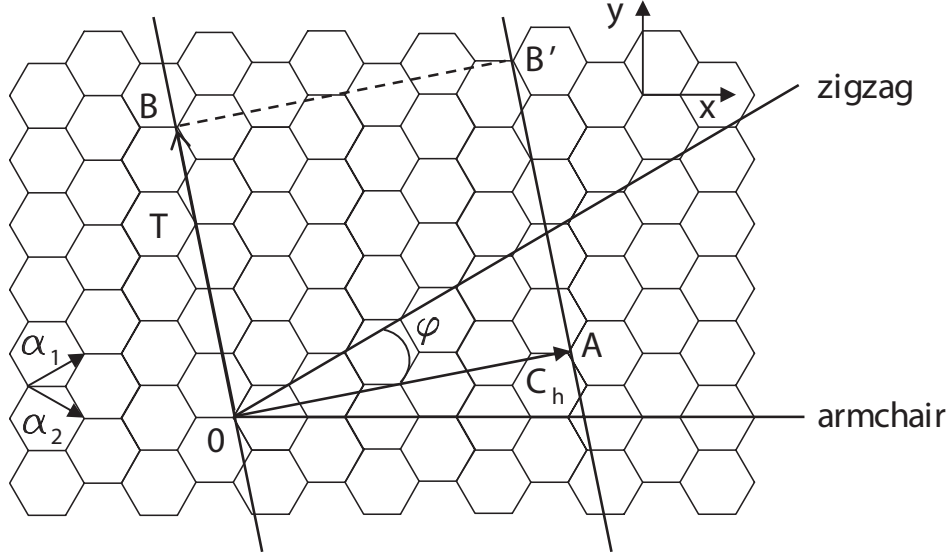


Figure 6.1: The unwrapped honeycomb lattice (graphene sheet) of a nanotube, where $OAB'B$ defines its unit cell, and α_1, α_2 are the unit vectors. C_h, \mathbf{T} represent the chiral and translational vector respectively, and φ is the wrapping, or chiral, angle.

The magnitudes of the chiral and translation vectors are

$$C_h = |\mathbf{C}_h| = \alpha\sqrt{n^2 + m^2 + nm} \equiv L \quad (6.5)$$

$$T = |\mathbf{T}| = \alpha\sqrt{t_1^2 + t_2^2 + t_1t_2} = \frac{\sqrt{3}L}{d_R}, \quad (6.6)$$

where

$$\alpha = |\alpha_1| = |\alpha_2| = 1.42 * \sqrt{3} = 2.46 \text{ \AA}, \quad (6.7)$$

is the lattice constant of the two-dimensional graphene sheet, and L is the length of the chiral vector. In other words, L is the circumference of the nanotube, since $C_h = \pi d_t$, where d_t is the diameter of the nanotube uniquely determined by the (n, m) :

$$d_t = \frac{C_h}{\pi} = \frac{\alpha_{C-C} \sqrt{3(n^2 + mn + m^2)}}{\pi} \quad (6.8)$$

with α_{C-C} being the nearest-neighbor carbon-carbon distance ($\alpha_{C-C} = \alpha/\sqrt{3} = 1.42 \text{ \AA}$ in graphite, where α is the lattice constant [84]).

Furthermore, the chiral angle ϕ , which can be expressed as:

$$\cos\phi = \frac{|\mathbf{C}_h \cdot \boldsymbol{\alpha}_1|}{|\mathbf{C}_h| |\boldsymbol{\alpha}_1|} = \frac{2n + m}{2\sqrt{n^2 + m^2 + nm}}, \quad 0^\circ \leq \phi \leq 30^\circ, \quad (6.9)$$

is the angle between the chiral vector \mathbf{C}_h and the unit vector $\boldsymbol{\alpha}_1$.

The area delineated by the translation and chiral vectors defines the unit cell area of the nanotube. The number of hexagons N contained in this unit cell area can be determined by the integer coefficients of the chiral vector (n, m) as follows

$$N = \frac{|\mathbf{C}_h \times \mathbf{T}|}{|\boldsymbol{\alpha}_1 \times \boldsymbol{\alpha}_2|} = \frac{2(n^2 + m^2 + nm)}{d_R}. \quad (6.10)$$

Every hexagon has one carbon atom in each vertex that is being shared with two neighbor hexagons, therefore only two carbon atoms belong to each hexagon, and hence there are $2N$ carbon atoms per unit cell. For example, for an armchair in which $n = m = 10$, using equations (6.8) and (6.10) we obtained $N = 20$, and thus there are 20 carbon atoms per unit cell.

6.1.1 Electronic Structure of Carbon Nanotubes

Several workers have investigated the electronic structures of isolated SWNTs using the tight-binding model for theoretical calculations. It has been predicted, that when $n = m$, the chiral vector goes through the diagonal lines of the hexagons, as shown in Figure 6.1, and forms a nanotube of zero energy gap. This nanotube is called ‘‘armchair’’ due to the shape of the nanotube perimeter. The wrapping angle in this case has its

maximum value, thus $\phi = 30^\circ$. In case $n = 0$ or $m = 0$, the chiral vector goes through the edge of the hexagons, as shown in Figure 6.1, and forms the “zigzag” nanotube, with a wrapping angle that has its minimum value, thus $\phi = 0^\circ$. For all other (n, m) , the nanotube formed is called “chiral”, and the value of the wrapping angle is within the range $0^\circ < \phi < 30^\circ$. The armchair SWNTs, and those SWNTs that satisfy the condition: $2n + m = 3k$, where k is a non-zero integer, are metallic, whereas all the other SWNTs are semiconductors with an energy band gap that scales as $1/d_t$, where d_t is the diameter of the nanotube given by equation (6.8) [83, 84]. The “ $2n + m = 3k$ ” condition for the SWNTs is obtained from the 2D graphene sheet by imposing the following periodic boundary condition: $n\lambda = \pi d_t$, where $\lambda = 2\pi/k$ is the de Broglie wavelength. The small diameters of the nanotubes allow only a few wave vectors to satisfy this condition in the circumferential direction.

Graphite is semi-metallic, whereas a single graphene sheet is a zero gap semiconductor due to the degeneracy of the bonding and anti-bonding energy bands at the corners of the first Brillouin zone (BZ). These corners correspond to K points. Therefore, metallic conduction occurs for the SWNTs only when one of the allowed wave vectors \mathbf{k} go through these K points in the two dimensional BZ. At these points, the valence and conduction bands are degenerate due the the special symmetry of the graphene lattice [84]. In any other case of (n, m) , the SWNTs are semiconducting.



Figure 6.2: Classification of SWNTs based on their geometry: a) armchair, b) zigzag, and c) chiral carbon nanotubes.

These predictions on whether a SWNT is metallic or semiconductor do not include the effect of the curvature of a carbon nanotube. Tight-binding calculations which have taken into account the curvature effect, have shown that it leads to an orbital hybridization which results in a small band gap, of the order of meV, for the chiral

nanotubes. This curvature induced, secondary, band gap scales as $1/d_t^2$, where d_t is the diameter of the nanotube, and hence renders the nanotubes in the semiconducting regime [85, 86]. Only the armchair nanotubes remain unaffected by the curvature, and show truly metallic behavior. However, in the case where these (n, n) , armchair, SWNTs are organized into bundles or ropes, the intertube couplings cause a broken symmetry of the nanotube, inducing a pseudogap at the Fermi level. Either of, or both, these effects could be responsible for a far infrared gap-like feature shown in experimental studies on SWNTs films which contain a mixture of all types of nanotubes [87]. The above theoretical calculations for the electronic structure of SWNTs also show that for SWNTs films of a mixture of nanotubes, about 1/3 of the nanotubes are metallic, and 2/3 are semiconducting, depending from the nanotube diameter, chiral angle, and their environment.

6.1.2 Density of States (DOS) of SWNTs

The electronic structure of the SWNTs is closely related to the electronic structure of a 2D graphene sheet, but the density of states of these two systems is significantly different. The continuous electronic density of states (DOS) in graphite, divides into a series of spikes in SWNTs caused by the quantum confinement of electrons in the radial and circumferential directions of the nanotubes. These spikes, which are not present in graphite, are referred to as van Hove singularities and they comprise a typical signature of 1D systems. The electronic transitions between these van Hove singularities give rise to prominent features that can be clearly observed by Scanning Tunneling Spectroscopy (STS) [88, 89], and optical spectroscopy [84, 90].

The two-dimensional energy dispersion relation for π bands of the graphite layer, based on the tight binding model in which only the nearest neighbor interactions are considered, can be written as follows

$$E(\mathbf{k}) = \pm t \sqrt{1 + 4 \cos\left(\frac{\sqrt{3}k_x\alpha}{2}\right) \cos\left(\frac{k_y\alpha}{2}\right) + 4 \cos^2\left(\frac{k_y\alpha}{2}\right)} \quad (6.11)$$

where t is the nearest neighbor overlap energy, also known as transfer integral. In the case of nanotubes, there is some mixing of the $\pi(2p_z)$ and $\sigma(2s$ and $2p_{x,y})$ carbon orbitals, that occurs due to the induced curvature, but since it is very small it can be neglected around the Fermi level [86] and thus, only the π orbitals are considered. By imposing periodic boundary condition along the nanotube circumference:

$$\mathbf{C}_h \cdot \mathbf{K} = 2\pi q \quad (6.12)$$

where \mathbf{C}_h is the chiral vector, \mathbf{K} is the reciprocal vector, and q is an integer ($q = 1, 2, \dots, N$ with N being the number of hexagons in the translational unit cell), and by using a rotation transformation:

$$k_x = k_{\perp} \cos \theta - k_{\parallel} \sin \theta \quad (6.13)$$

$$k_y = k_{\perp} \sin \theta + k_{\parallel} \cos \theta, \quad (6.14)$$

where

$$\cos \theta = \frac{\sqrt{3}}{2} \frac{n+m}{\sqrt{n^2+m^2+nm}} \quad (6.15)$$

$$\sin \theta = \frac{1}{2} \frac{n-m}{\sqrt{n^2+m^2+nm}}, \quad (6.16)$$

the energy dispersion relation for a (n, m) carbon nanotube can be expressed as a function of the wavevector k_{\parallel} , describing the electron motion parallel to the nanotube axis.

Using this method, we can plot the energy dispersion relation and the density of states for two special cases. First, for a transformation angle of zero $\theta = 0^\circ$, the SWNTs are of armchair type (n, n) with an energy dispersion relation shown in Figure 6.3 and given by:

$$E_q(k) = \pm t \sqrt{1 + 4 \cos\left(\frac{q\pi}{n}\right) \cos\left(\frac{k\alpha}{2}\right) + 4 \cos^2\left(\frac{k\alpha}{2}\right)} \quad (6.17)$$

where

$$k_x = k_\perp = \frac{2\pi q}{\sqrt{3}\alpha n} \quad (6.18)$$

with $q = 1, 2, \dots, N$, and

$$k_y = k_\parallel = k. \quad (6.19)$$

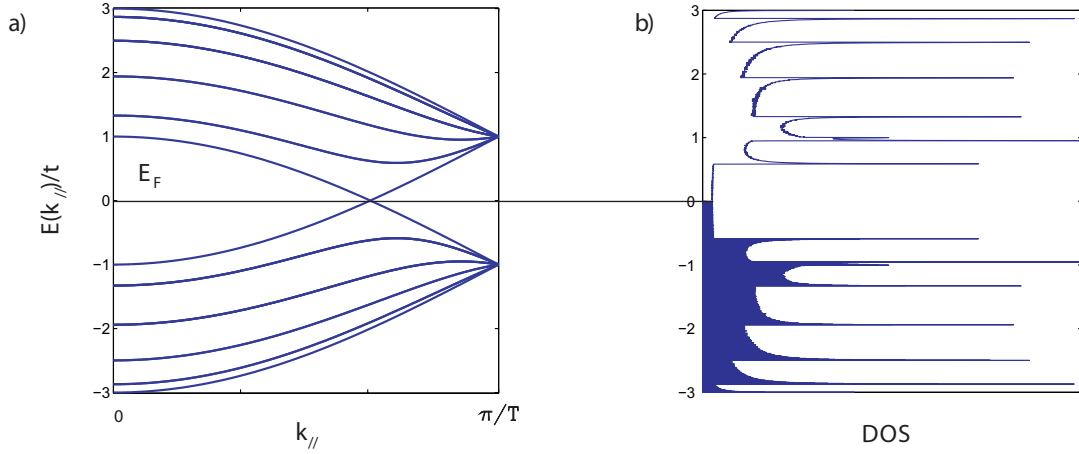


Figure 6.3: a) One-dimensional energy dispersion, and b) one-dimensional electronic density of states per unit cell, for a metallic SWNTs, armchair (10, 10), for $N = 20$.

The second special case is for a transformation angle of $\theta = 90^\circ$, for which the SWNTs are of zigzag type $(n, 0)$ with an energy dispersion relation shown in Figure 6.4 and given by:

$$E_q(k) = \pm t \sqrt{1 + 4 \cos\left(\frac{\sqrt{3}\alpha k}{2}\right) \cos\left(\frac{q\pi}{n}\right) + 4 \cos^2\left(\frac{q\pi}{n}\right)} \quad (6.20)$$

where

$$k_y = k_\perp = \frac{2\pi q}{\alpha n} \quad (6.21)$$

with $q = 1, 2, \dots, N$, and

$$k_x = k_{\perp} = k. \quad (6.22)$$

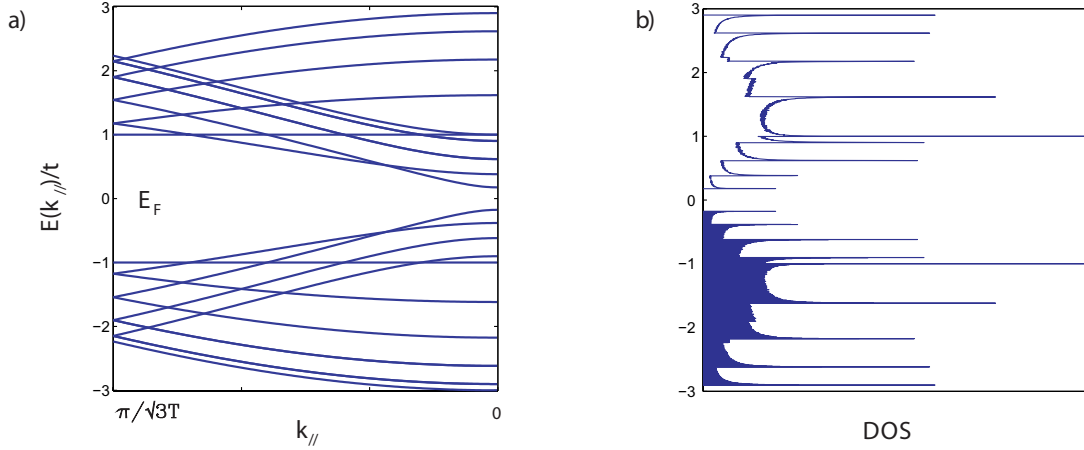


Figure 6.4: a) One-dimensional energy dispersion, and b) one-dimensional electronic density of states per unit cell, for a semiconducting SWNTs, zigzag (10, 0), for $N = 20$.

As can be seen in Figure 6.3, the 1D electronic density of states for the case of metallic nanotubes has a non-zero value at the Fermi level E_F , and this non-vanishing density of states is independent of energy, until the energy is equal to the energy difference between the sub-band edges of the valence and conduction bands. These sub-band edges or singularities, which are characteristic of 1D systems, correspond to extrema of the energy dispersion relation. In comparison, for the case of a graphene sheet, the 2D density of states vanishes at the Fermi level, and varies linearly with energy moving away from E_F (Figure for the 2D density of states for graphene sheet can be found in literature, for example in references [84, 86]).

Furthermore, as can be seen in Figure 6.4, the density of states of semiconducting nanotubes is zero within the energy band gap E_g , which is equal to the energy difference between the first two van Hove singularities in the 1D density of states. These singularities, also correspond to extrema of the energy dispersion relation. When the photon energy is equal to the energy separation between an occupied and an unoccupied peak

in the electron density of states, strong optical absorptions (the ones allowed by the dipole selection rules) are expected to be observed. These electronic transitions between the sub-band edge states are characteristic of both types, metallic and semiconducting, SWNTs. Further confirmation of the theory is provided by the fact that the energy of the lowest of these interband transitions in the metallic nanotubes, falls in between the second and third transition in the semiconducting tube of the same diameter.

6.1.3 Carbon Nanotube Synthesis and Purification

Carbon nanotubes can be produced by three techniques: arc discharge, laser ablation, and chemical vapor deposition (CVD). The choice of the most suitable synthesis method depends on the type of carbon nanotubes, SWNTs or MWNTs, and the diameter range that are needed. The production efficiency between the different methods as well as the level of purity of the nanotubes vary significantly. Among these techniques, the laser ablation procedure is known to produce the highest quality SWNT material, in terms of yield and the resulting nanotube defect densities [91], and a characteristic narrow diameter distribution range.

Typically, the carbon nanotubes in all these techniques are formed on the surface of catalysts, e.g., Co, Ni, Fe, or Y. The produced or as-prepared carbon nanotubes are not pure and hence, further purification is needed. The impurities that are generally found in the as-prepared nanotubes are metal catalyst particles and amorphous carbon. Due to the fact that high purity carbon nanotubes are required for applications, several purification techniques have been developed. Some major categories of these techniques are oxidation, filtration, ultra-sonication, and chromatography. These purification methods attempt to remove the metal catalyst particles and unwanted amorphous carbon, without affecting the carbon nanotubes. More detailed description concerning the different techniques of carbon nanotube growth and purification can be found in the literature [92, 93].

6.1.4 General Applications of CNs

The remarkable electronic properties of carbon nanotubes (CNs) and their dependency on simple geometrical parameters, i.e., diameter and chirality makes them very attractive for numerous potential applications. CNs are quasi 1D systems and the electronic transport in metallic nanotubes occurs without scattering (ballistically) over long paths, which enables them to carry high density currents without significant heating [83]. In addition to their exceptional electronic properties, CNs also possess exquisite mechanical properties. They are quite stiff and very strong (for objects of such small diameter), with high Young's modulus and high tensile strength [83]. Therefore, CNs combine excellent electrical, and mechanical properties, and until now there is no counterpart material that could compete with them.

CNs offer a candidate to replace silicon in electronic devices. Silicon devices are moving towards their scaling limits as they continuously shrink, in an effort to achieve higher speed and higher densities. CNs provide an alternative solution to this limitation problem. Their unique electronic and mechanical properties though make them good candidates for a number of other devices too, e.g., CN logic gates (nanotube-based field effect transistors CNFET), energy storage devices (hydrogen storage), electrochemical devices (supercapacitors), nanoprobes (AFM, STM, SFM probe tips), nanotweezers (actuators to grab and manipulate sub-micron clusters and nanowires), sensors (chemical sensors, biosensors, infrared sensors), nanothermometers, and nanotube composite materials (incorporation of nanotubes into plastics, to obtain ultrahigh strength materials).

Although this picture provides a very optimistic view for the future of these materials, there are still enormous challenges that need to be dealt with before carbon nanotubes are successfully incorporated into useful device technology. Some of the issues that need to be addressed are initially the small scale growth techniques that are currently available and the manufacturing cost, since highly purified CNs are very expensive. Moreover, CN films are produced as a mixture of metallic and semiconducting

nanotubes, and so far there is no effective method that would sort them out according to their electronic properties.

Nevertheless, in the last few years there have been an exponential increase in publications and patents, that indicates that not only the academic but also the industrial interest in carbon nanotubes is growing fast [83]. Independent of whether carbon nanotubes will be successfully incorporated into commercial production technology or not, these systems have paved the way for the advances and the future of nanotechnology.

6.2 Free-Standing SWNT Films: Transparency, and Optical Conductivity

Transparent electrical conductors are in high demand for a number of modern technological applications, such as displays, light emitting devices, and solar cells. Prof. Rinzler's group has developed a novel technique for the production of a class of a transparent conducting material based on continuous films of pure SWNTs [90]. These films contain a mixture of metallic ($\sim 1/3$) and semiconducting ($\sim 2/3$) carbon nanotubes, and therefore are intrinsically conducting. In addition, they can be formed into films that are optically homogeneous, ultra-thin, with good electrical conductivity throughout the whole film. These films can be made free-standing (due to their high mechanical strength and flexibility) or they can be transferred to a substrate of choice, rigid or flexible. The next section provides a very brief description of this method. Further information about this method can be found in [94].

6.2.1 Sample Preparation

Laser-ablation grown SWNTs with an average diameter of 1.4 nm are commercially purchased, and acid purified (HNO_3) to remove impurities embedded in the nanotubes during the growth process. The nanotubes are then dispersed through ultra-sonication into a solution, which acts as a stabilizing agent to suspend the nanotubes. This mixture is vacuum filtered across a mixed cellulose ester membrane (of 100 nm pore size) and as the solution is removed through the membrane, a nanotube film is formed on the membrane surface. Any remaining surfactant is washed away with purified water.

This vacuum filtering process produces very homogeneous nanotube films of a desired thickness. The control of the thickness is achieved with nanoscale precision through the nanotube concentration in the mixture, and the volume of the solution that is initially used. The final steps are the transfer of the film in a substrate of choice, flexible or rigid, and the dissolution of the membrane in solvent (baths in methanol and then acetone). The nanotube films can be made into any shape and size by simply cutting them before the dissolution of the membrane.

For the transmittance measurements described in this chapter, the SWNT films were transferred to a substrate with a hole, over which the film was laid before the membrane dissolution. This allowed us to perform transmittance measurements over a wide part of the electromagnetic spectrum, from far infrared to visible region. The substrate was either a pyrolytic graphite template with approximately a 5 mm hole which was then mounted on a metal frame with a smaller size aperture, or the metal frame itself. The graphite template was used for temperature dependent studies due to the fact that the thermal properties of this substrate are closer to the thermal properties of carbon nanotubes, and thus the stretching of the nanotube film during the change of the temperature is minimized.

The metal frame, shown in Figure 6.5 bottom, is a copper plate which is part of our transmittance sample holder configuration. In Figure 6.5 top, a top view of this sample holder is also shown, in which two identical copper plates (the same size aperture) are mounted in a 90° angle relevant to each other. The second copper plate does not have anything over the hole and is used for the “background” measurements. After the plates are mounted in the sample holder, the holder is attached to a liquid helium cryostat which will permit us to perform temperature dependent transmittance measurements. The shift due to thermal contraction of the cryostat cold finger is compensated by a remote-operated z -stage, which can reposition the sample to its original place with great accuracy.

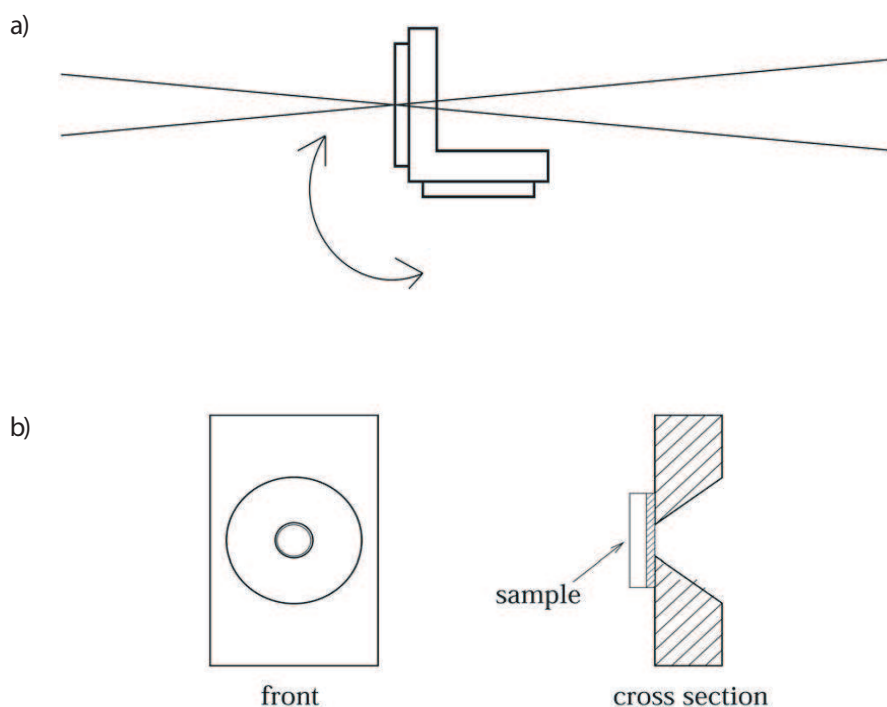


Figure 6.5: A schematic diagram of a) the transmittance sample holder, and b) the plate, on which the sample under consideration is mounted.

Figure 6.6 shows an atomic force microscopy (AFM) image of a, 150 nm thick, transparent SWNT film surface prepared with the method described above. The film thickness is obtained by AFM at the film edge. As can be seen, the nanotubes are randomly distributed over the space, and they form into bundles due to van der Waals forces. It should be noted, that the morphology of these films is highly uniform and they possess nanoscale porosity. The sufficient nanotube-nanotube overlap ensures that these films have good electrical conductivity.

The density of this material determined by weighing a film of known thickness is 0.4 g/cm^3 . This value is very low, much lower than the graphite density, and as a consequence these films tend to float on the surface of water and organic liquids [F. Borondics et al. unpublished results 2005].

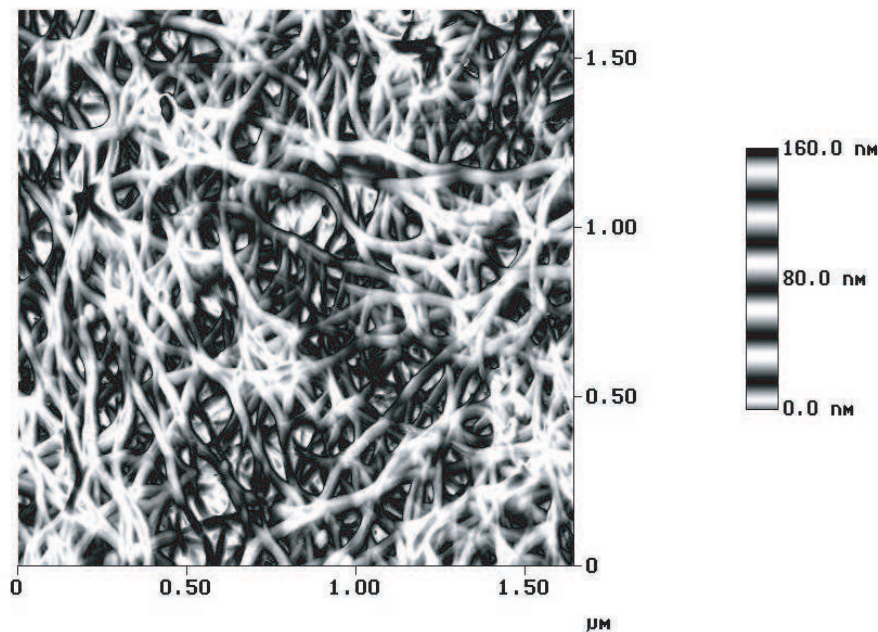


Figure 6.6: AFM image of a 150 nm thick transparent SWNT film surface.

6.2.2 In-situ Transmittance Measurements

Optical spectroscopy is one of the most widely used methods for the characterization of carbon nanotube films. Spectroscopic studies on high quality macroscopic samples reflect the unique characteristics of these one dimensional systems. In the near infrared and visible regions, where the transitions between the van Hove singularities occur, spectroscopic measurements reveal the electronic structure characteristics of these systems. Important information about the free-carrier dynamics is studied in the far infrared region.

Free carriers are intrinsic in metallic nanotubes, and can be introduced by doping with electrons (alkali metals) or holes (halogens or oxidizing agents) in semiconducting tubes. Some hole doping is commonly the case for purified samples. Purification methods, which serve to remove the metal catalyst particles and the unwanted amorphous carbon leave the carbon nanotubes hole-doped. Annealing of the purified samples under vacuum reverts them to their un-doped state, and this change can be followed by infrared spectroscopy due to the accompanying change in the oscillator strength of the optical transitions [95].

Although theoretical models have predicted many interesting phenomena for the far infrared part of the electromagnetic spectrum, little attention has been experimentally devoted to this region so far [95–97]. Far infrared spectroscopy provides a powerful tool for pristine carbon nanotubes, and can compliment fluorescence measurements [98] because it gives us the opportunity to study only the metallic and the low band gap carbon nanotubes. There are exist two kinds of theoretical predictions for the origin of the far infrared optical transition due to low band gaps: one is the secondary band gap induced by the curvature for semiconducting nanotubes with chirality index of $2n + m = 3k$, where k is a non-zero integer, and the other one, at lower energies, is a pseudogap caused by the symmetry-breaking effect of neighbors in a bundle of metallic tubes.

In this work, transmittance measurements have been performed on transparent free-standing SWNT films of different thicknesses. The free-standing films give us the capability to cover a wide range of the electromagnetic spectrum, from far infrared to ultraviolet. Under other circumstances several different substrates would have to be used, and a difficult normalization procedure would be required in order for the data of all regions to be merged. Furthermore, this configuration also simplifies the temperature studies and the vacuum annealing process of the purified samples, where the thermal properties of the film would have to be matched with the thermal properties of each substrate.

Transmittance spectra of as-prepared (purified) free-standing SWNT, of 1.4 nm mean diameter, films of different thicknesses will be presented from the far infrared through the ultraviolet region, at different temperatures. These samples exhibit increased metallic absorption in the far infrared region, and decreased interband transitions, in the near infrared and visible regions, due to nitrate doping. Acid treatment (HNO_3) during the purification process leaves the semiconducting nanotube films hole-doped (p-doped) and therefore, shifts the spectral weight from the first van Hove transition into the infrared region. Transmittance spectra of these samples after heat

treatment under vacuum, a process which results in the removal of the nitrate dopants and thus de-dopes the films, are also presented for comparison. In addition, heat-treated samples are considered to be closest to pristine carbon nanotubes, and hence provides us the opportunity to study the metallic, and low band gap nanotubes.

The transmittance measurements of the free-standing carbon nanotube films were performed in the spectral range from 30 - 30,000 cm^{-1} (4 meV - 4 eV). For the far infrared and mid-infrared regions a Bruker 113v interferometer was used at temperatures between 50 K and 300 K, while for the near infrared through ultraviolet a Perkin-Elmer dual beam spectrometer (Lambda 900) or a modified Perkin-Elmer (PE) 16U monochromator were used at the same temperatures. The spectrometers have sufficient spectral overlap to allow unambiguous merging of the transmittance spectra between the different part of the electromagnetic spectrum.

The analysis of the obtained data was based on the fact that the transmittance of a film is subject to the same causality restrictions as the reflectance. This means that one can use Kramers-Kronig analysis of transmittance in order to estimate the phase shift on transmittance, just as it is used for reflectance measurements. Once the phase shift is known, the optical constants can then be calculated by numerical inversion of

$$\sqrt{\mathcal{T}}e^{i\theta} = \frac{4N}{(\tilde{n} + 1)^2e^{-i\delta} - (\tilde{n} - 1)^2e^{i\delta}} \quad (6.23)$$

where

$$\delta = \frac{\omega Nd}{c}, \quad (6.24)$$

is the complex phase through a film, of thickness d , and

$$N = \sqrt{\epsilon_1 + \frac{4\pi i\sigma_1}{\omega}} \quad (6.25)$$

is the complex refractive index of the film. An important caveat that should be made at this point is that the phase the radiation gains passing a thickness d of vacuum must be added to θ before one proceeds to calculate N .

Room Temperature Spectra

Transmission studies on free-standing SWNT films were performed over a wide frequency range at room temperature. The films under investigation were of different thicknesses, 250 nm and 150 nm as determined by AFM measurements at step edges. The transmittance spectra were obtained initially for the as-prepared (purified) or “unbaked” samples and then, for vacuum annealed or “baked” samples. The purpose of this, was to study extrinsic effects, such as nitrate doping, which occurs during the last step of the purification of the SWNTs by nitric acid HNO_3 and intrinsic features, such as the curvature induced or bundle induced energy gap.

The purification process leaves the semiconducting SWNTs hole-doped, which leads to free-carrier absorption in the far infrared spectral range. The depletion of electrons from the van Hove singularities in the valence band decreases the rate of the interband electronic transitions. Thermal processing in inert gas desorbs the dopants transferring the spectral weight from the far infrared region to the interband transitions. This results in maximizing the strength in absorption bands, which correspond to the first two interband transitions in the semiconducting nanotubes S1 and S2, and the first transition in the metallic nanotubes M1, as shown in Figure 6.7. Furthermore, in some cases in the transmission spectra of the de-doped SWNT films a peak is apparent in the far infrared region at $\sim 100 \text{ cm}^{-1}$. This peak is probably due to the curvature induced energy gap in the DOS of the semiconducting nanotubes with chirality index of $2n + m = 3k$, where k is a non-zero integer [95].

Experimental details of the processing for the measured samples are shown in Table 6.1. Samples A and B are two samples of 250 nm thickness from the same batch, and samples C, C' of 150 nm thickness, are identical, and come from a different batch than A, B samples. Sample A has been measured as-prepared (purified), unbaked, whereas

sample B has been first vacuum annealed, baked, at 1000°C for 12h, and then measured. Samples C, C' are the same sample, which was first measured as-prepared (purified) and then measured again after heat treatment.

Table 6.1: Processing details of the different samples studied. Samples C and C' were identical, measured before and after thermal treatment, respectively.

Sample ID	Thickness (nm)	Processing temperature (°C)	time (hours)
A	250	as-prepared (purified)	
B	250	heat-treated (1000°C)	12
C	150	as-prepared (purified)	
C'	150	heat-treated (1000°C)	12

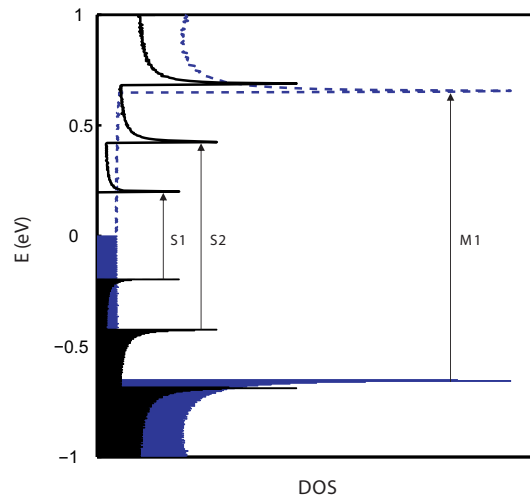


Figure 6.7: Density of states (DOS) for a representative (10, 0) semiconducting nanotube (solid curve), and a superimposed (10, 10) metallic nanotube (dashed curve) calculated using the tight binding model. The drawn arrows between the van Hove singularities represent the S1, S2, and M1 electronic transitions.

The transmittance spectra of samples A (black curve) and B (red curve) at room temperature are shown in Figure 6.8, where logarithmic scales have been used for both

the transmittance and the frequency axes. From these spectra can be clearly seen that the transmittance of the as-prepared (purified) SWNT film towards the far infrared region is limited by the free carrier absorption, while for the vacuum annealed SWNT film the transmittance is a higher in this range, which is the result of the loss of free carriers upon baking.

In the far infrared region, the transmittance is related to the optical conductivity by the well known ‘‘Glover-Tinkham’’ formula:

$$\mathcal{T} = \frac{1}{\left(1 + \frac{2\pi\sigma_1 d}{c}\right)^2 + \left(\frac{2\pi\sigma_2 d}{c}\right)^2}, \quad (6.26)$$

where σ_1 and σ_2 represent the real and imaginary parts of the optical conductivity and d is the film thickness. Therefore, the lower transmittance of the as-prepared (purified) sample results from a higher low-frequency (and dc) conductivity compared to the heat-treated sample. This is consistent with a higher mobile charge density in this sample, and hence supports the above assumption.

At higher frequencies, in the near infrared and visible regions, the transmittance dips are due to the interband electronic transitions. The first two dips correspond to S1 and S2 transitions in the semiconducting nanotubes, and the third to M1 transition in the metallic nanotubes, shown in Figure 6.7. These interband transitions are very prominent in the transmittance spectrum of the heat-treated sample, whereas in the as-prepared (purified) sample due to the transferring of the spectral weight to lower frequencies the dips, although still evident are diminished. The breadth of these dips results from the distribution of the nanotube diameters within the films, and also from bundling.

At even higher frequencies the transmittance of both samples is very similar. The dip which appears at the region above $30,000 \text{ cm}^{-1}$ is attributed to the π plasmon excitation absorption, which extends to much higher, up to $50,000 \text{ cm}^{-1}$, frequencies and therefore, no attempt has been done to analyze this part of the spectrum since our data do not extend as far.

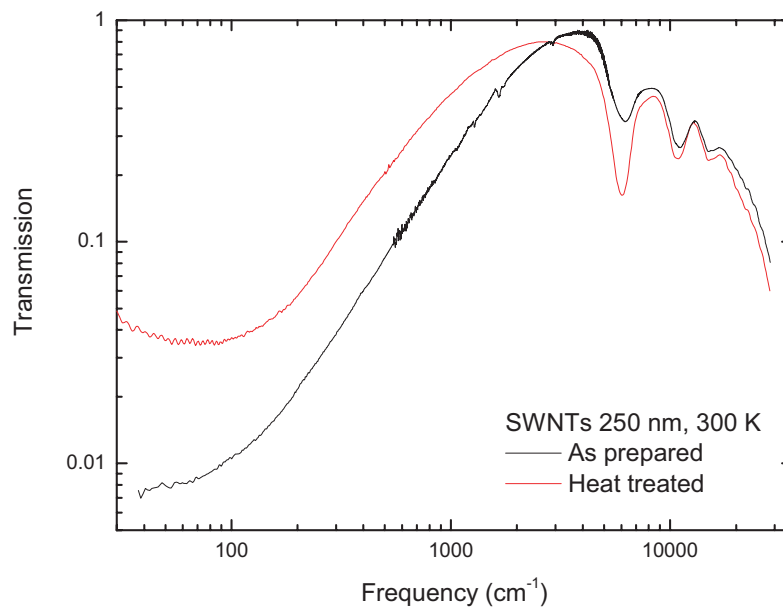


Figure 6.8: Transmittance spectra for two free-standing SWNT films, from the same batch, of thickness 250 nm. The black curve corresponds to a purified (as-prepared) sample (hole-doped), and the red curve to a heat-treated sample (de-doped).

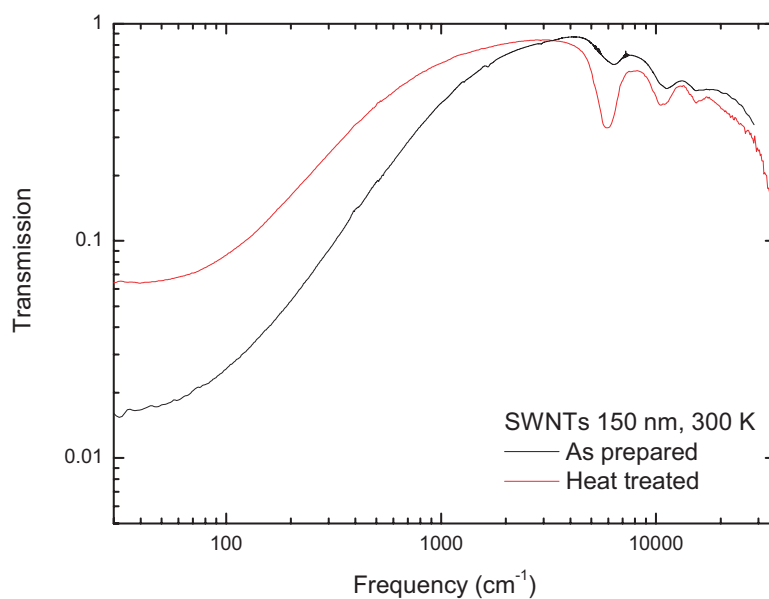


Figure 6.9: Transmittance spectra for a free-standing SWNT films of thickness 150 nm, before and after heat treatment. First the sample was measured after the purification process which leaves the film hole-doped (black curve), and then the sample was annealed under vacuum (de-doped) and it was measured again.

An important characteristic in the transmittance spectra of the heat treated sample, shown in Figure 6.8, is the transmittance dip below 100 cm^{-1} . This dip is ascribed to a curvature induced energy gap in the DOS of the semiconducting nanotubes with chirality index of $2n + m = 3k$, where k is a non-zero integer. This has been observed by other groups too [95].

Figure 6.9 shows the transmittance spectra of the 150 nm SWNT film before and after heat treatment. Here also, the transmittance and the frequency axes are shown on logarithmic scales. The main characteristics of the transmission spectra of this sample are the same as those described for the thicker ones. An important difference is in the spectrum of the sample after the heat treatment C', and is the absence of the dip below 100 cm^{-1} , which is observed in the thicker sample. This might be due to accidental doping by atmospheric oxygen, since it has been reported that exposure of carbon nanotubes to air or oxygen can alter their electronic properties [99]. Even a low doping could result to smear out the energy band gaps of some number of nanotubes and consequently change the distribution of gaps, so that the median shifts to lower frequencies where it can not be observed from these measurements.

Finally, Figure 6.10 shows the transmittance spectra of all four measurements for comparison. In general, the as-prepared (purified) samples have lower transmittance in the far infrared region due to the free carrier absorption, and higher transmittance in the near infrared and visible regions compared with the same thickness heat-treated samples. Samples C and C' are, of course, more transparent throughout the measured range compared to samples A, B respectively due to the difference in thickness. It has been reported [90] that a SWNT film of 50 nm thickness exhibits transmittance greater than 70% over the visible region of the electromagnetic spectrum, higher than 90% in the near infrared part, and is expected to retain this value over the mid-infrared region too. The sheet resistance for this 50 nm film in the as-prepared (purified) state was measured to be $30\ \Omega/\text{S}$. Therefore, SWNTs can be excellent transparent electrodes possessing high transmittance for low sheet resistance. It should also be noted that,

the as-prepared (purified) samples are not maximally doped and hence, the above value does not represent the lower limit.

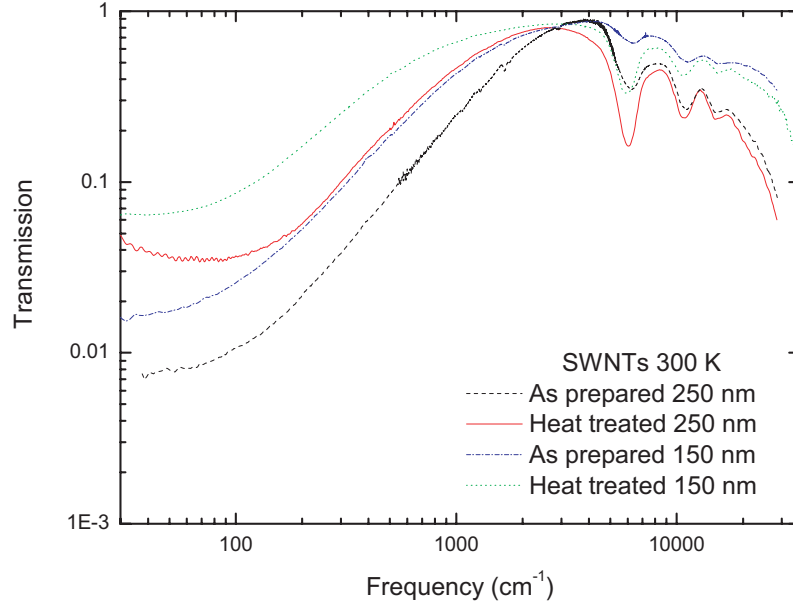


Figure 6.10: Transmittance spectra for free-standing SWNT films of different thicknesses, 250 nm and 150 nm. The black (dash) and blue (dash dot) curves corresponds to purified (as-prepared) samples (hole-doped), and the red (solid) and green (dot) curves to heat-treated samples (de-doped).

Temperature Dependence Spectra

The temperature-dependence of the transmittance spectrum of the 150 nm film is shown in Figure 6.11 for the sample as-prepared (purified), and Figure 6.12 shows the temperature-dependence of the transmittance of the same sample after heat treatment. At low frequencies the transmittance decreases with decreasing temperature, which is consistent with an increasing conductivity at low temperatures, whereas at high frequencies the temperature dependence becomes too weak to be observed. Therefore, only room temperature measurements are performed for this spectral region for the rest of the samples.

The temperature-dependence of the transmittance spectrum of the 250 nm SWNT film after vacuum annealing is shown in Figure 6.13. In this spectra, the important feature is the weak minimum in the far infrared region, which is inconsistent with a

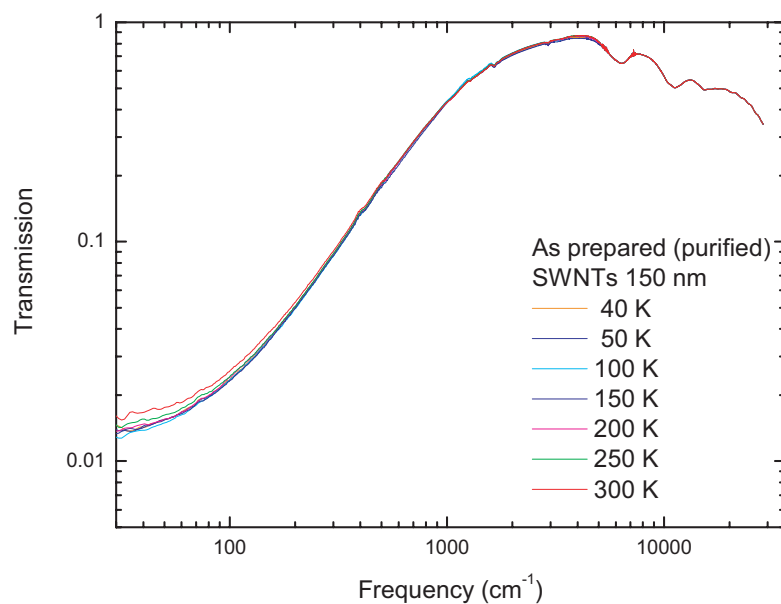


Figure 6.11: Temperature-dependence of transmittance spectra for the as-prepared 150 nm free-standing SWNT film.

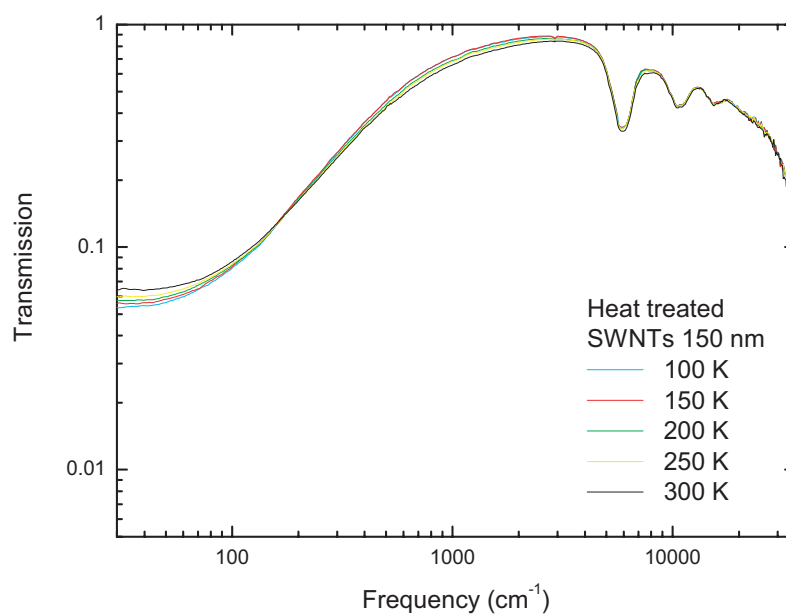


Figure 6.12: Temperature-dependence of transmittance spectra for the heat-treated 150 nm free-standing SWNT film.

simple free carrier (Drude) conductivity in this region. This will be discussed further in the next section. First, attention is given to the vacuum annealed films as in this state they are considered to be closest to pristine carbon nanotube.

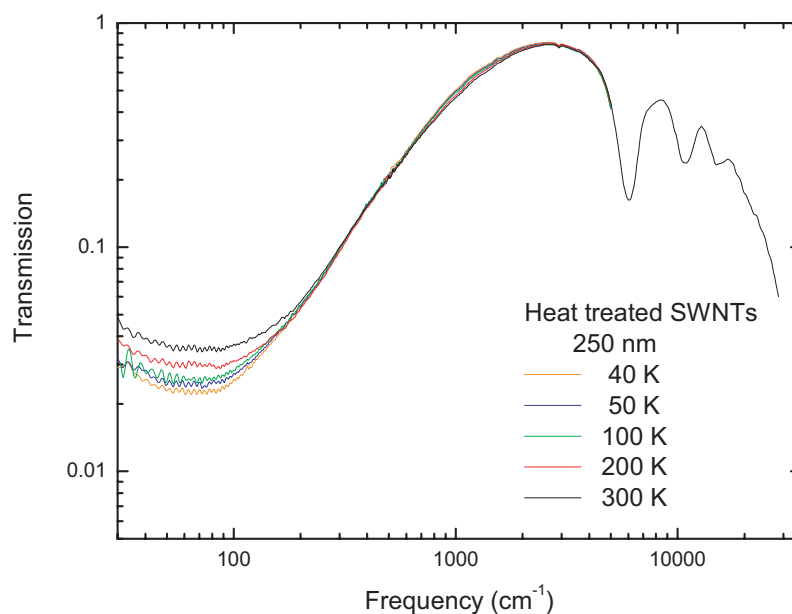


Figure 6.13: Temperature-dependence of transmittance spectra for the heat-treated 150 nm free-standing SWNT film.

6.2.3 Optical Constants, Data Analysis and Model Fit

The optical constants, optical conductivity and absorbance of the free-standing SWNT films are determined by Kramers-Kronig analysis of the transmittance data, as it was previously explained. Figure 6.14 shows the optical conductivity of the samples of different thicknesses at room temperature, and in as-prepared and heat-treated states. The conductivity is comparable for the two samples when at the same state, as-prepared or heat-treated, and in general appears to be independent of thickness. At very low frequencies there is a difference for the heat-treated samples, where for the thinner film the peak seems to have shifted at lower frequencies. This difference might be due to accidental doping of the carbon nanotubes by atmospheric oxygen.

The effect of nitrate doping of the semiconducting carbon nanotubes during the purification process is quite obvious in the optical properties. As can be seen in Figure 6.14, there is a significant increase in the conductivity in the far infrared region between the as-prepared (purified) and heat-treated films. In the near infrared region, a decrease

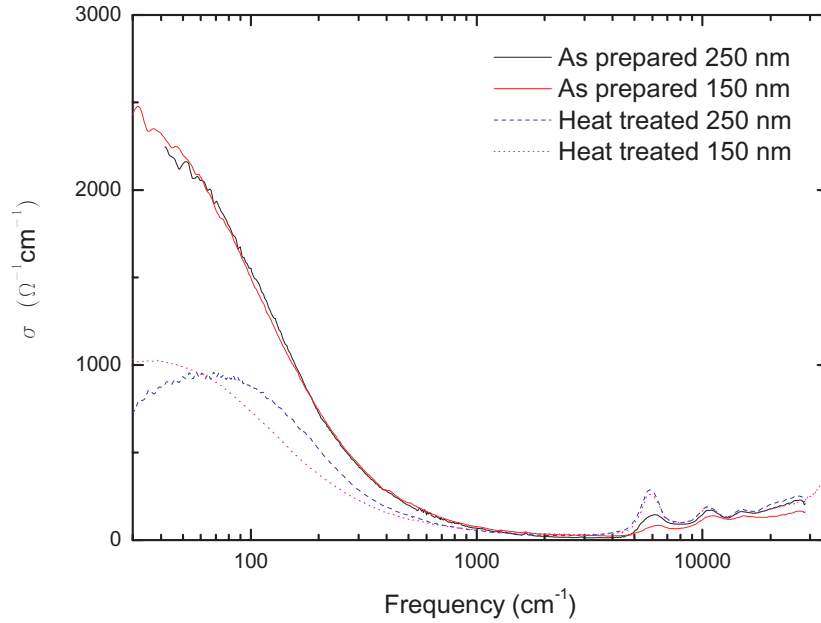


Figure 6.14: Room temperature optical conductivity of two SWNT free-standing SWNT films of different thicknesses in as-prepared (purified) and heat-treated states.

of the conductivity around the first electronic transition S1 in the as-prepared (purified) film when compared to the heat-treated film can also be observed.

The conductivity values of the heat-treated samples at low frequencies are $800 \Omega^{-1}\text{cm}^{-1}$ and $1000 \Omega^{-1}\text{cm}^{-1}$ for the 250 nm and 150 nm films respectively. These values are in agreement with the values determined from the sheet resistance of these films [90]. The DC conductivity of the as-prepared (purified) samples is around $2600 \Omega^{-1}\text{cm}^{-1}$. This value is lower than the value determined from the sheet resistance of these films [90], but very close to other experimental results of high-resolution electron energy-loss spectroscopy (EELS) [100].

The temperature dependence of the optical conductivity is shown in Figure 6.15. The dependence of conductivity from temperature is basically confined in the far infrared region, where the Drude feature becomes narrow, while in the mid-infrared range the conductivity is decreasing as the temperature decreases from 300 K to lower values. More specifically, the conductivity at low frequencies is decreasing as the temperature

increases, while beyond 120 cm^{-1} this dependence reverses. At frequencies higher than 2000 cm^{-1} the temperature dependence becomes too weak to be observed.

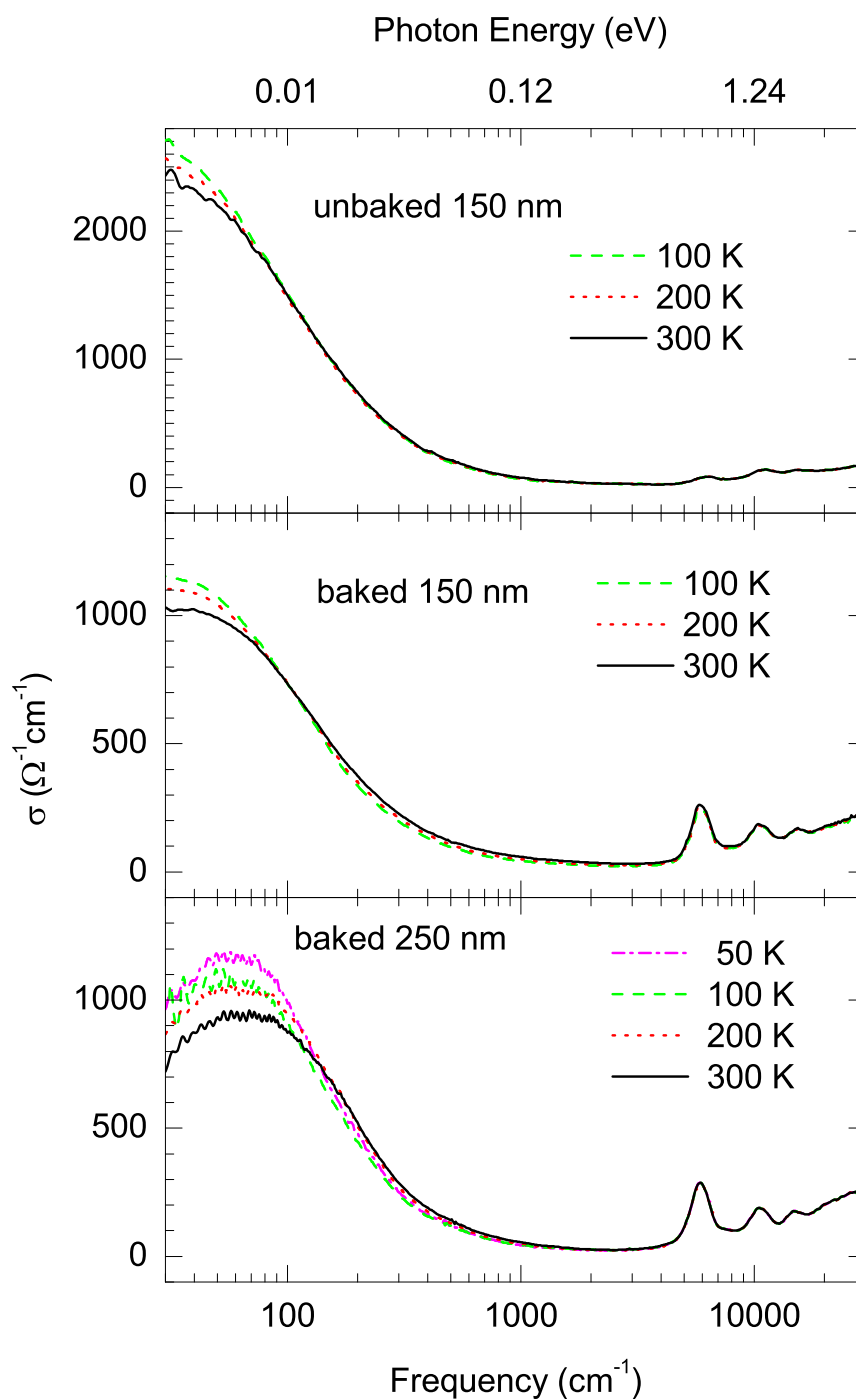


Figure 6.15: Temperature-dependence of optical conductivity for the 150 nm as-prepared (upper panel) and heat-treated (middle panel), and the 250 nm heat-treated (lower panel) free-standing SWNT film.

A multi-oscillator fit was applied to the transmittance data for thin free-standing films. The transmittance was fit using the following, Drude-Lorentz, model:

$$\tilde{\epsilon}(\omega) = \epsilon_{\infty} + \sum_j \frac{\omega_{pj}^2}{\omega_j^2 - \omega^2 - i\gamma_j\omega} - \frac{\omega_{Dp}^2}{\omega^2 + i\omega/\tau_D} \quad (6.27)$$

which yields estimates of the high frequency dielectric constant ϵ_{∞} , the Drude plasma frequency ω_{pD} , the Drude lifetime τ_D , as well as the plasma frequency or oscillator strength ω_{pj} , center frequency ω_j , and damping γ_j for each mode. The fitting parameters that were obtained from this model for all samples are shown in Tables 6.2 and 6.3.

Table 6.2: Drude-Lorentz fitting parameters for the optical conductivity of each sample studied at several temperatures. The parameters for high-frequency oscillators are given in Table 6.3.

	ω_{p0}	γ_0	ω_{p1}	ω_1	γ_1	ω_{p2}	ω_2	γ_2	ω_{p3}	ω_3	γ_3
A: doped											
300 K	2057	762	4054	35	128	3375	6184	1406	5179	10617	3859
B: de- doped											
50 K	1848	2424	3255	57	152	4654	5933	1287	4553	10,463	2899
100 K	1959	2591	3254	56	157	4655	5929	1299	4536	10,467	2881
200 K	1915	2120	3244	65	164	4632	5934	1264	4567	10,457	2922
300 K	1973	2155	3230	66	186	4660	5930	1298	4545	10,467	2890
C: most doped											
100 K	2426	3852	4425	0	135	2478	6260	1801	4798	10,880	4207
200 K	2411	3363	4408	0	140	2500	6253	1825	4790	10,873	4205
300 K	2368	2858	4365	0	146	2502	6254	1792	4791	10,857	4203
C': de- doped											
100 K	2051	2223	2918	20	120	4113	5964	1190	5033	10,477	3502
200 K	2286	2373	2931	20	128	4114	5948	1177	5080	10,444	3552
300 K	2635	2561	2936	20	139	4269	5965	1234	5078	10460	3520

The peak of the optical conductivity at low frequencies ($\sim 100 \text{ cm}^{-1}$ or 10 meV) in the thicker heat-treated sample cannot be well fitted by a Drude free carrier response alone; hence, a Lorentz oscillator is also required at this frequency range. The Drude

Table 6.3: Drude-Lorentz fit parameters for the optical conductivity of each sample for the high-frequency oscillators (where $\epsilon_\infty = 1.04$).

Sample	State	ω_{p4}	ω_4	γ_4
250 nm:	doped	22,351	30,000	31,000
	de-doped	33,300	35,000	53,400
150 nm:	doped	22,000	34,000	40,000
	de-doped	39,800	47,000	64,000

component originates from the truly metallic carbon nanotubes in the films, while the Lorentz component is attributed to the curvature induced energy gap, or a mean value of energy gaps of semi-metallic tubes of different diameter and chirality. For the thinner heat-treated sample, the best fit was accomplished by the use of two Drude components of different damping constants. However, if we had data below the measured range, i.e., 30 cm^{-1} and the conductivity peak was indeed red shifted, then maybe one Drude and one Lorentz component would provide a better fit for this sample too. Because we have no data at lower frequencies to support this assumption, we keep the two Drude contributions for sample C'. Finally, no evidence of a bundle induced pseudogap in metallic carbon nanotubes was seen in our samples ($\sim 800 \text{ cm}^{-1}$ or 100 meV), as this effect was observed elsewhere [87].

The effect of doping can also be seen if we follow the changes in the fitting parameters between the as-prepared (purified) and the heat-treated samples. Upon hole doping of the samples the intensity of the first two peaks, Drude and Lorentz for samples A and B and two Drude components for C and C' are increasing, while at the same time the intensity of the next two peaks, which correspond to the S1 and S2 electronic transitions for semiconducting tubes are decreasing. This change is consistent with the theory, where a redistribution of the oscillator strength in the nanotubes is expected upon doping of the semiconducting nanotubes in the films. Hence, the free carrier density increases and consequently the low frequency absorption and the conductivity

increase too, whereas the intensity of the transitions between the van Hove singularities is decreasing.

Figure 6.16 shows the room temperature absorption coefficient of the films in the as-prepared and heat treated states. At low frequencies, the absorption of the as-prepared (purified) samples is considerably higher than the heat-treated samples and very broad, while at higher frequencies the situation reverses, as is expected. The first van Hove singularity peak, which corresponds to the S1 transition in the semiconducting nanotubes is much stronger in the heat-treated than the as-prepared (purified) samples. The difference in the absorption of the peaks that correspond to the S2 and M1 transitions in the semiconducting and metallic nanotubes respectively, between the doped and un-doped samples is smaller. At high frequencies, above $\sim 20,000 \text{ cm}^{-1}$, the absorption due to π -electron excitation begins to show. This absorption extends to much higher frequencies than the measured range presented here.

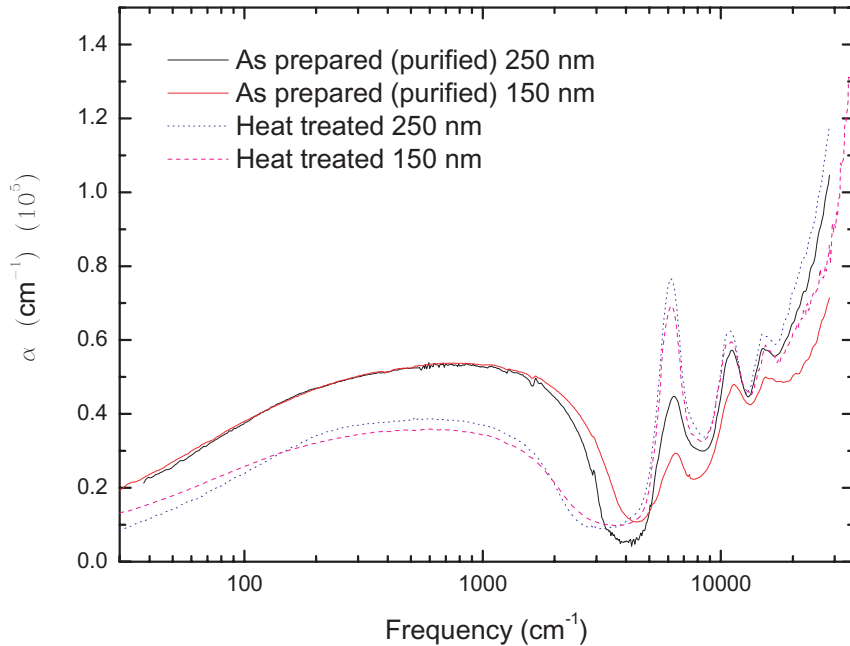


Figure 6.16: Room temperature absorption coefficient of two SWNT free-standing SWNT films of different thicknesses in as-prepared (purified) and heat-treated states.

6.2.4 Infrared Spectral Weights

The effective number of carriers N_{eff} per formula unit participating in optical transitions below frequency ω is given by:

$$N_{\text{eff}}(\omega) \frac{m}{m^*} = \frac{2mV_{\text{cell}}}{\pi e^2} \int_0^{\omega} \sigma_1(\omega') d\omega' \quad (6.28)$$

where m^* is the carrier effective mass and V_{cell} is the volume occupied by one formula unit. Here, based on the experimental density results where the density of this material was determined to be 0.4 g/cm^3 [F. Borondics et al. unpublished results 2005], the volume V_{cell} is taken to be 50 \AA^3 .

The results for the partial sum rule for σ_1 for our samples are shown in Figures 6.17 and 6.18. Both groups of samples, as-prepared (purified) and heat-treated show the same trends. The plateau value around 1000 cm^{-1} provides a good estimate of the low energy spectral weight of the metallic carriers. The larger number of free carriers in the as-prepared (purified) samples is quite obvious. The near agreement of the two curves in both figures at higher densities indicates that the doping reduces the intensity of the energy band gap transition of the semiconducting nanotubes and transfers weight to the far infrared region. This effect was seen above as a redistribution of the oscillator strength in the semiconducting nanotubes. Upon hole doping the oscillator strength corresponding to the energy band gap transition S1 is decreasing due to the decreasing electron concentration in the valence band, while at the same time there is an increase of the free carrier oscillator strength.

6.2.5 Conclusions

In conclusion, transmittance measurements have been performed on high quality free-standing SWNT films of different thicknesses over a wide frequency, $30 - 30,000 \text{ cm}^{-1}$ ($4 \text{ meV} - 4 \text{ eV}$), and temperature, $50 \text{ K} - 300 \text{ K}$, range. Room temperature transmittance spectra were initially obtained for as-prepared (purified) and after vacuum annealing (baking) samples and the effect of doping was studied. The last step of the purification

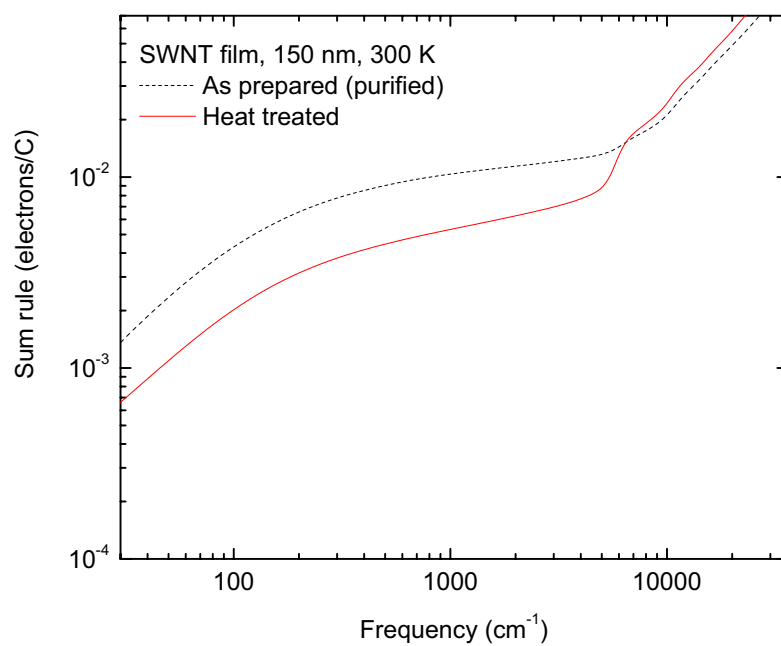


Figure 6.17: Room temperature sum rule for as-prepared (purified) and heat-treated samples of 150 nm thickness.

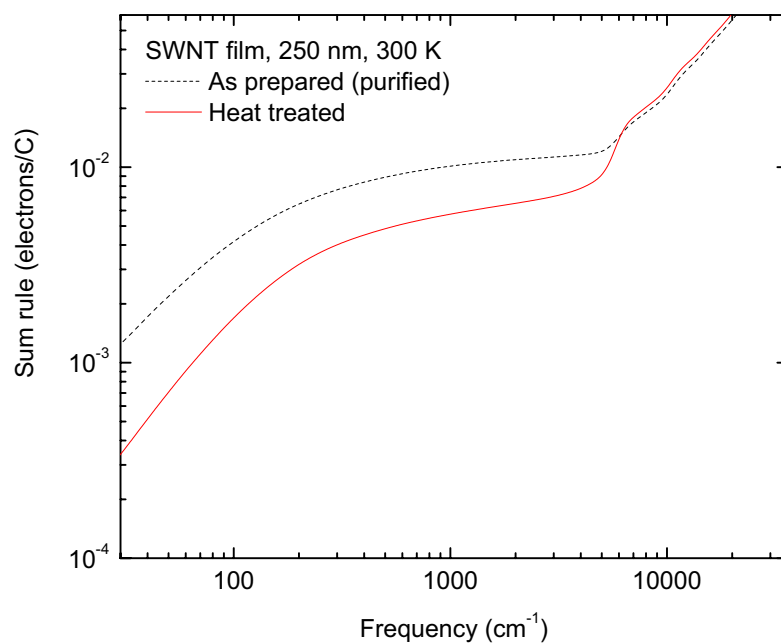


Figure 6.18: Room temperature sum rule for as-prepared (purified) and heat-treated samples of 250 nm thickness.

process, acid treatment (HNO_3), which removes metal catalyst particles and amorphous carbon that have been introduced in the films during synthesis, leaves the semiconducting carbon nanotubes hole doped. These samples exhibit increased metallic absorption in the far infrared region and decreased interband transitions in the near infrared and visible regions, due to nitrate doping. This effect, shifts the spectral weight from the first van Hove transition into the infrared region. Heat treatment of the purified samples removes the nitrate dopants, and hence de-dopes the films.

The vacuum annealed films are considered to be closest to pristine carbon nanotubes and thus, provide us the opportunity to study the truly metallic and small band gap semiconducting carbon nanotubes. Therefore, the far infrared spectroscopy can serve as a complimentary method, for example, to fluorescence experiments, helping researchers to acquire a more complete understanding of this unique system.

By Kramers-Kronig analysis of the transmittance data, the optical constants, optical conductivity and absorbance, as well as the partial sum rule for the conductivity of the free-standing carbon nanotubes were obtained. The results of this analysis for samples of different thicknesses and in different states, doped and un-doped, support the theoretical predictions very well. In addition, a gap feature below 10 meV that was observed in one of the samples was attributed to the curvature induced band gap of semiconducting nanotubes. Finally, no evidence were found of a bundle induced pseudogap in metallic carbon nanotubes in our samples, as this effect is theoretically predicted and has been observed elsewhere at $\sim 800 \text{ cm}^{-1}$ or 100 meV [87].

CHAPTER 7 TRANSMISSIVE/ABSORPTIVE EC DEVICES

A transmissive/absorptive electrochromic (EC) device exhibits reversible switching of an EC material between a transmissive (bleached) and a colored (absorptive) state on a transparent conducting substrate. The construction of a transmissive/absorptive device that operates not only throughout the visible but in the infrared region also had been impossible until now due to the absence of a suitable, infrared transparent, conducting material. We built the first transmissive/absorptive device using SWNT films as the conducting surfaces. The extensive study on carbon nanotubes as free-standing films that was described in Chapter 6 showed that these films have the highest transmittance (around 90% for thicknesses between 50-350 nm) of any transparent conductor in the 2-5 μm spectral range for very low sheet resistance (resistivity of $1.5 \times 10^4 \Omega\text{-cm}$ [90]).

7.1 Sample Preparation

7.1.1 Purification of Laboratory Chemicals and Materials

In order to avoid the introduction of water in the EC cells (O-H stretching mode around 3500 cm^{-1} or $2.85 \mu\text{m}$) the preparation and the assembly of the device have taken place in the dry box under argon (Ar) environment. Since the controlled environment in the dry box is sensitive to water, it is crucial that solvents and electrolytes employed were adequately dry. The following procedures have been used before the chemicals were placed inside the dry box:

- Acetonitrile (ACN) purchased from Aldrich in Sure Seal[®] was distilled (at atmospheric pressure under Ar) over calcium hydride (CaH_2) and then it was freeze-pump-thawed over liquid nitrogen (LN_2) for three cycles. Finally, activated molecular sieves were added to the solvent to remove any residual water.

- Propylene carbonate (PC) purchased from Aldrich in Sure Seal[®] was dried by running through a column of activated alumina and fractionally distilled under vacuum with the middle fraction collected. Then, PC was freeze-pump-thawed over liquid nitrogen (LN₂) for three cycles. Finally, activated molecular sieves were added to the solvent to remove any residual water.
- Tetrabutylammonium perchlorate (TBAP) purchased from Aldrich was recrystallized from isopropanol and dried over phosphorus pentoxide (P₂O₅) for about 48 hours. Then, it was stored under vacuum for 24 hours.
- Poly (methyl methacrylate) (PMMA) purchased from Aldrich was stored in a desiccator under vacuum or argon for about 48 hours.
- 3,4-ethylenedioxythiophene (EDOT) commercially available was distilled under vacuum over calcium hydride (CaH₂) and then it was freeze-pump-thawed.
- 2,5-bis(2-ethylenedioxythienyl)-dihexyl-pyridopyrazine (BEDOT-Hx₂-Pyr-Pyr) synthesized by Prof. J. R. Reynolds' group was stored in a desiccator under vacuum or argon for about 24 hours.
- Lithium bis(trifluoromethane-sulfonyl)imide (Li[N(CF₃SO₂)₂]) purchased from 3M was used as received.
- Single Wall Carbon nanotubes (SWNTs) on plastic (PET-polyethylene terephthalate) provided by Prof. Rinzler's group, and gold on KaptonTM commercially available were used as received.
- Indium-Tin-Oxide (ITO) on glass slides purchased from Delta Technologies were sonicated for 5 minutes first in distilled water and then in acetone to remove any inorganic and organic residue respectively. Slides were dried in air.

Chemicals and electrodes were placed in the antechamber of the dry box and pumped for three cycles of 45 minutes each with an exception of the lithium based salt, which is pumped overnight.

7.1.2 Electrode Preparation

Different electrodes were used for the fabrication of the transmissive/absorptive EC devices studied in this chapter. The working electrode in all the devices consists of a carbon nanotube film ($60\text{ nm} \pm 10\text{ nm}$) on plastic (PET) substrate. The production of the highly uniform, optically transparent and electrically conductive pure single wall nanotubes (SWNT) films was described in the previous chapter. For electrical contact, palladium (Pd) metal ($50\text{ - }60\text{ nm}$) is sputtered across one end of the nanotube film. The work functions of carbon nanotube and palladium are very close, thus a contact with ohmic-like behavior is expected to occur between them.

Indium-Tin-Oxide (ITO) coated glass slides have also been used in some cases, only for comparison reasons in order to enhance our understanding of the new electrodes in the electrochromic devices. Another electrode that was also used consists of gold (100 nm) coated kapton sheet that is commercially available. In this electrode a punched hole of $3\text{ - }4\text{ mm}$ diameter was made on it, so that the light beam could go through the device and thereby, transmittance measurements to be obtained. The hole can be sealed with an infrared transmissive window, which can be plastic (PET) or Zinc Selenide (ZnSe).

7.1.3 Electrochemical Polymerization

The electrochemistry is performed using an EG&PAR model 273A potentiostat/galvanostat. The polymer films used for the devices were prepared potentiostatically at potentials slightly over the monomer onset. The three electrode configuration used for the film deposition consists of a working electrode (WE), which in our case is one of the three electrodes mentioned above, SWNTs/PET, gold/kapton or ITO/glass; a platinum (Pt) flag as the counter electrode (CE); and a silver wire (Ag) as the pseudo-reference electrode (RE). The pseudo-reference silver wire (Ag) is calibrated versus ferrocene/ferrocenium (Fc/Fc^+) by dissolving ferrocene in the electrolyte solution, 5 mM ,

and determining the $E_{1/2}$ ¹ of the ferrocene/ferrocenium (Fc/Fc⁺) against the silver wire, in order to report the applied voltage versus a standard reference.

Electrochemical polymerization is carried out in a monomer electrolyte solution, initially containing the monomer EDOT (10mM), in TBAP (0.2 M) and PC, at constant potential, +1.26 V vs Fc/Fc⁺. ACN can also be used as a solvent for the SWNTs/PET electrode, but not for the gold on kapton electrode because in ACN the kapton support swells and curls during polymerization. The polymer films deposited using this method were within 150-200 nm range. The thickness of the films was controlled by monitoring the charged density passed during electrosynthesis. After the polymer growth, the polymer-coated electrodes were removed from the monomer solution and rinsed with solvent, in this case PC. The films at this stage are p-doped and they can be neutralized by the application of a proper voltage in monomer free solution; TBAP (0.2 M) and PC.

Same type of electrochemical polymerization has taken place for the deposition of another monomer, the BEDOT-Hx₂-Pyr-Pyr, that has also been used in the transmissive/absorptive devices. The monomer electrolyte solution contains the monomer BEDOT-Hx₂-Pyr-Pyr (10 mM), in TBAP (0.1 M), ACN and DCM (dichloromethane or CH₂Cl₂) with weight ratio of 1:1, at constant potential +1.21 V vs Fc/Fc⁺. Although most of conjugated polymers are stable only in their p-doped state, this particular polymer, PBEDOT-Hx₂-Pyr-Pyr, has the ability to form a stable n-doped state in addition to the p-doped state along the polymer backbone. This offers us the possibility of using the same polymer on both electrodes in a EC transmissive/absorptive device, in which both films will be in their neutral state at the same time and upon the application of a voltage, one will form a n-doped state and the other one a p-doped state. The resulting

¹ $E_{1/2}$ is the potential at which the concentrations of the oxidized and reduced species are equal, and $E_{1/2} = E$, where $E = E^0 + \frac{RT}{nF} \ln \frac{\alpha_{oxid}}{\alpha_{red}}$ (Nernst equation for the half reaction) where E^0 is the standard electrode potential, R is the universal gas constant, T is the temperature (K), n is the number of electrons transferred in the half-reaction, F is the Faraday constant, and $\alpha_{oxid}, \alpha_{red}$ are the chemical activities on the reduced and oxidized side, respectively. The $E_{1/2}$ for a reversible cyclic voltammogram can be calculated from $E_{1/2} = (E_{pa} + E_{pc})/2$, where E_{pa} and E_{pc} are the anodic and cathodic peak potentials respectively.

color of the device in the latter case will be the combination of the two colors of the polymer films in the different doped states.

Figure 7.1 depicts the chemical structures of the two polymers used in the EC devices in this chapter, and their colors upon oxidation and reduction.

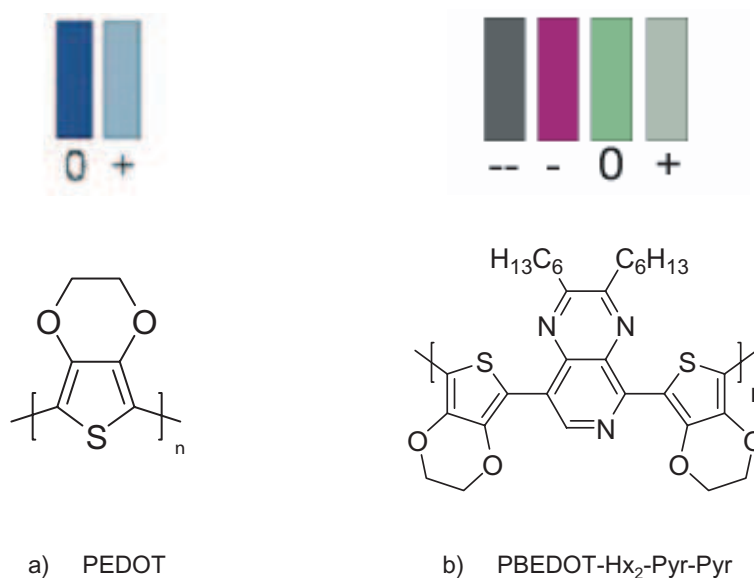


Figure 7.1: Chemical structures of a) poly-3,4-ethylenedioxythiophene (PEDOT) and b) poly-2,5-bis(2-ethylenedioxythienyl)-dihexyl-pyrido-pyridine (PBEDOT-Hx₂-Pyr-Pyr), and their colors upon oxidation and reduction.

7.1.4 Gel Electrolyte Preparation

An important component in electrochromic devices is the supporting electrolyte, which serves as the ion transport medium. The conductivity of the electrolyte and the ion's ability to move in and out of the electroactive polymer films are two things that should be taken into account for the formulation of the gel. Although the electrolytes should be ionically conductive, at the same time they should electronically insulating in order to prevent shorts between the two electrodes. Furthermore, for a gel electrolyte to be suitable for use in transmissive/absorptive EC devices, transparency is also a requirement.

The preparation of the gel has taken place in a dry environment in order to yield a water-free electrolyte. The electrolyte gel that has been used in our devices consisted

of four chemical components ACN:PC:PMMA:Li[N(CF₃SO₂)₂] with weight ratio of 70:20:7:3. In this gel, the solid polymer matrix of PMMA provides dimensional stability of the electrolyte, whereas the high permittivity of the solvents enables extensive dissociation of the salt and minimizes the ion-pairing.

The mixing procedure of these four chemical components is the following. The acetonitrile (ACN) was put in a glass container on a heated plate and stirred vigorously. After about ten minutes, the salt Li[N(CF₃SO₂)₂] was added. Upon dissolution of the salt, the addition of poly (methyl methacrylate) (PMMA) followed. The latter component is not easily dissolved, so it was stirred and heated at 60 °C on the plate for about two hours. During that time the ACN evaporated. As soon as the PMMA was dissolved, propylene carbonate (PC) was introduced to the medium and when the mixture had a viscous consistency, after about two more hours of stirring and heating, it was either stored under argon (Ar) environment, or used in a device. This type of gel electrolyte in addition of being the ion transport medium, it also encapsulates the EC device. At the edges of the device, the ACN evaporates leaving behind the PMMA which becomes insoluble. This process minimizes further solvent evaporation and prevents leaking.

7.2 PEDOT on SWNT Electrodes

7.2.1 Spectroelectrochemistry of PEDOT

Spectroelectrochemistry is a very important method for probing the electronic structure of conducting polymers and for providing information, through the optical changes that occur upon doping or de-doping, about the material's band gap and intraband transitions. Measurements were carried out with a StellarNet UV/VIS-NIR Spectrophotometer using the same three-electrode configuration described above. This configuration allows the application of different potentials while monitoring the transmission/absorption spectra. The polymer-coated electrodes were placed in a monomer free solution TBAP/PC, and different voltages were applied while a spectrum in the near infrared or visible region was obtained.

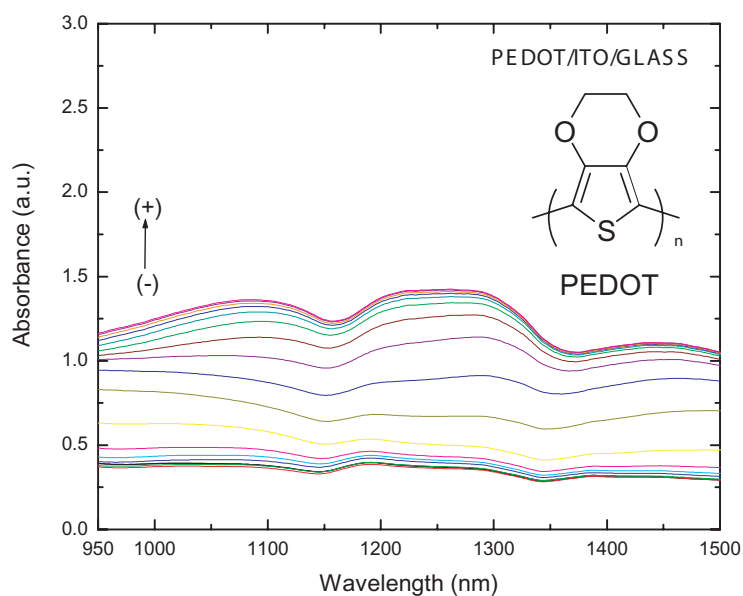


Figure 7.2: Absorption measurements of PEDOT on ITO/glass in the near infrared region (NIR) at applied voltages within the range from -0.7 V to +1.0 V vs Ag.

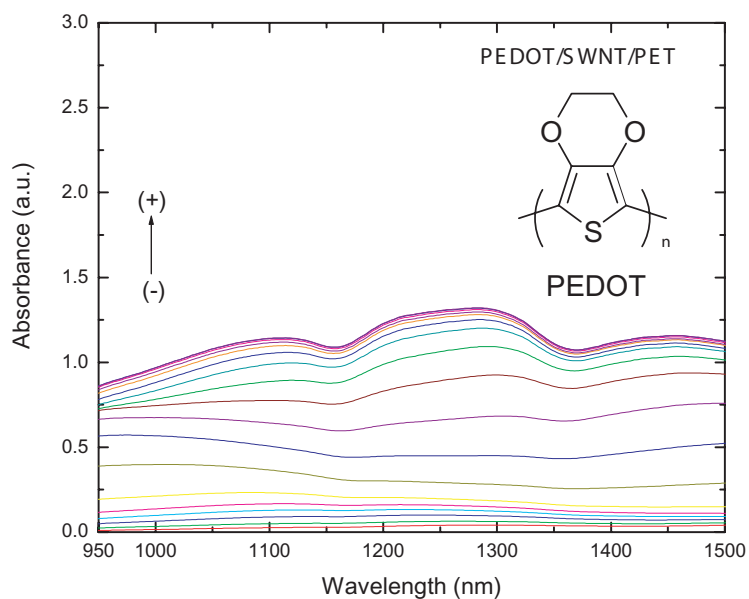


Figure 7.3: Absorption measurements of PEDOT on SWNTs/PET in the near infrared region (NIR) at applied voltages within the range from -0.7 V to +1.0 V vs Ag.

Before the carbon nanotube films were used to build EC devices, we wanted to study their suitability as electrodes for this specific type of devices. For this reason,

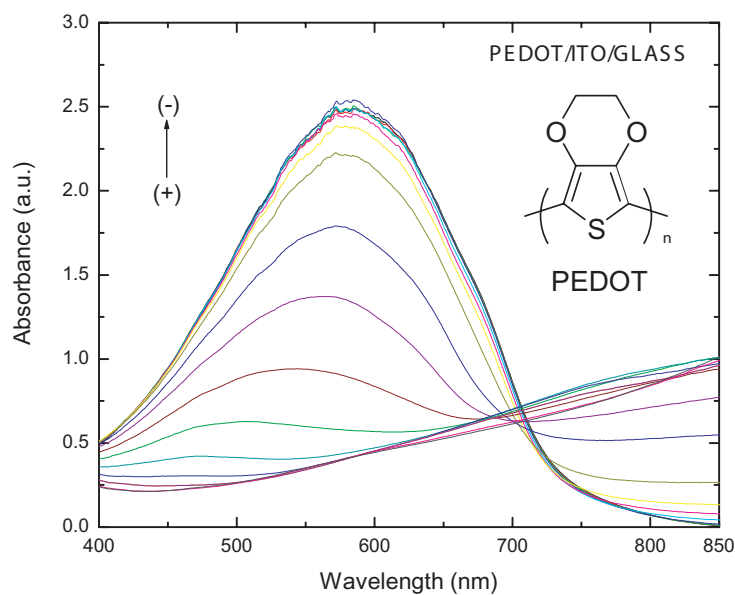


Figure 7.4: Absorption measurements of PEDOT on ITO in the visible region (VIS) at applied voltages within the range from -0.7 V to +1.0 V vs Ag.

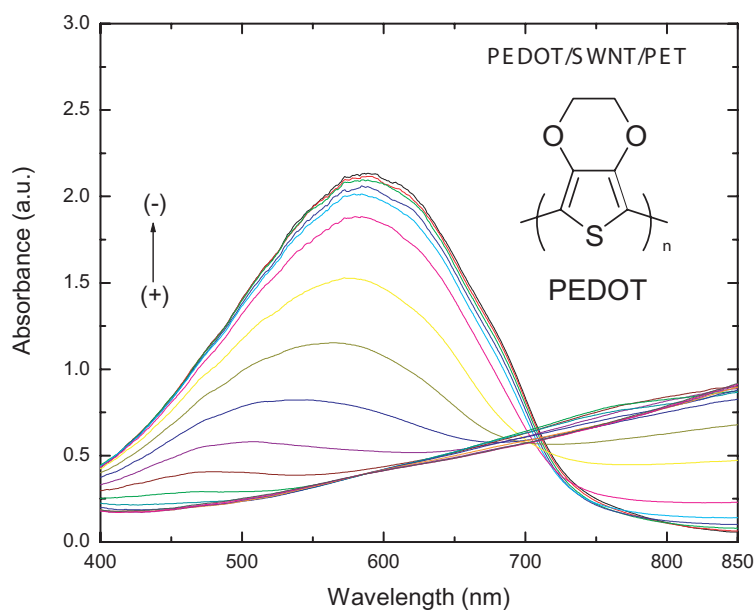


Figure 7.5: Absorption measurements of PEDOT on SWNTs/PET in the visible region (VIS) at applied voltages within the range from -0.7 V to +1.0 V vs Ag.

a polymer film was electrodeposited on a carbon nanotube electrode, and the electrochromic changes of the polymer were monitored at different applied voltages in the

near infrared and visible regions. For comparison, the same type of measurements were performed on the ITO/glass electrode, which has been extensively studied and widely used in EC devices. The polymer chosen for this experiment is PEDOT, the electrochromic behavior of which on ITO/glass is very well known [78].

Two films of PEDOT were prepared electrochemically on the two different substrates, and their absorption was monitored at different voltages. Figures 7.2 through 7.5 show the transmission/absorption spectra for near infrared and visible regions of the PEDOT on ITO/glass electrode and the PEDOT on the new carbon nanotube/plastic (SWNTs/PET) electrode at a voltage range from -0.7 V to +1.0 V.

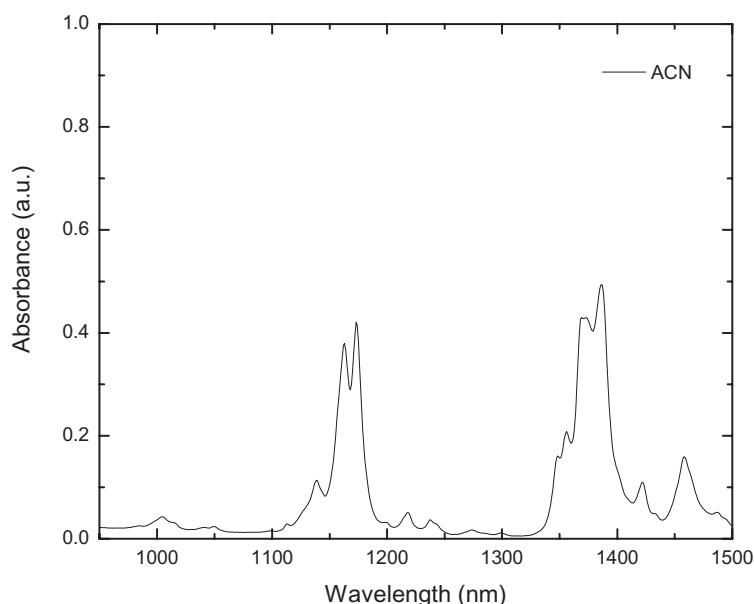


Figure 7.6: Absorption measurements of acetonitrile in the near infrared region (NIR).

These figures show that the behavior of the carbon nanotube film is very similar to that of the widely used ITO film. Therefore, the carbon nanotube films can be used as the conductive layer in EC devices. The difference in the absorption between the film on the different electrodes could be either due to the fact that the PEDOT film on the ITO/glass electrode is a little bit thicker than the PEDOT film on SWNTs/PET electrode, or due to the different values of the work function of ITO and carbon nanotubes. In order to

be able to determine what other factors might be responsible for this difference, further investigation is needed.

The dips in the near infrared region, at ~ 1170 nm and ~ 1370 nm are due to ACN absorption, as can be seen from Figure 7.6, and they were consistent in all the absorption measurements performed in solution. These dips, which in some other measurements appear as peaks are due to the systems deficiency to subtract the background absorbance correctly.

7.2.2 Thickness Determination of PEDOT on SWNT Electrodes

The thickness of the electrochemically grown PEDOT films was determined by the amount of charge passed during the potentiostatic growth of the polymer. By measuring the polymer film thickness on ITO/glass electrode with a technique such as profilometry, a calibration plot can be made, which would provide an accurate connection between the amount of charge passed during the growth and the resulted film thickness. Therefore, for our experiments we needed to check if the same parameters used for carbon nanotube electrodes would result in the same polymer thickness, or if a similar calibration plot was needed to be made.

Due to the porous morphology of the carbon nanotube films (bigger surface area), the deposition time for the same amount of charge was much less for them when compared with the deposition time on ITO because the deposited polymer does not grow only on top of the electrode surface but in between the nanotube bundles too due to the presence of voids. However theoretically, since the same amount of charge is passed during the polymer growth on both electrodes, the resulted film thickness should be the same. Experimentally though, since a simple profilometry measurement that would verify this assumption could not be performed due to the very rough surface of the nanotube films and their porous nature, another method had to be found. Therefore, the determination of the film thickness was obtained through spectroscopic measurements and, the analysis and fit of the data using the Drude-Lorentz model.

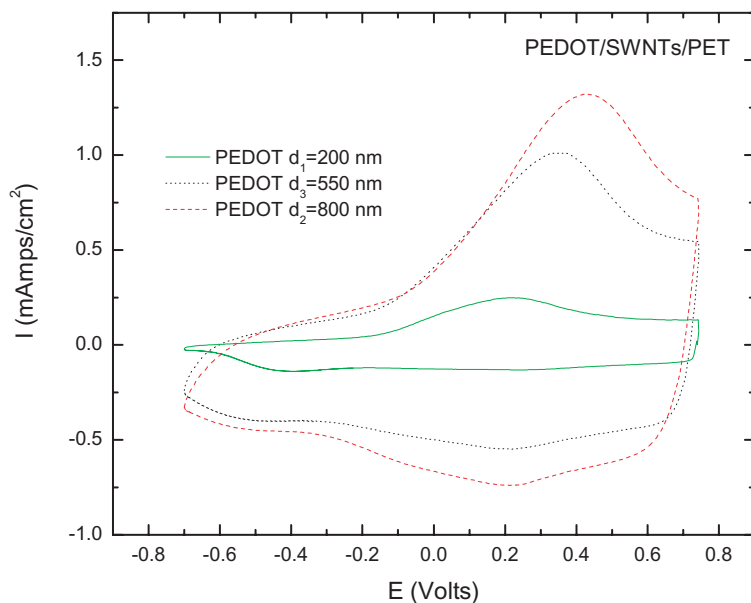


Figure 7.7: Cyclic voltammetry measurements of three films of different thicknesses ($d_1 \sim 200$ nm, $d_3 \sim 550$ nm, and $d_2 \sim 800$ nm) of PEDOT on SWNTs/PET in solution, at applied voltages from -0.70 V to $+0.75$ V vs Ag.

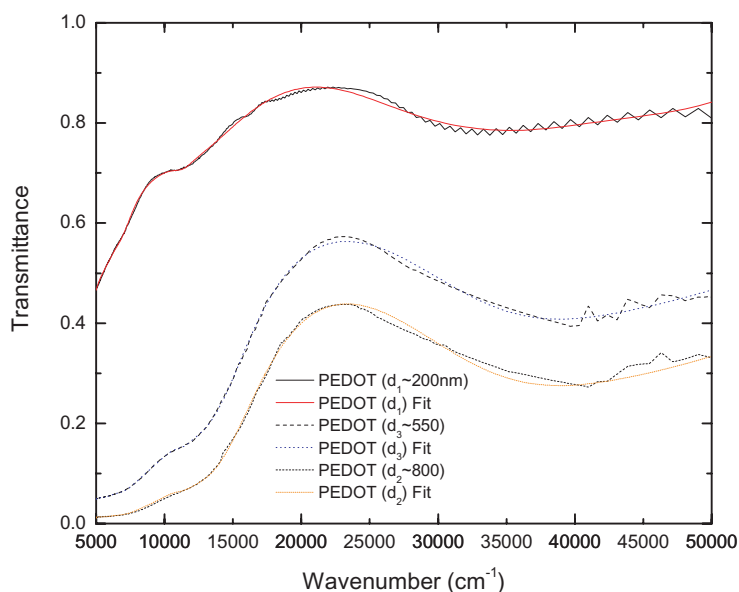


Figure 7.8: Transmittance measurements of three films of different thicknesses ($d_1 \sim 200$ nm, $d_3 \sim 550$ nm, and $d_2 \sim 800$ nm) of PEDOT on SWNTs/PET in p-doped state, from mid-infrared to ultraviolet region.

For these measurements, three PEDOT films of different thicknesses were grown potentiostatically on SWNTs/PET under the same conditions except the amount of the

deposited charge. The cyclic voltammograms of the three films are shown in Figure 7.7, where can be seen that the anodic and cathodic currents increase with the increase of the polymer thickness.

The results of the transmittance measurements that were performed on these samples, p-doped PEDOT films of different thicknesses, from the near infrared to the ultra-violet region and the Drude-Lorentz based modeling that was performed are shown in Figure 7.8. The parameters used to fit all three samples are given in Appendix B and are all the same except the thickness parameters that were left free to adjust. The results that we obtained from this study led us to the conclusion that for the same amount of charge the “optical” thickness of the resulting film is the same for both electrodes, SWNTs and ITO. Therefore, the same calibration plot could be used.

7.2.3 Atomic Force Microscopy (AFM) Images

Figures 7.9 and 7.10 show AFM images of the SWNTs/PET electrode substrates before and after the electrochemical growth of PEDOT films of different thicknesses.

In more detail, the left hand side image of Figure 7.9 shows a 50 nm SWNTs on PET film. The carbon nanotubes, which can be clearly seen in this image, form into bundles and are randomly distributed over the film surface. Although there are a lot of voids, which reveal the microporous nature of the carbon nanotube films there is enough overlapping to ensure good conductivity over the whole surface of the film. The right hand side image in this figure shows a 200 nm PEDOT film grown on the 50 nm SWNTs on PET substrate. One thing that should be noticed is that the carbon nanotubes are not visible any more after the polymer growth, and therefore a 200 nm polymer film thickness covers adequately the voids between the nanotube bundles, and the electrode surface. The polymer surface of the 200 nm film thickness appears not to be very smooth due the formation of islands.

Figure 7.10 shows a 50 nm SWNTs on PET film in a different scale in comparison with Figure 7.9. The carbon nanotube film of this figure has the same characteristics as described above. The right hand side image in this figure shows a much thicker, 500 nm,

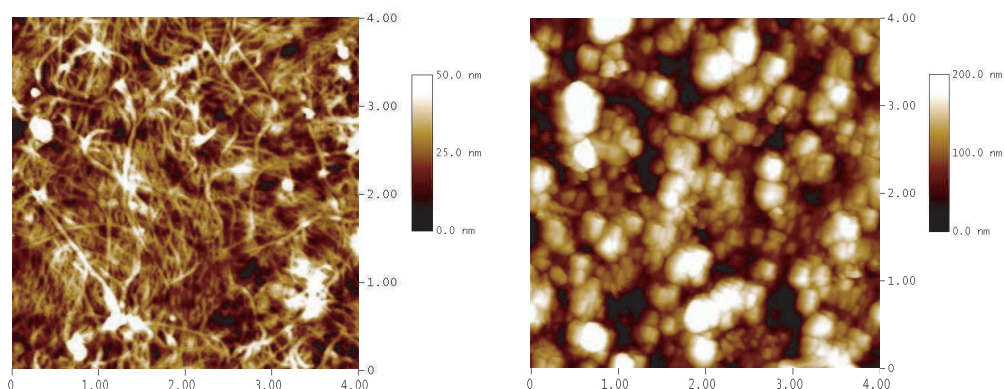


Figure 7.9: AFM images of a 50 nm SWNTs/PET electrode (left hand side) and a 200 nm PEDOT film grown electrochemically on a 50 nm SWNTs/PET electrode.

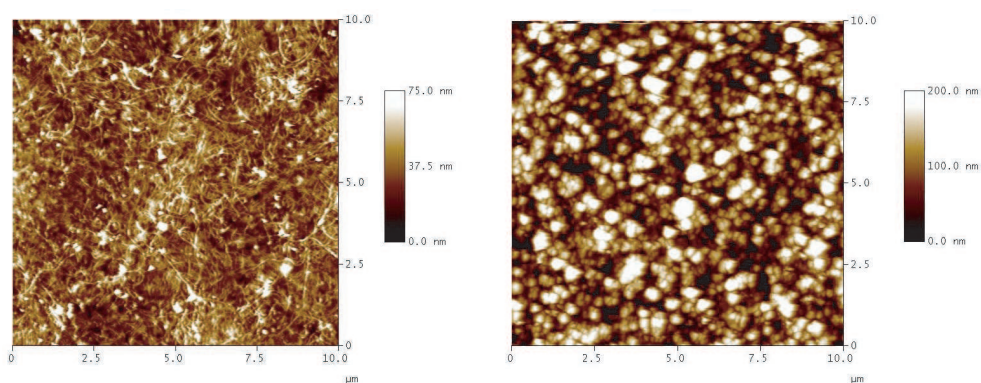


Figure 7.10: AFM images of a 50 nm SWNTs/PET electrode (left hand side) and a 500 nm PEDOT film grown electrochemically on a 50 nm SWNTs/PET electrode (right hand side). Notice that the scale is different compared to the previous image.

PEDOT film grown on the 50 nm SWNTs/PET substrate. After the electrochemical growth of the polymer film, the carbon nanotubes are not visible any more, and the polymer surface of the 500 nm film thickness appears to be a lot smoother compared to the surface of the 200 nm PEDOT film. Therefore, as the polymer thickness increases the surface becomes smoother.

7.3 PBEDOT-Hx₂-Pyr-Pyr on SWNT Electrodes

7.3.1 Cyclic Voltammetry of PBEDOT-Hx₂-Pyr-Pyr

Cyclic voltammetry of an electroactive polymer film is often accompanied by a capacitive current which broadens the anodic and cathodic peaks due to the microporous nature of some films [57]. Electroactive films presented in this work can be reversibly cycled between neutral and doped states in a non-aqueous solution. PEDOT is reversibly cycled between neutral and p-doped states, whereas PBEDOT-Hx₂-Pyr-Pyr can be reversibly cycled between neutral and p-doped states, as well as between neutral and two n-doped states. However, while its first reduction at $E_{pa} = -1.52$ V (vs SCE) is easily accessible and reversibly, the second one at $E_{pc} = -2.10$ V (vs SCE) appears to be unstable.

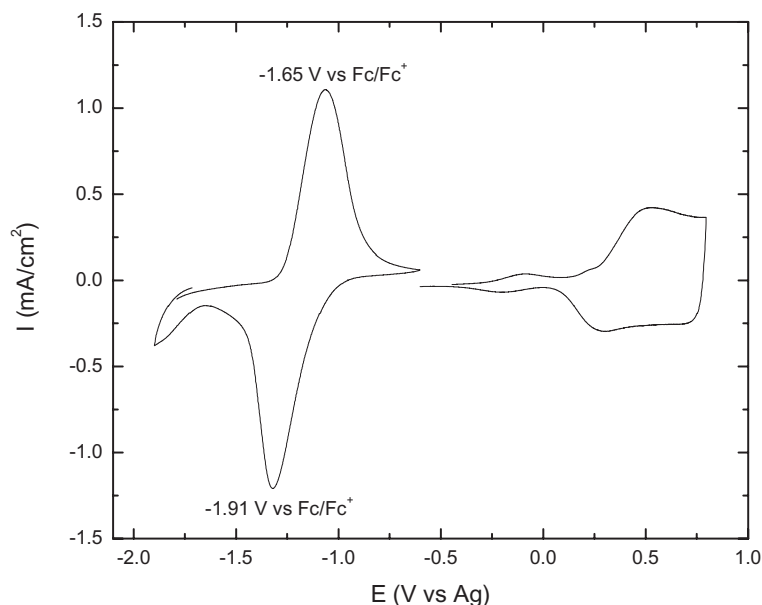


Figure 7.11: Cyclic voltammogram of the oxidation and the first reduction of PBEDOT-Hx₂-Pyr-Pyr on ITO/Glass.

Figure 7.11 shows the cyclic voltammogram of the oxidation and the first reduction of PBEDOT-Hx₂-Pyr-Pyr on ITO/Glass in solution. PBEDOT-Hx₂-Pyr-Pyr is one of the few polymers capable of forming a p-doped state as well as a stable n-doped state. The n-doped state of electroactive polymers is usually not stable due to the high

reactivity of of the anion charge carrier to oxygen and water. There are two reduction states that this polymer can form from which the second² one is not very stable.

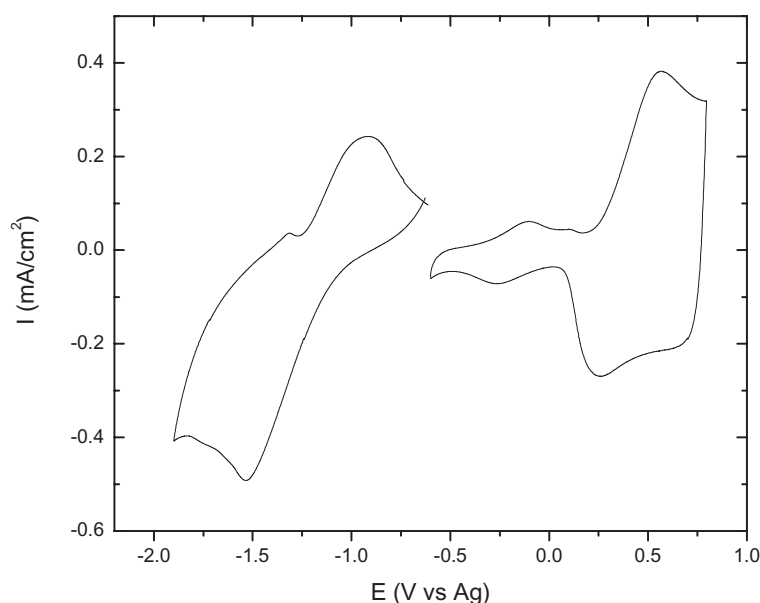


Figure 7.12: Cyclic voltammogram of the oxidation of PBEDOT-Hx₂-Pyr-Pyr on SWNTs/PET.

Figure 7.12 shows the cyclic voltammogram of the oxidation of PBEDOT-Hx₂-Pyr-Pyr on SWNTs/PET in solution. The two plots follow the same trends, with the current being slightly smaller for the carbon nanotube electrode. This is possibly due to the difference in the thickness of the polymer films grown on the two electrodes, since, although the same amount of charge has been used for the electropolymerization the area of the electrodes has not been matched and therefore, is different.³

7.3.2 Spectroelectrochemistry of PBEDOT-Hx₂-Pyr-Pyr

Two films of PBEDOT-Hx₂-Pyr-Pyr of approximately the same thickness were prepared electrochemically on ITO/Glass and SWNTs/PET substrates, and their absorptions in solution were monitored at different voltages, from neutral to oxidized states. Figures 7.13 through 7.16 show the transmission/absorption spectra for near infrared and

² A cyclic voltammogram of PBEDOT-Hx₂-Pyr-Pyr on ITO/glass in solution, where both reduction peaks, and also the color of the film at each state are shown, can be found in Appendix C.

³ The current density has been calculated using an area of 1 cm² and therefore the correct area of the electrodes has not been taken into account.

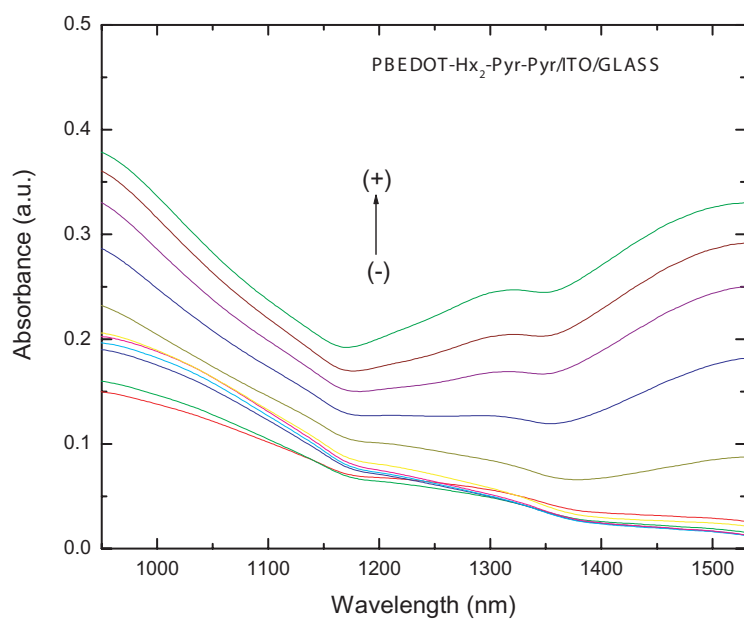


Figure 7.13: Absorption measurements of the oxidation of PBEDOT-Hx₂-Pyr-Pyr on ITO/glass in the near infrared region (NIR) at applied voltages within the range from -0.4 V to +0.8 V vs Ag/Ag⁺.

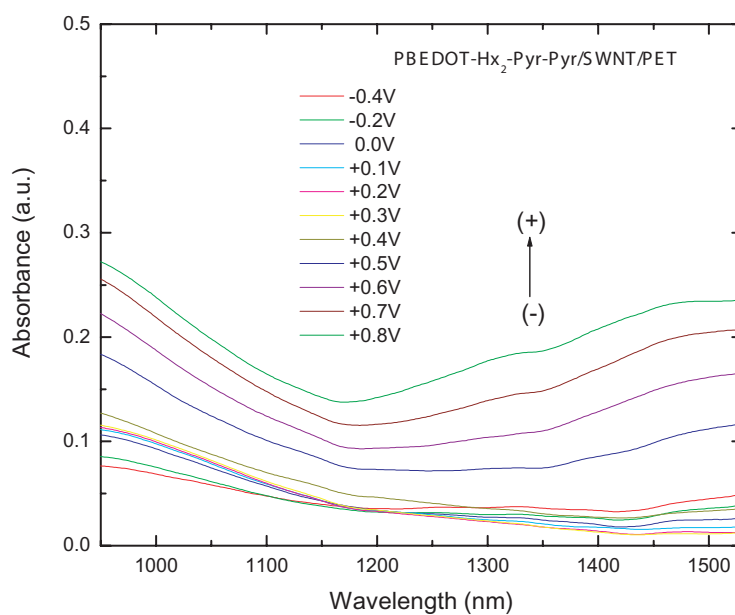


Figure 7.14: Absorption measurements of the oxidation of PBEDOT-Hx₂-Pyr-Pyr on SWNTs/PET in the near infrared region (NIR) at applied voltages within the range from -0.4 V to +0.8 V vs Ag/Ag⁺.

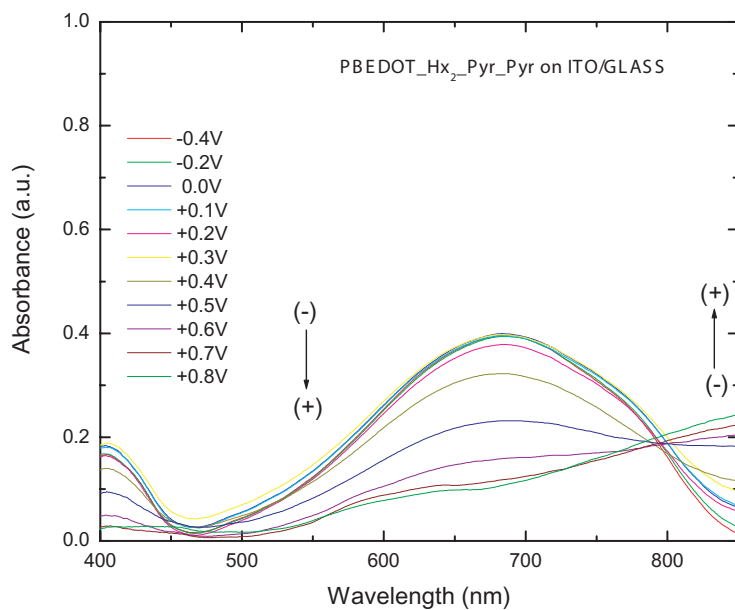


Figure 7.15: Absorption measurements of the oxidation PBEDOT-Hx₂-Pyr-Pyr on ITO in the visible region (VIS) at applied voltages within the range from -0.4 V to +0.8 V vs Ag/Ag⁺.

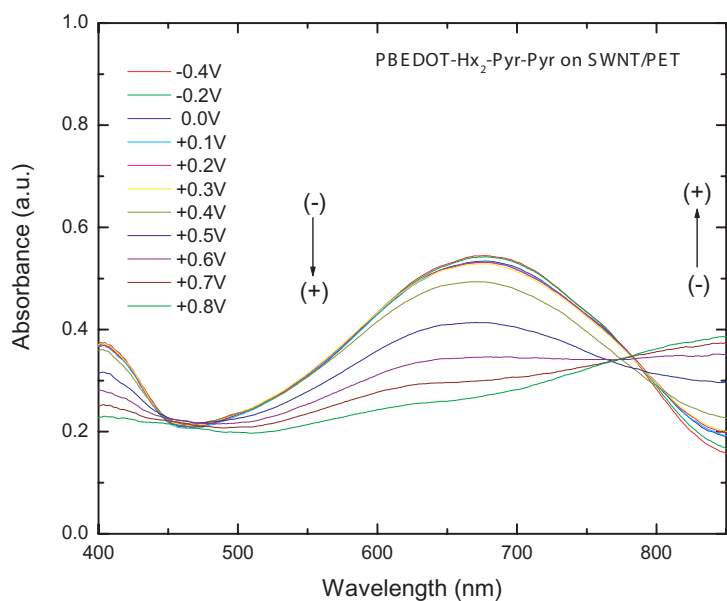


Figure 7.16: Absorption measurements of the oxidation PBEDOT-Hx₂-Pyr-Pyr on SWNTs/PET in the visible region (VIS) at applied voltages within the range from -0.4 V to +0.8 V vs Ag/Ag⁺.

visible regions of the PBEDOT-Hx₂-Pyr-Pyr at a voltage range from -0.4 V to +0.8 V. From these figures we see that the behavior of PBEDOT-Hx₂-Pyr-Pyr on SWNTs is very similar to that of the widely used ITO film. The difference in the absorption values between the different electrodes could be due to slightly differences in the thicknesses of the polymer films, or could be due to the different values of the work function of ITO and carbon nanotubes. In order to be able to determine on which factor or what other factors might be responsible for this difference, further investigation is needed.

7.4 Transmissive/Absorptive EC Device Construction

EC devices that operate in the transmissive/absorptive mode consist of two polymer films deposited on transparent electrodes (dual cells). The two polymer films are facing each other, separated by electrolyte gel and are simultaneously in their transmissive or absorptive states. As a result the device is respectively transparent, bleached, or colored. For preliminary studies of this type of devices, we constructed cells based on a slightly modified scheme. These modified cells will consist of six layers as shown in Figures ?? and 7.17. Starting from the top, the working electrode SWNTs on PET is coated with a PEDOT film (150-200 nm) in its p-doped state. The polymer has been electrochemically deposited as described above. The next layer is a separator paper soaked in electrolyte gel⁴ used to isolate the polymer film on the working electrode from the counter polymer layer. The counter electrode that follows, gold on kapton is coated with a PEDOT film (150-200 nm) in its neutral state and is facing the working electrode. In order for the light beam to go through this device, i.e., in order for transmission/absorption measurements to take place, a hole of a size of 3-4 mm has been punched on both the separator paper and the gold on kapton electrode. Therefore, during the electropolymerization, the counter polymer was grown around the hole on the gold/kapton electrode. Then, the hole can be sealed with an infrared transmissive window, either PET as the substrate of the working electrode or zinc selenide (ZnSe).

⁴ACN:PC:PMMA:Li[N(CF₃SO₂)₂] with weight ratio of 70:20:7:3.

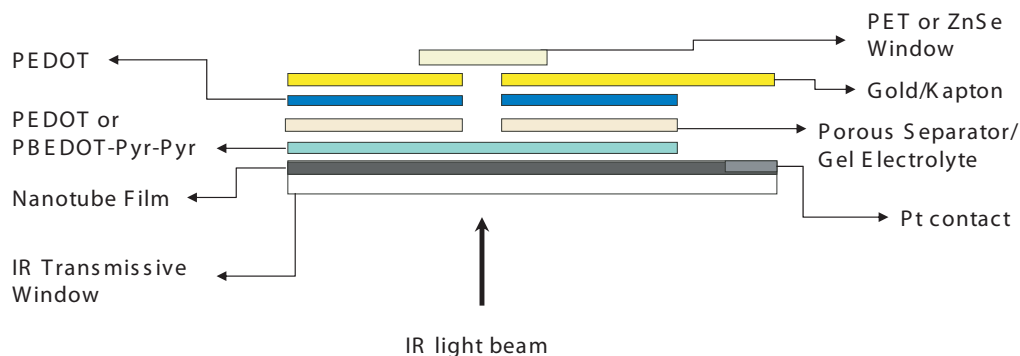


Figure 7.17: Side-view schematic diagram of the EC device (with hole) for transmittance measurements.

One thing that should be pointed out is that during the spectroscopic measurements, the light beam going through the device passes only through the working electrode polymer and thus, the data obtained from this devices depict the electrochromic changes of one polymer film. Otherwise, in case the CE electrode was transparent too, we would not be able to use PEDOT as a film on both electrodes since this polymer can access only a neutral and an oxidized state. This means that by changing the applied voltage, one film will be oxidized (bleached) and the other will be reduced (neutral-colored), and thus in a dual device no change in transmittance or absorbance would be recorded. Transmittance measurements were also obtained from a device of this type that uses PBEDOT-H_x2-Pyr-Pyr on both electrodes with the light beam going through only one of the films.

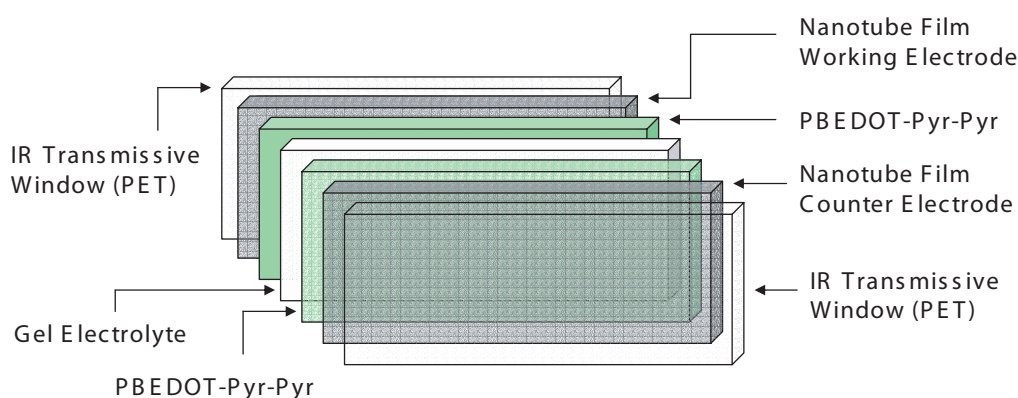


Figure 7.18: Front-view schematic diagram of Dual EC device.

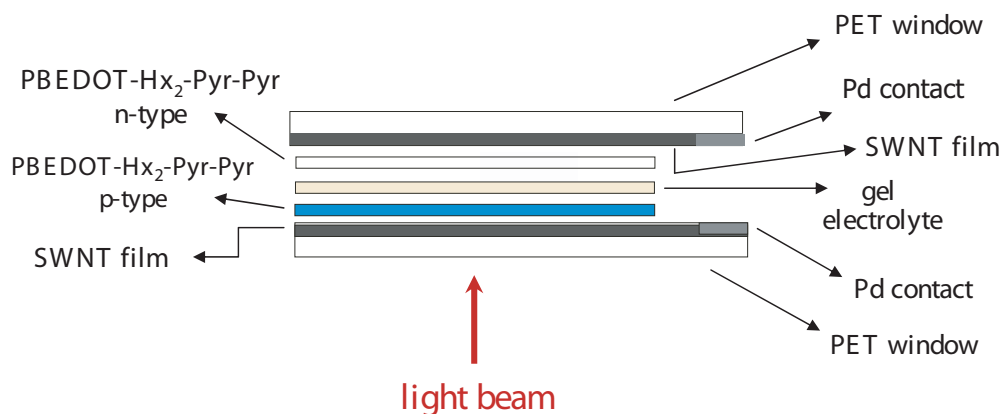


Figure 7.19: Side-view schematic diagram of the dual EC device for transmittance measurements.

The second type of devices that we constructed is depicted in Figures 7.18 and 7.19. This device consists of two PBEDOT-Hx₂-Pyr-Pyr (~ 300 nm) coated nanotubes films on PET electrodes, facing each other. The electrodes are separated by gel electrolyte. In this case, both electrodes are transparent, from the mid-infrared through the visible region and therefore, no holes are necessary. This particular polymer differs from PEDOT because it can access three different states: p-doped, neutral, and n-doped. Therefore, the two PBEDOT-Hx₂-Pyr-Pyr films are initially in their neutral state for the assembling of the device and upon the application of voltage one film is oxidized (p-doped state) while the other is reduced (n-doped state). In this case, the resulting color is a combination of the colors of p- and n- doped films and the spectral changes will also be a combination of those seen in the separate p- and n-doping experiments.

7.5 In-Situ Transmittance Measurements of EC Devices

The structure of the electrochromic cells described above allows us to probe the electronic properties of polymers through in-situ transmittance measurements in a wide range of the electromagnetic spectrum. For these wide range measurements, three different instruments have been employed; a Bruker 113v is used for mid-infrared (MIR) region measurements, a Zeiss MPM 800 microscope photometer for near infrared (NIR),

and visible (VIS) region measurements, and a UV/Vis - NIR Varian Cary 500 spectrophotometer.

7.5.1 Analysis of the Different Layers in the EC Device

The structure of the device underlines the fact that the optics of the cell is quite complicated. Even though we probe the optical properties of the EC material in transmittance mode, we do not measure the real transmittance/absorbance of the polymer. The measured transmittance contains contributions from all five layers of the cell; PET, SWNTs, polymer, electrolyte gel, and one more PET layer. In order for the optical properties of the polymer film itself to be extracted, a Drude-Lorentz model for multi-layered systems is necessary to fit the transmittance data. Each layer is fitted separately, using a parameter file that contains information about the center frequency, plasma frequency, and oscillator strength of each oscillator, as well as the dielectric function at infinity, and thickness of the fitted film. From the parameters obtained, we compute optical constants which yield information about the electronic structure of the neutral and doped states of the polymer film. For the interested reader, the parameter files for all four layers (there were two PET films, which are the same) can be found in Appendix B.

Figures 7.20 through 7.23 depict the transmittance data along with the fitting results from mid-infrared to the visible region. The PET substrate shown in Figure 7.20 is fitted first as a single layer and then the electrolyte gel confined in between two PET layers is fitted, the result is shown in Figure 7.21. For the fitting of the gel layer, the fitting parameters of the PET layer are taken into account, and this way at the end of the analysis of all layers, we have obtained a parameter file for each layer that, ideally, describes solely the optical properties of the specific layer. Figure 7.23 shows the transmittance and fitting results of a device (with the hole), in which the polymer under study, which is the PEDOT in this case is in its neutral state. The transmittance of a reference device has been subtracted from the data and the fitting.

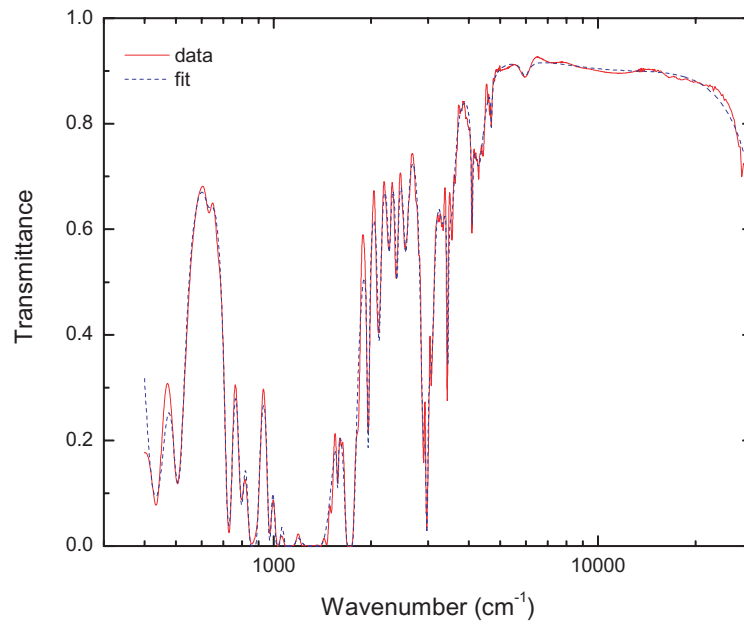


Figure 7.20: Transmittance data and fitting of a PET layer.

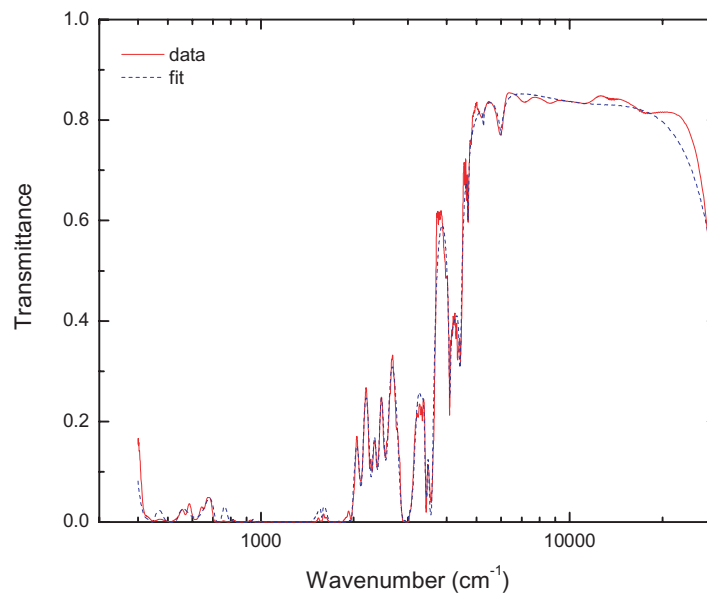


Figure 7.21: Transmittance data and fitting of a PET\Gel\PET configuration.

7.5.2 Analysis of a PEDOT EC Device (with hole)

Figure 7.24 shows the transmittance data for a PEDOT device (with hole). More specifically, the red line shows the transmittance of a reference device which includes

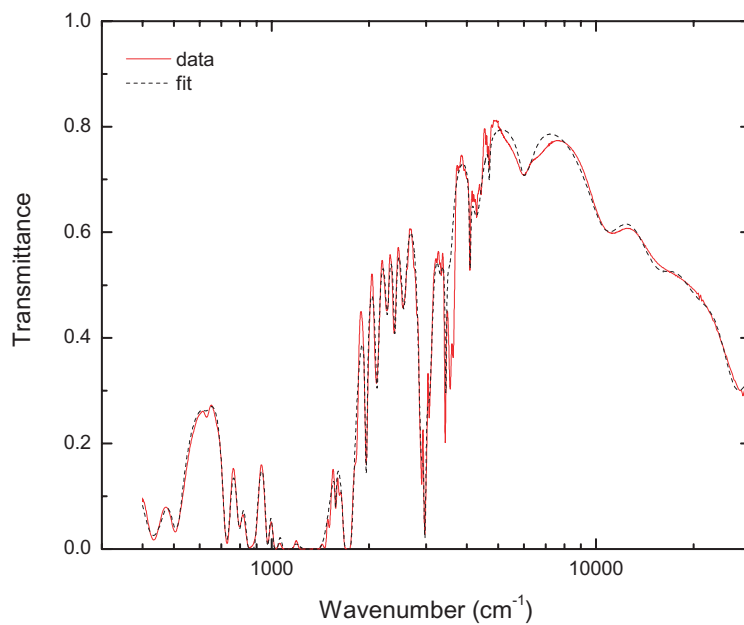


Figure 7.22: Transmittance data and fitting of SWNTs on PET layers.

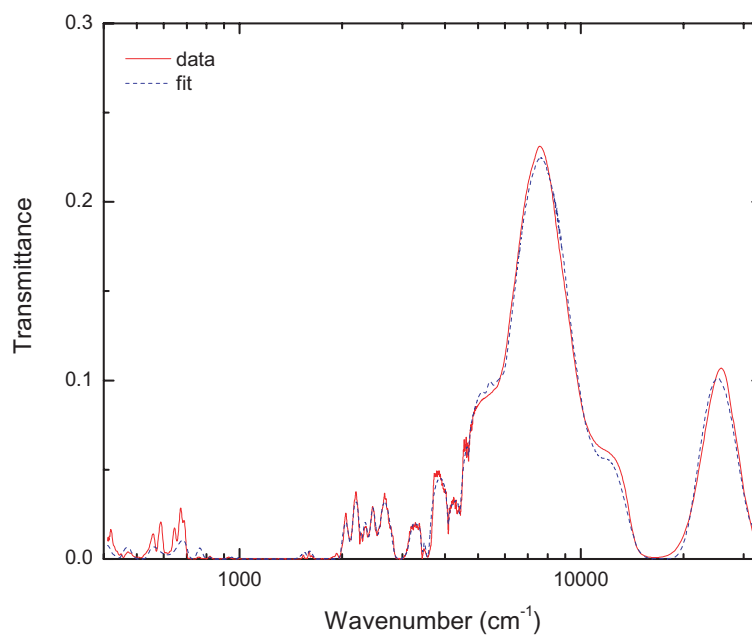


Figure 7.23: Transmittance data and fitting of EC device in the polymer under study in its neutral state. The transmittance of a reference device has been subtracted from the data and the fitting.

everything except the working polymer film on the working electrode, while the rest of the curves show the actual device divided by the reference device. This ideally depicts the transmittance of PEDOT film by itself. The applied voltage range is -1.8 V to $+1.0\text{ V}$. Notice that we cannot see very much below 3600 cm^{-1} and this is due to absorptions mostly from the electrolyte gel but also from the PET layers. Above 3600 cm^{-1} the electrochromic effect is obvious, with a contrast $\% \Delta \mathcal{T}$, between the extrema states at $\lambda_{max} = 7500\text{ cm}^{-1}$, about 23%. The transmittance values of this device are not high, and the reason for this is mainly the fact that it was constructed solely to study if the electrochromic effect could be observed in a configuration like this with the SWNT film as a conducting layer and therefore, it has not been optimized.

In Figure 7.24 can be seen that the polymer in its neutral, un-doped, state ($V_{cell} = -1.8\text{ V}$) is strongly absorbing in the visible region where the $\pi - \pi^*$ transition is. Therefore, the transmittance of the device in this region is highest compared to all other states. At frequencies less than 3600 cm^{-1} , the transmittance of the device is diminished due to strong absorptions mainly from the electrolyte gel and therefore, no conclusions can be drawn for this part of the spectrum. When the polymer is in its fully p-doped state ($V_{cell} = +1.0\text{ V}$) the visible absorption is reduced. At the intermediate doped states the visible absorption decreases as the doping level increases. In general, at these intermediate doped states the transmittance of the EC cell lies between the transmittance of the two extrema states; fully oxidized (p-doped) and fully reduced (neutral) states. This holds true for the whole spectrum range that was measured.

Figure 7.25 shows the transmittance data for the PEDOT device (with hole) divided by the reference device in three states; fully p-doped, slightly p-doped and neutral. In the same figure is also shown the fit of the data based on the Drude-Lorentz model. The conclusions drawn from this spectrum and the obtained parameters (Appendix B) are depicted more clearly through the absorption spectra described in the next subsection. One thing that can be noticed from the spectra shown in Figure 7.25 is the big

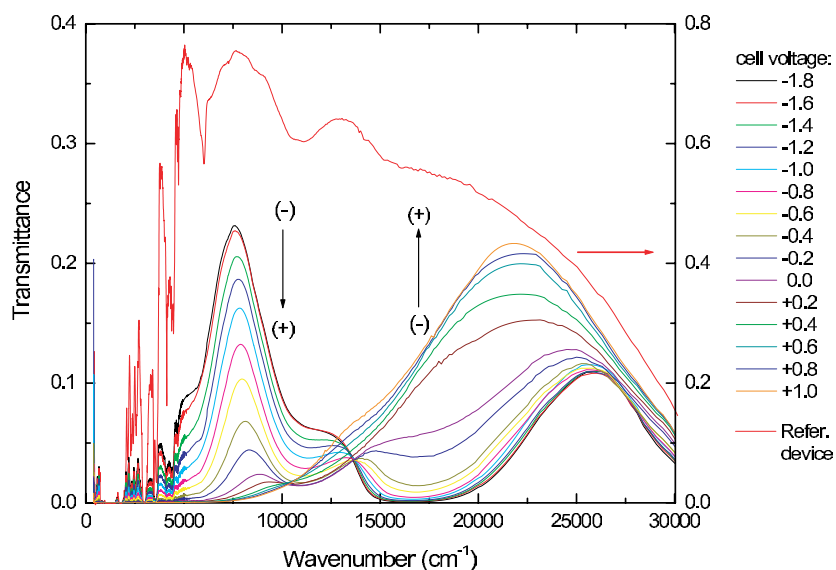


Figure 7.24: Transmittance spectrum of a PEDOT EC device (with hole) upon the application of voltages within the range -1.8 V to +1.0 V and of a reference device (red curve) containing everything except the working polymer.

change of the transmittance upon the application of the different voltages, which depicts nicely the electrochromic effect.

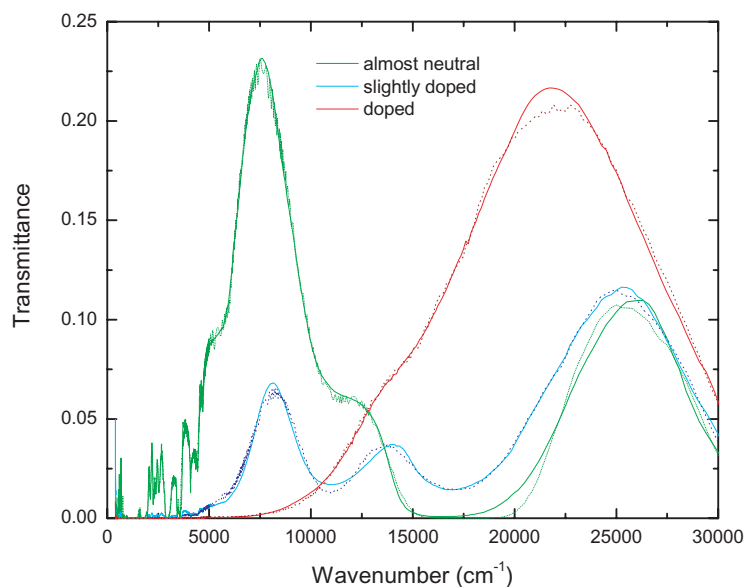


Figure 7.25: Transmittance spectrum of a PEDOT EC device (with hole) in three states, fully p-doped, slightly p-doped and neutral.

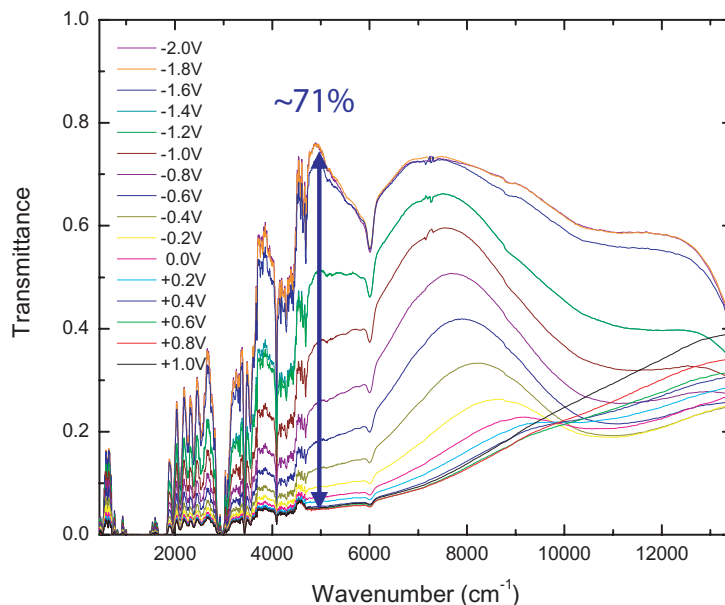


Figure 7.26: Transmittance spectrum of a PEDOT EC device (with hole) upon the application of voltages within the range -2.0 V to +1.0 V.

Preliminary transmittance results of a better optimized PEDOT EC device (with hole) are shown in Figure 7.26. The spectra in this figure correspond to the transmittance of the actual EC device, and no subtraction of a reference device has taken place. This is obvious from the strong peak at $\sim 6000 \text{ cm}^{-1}$, which appears in the reference device as can be seen in Figure 7.24. Data analysis has not been performed for this device but the transmittance is substantially higher than the previous device with values ranging from 5% to almost 80%, and an electrochromic contrast $\% \Delta \mathcal{T}$ of $\sim 71\%$ at $\lambda_{max} \sim 4891 \text{ cm}^{-1}$. These results are very promising and indicate that with a more careful optimization very good performance can be achieved.

Absorption Coefficient of PEDOT

Figure 7.27 shows the absorption coefficient of the actual device divided by the reference device (the transmittance of which is shown in Figure 7.24), which ideally is the absorption coefficient of PEDOT itself. The spectra show the absorption coefficient at different voltages within the applied voltage range. Figure 7.28 shows the absorption coefficient of only three states; fully p-doped, slightly p-doped and neutral. The black

line is the absorption coefficient of PEDOT in the neutral state. The $\pi - \pi^*$ absorption in the visible region is very strong and clear, but there are also two very small polaron bands in the near and mid-infrared that commence to show. These small peaks lead us to believe that in this state PEDOT is not completely neutral. Furthermore, the green line shows a medium p-doped state where the $\pi - \pi^*$ absorption is reduced and the two polaronic peaks in the infrared region are well defined. Finally, the orange line corresponds to the fully p-doped state of PEDOT, where there is only a very broad bipolaron absorption in the infrared region.

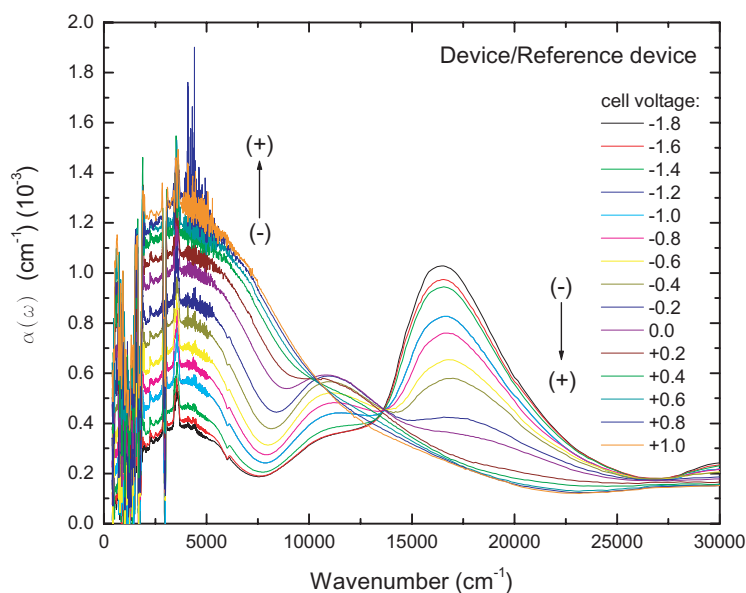


Figure 7.27: Absorption coefficient of the PEDOT EC device (with hole) where the absorption coefficient of the reference device has been subtracted, at different voltages within the applied voltage range.

To summarize, the neutral (un-doped) PEDOT has its $\pi - \pi^*$ transition in the visible region, and it is transparent in the infrared region, except from vibrational absorptions. At the lightly p-doped states, two symmetric sub-gap states are introduced upon doping and thus, absorption bands appear in the spectrum at lower frequencies/energies due to the presence of polaron states. The $\pi - \pi^*$ transition in these intermediate states is still present but diminished. At the fully p-doped state, a single broad bipolaron absorption band is produced, whereas the polaron and $\pi - \pi^*$ transitions are absent.

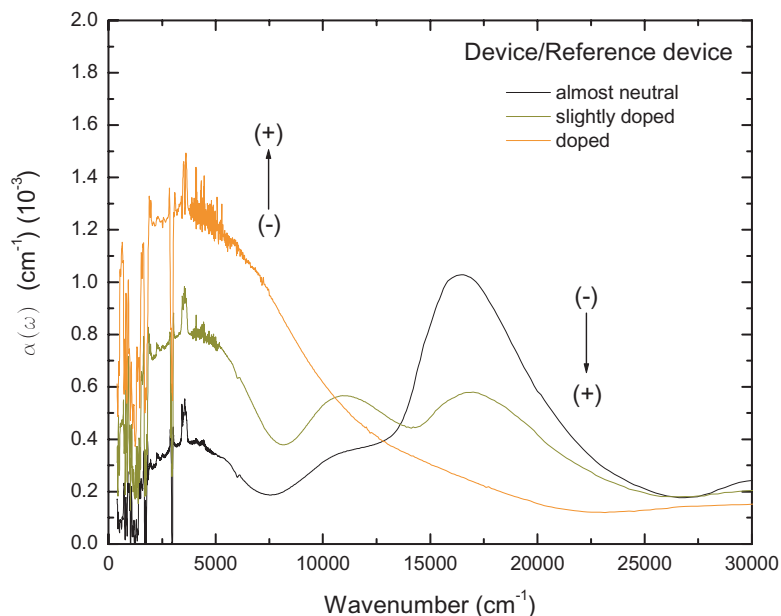


Figure 7.28: Absorption coefficient of the PEDOT EC device (with hole) where the absorption coefficient of the reference device has been subtracted, at three states; fully p-doped, slightly p-doped and neutral.

In conclusion, we were able to observe and follow the doping induced states upon the application of a voltage on a PEDOT EC transmissive/absorptive device (with hole). These results agree with what is expected from theoretical studies of this systems as well as experimental results from reflective devices like the ones studied in Chapter 5 of this dissertation.

Long Term Switching Stability of PEDOT EC Device (with hole)

Some preliminary and indicative results concerning the long-term redox switching stability of the transmissive/absorptive PEDOT EC devices (with hole) are shown in Figures 7.29 and 7.30. A square wave was applied to the device between -1.0 V and +1.0 V (in 20 sec double potential steps), while the absorbance at λ_{max} was monitored. For this device λ_{max} was found from the transmittance spectrum, shown in Figure 7.24 to be at 7500 cm^{-1} .

As can be seen from the absorbance spectrum, there is some degradation in the performance of the PEDOT EC device (with hole) during the first 200 cycles but after

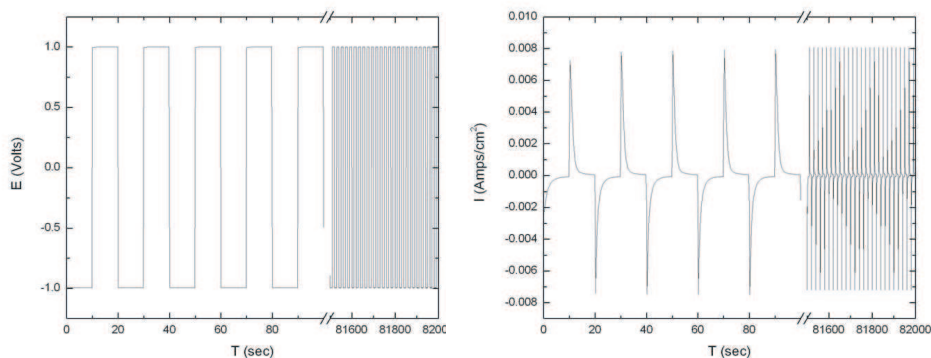


Figure 7.29: Applied square potential between -1.0 V and +1.0 V on a PEDOT transmissive/absorptive EC device (with hole), left hand side plot, while the current density is recorded as a function of time, right hand side plot.

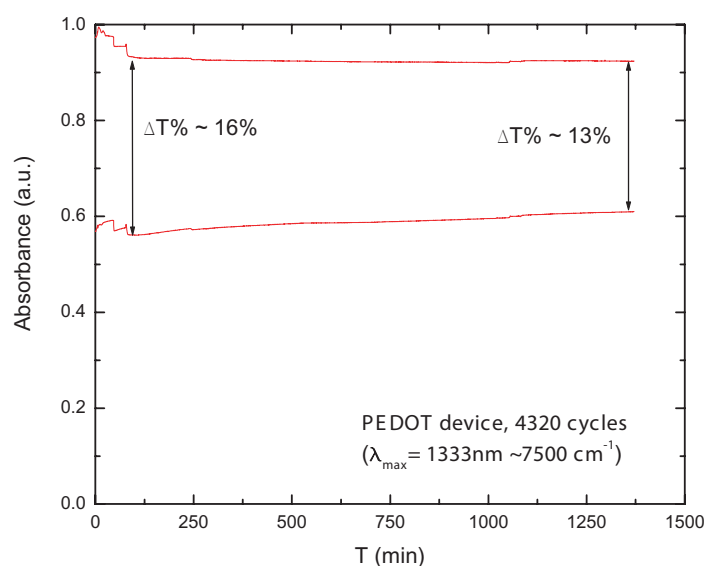


Figure 7.30: Absorbance change of a PEDOT transmissive/absorptive EC device (with hole) recorded at $\lambda_{max} = 7500 \text{ cm}^{-1}$ as a function of time as the applied potential is switched between -1.0 V and +1.0 V.

that, the EC device (with hole) appears to be very stable showing a difference in transmittance of $\sim 13\%$ - 16% . It should be noted again that this is not an optimized device and therefore better performance could certainly be achieved.

7.5.3 Results on PBEDOT-Hx₂-Pyr-Pyr EC Device (with hole)

The same type of transmissive/absorptive EC device (with hole), as the one described above, has been constructed using PBEDOT-Hx₂-Pyr-Pyr on both electrodes,

working and counter. The transmittance spectra obtained from this device depicts only the electrochromic changes of the working polymer. Therefore, we can perform transmittance measurements and follow the doping induced optical changes from all three accessible states of PBEDOT-Hx₂-Pyr-Pyr film; the neutral, oxidized, and reduced states.

Figure 7.31 shows the transmittance changes of the actual device (with hole) upon the application of voltage within the range from -0.5 V to +0.9 V. In this voltage range PBEDOT-Hx₂-Pyr-Pyr changes from a neutral state to an oxidized state. The electrochromic contrast $\% \Delta \mathcal{T}$ throughout the visible region is small $\sim 10\%$, while it becomes quite bigger in the near infrared region where at $\lambda \sim 2000$ nm or 5000 cm⁻¹ reaches a value of almost 45%.

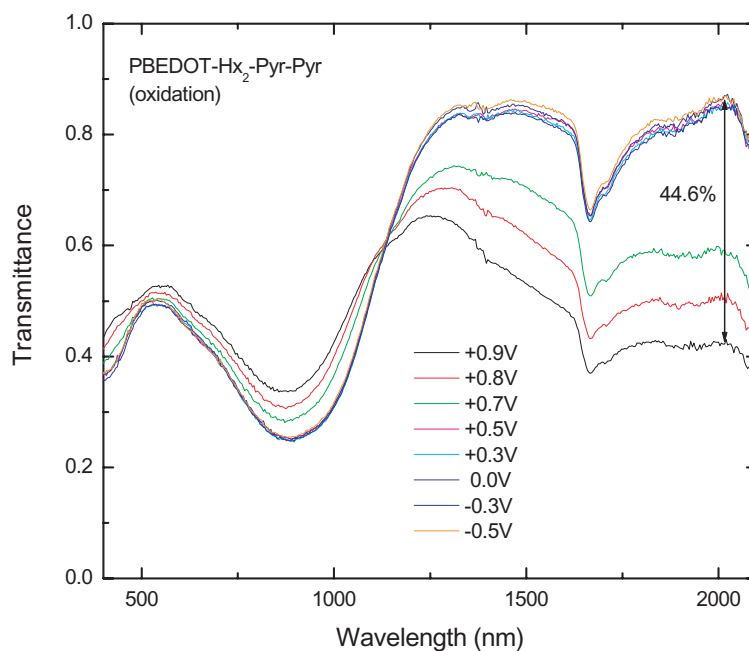


Figure 7.31: Transmittance spectrum of a PBEDOT-Hx₂-Pyr-Pyr EC device (with hole) upon the application of voltages within the range -0.5 V to +0.9 V (neutral to oxidized states).

Figure 7.32 shows the transmittance changes of the actual device (with hole) upon the application of voltage within the range from -0.5 V to -2.6 V. In this voltage range PBEDOT-Hx₂-Pyr-Pyr changes from a neutral state to a reduced state. During these measurements, after reaching the first reduction of the polymer and obtained all the

transmittance spectra from the neutral to the first reduction state, we decided to try and reach the second reduction state which occurs at $E_{pc} = -2.10$ V vs SCE. It should be noted, that there is no accurate way to compare the potential E_{pc} obtained from a three-electrode configuration where a reference electrode has been used, with the applied potential on the device which is a two-electrode configuration with no reference electrode in use. In the two-electrode configuration, the applied voltage simply corresponds to the voltage difference between the electrodes relative to each other.

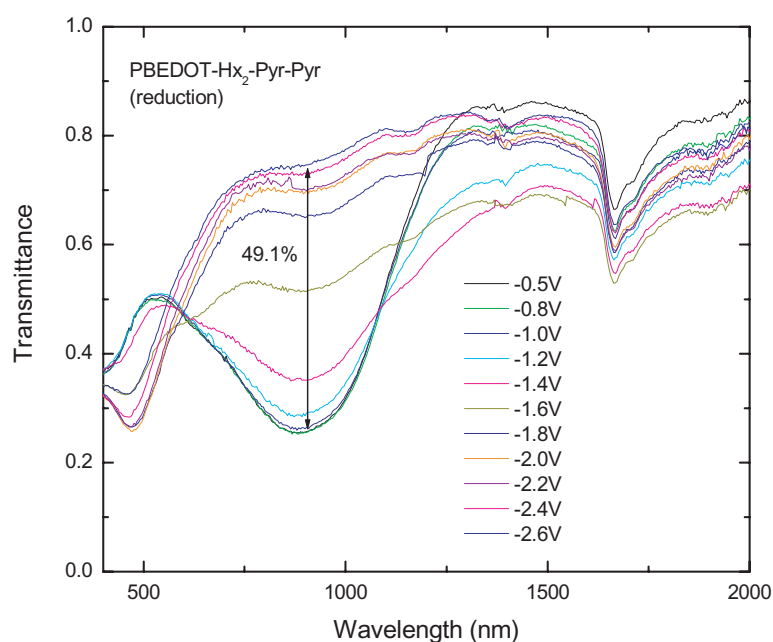


Figure 7.32: Transmittance spectrum of a PBEDOT-Hx₂-Pyr-Pyr EC device (with hole) upon the application of voltages within the range -0.5 V to -2.6 V (neutral to reduced states).

The electrochromic contrast $\% \Delta \mathcal{T}$ of the PBEDOT-Hx₂-Pyr-Pyr EC device (with hole) between the neutral and the reduction states is bigger compared to the contrast obtained between the neutral and oxidized states throughout the whole spectral region. Furthermore, in this case, the maximum contrast is obtained at $\lambda \sim 880$ nm ($11,364 \text{ cm}^{-1}$) and it reaches a value of almost 50 %.

The transmittance of the reference device has not been subtracted from the above results, which depict the transmittance of the actual device itself. Therefore, the peak at ~ 1666 nm or ~ 6000 cm^{-1} is present in these data also.

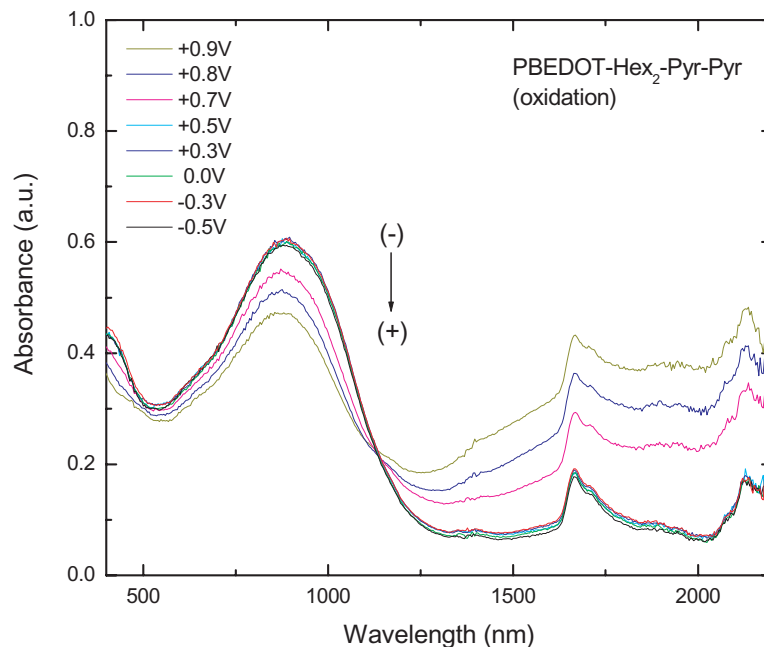


Figure 7.33: Absorbance spectrum of a PBEDOT-Hx₂-Pyr-Pyr EC device (with hole) -0.5 V to +0.9 V (neutral to oxidized states).

Figures 7.33 and 7.34 show the absorbance spectra of the PBEDOT-Hx₂-Pyr-Pyr EC device (with hole) at different applied voltages, from neutral to oxidized and neutral to reduced states respectively. In Figure 7.33 the $\pi - \pi^*$ absorption band has not been fully depleted and this may be due to the fact that higher applied voltages were needed. A bigger electrochromic contrast is observed in the near infrared region for the same voltage range. In Figure 7.34 the $\pi - \pi^*$ absorption band has been fully depleted within the applied voltage range exhibiting high electrochromic contrast in this region, whereas at the near infrared region the exhibited contrast is small.

Long Term Switching Stability of PBEDOT-Hx₂-Pyr-Pyr EC Device (with hole)

Preliminary and indicative results concerning the long-term redox switching stability of the transmissive/absorptive PBEDOT-Hx₂-Pyr-Pyr EC device (with hole) are

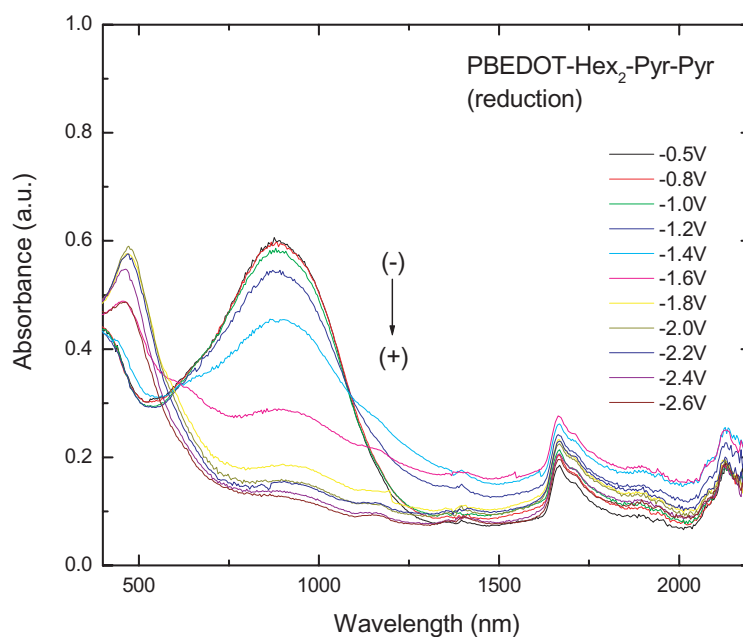


Figure 7.34: Absorbance spectrum of a PBEDOT-Hx₂-Pyr-Pyr EC device (with hole) upon the application of voltages within the range -0.5 V to -2.6 V (neutral to reduced states).

shown in Figures 7.35 and 7.36. A square voltage was applied to the device, between -0.3 V and +0.9 V (in 40 sec double potential steps), while the absorbance at λ_{max} was monitored. For this device the λ_{max} was found from the transmittance spectrum, shown in Figure 7.31, to be at 2000 cm^{-1} . This long term switching stability experiment was performed between the neutral and oxidized states since the polymer considers to be more stable in the p-doped state compared to the n-doped states.

The absorbance of PBEDOT-Hx₂-Pyr-Pyr EC device (with hole) when the polymer was in its oxidized state was increasing during the first 200 cycles and then it stabilized, whereas when the polymer was in its neutral state the absorbance was stable throughout the whole time of the experiment. This EC device between the neutral and oxidized states show a difference in transmittance of $\sim 32\%$. It should be noted that this is not an optimized device either and therefore, better performance could certainly be achieved. Further investigation is needed in order to determine if the difference in $\% \Delta \mathcal{T}$ between the PEDOT and PBEDOT-Hx₂-Pyr-Pyr EC devices (with hole) is due to

the specific devices (different polymer thicknesses, as well as handling and assembling) or if the devices using the latter polymer have greater potential.

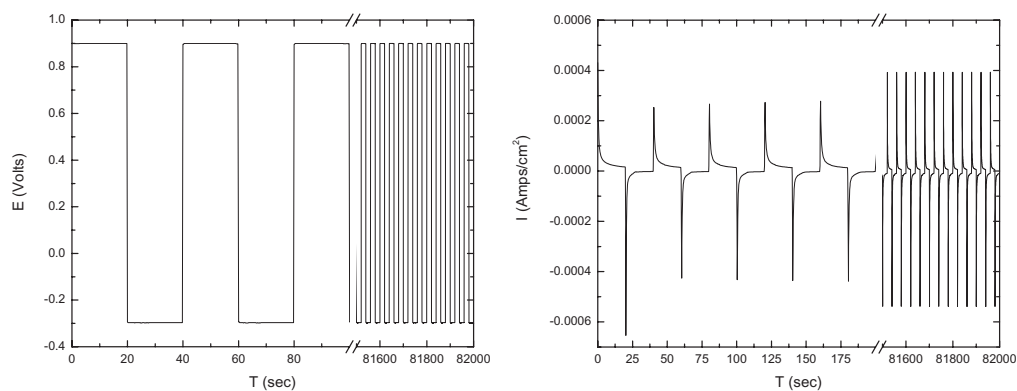


Figure 7.35: Applied square potential between -0.3 V and $+0.9$ V (neutral to oxidized states) on a PBEDOT-Hx₂-Pyr-Pyr transmissive/absorptive EC device (with hole), left hand side plot, while the current density is recorded as a function of time, right hand side plot.

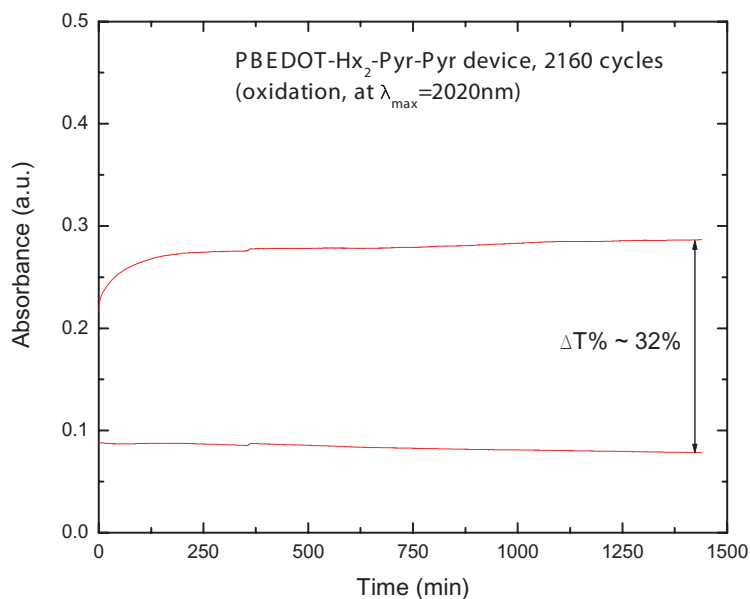


Figure 7.36: Absorbance change of a PBEDOT-Hx₂-Pyr-Pyr transmissive/absorptive EC device (with hole) recorded at $\lambda_{max} = 2000$ nm as a function of time as the applied potential is switched between -0.3 V and $+0.9$ V (neutral to oxidized states).

7.6 Towards the construction of a Dual Device

The ultimate goal of this study was the construction of a dual EC device using the PBEDOT-Hx₂-Pyr-Pyr as the electrochromic polymer on both electrodes as shown in Figure 7.19. As was mentioned earlier, this device consists of two PBEDOT-Hx₂-Pyr-Pyr-coated nanotubes films on plastic electrodes facing each other. The electrodes are transparent from the mid-infrared through the visible region and are separated by a thin layer of gel electrolyte. The polymer used that was used, PBEDOT-Hx₂-Pyr-Pyr can access three different states; p-doped, neutral, and n-doped. The two polymer films were initially in their neutral state for the assembling of the device, and upon the application of voltage one film was oxidized (p-doped state) while the other one was reduced (n-doped state). In the doped state of the device, the resulting color and optical properties will be a combination of the colors and optical properties of the p- and n-doped states of the two PBEDOT-Hx₂-Pyr-Pyr films.

7.6.1 Cyclic Voltammetry of PBEDOT-Hx₂-Pyr-Pyr dual device

Figure 7.37 shows the scan rate dependence cyclic voltammograms of a reference dual device, which contains two SWNTs/PET electrodes facing each other and are separated by a thin electrolyte gel layer. Different scan rates ranging from 25 mV/s to 200 mV/s have been used while the applied voltage, from -1.0 V to +1.0 V, and the current through the reference device configuration are monitored. The use of different scan rates allows for different reactions, slow or fast, to be followed. This type of measurements can provide information about the dependence of the current peak on the scan rate and thus, a useful insight about the electrochemical behavior of the system under consideration.

We performed these measurements in order to generally compare a dual reference device with a dual polymer device. The scan rate dependence cyclic voltammograms of a PBEDOT-Hx₂-Pyr-Pyr dual EC device is shown in Figure 7.38. In Figures 7.37 and 7.38 can be seen that as the scan rate increases the current, i_p increases too. In Figure 7.39, the cyclic voltammogram of the dual reference device, for the 25 mV/s scan

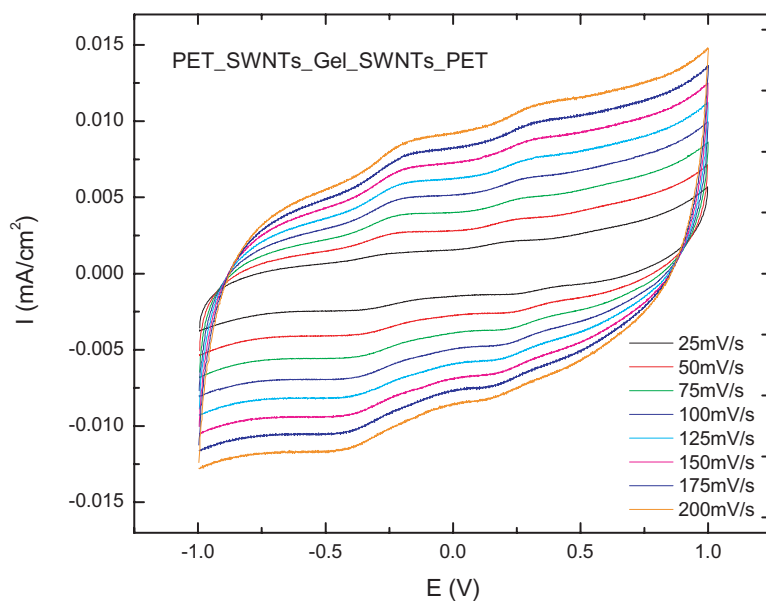


Figure 7.37: Scan rate dependence (with rates ranging from 25 mV/s to 200 mV/s) of cyclic voltammograms obtained from a reference dual device for applied voltage range from -1.0 V to +1.0 V.

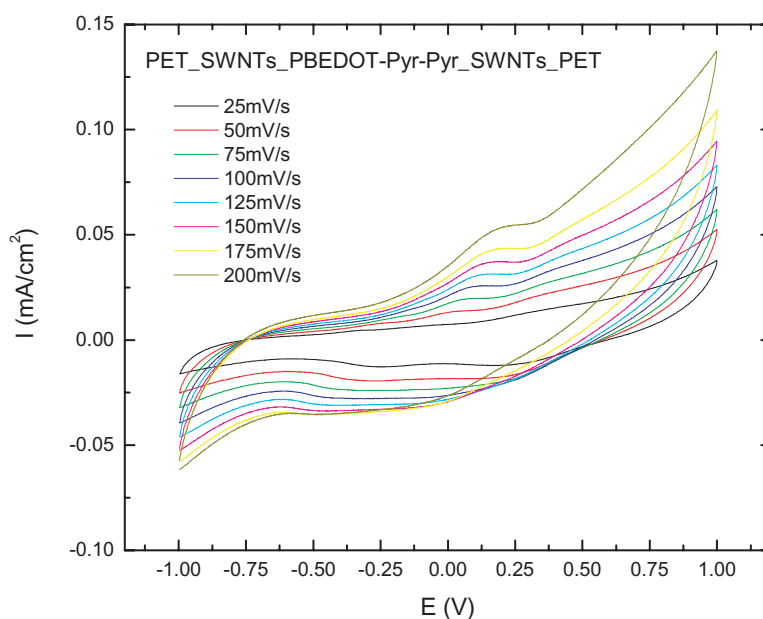


Figure 7.38: Scan rate dependence (with rates ranging from 25 mV/s to 200 mV/s) of cyclic voltammograms obtained from a polymer (PBEDOT- Hx_2 -Pyr-Pyr) dual device for applied voltage range from -1.0 V to +1.0 V.

rate has been plot with the cyclic voltammograms of all scan rates of the dual polymer device. By comparing the cyclic voltammograms of the reference and the actual device,

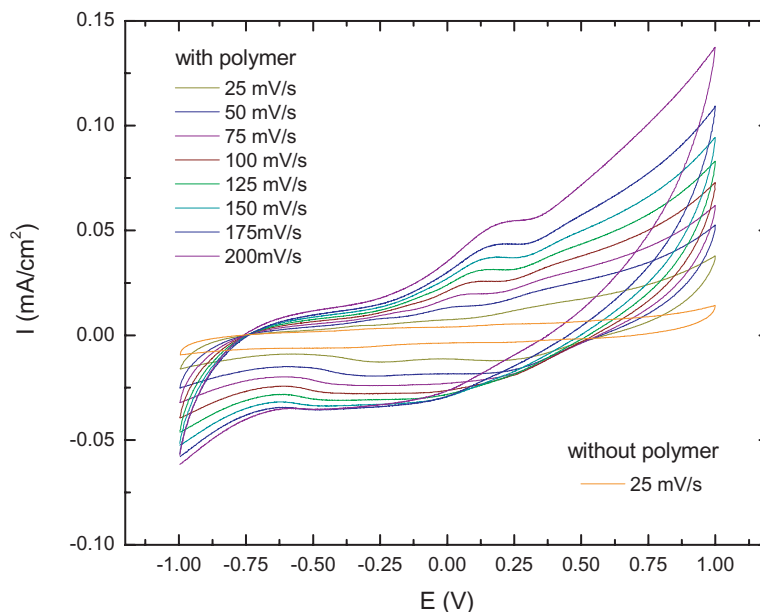


Figure 7.39: Scan rate dependence (with rates ranging from 25 mV/s to 200 mV/s) of cyclic voltammograms obtained from a polymer (PBEDOT-Hx₂-Pyr-Pyr) dual device, and cyclic voltammogram of a reference dual device at 25 mV/s, for applied voltage range from -1.0 V to +1.0 V.

we conclude that the current passing through the device is mainly due to the polymer films and not to the other layers in the polymer dual device.

7.6.2 In-Situ Absorbance Measurements

A PBEDOT-Hx₂-Pyr-Pyr dual EC device has been constructed, as it has been described in previous sections, using SWNT films as the conducting layers in both sides. The absorbance of this device has been recorded from the visible to near infrared region at different applied voltages. The two PBEDOT-Hx₂-Pyr-Pyr films are initially in their neutral states ($V_{cell} = 0.0$ V), and as the applied voltage was increased one film was becoming oxidized while the other one was becoming reduced (first reduction). The resulting absorbance spectrum is depicted in Figure 7.40.

When the polymer films are in their neutral state ($V_{cell} = 0.0$ V) the device is strongly absorbing at the boundary between the visible and the near infrared region where the $\pi - \pi^*$ transition of PBEDOT-Hx₂-Pyr-Pyr is ($E_g = 1.4$ eV). Therefore, the absorbance of the device in this region is very high compared to all other states. At higher

wavelengths, above ~ 1100 nm (9090 cm^{-1}) and up until about ~ 2750 nm (3636 cm^{-1}) the device is quite transparent. As the applied voltage is increased from 0.0 V to $+1.7$ V, the absorbance of the device in the visible/near infrared border is gradually decreasing, whereas at higher wavelengths is increasing. As the applied voltages further increase from $+1.7$ V to $+2.6$ V, the absorbance of the device continues to decrease in the visible/near infrared border, while it decreases at higher wavelengths too. Finally, at the highest applied potential, $+2.6$ V, the absorbance of the device in the visible/near infrared border is minimum and the $\pi - \pi^*$ transition is depleted, and the electrochromic contrast has reached its highest value. However, as we are moving further into the infrared region, at the same applied voltage, the difference in the absorbance of the device between its neutral and highly doped states has become very small.

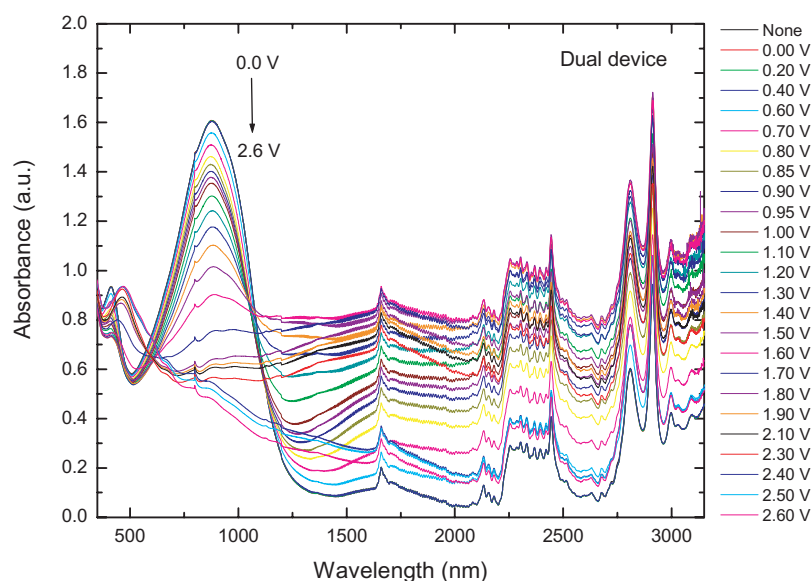


Figure 7.40: Absorbance spectrum of a PBEDOT-Hx₂-Pyr-Pyr dual EC device upon the application of voltages within the range from 0.0 V to $+2.6$ V (neutral to doped states).

In general, at the intermediate doped states, the absorbance of the EC cell lies between the absorbance of the two extrema states, neutral and doped. Although this is true around the region where the $\pi - \pi^*$ transition occurs, this is no longer the case for higher wavelengths. These changes can be seen clearer in Figure ?? where fewer spectra have been plotted through a narrower spectral region. The electrochromic contrast $\% \Delta T$

between the two extrema states that was achieved with this dual device at $\lambda_{max} = 880$ nm is $\sim 32\%$. It should be noted that this is the first attempt of constructing a device of this type and no optimization has been attempted. Therefore, better performance could certainly be achieved.

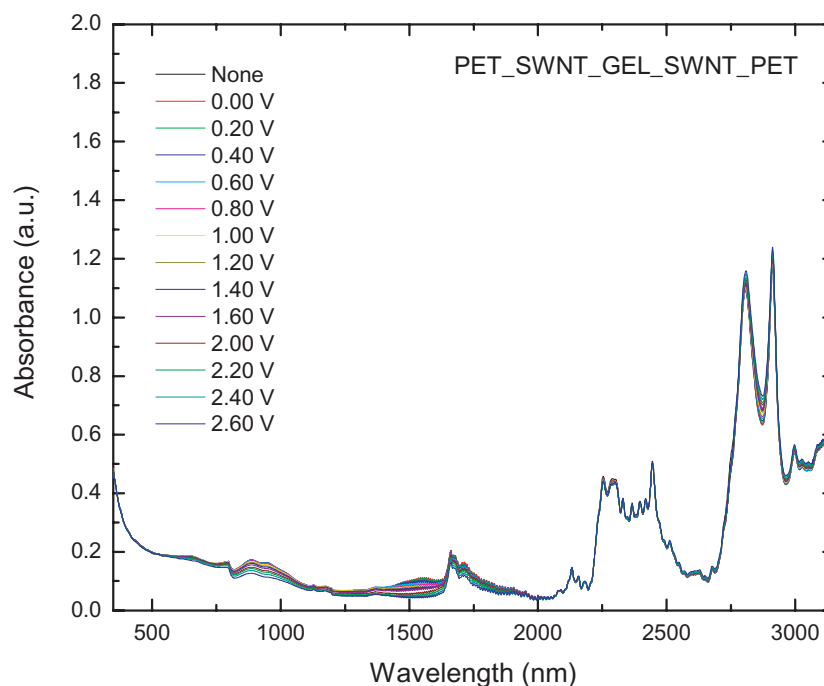


Figure 7.41: Absorbance spectrum of a reference EC device upon the application of voltages within the range from 0.0 V to +2.6 V.

Figure 7.41 depicts the absorbance of the dual reference device over the same spectral region and the same applied voltage range used for the actual device. These measurements were performed in order to be able to determine if the dual reference device is responsible for any of the absorbance changes seen in the dual polymer device. For the spectral region between ~ 350 nm ($28,571$ cm^{-1}) and ~ 2250 nm (4444 cm^{-1}) where the absorbance changes discussed above occur, the change of the absorbance of the dual reference device is negligible. Therefore, the observed changes are due solely to the doping induced states, upon the application of a voltage, of the PBEDOT-Hx₂-Pyr-Pyr films.

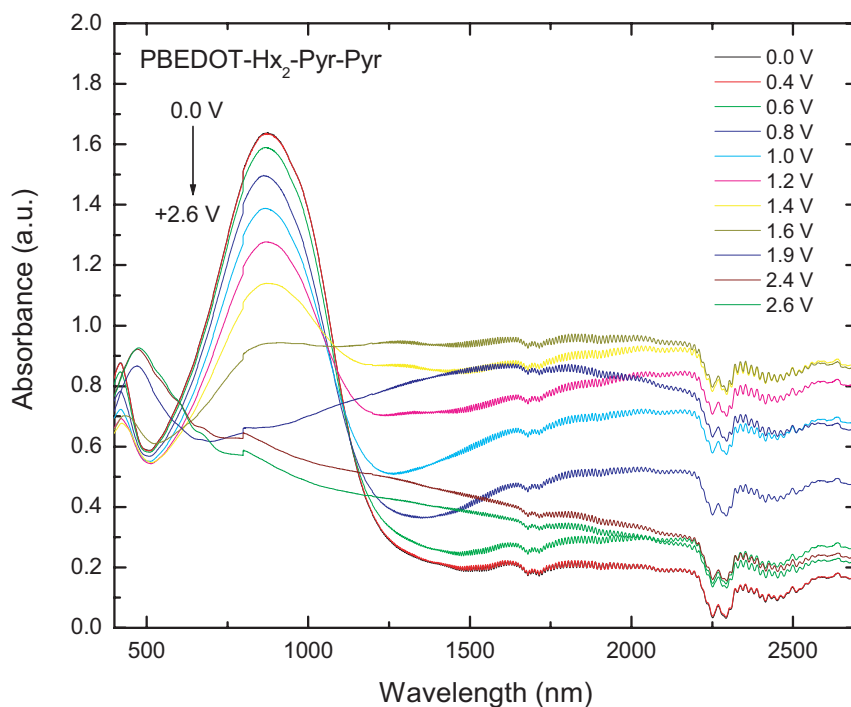


Figure 7.42: Absorbance spectrum of a PBEDOT-Hx₂-Pyr-Pyr dual EC device where the absorbance of the reference device has been subtracted, at different voltages within the applied range.

Figure 7.42 depicts the absorbance of the PBEDOT-Hx₂-Pyr-Pyr dual EC device, where the absorbance of the reference device has been subtracted, at different voltages within the applied range. Therefore, ideally, it depicts the combined absorbance of the two PBEDOT-Hx₂-Pyr-Pyr films changing from a neutral state to doped states.

Figure 7.43 depicts the absorbance of the PBEDOT-Hx₂-Pyr-Pyr dual EC device, where the absorbance of the reference device has been subtracted, at voltages from 0.0 V (neutral state) to +1.6 V (intermediate doped state). At this voltage range, the absorbance of the $\pi - \pi^*$ transition is decreasing, whereas the absorbance in the near infrared region is increasing. Figure 7.44 depicts the absorbance of the PBEDOT-Hx₂-Pyr-Pyr dual EC device, where the absorbance of the reference device has been subtracted, at voltages from +1.6 V (intermediate doped state) to +2.6 V (fully doped state). At this voltage range, the absorbance of the $\pi - \pi^*$ transition continues to decrease, whereas the absorbance in the near infrared region is also decreasing.

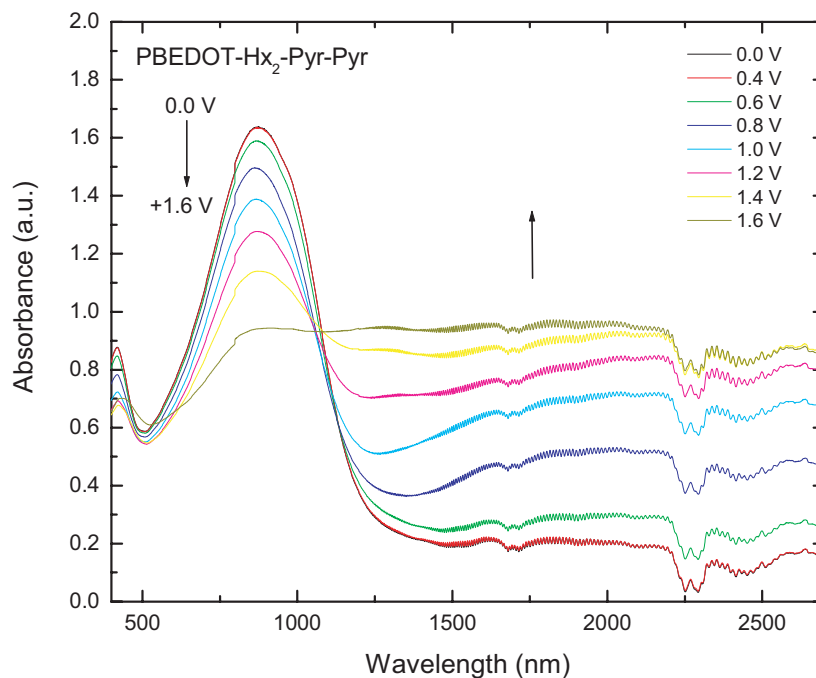


Figure 7.43: Absorbance spectrum of a PBEDOT-Hx₂-Pyr-Pyr dual EC device where the absorbance of the reference device has been subtracted, at different voltages within the applied range.

Figure 7.45 depicts the transmittance of the actual PBEDOT-Hx₂-Pyr-Pyr dual EC device, at voltages from 0.0 V (neutral state) to +2.6 V (fully doped state). These results confirm that after applying a voltage of +2.6 V during the previous measurements, the device is still working and it exhibits an electrochromic contrast of 65% at 5000 cm⁻¹. Therefore, the decrease of absorbance in the near infrared region that was observed is not related to any damage of the device. Strong absorptions in the mid-infrared region from the electrolyte gel prohibit us to draw any conclusion. Further investigation is needed in order to determine the source of the near infrared decrease.

7.6.3 Switching Time

Preliminary results concerning the long-term redox switching stability of the transmissive/absorptive dual EC device utilizing the p- and n-dopable electroactive polymer PBEDOT-Hx₂-Pyr-Pyr in an electrochromic application are shown in Figure 7.46.

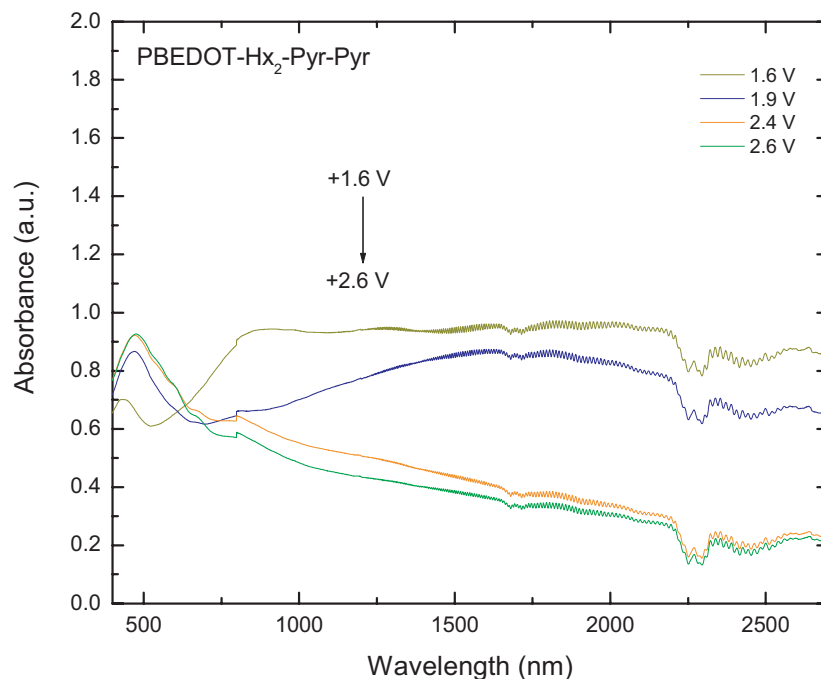


Figure 7.44: Absorbance spectrum of a PBEDOT-Hx₂-Pyr-Pyr dual EC device where the absorbance of the reference device has been subtracted, at different voltages within the applied range.

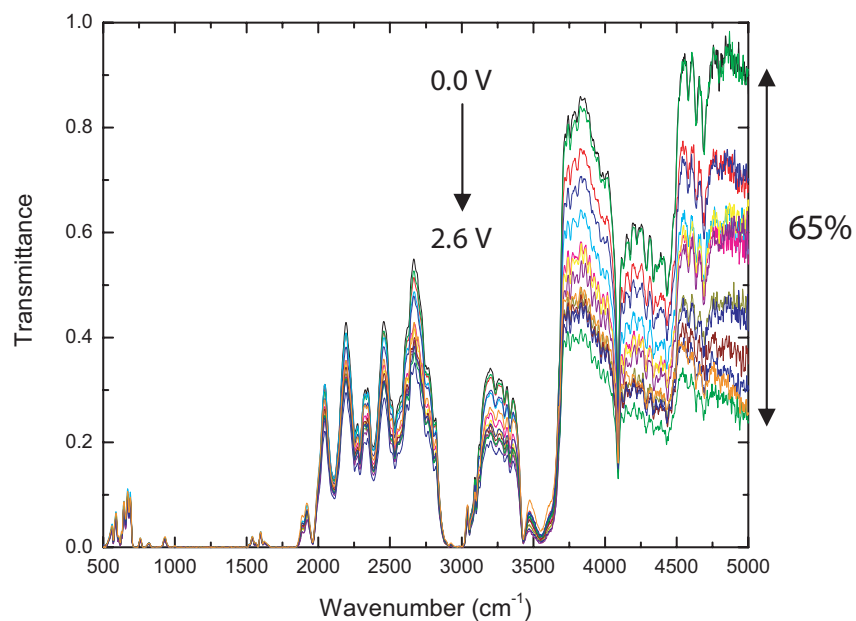


Figure 7.45: Transmittance spectrum of a PBEDOT-Hx₂-Pyr-Pyr dual EC device in the mid-infrared region, at different voltages within the applied range. Strong absorption bands due to the electrolyte gel hinder the electrochromic effect.

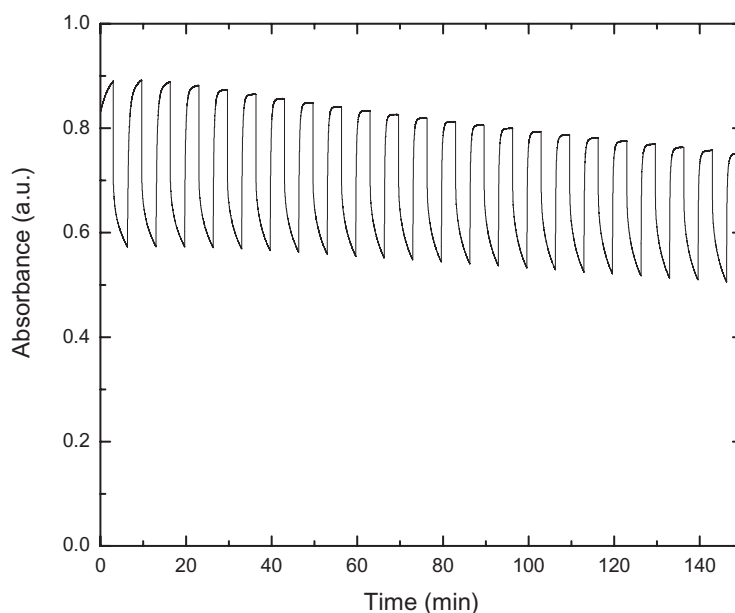


Figure 7.46: Absorbance change of a PBEDOT-Hx₂-Pyr-Pyr transmissive/absorptive dual EC device recorded at $\lambda_{max} = 880 \text{ nm}$ or 11364 cm^{-1} as a function of time, as the applied potential is switched between 0.0 V and +2.6 V (neutral to oxidized states).

A square wave was applied to the device, between 0.0 V and +2.6 V (in 100 sec double potential steps), while the absorbance at λ_{max} was monitored. For this device the λ_{max} was found from the absorbance spectrum, shown in Figure 7.40, to be at $\sim 880 \text{ nm}$ ($\sim 11,365 \text{ cm}^{-1}$). This long term switching stability experiment was performed between the neutral and doped states of the device.

In Figure 7.46 can be noticed that, the difference in the absorbance of PBEDOT-Hx₂-Pyr-Pyr EC dual device between the extrema states is diminishing throughout the time of the experiment. It should be kept in mind though that, this is not an optimized device and therefore better performance could be achieved.

7.7 Conclusions

Transmissive/absorptive EC devices were built using two different electroactive polymers and, for the first time to the best of our knowledge, SWNT films were used as the conductive layers in EC devices. Initially, we conducted a comparison study between the performance of SWNT films used as the conductive electrodes, and the well

studied and extensively used ITO. Cyclic voltammograms and absorbance measurements in solution for both polymers that were used in the devices were performed, and the conclusion is that SWNTs are suitable to be used in EC devices in order to record electrochromic changes of the electroactive polymer films.

Furthermore, two different configurations were used and transmittance or absorbance measurements were performed. The first configuration, EC device with hole, employed PEDOT as the electroactive film which can be switched between a neutral and a p-doped state. For this reason, a hole was punched through the counter electrode to allow us to probe the changes of only one PEDOT film in the device. Having the second PEDOT film be in the path of the light beam, the electrochromic changes of one film would cancel the changes of the other and overall, no change would be observed. This type of devices exhibit nicely the electrochromic effect over the spectral range from visible to mid-infrared, proving the SWNT films suitable for the use in EC devices, and also showed improved and promising results simply by carefully preparing and handling of the device. Data analysis and fitting based on the Drude-Lorentz model were also presented and showed that we can observe the doping induced states with this transmissive/absorptive EC configuration, polaronic and bipolaronic states, as they have been described in the literature and have been observed in reflective type of EC devices like the ones presented in Chapter 5. Furthermore, indicative stability experiments were performed and showed potential. An optimization study will greatly improve the performance of these devices, since there are many parameters that can be adjusted.

This configuration was also tested by using the PBEDOT-Hx₂-Pyr-Pyr on both electrodes and the changes in transmittance upon the application of different voltages were recorded for all three states of the polymer film; oxidized, neutral, and reduced. Preliminary results of the redox stability were performed and showed potential. An optimization study is necessary and will greatly improve the performance of these devices.

The second configuration that we used, dual EC device, employed PBEDOT-Hx₂-Pyr-Pyr as the electroactive film, which is one of a few polymers that can be switched not only between neutral and p-doped states, but also between neutral and n-doped states. Due to the ability of this polymer to access p- and n- doped states, a dual device can be built using the same polymer on both electrodes. The two PBEDOT-Hx₂-Pyr-Pyr films were initially in their neutral states, and upon the application of voltage, one film became oxidized while the other one became reduced. The absorbance spectrum of this dual device was recorded over the spectral range from visible to near infrared at different applied voltages. As the state of the polymer films in the device changed from neutral to doped, we were able to follow the depletion of the $\pi - \pi^*$ transition, which for this polymer occurs at the border of the visible and near infrared region ($E_g = 1.4\text{ eV}$) and the rise of the doping induced interband transitions further in the infrared region. Moreover, indicative switching stability experiments were performed and showed potential. An optimization study is expected to improve the performance of these devices.

In conclusion, we constructed a transmissive/absorptive dual EC device that exhibits electrochromic changes from the visible to the infrared region. This is the first transmissive/absorptive dual EC device, to our knowledge, that exhibits electrochromism in the infrared region. The substitution of the electrolyte gel that was used in this work, with a different one that will not exhibit such a big absorbance below 3600 cm^{-1} , will probably extend the working range of these devices deeper in the infrared region. The performance of devices of this type will certainly benefit from optimization.

APPENDIX A NEXT GENERATION OF REFLECTIVE ECDS USING MICROPOROUS GOLD ELECTRODES

In chapter 5, an extensive study on reflective electrochromic devices was presented in detail. This study was based on reflectance measurements, that led to a deep understanding of the optical and electrochemical properties of conjugated polymers, and the construction of electrochromic devices with enhanced performance. Variable reflective electrochromic devices based on PProDOT-Me₂ and PBEDOT-NMeCz were initially optimized to exhibit contrast ratios of 60-70 % in the mid-infrared region where two strong absorption peaks, water absorption (O-H stretching mode), and C-H stretching mode, were hindering the performance of the devices. A novel technique was developed in order to build water-free devices, and a new sample holder was designed, that allows control of the electrolyte gel thickness and thus, significantly reduces the C-H signature. However, the use of the new sample holder has a major drawback; due to the applied pressure, the slits on the working electrode are squeezed together and thus, the diffusion of the electrolyte gel through the slits and the ion transport is very difficult. As a consequence, the switching time of the device is very slow. More specifically, the switching time for an EC device mounted in the new sample holder increased by a factor of 10³, compared to the switching time of the same device under no pressure.

In addition to the absorption bands due to O-H and C-H stretching modes that were initially hindering the performance of this type of reflective EC devices in the mid-infrared region, and the slow switching times due to the new sample holder design, there were more problems, that affected the whole spectrum range and needed to be resolved. First, the slits on the working electrode are not flat, hence they tend to scatter and absorb part of the incident light. Therefore, the intensity of the signal that reaches the detector is low due to the diffusion of the reflected light, and the effective electrochromic contrast

is diminished through this process. Furthermore, the ion diffusion path through the slits is long and time consuming, which results to an additional increase of the switching time. Finally, the ion diffusion is not always homogeneous; the color change starts from the slits and then spreads out over the whole polymer active surface. Thus, a modification of the existing sample holder, and a search for an alternative way to control the thickness of the electrolyte gel is required in order to avoid or diminish these problems, and optimize the device function. Furthermore, the search of an alternative solution to the slits is also needed.

An effort towards the optimization of this type of devices led to the replacement of the slitted gold-coated Mylar by a highly porous metallized membrane. This membrane is a polycarbonate membrane, purchased from Osmonics Inc., with $10\ \mu\text{m}$ pore size, on which a thin film of gold has been deposited through a metal vapor deposition process (MVD). The gold layer needs to have sufficient thickness in order to yield high reflectance, while at the same time maintaining the porous nature of the flexible membrane. Typically, a gold layer of $50\ \text{nm}$ meets adequately these requirements [42]. This replacement facilitates the diffusion of the electrolyte gel by shortening the path-length that the ions have to travel, and thus the doping process becomes rapid and more homogeneous. Therefore, an even thinner layer of electrolyte gel can be used, which results in a further reduction of the C-H absorption band. Under these circumstances, better switching times are achieved, of the order of sub-seconds, and high reflectance contrast for the entire region from $0.9\ \mu\text{m}$ to $5.0\ \mu\text{m}$ are expected [42, 75].

Measurements of the specular reflectance in the far infrared region showed relatively low values for gold, approximately 40% as shown in Figure A.1. For the mid-infrared region the specular reflectance was even lower, varying between approximately 10% and 30%, Figure A.2. Measurements of diffuse reflectance have shown high values, approximately 70% for near infrared (NIR) [42]. It is expected that diffuse reflectance will be high for mid- and far infrared regions too. In addition to specular reflectance measurements of the highly porous membranes, transmittance measurements were per-

formed in the same range, from mid- to far infrared. As shown in Figure A.1, the transmittance was very low between $\sim 1\%$ and 2.5% , throughout the whole measured range, as it was expected.

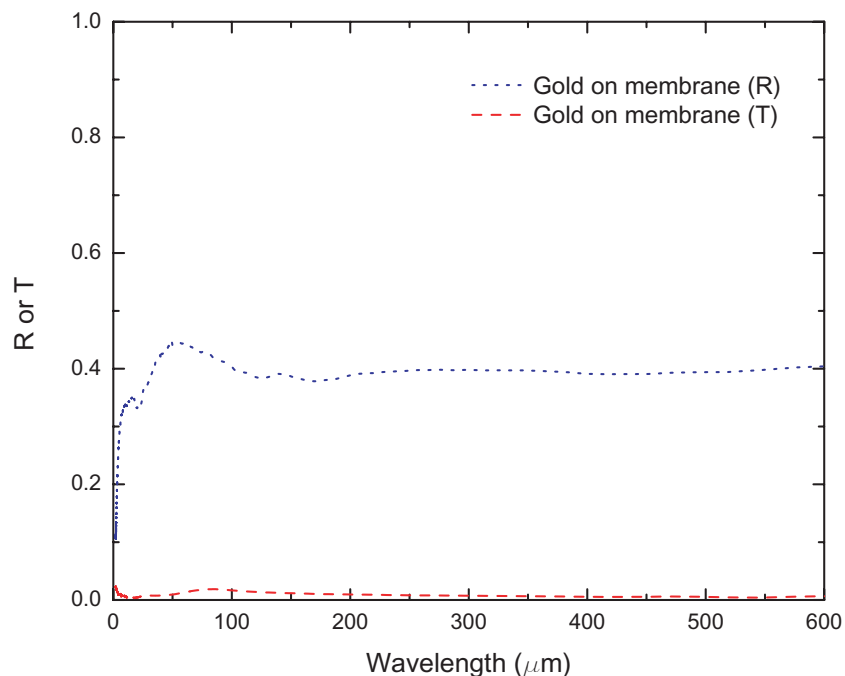


Figure A.1: Reflectance and transmittance measurements of the highly porous metallized membrane in the mid-infrared (MIR), and far infrared (FIR) regions.

Figure A.3 shows the new PProDOT-Me₂ EC cell, the structure of which is the same as the one described in chapter 5, at its two extrema states. The switching time for this EC device is 0.2 seconds. Lifetime, or long term stability, tests revealed that when this type of devices are assembled in inert (Ar) environment, they can be switched for hundreds of thousands of cycles with less than 10% loss of electrochromic contrast, $\% \Delta \mathcal{R}$ in the near infrared [38, 42].

Figure A.4 shows the specular reflectance of a PProDOT-Me₂ EC cell, as the one shown in Figure A.3 for part of the far infrared region, from $20 \mu\text{m}$ to $200 \mu\text{m}$. Since the specular reflectance of the substrate, gold on membrane is very low, about 40% in the above region, we did not expect the reflectance of the cell, which also includes a polyethylene window, an electrolyte gel layer, and an 150 nm PProDOT-Me₂ film on the gold on membrane substrate, to be high. The electrochromic contrast of the cell was

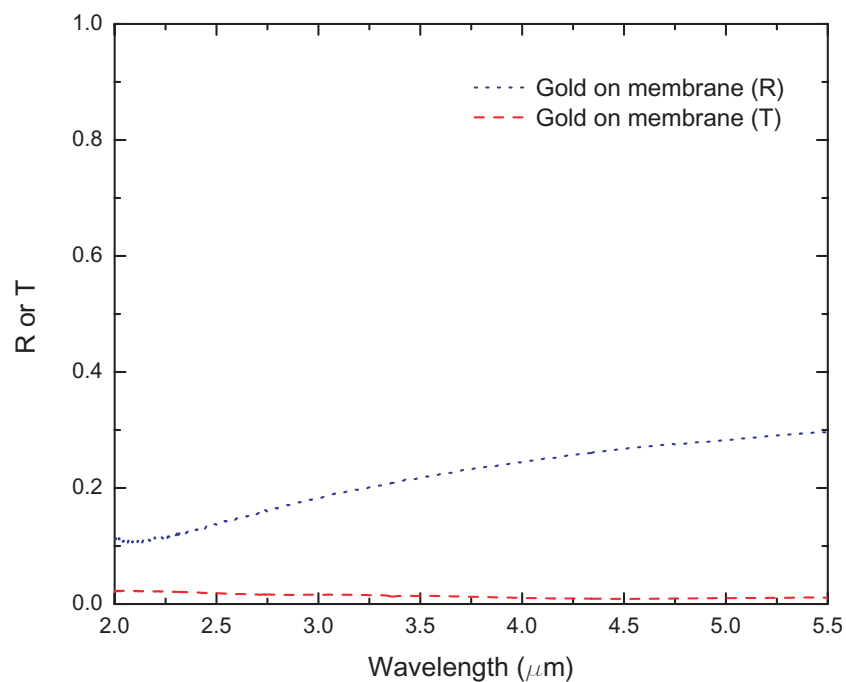


Figure A.2: Reflectance and transmittance measurements of the highly porous metallized membrane in the mid-infrared (MIR) region.

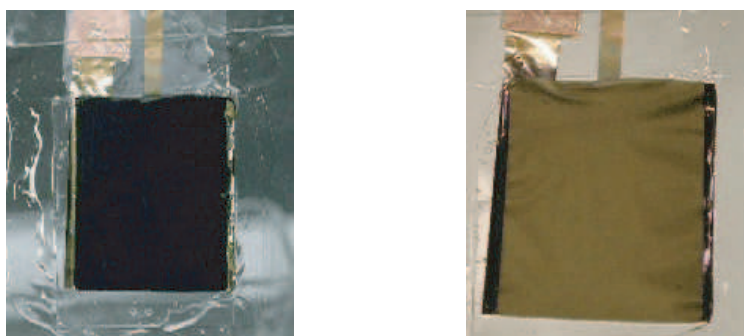


Figure A.3: Top-view photograph of a PProDOT-Me₂ polymer EC device (with metallized porous membrane as the WE) in its two extreme states. Left side: PProDOT-Me₂ in neutral state ($V_{cell} = -1.5\text{ V}$, dark blue). Right side: PProDOT-Me₂ in p-doped state ($V_{cell} = +1.0\text{ V}$, transparent).

investigated and, as can be seen from Figure A.5, it is very small for the far infrared region. This is mainly due to the thickness of the working polymer layer. Based on a thickness optimization study that have been performed [77], the electrochromic contrast for the region of interest becomes higher for much thicker films, more than 350 nm with optimum thickness around 500 nm. Consequently, these measurements will need to be repeated on a new EC cell with a thicker polymer film on the working electrode

before any conclusions could be drawn. Therefore, further work is needed concerning the specular reflectance of these microporous membrane reflective ECDs.

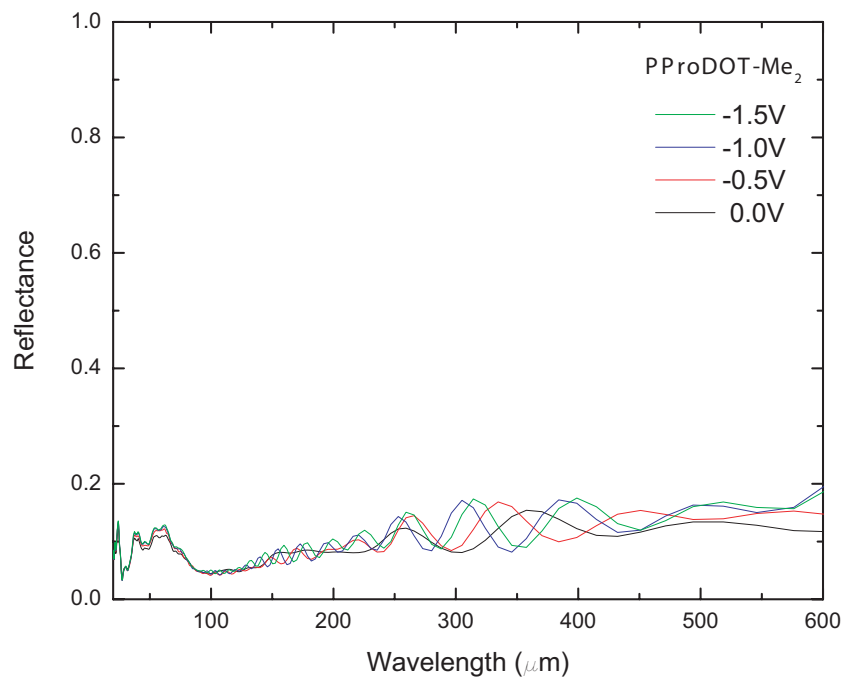


Figure A.4: Reflectance measurements of PProDOT-Me₂ on the highly porous metallized membrane in the far infrared (FIR) region, from 20 μm to 200 μm.

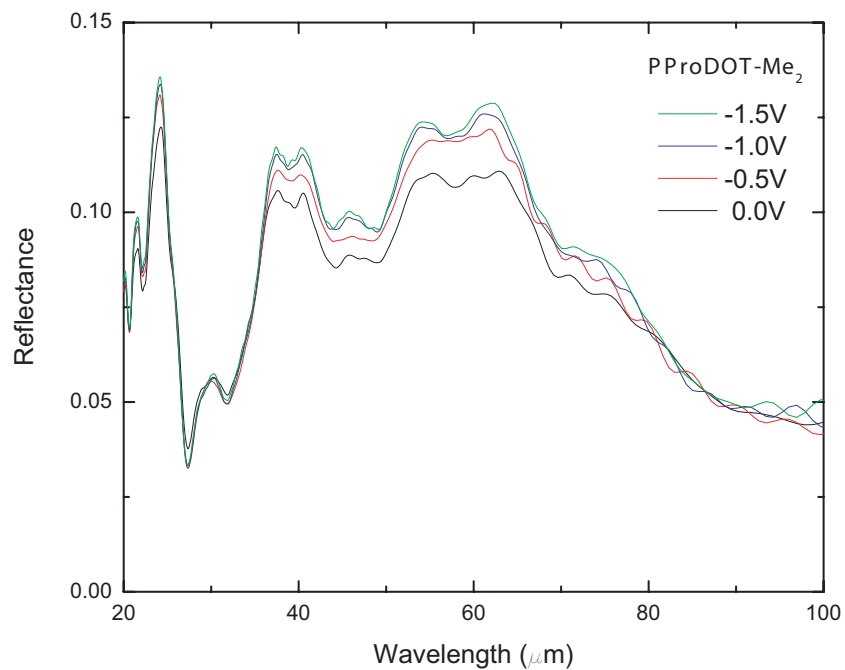


Figure A.5: Reflectance measurements of PProDOT-Me₂ on the highly porous metallized membrane in the far infrared (FIR) region, from 20 μm to 100 μm.

APPENDIX B
DRUDE-LORENTZ FITTING PARAMETERS

Table B.1: Drude-Lorentz fitting parameters for p-doped PEDOT films of three different thicknesses on SWNTs/PET.

ω_{pj}	ω_j	γ_j
5	14	19514
2338	3857	4122
2844	5628	1507
2767	1973	2950
1378	6931	2199
3387	9054	8308
707	11,346	2078
2890	13,110	8420
6865	37,460	24420
6718	52,581	439,232
$\epsilon_\infty =$	1.55	
$d_1 =$	2069 Å	
$d_2 =$	7982 Å	
$d_3 =$	5507 Å	

Table B.2: Drude-Lorentz fitting parameters for the PET film.

ω_{pj}	ω_j	γ_j
62	432	63
44	508	43
10	631	49
50	728	32
40	797	34
100	864	23
71	1030	24
186	1119	17
216	1320	155
17	1577	16
133	1718	43
31	1958	31
32	2115	63
24	2273	74
26	2400	62
100	864	23
33	2557	116
61	2901	120
47	2969	31
55	3063	161
35	3320	197
27	3446	40
39	3549	214
19	4093	52
50	4290	410
11	4692	51
18	5967	392
160	10,915	16,685
1431	42,317	4141
$\epsilon_\infty =$	1.60	
$d =$	747,240 Å	

Table B.3: Drude-Lorentz fitting parameters for the electrolyte gel layer.

ω_{pj}	ω_j	γ_j
20	445	35
31	513	19
54	613	108
83	890	19
107	1870	63
12	2092	57
30	2282	94
19	2374	78
25	2527	103
73	2948	220
15	3417	32
37	3552	86
30	4121	267
22	4420	93
5	5263	43
5	5999	41
$\epsilon_\infty =$	1.63	
$d =$	2,819,014 Å	

Table B.4: Drude-Lorentz fitting parameters for a PEDOT film in three different states; p-doped, slightly p-doped, and almost neutral.

p-doped			slightly	p-doped			neutral		
ω_{pj}	ω_j	γ_j	ω_{pj}	ω_j	γ_j	ω_{pj}	ω_j	γ_j	
13852	0	5038	10387	1419	2538	2182	3322	1195	
4083	0	23680	1105	57	1892	2369	5493	1766	
1997	14,889	4362	5363	10691	3613	2767	2417	2019	
416	16,248	2691	8404	17036	7533	4134	1957	3564	
897	17,399	2001	1333	22262	3286	5148	10765	4609	
9588	37,218	3997	4422	34248	4593	12376	16756	3593	
14,811	37,895	6055	11373	35246	7306	23402	36259	1411	
$\epsilon_\infty =$	1.77		$\epsilon_\infty =$	1.66		$\epsilon_\infty =$	2.06		
$d_{doped} =$	6712 Å		$d_{s-doped} =$	6314 Å		$d_{neutral} =$	6066 Å		

APPENDIX C PBEDOT-HX₂-PYR-PYR

Figure C.1 shows the cyclic voltammogram of PBEDOT-Hx₂-Pyr-Pyr on ITO/Glass in solution for an applied voltage range between -2.2 V and +0.9 V. In this measurements, both reduction states have been reached and the potential for each peak is shown versus SCE. The colors of the polymer film in n-doped (first reduction), neutral, and p-doped states are also shown. PBEDOT-Hx₂-Pyr-Pyr is one of the few polymers capable of forming a p-doped state as well as a stable n-doped state. The n-doped state of electroactive polymers is usually not stable due to the high reactivity of of the anion charge carrier to oxygen and water.

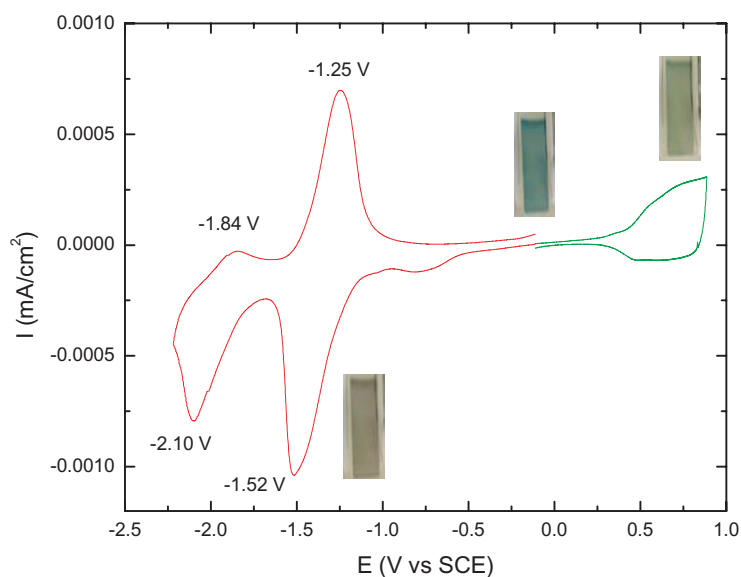


Figure C.1: Cyclic voltammogram of the oxidation and both reductions of PBEDOT-Hx₂-Pyr-Pyr on ITO/Glass. The color of the films at each states are also shown.

Figure C.2 shows the absorbance of PBEDOT-Hx₂-Pyr-Pyr on ITO/Glass in solution for an applied voltage range between -1.09 V to +0.81 V vs SCE. In this figure,

the depletion of the $\pi - \pi^*$ transition centered at around 1.8 eV and the doping induced interband transitions upon application of a voltage can be clearly seen.

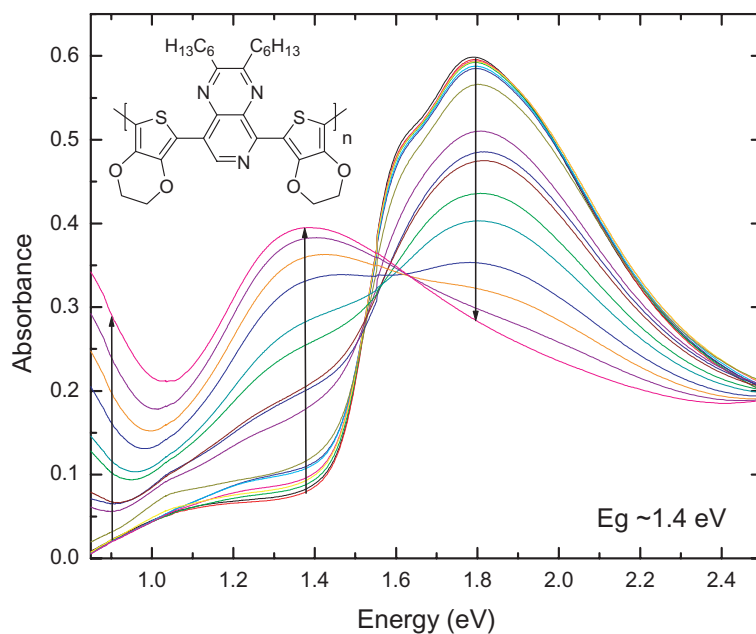


Figure C.2: Absorption measurements of PBEDOT-Hx₂-Pyr-Pyr on ITO/glass in the near infrared and visible regions at applied voltages within the range from -1.09 V to +0.81 V vs SCE.

The measurements presented in this Appendix have been performed by my collaborator in the Chemistry department, Timothy Steckler.

REFERENCES

- [1] C. K. Chiang, C. R. Fincher, Y. W. Park, A. J. Heeger, E. J. Louis H. Shirakawa, S. C. Gau, and A. G. MacDiarmid. *Phys. Rev. Lett.*, 39:1098, 1977.
- [2] H. Letheby XXIX. *J. Chem. Soc.*, 15:161, 1862.
- [3] A. G. MacDiarmid, M. Akhtar, C. K. Chiang, M. J. Cohen, J. Kleppinger, A. J. Heeger, E. J. Louis, J. Milliken, M. J. Moran, D. L. Peebles, and H. Shirakawa. *Journal of Electrochemistry Society*, 124:C304, 1977.
- [4] H. Shirakawa, E. J. Louis, A. G. MacDiarmid, C. K. Chiang, and A. J. Heeger. *Journal of the Chemical Society-Chemical Communications*, 16:578, 1977.
- [5] A. J. Heeger. *Rev. Mod. Phys.*, 73:681, 2001.
- [6] A. G. MacDiarmid. *Rev. Mod. Phys.*, 73:701, 2001.
- [7] H. Shirakawa. *Rev. Mod. Phys.*, 73:713, 2001.
- [8] W. R. Salaneck, R. H. Friend, and J. L. Brédas. *Physics Reports*, 319:231, 1999.
- [9] A. J. Heeger, S. Kivelson, J. R. Schrieffer, and W. P. Su. *Rev. Mod. Phys.*, 60:781, 1988.
- [10] J. L. Brédas. *Handbook of Conducting Polymers II*. Eds., T. A. Skotheim, Marcel Dekker, Inc., New York, 1986.
- [11] W. P. Su, J. R. Schrieffer, and A. J. Heeger. *Phys. Rev. B*, 22:2099, 1980.
- [12] J. L. Brédas and J. B. Street. *Acc. Chem. Res.*, 18:309, 1985.
- [13] R. S. Kohlman and A. J. Epstein. *Physical Properties of Polymers Handbook II*. Eds., J. E. Mark, AIP Press, Woodbury, New York, 1996.
- [14] W. P. Su, J. R. Schrieffer, and A. J. Heeger. *Phys. Rev. Lett.*, 42:1698, 1979.
- [15] Z. G. Soos and S. Ramasesha. *Phys. Rev. B*, 29:5410, 1984.
- [16] R. Kiebooms, A. Aleshin, K. Hutchison, F. Wudl, and A. J. Heeger. *Synthetic Metals*, 101:436, 1999.
- [17] P. Chandrasekhar. *Conducting Polymers, Fundamentals and Applications: A Practical Approach*. Ashwin-Ushas Corp., Inc, 1999.
- [18] K. Sengupta, I. Žutić, H. J. Kwon, V. M. Yakovenko, and S. Das Sarma. *Phys. Rev. B*, 63:144531, 2001.

- [19] K. Takimiya, M. Kodani, Y. Kataoka, Y. Aso, T. Otsubo, T. Kawamoto, and T. Mori. *Chem. Mater.*, 15:3250, 2003.
- [20] N. F. Mott. *Journal of Solid State Chemistry*, 88:5, 1990.
- [21] N. F. Mott and E. A. Davis. *Philosophical Magazine*, 17:1269, 1968.
- [22] N. F. Mott. *Rev. Mod. Phys.*, 40:677, 1968.
- [23] R. Menon, C. O. Yoon, D. Moses, and A. J. Heeger. *Handbook of Conducting Polymers*. 2nd edition; Eds., T. A. Skotheim, R. L. Elsenbaumer, J. R. Reynolds, Marcel Dekker, Inc., New York, 1998.
- [24] C. R. Fincher, M. Ozaki, M. Tanaka, D. L. Peedles, and A. G. MacDiarmid L. Lauchlan, A. J. Heeger. *Phys. Rev. B.*, 20:1589, 1979.
- [25] J. Hwang, D. B. Tanner, I. Schwendeman, and J. R. Reynolds. *Phys. Rev. B.*, 67:115205, 2003.
- [26] P. J. Nigrey, A. G. MacDiarmid, and A. J. Heeger. *Chem. Commun.*, 96:594, 1976.
- [27] J. H. Burroughes, D. D. C. Bradley, A. R. Brown, R. N. Marks, K. Mackay, R. H. Friend, P. L. Burns, and A. B. Holmes. *Nature*, 347:539, 1990.
- [28] I. D. Parker. *J. Appl. Phys.*, 75:1656, 1994.
- [29] J. R. Platt. *J. Chem. Phys.*, 34:862, 1961.
- [30] S. K. Deb. *Appl. Optics., Suppl.*, 3:192, 1969.
- [31] G. V. Granqvist. *Phys. Thin Films*, 17:301, 1993.
- [32] R. J. Mortimer. *Electrochimica Acta*, 44:2971, 1999.
- [33] D. R. Rosseinsky and R. J. Mortimer. *Adv. Mater.*, 13:783, 2001.
- [34] R. J. Mortimer. *Phys. Rev. Lett.*, 26:147, 1997.
- [35] C. J. Schoot, J. J. Ponjée, H. T. van Dam, R. A. van Doorn, and P. J. Bolwijn. *Appl. Phys. Lett.*, 64:23, 1973.
- [36] P. R. Somani and S. Radhakrishnan. *Materials Chemistry and Physics*, 77:117, 2003.
- [37] H. W. Heuer, R. Wehrmann, and S. Kirchmeyer. *Advanced Functional Material*, 12:89, 2002.
- [38] A. A. Argun, P-H. Aubert, B. C. Thompson, I. Schwendeman, C. L. Gaupp, J. Huang, N. J. Pinto, D. B. Tanner, A. G. MacDiarmid, and J. R. Reynolds. *Chem. Mater.*, 16:4401, 2004.
- [39] R. B. Bennett, W. E. Kokonasky, M. J. Hannan, and L. G. Boxall. Us patent 5,446,577. 1995.

- [40] P. Chandrasekhar. Us patent 5,995,273. 1999.
- [41] I. Schwendeman, J. Hwang, D. M. Welsh, D. B. Tanner, and J. R. Reynolds. *Adv. Mater.*, 13:634, 2001.
- [42] P. H. Aubert, A. A. Argun, A. Cirpan, D. B. Tanner, and J. R. Reynolds. *Chem. Mater.*, 16:2386, 2004.
- [43] A. A. Argun, M. Berard, P. H. Aubert, and J. R. Reynolds. *Adv. Mater.*, 17:422, 2005.
- [44] P. M. S. Monk, R. J. Mortimer, and D. R. Rosseinsky. *Electrochromism: Fundamentals and Applications*. VCH, Weinheim, Germany, 1995.
- [45] J. D. Jackson. *Classical Electrodynamics*. 3rd edition, John Wiley & Sons, Inc, New York, NY, 1998.
- [46] D. J. Griffiths. *Introduction to Electrodynamics*. 2nd edition, Part II, Prentice Hall, Englewood Cliffs, NJ, 1997.
- [47] M. Fox. *Optical Properties of Solids*. Oxford University Press, Inc, New York, NY, 2001.
- [48] F. Wooten. *Optical Properties of Solids*. Academic Press, New York, NY, 1972.
- [49] O. S. Heavens. *Optical Properties of Thin Films*. Dover Publications, Inc, New York, NY, 1991.
- [50] A. Vašíček. *Optics of thin films*. North-Holland Publishing Company, Amsterdam, Holland, 1960.
- [51] Advisor Editor Z. Knittl. *Optics of thin films. An Optical Multilayer Theory*. John Wiley & Sons, Inc, New York, NY, 1976.
- [52] A. W. Crook. *J.O.S.A.*, 38:954, 1948.
- [53] N. W. Ashcroft and N. D. Mermin. *Solid State Physics*. Thomson Learning, Inc, 1976.
- [54] VAC Vacuum/Atmospheres. *Inert Atmosphere & Vacuum Deposition Equipment*. Manual, New York, NY.
- [55] A. J. Bard and L. R. Faulkner. *Electrochemical Methods Fundamentals and Applications*. 3rd edition, Wiley, New York, 2001.
- [56] C. A. Thomas. *Donor-Acceptor methods for band gap reduction in conjugated polymers: the role of electron rich donor heterocycles*. PhD dissertation, University of Florida, Gainesville, Florida, 2002.
- [57] K. Doblhofer and K. Rajeshwar. *Handbook of Conducting Polymers*. 3rd edition; Eds., T. A. Skotheim, R. L. Elsenbaumer, J. R. Reynolds, Marcel Dekker, New York, 1998.

- [58] K. D. Möller and W. G. Rothschild. *Far Infrared Spectroscopy*. Wiley, New York, 1971.
- [59] R. J. Bell. *Introductory Fourier Transform Spectroscopy*. Academic Press, New York, 1972.
- [60] P. L. Richards. *Spectroscopic Techniques for the Far Infrared, Submillimeter and Millimeter Waves*. Ed., D. H. Martin, Amsterdam, Holland, 1967.
- [61] W. Herres and J. Gronholz. *Understanding FT-IR Data Processing; Part 2: Details of the spectrum calculation*. Bruker Analytische Messtechnik GmbH, Karlsruhe 21, West Germany, 1985.
- [62] W. Herres and J. Gronholz. *Understanding FT-IR Data Processing; Part 1: Data Aquisition and Fourier Transformation*. Bruker Analytische Messtechnik GmbH, Karlsruhe 21, West Germany, 1985.
- [63] E. L. Dereniak and G. D. Boreman. *Infrared Detectors and Systems*. Wiley, New York, 1996.
- [64] E. Hecht. *Optics*. 3rd edition, Addison-Wesley Longman, Inc, 1998.
- [65] M. Abramowitz. *Microscope: Basics and Beyond*. Vol. 1, Fellow New York Microscopical Society, for Olympus America Inc.
- [66] M. W. Davidson and M. Abramowitz. *Optical Microscopy*. Web site:, <http://micro.magnet.fsu.edu/primer/opticalmicroscopy.html>, August 2005.
- [67] Carl Zeiss Microscope Systems. *MPM 800 Microscope Photometer: Operation Instructions*. Carl Zeiss, Inc., Germany, 1993.
- [68] Carl Zeiss Microscope Systems. *Axioskop: Routine microscope for transmitted and incident light fluorescence, Operation Instructions*. Carl Zeiss, Inc., Microscope Division, Germany, 1993.
- [69] K. D. Cummings. *Optical Properties of a Random Small-Particle Composite*. PhD Dissertation, University of Florida, Gainesville, Florida, 1982.
- [70] R. D. Rauh. *Electrochimica Acta*, 44:3165, 1999.
- [71] P. Topart and P. Hourquebie. *Thin Solid Films*, 352:243, 1999.
- [72] A. Bessiere, L. Beluze, M. Morcrette, V. Lucas, B. Vianna, and J. C. Badot. *Chem. Mater.*, 15:2577, 2003.
- [73] H. Pages, P. Topart, and D. Lemordant. *Electrochimica Acta*, 46:2137, 2001.
- [74] Y. H. Chang, K. Lee, R. Kiebooms, A. Aleshin, and A. Heeger. *Synthetic Metals*, 105:203, 1999.
- [75] P. Chandrasekhar, B. J. Zay, G. C. Birur, S. Rawal, E. A. Pierson, L. Kauder, and T. Swanson. *Advanced Functional Materials*, 12:95, 2002.

- [76] J. S. Hale and J. A. Woolam. *Thin Solid Films*, 339:174, 1999.
- [77] J. Hwang. *Electrochemical spectroscopy of conjugated polymers*. PhD dissertation, University of Florida, Gainesville, Florida, 2001.
- [78] I. Schwendeman. *Optical and transport properties of conjugated polymers and their applications to electrochromic devices*. PhD dissertation, University of Florida, Gainesville, Florida, 2002.
- [79] K. Nakanishi and P. H. Solomon. *Infrared Absorption Spectroscopy*. 2nd edition, Holden-Day, San Francisco, 1977.
- [80] C. O. Banwell and E. McNash. *Fundamentals of Molecular Spectroscopy*. 4th edition, McGraw-Hill, London, 1994.
- [81] M. Cornick, M. Nikolou, D. B. Tanner, I. Schwendeman, and J. R. Reynolds. *Infrared spectral enhancement of an EC by water removal*. REU project, University of Florida, <http://www.phys.ufl.edu/REU/2002/reports/cornick.pdf>, August 2005.
- [82] S. Iijima. *Nature*, 354:56, 1991.
- [83] R. H. Baughman, A. A. Zakhidov, and W. A. de Heer. *Science*, 292:787, 2002.
- [84] M. S. Dresselhaus and P. C. Eklund. *Advances in Physics*, 49:705, 2000.
- [85] X. Blase, Lorin X., Benedict, Eric L. Shirley, and Steven G. Louie. *Phys. Rev. Lett.*, 72:1878, 1994.
- [86] R. Saito, M. Fujita, G. Dresselhaus, and M. S. Dresselhaus. *Appl. Phys. Lett.*, 60:18, 1992.
- [87] M. Ouyang, J. L. Huang, C. L. Cheung, and C. M. Lieber. *Science*, 292:702, 2001.
- [88] J. W. G. Wildöer, L. C. Venema, A. G. Rinzler, R. E. Smalley, and C. Dekker. *Nature*, 391:59, 1998.
- [89] T. W. Odom, J. L. Huang, P. Kim, and C. M. Lieber. *Nature*, 391:62, 1998.
- [90] Z. Wu, Z. Chen, X. Du, J. M. Logan, J. Sippel, M. Nikolou, K. Kamaras, J. R. Reynolds, D. B. Tanner, A. F. Hebard, and A. G. Rinzler. *Science*, 305:1273, 2004.
- [91] T. Guo, P. Nikolaev, A. Thess, D. T. Colbert, and R. E. Smalley. *Chem. Phys. Lett.*, 243:49, 1995.
- [92] A. G. Rinzler, J. Liu, H. Dai, P. Nikolaev, C. B. Huffman, F. J. Rodriguez-Marcias, P. J. Boul, A. H. Lu, D. Heymann, D. T. Colbert, R. S. Lee, J. E. Fischer, A. M. Rao, P. C. Eklund, and R. E. Smalley. *Appl. Phys. A*, 67:29, 1998.
- [93] I. W. Chiang, B. E. Brinson, R. E. Smalley, J. L. Margrave, and R. H. Hauge. *J. Phys. Chem.*, 105:1157, 2001.

- [94] Z. Chen. *Electric field induced transparency modulation in single wall carbon nanotube ultra-thin films and a method to separate metallic and semiconducting nanotubes*. PhD Dissertation, University of Florida, Gainesville, Florida, 2003.
- [95] M. E. Itkis, S. Niyogi, M. E. Meng, M. A. Hamon, H. Hu, and R. C. Haddon. *Nano Letters*, 2:155, 2002.
- [96] A. Ugawa, A. G. Rinzler, and D. B. Tanner. *Phys. Rev. B*, 60:R11 305, 1999.
- [97] A. Ugawa, J. Hwang, H. H. Gommans, H. Tashiro, A. G. Rinzler, and D. B. Tanner. *Curr. Appl. Phys.*, 1:45, 2001.
- [98] S. M. Bachilo, M. S. Strano, C. Kittrell, R. H. Hauge, R. E. Smalley, and R. B. Weisman. *Science*, 298:2361, 2002.
- [99] P. G. Collins, K. Bradley, M. Ishigami, and A. Zett. *Science*, 287:1801, 2000.
- [100] X. Liu, T. Pichler, M. Knupfer, and J. Fink. *Phys. Rev. B*, 70:205405, 2004.

BIOGRAPHICAL SKETCH

I was born in Athens, Greece. After finishing high school, I enrolled in the Physics Department of the University of Crete, where I obtained a B.S. in physics (2000), with a specialization in microelectronics. The thesis work was completed working in the Microelectronics Research Group (MRG). In 1999, under the auspices of the Erasmus student exchange program, I studied for six months at the Department of Experimental Solid State III, in the Research Institute for Materials (RIM) of the University of Nijmegen in Holland. My interests at that time were focused in the growth and optical characterization of inorganic semiconductors.

In 2000 I joined the graduate school of the Physics Department of the University of Florida. After a year of core courses, I joined Professor Tanner's research group. Two joint projects immediately drew my attention: one on electrochemically prepared conjugated polymers in collaboration with Professor Reynolds' group from the Chemistry Department and Professor Rinzler's research on transparent, single walled nanotube films. Both projects appeared fascinating from the very beginning. I have actively pursued research in these areas, an endeavor that has been very rewarding since.